NANYANG TECHNOLOGICAL UNIVERSITY

DEVELOPMENT OF AN AIR CONDITIONING COMPRESSOR FOR A 2-IN-1 ELECTRIC MOTOR FOR ELECTRIC VEHICLES

N. SATHEESH KUMAR

INTERDISCIPLINARY GRADUATE SCHOOL
ENERGY RESEARCH INSTITUTE @ NTU (ERI@N)

2016

DEVELOPMENT OF A DRIVE MOTOR FOR ELECTRIC VEHICLES WITH INTEGRATED REFRIGERANT COMPRESSOR

N. SATHEESH KUMAR

Interdisciplinary Graduate School

Energy Research Institute @ NTU (ERI@N)

A thesis submitted to the Nanyang Technological University in partial fulfilment of the requirement for the degree of

Doctor of Philosophy

2016

Statement of Originality

I hereby certify that the work embodied in this thesis is the result of original research and has not been submitted for a higher degree to any other University or Institution.

24-08-2016

. . . . . .

Date

. . . . . .

N. Satheesh kumar

Abstract

Electric Vehicles (EVs) are gaining popularity over gasoline powered vehicles due to its eco-friendly appeal. However, the market penetration of EVs is comparatively low, owing to its poor cruise range, cost and performance characteristics. Part of the reason for rapid battery drainage leading to poor cruise performance is due to the large electrical load contributed by the air-conditioning system. Data published by Mitsubishi Motors reveals that the air-conditioning system reduces the cruise-range of the EV by as much as 50% when operated at full capacity. Keeping this in focus, the objective of the present thesis is to design a new 2-in-1 motor electric motor for EVs that integrates the air-conditioning compressor, its motor and the traction motor in a single system. Thereafter the focus shifts to the design and development of a suitable compressing mechanism that suits the 2-in-1 motor design.

The 2-in-1 motor uses a coaxial shaft to achieve concentric placement of the traction and compressor drives. This arrangement provides the flexibility of independent torque and speed control of the motor drives and enables the drivetrain to operate at six unique modes never before achieved in conventional drivetrain architecture. A simulation based study has been performed on the 2-in-1 motor drivetrain architecture and the analysis point that cruise range of EV can be improved by 3.2%. Based on the findings, it is evident that the integration of the air-conditioning compressor with the traction drive results in enhancing the energy capturing capacity of the regenerative braking mechanism and decreases the power consumed from the battery. Further, the integrated unit boosts other advantages such as reduced material cost, improved reliability, a compact and light weight design.

The thesis also explores a new design variant of the fixed vane compressor. Significant reduction in re-expansion losses is the primary highlight of the newly designed compressor. Mathematical models of the conventional swing vane compressor and the new fixed vane compressor design are quantitatively

assessed. The theoretical study shown that the new compressor is 6.2% more efficient than the conventional swing vane compressor. Following that, experimental investigations has been performed on the new fixed vane compressor design to validate the compressor models. In general, there is a close agreement between the predicted and experimental mechanical power requirements.

In general, this research project shows that the 2-in-1 motor design is a practical solution that is expected to enhance the performance of EVs. In addition, the newly developed fixed vane compressor has the potential to outperform the existing state of the art rotary compressors.

Acknowledgements

Though I have devoted my efforts and time to this project, it would not have been made possible without the guidance, supervision and support of several individuals and organisations. First, I would like to thank my immediate family members for the love, support and kindness they have shown me.

I extend my deepest appreciation to Prof. Ooi Kim Tiow, main supervisor and Dr. Michael Schier, co-supervisor for providing unparalleled support and supervision. Both Prof. Ooi and Dr. Schier are more than just supervisors, they have become family friends and mentors who showed deep interest in my wellbeing and progress.

The Energy Research Institute at Nanyang Technological University (ERI@N), Prof. Subodh Mhaisalkar and Dr. Narasimalu Srikanth supported the author's research by providing sufficient financial backing and laboratory assistance.

The staff at Deutsches Zentrum für Luft- und Raumfahrt e.V. (DLR – German Aerospace Centre) played a critical role in the timely execution of the project. The unrestricted access to various tools and equipment enabled swift materialisation of this project. The author extends his appreciation to the support provided by DLR during his stay in Germany.

Lastly, I would like to thank the Almighty God for providing me with the strength, courage and blessing to endure this journey without much hindrance. In particular, I would convey my prayers to Lord Ganesh.

Abstract **i**

Acknowledgements **iii**

Figure Captions **ix**

Table Captions **xv**

1 Chapter 1 - INTRODUCTION **1**

1.1 Background 2

1.1.1 Environmental concern 2

1.1.2 History of EVs 3

1.1.3 Challenges faced by EVs 3

1.1.4 Electric vehicle cabin climatisation and challenges 4

1.2 Project motivation and purpose 5

1.3 Project Objectives and Scope 6

1.4 Dissertation Overview 7

2 Chapter 2 - LITERATURE REVIEW **9**

2.1 Impact of air conditioning on EV's cruise performance 10

2.2 Review of electronic integration of drive motors 13

2.3 Review of refrigeration cycle and compressor designs 15

2.3.1 Compressor classifications 15

2.3.2 Compressor variants 16

2.3.3 Capacity control 17

2.3.4 Compressor lubrication 19

2.3.5 Automobile air-conditioner compressors 21

2.3.6 Refrigerants for automobile compressors 26

2.4 Review of compressor mathematical models 30

2.4.1 Geometric model 30

2.4.2 Thermodynamic model 30

2.4.3 Heat transfer model 31

2.4.4 Valve model 32

2.4.5 Leakage model 33
2.4.6 Lubrication model 33
2.5 Concluding remarks 33

3 Chapter 3 – 2-IN-1 MOTOR AND COMPRESSOR SELECTION 35

3.1 2-in-1 Motor Structure 36
3.2 Operating modes for 2-in-1 motor 37
3.3 2-in-1 Motor design 42
3.4 Compressor selection 44
3.5 Compressor drive 47
3.6 Concluding remarks 49

4 Chapter 4 – COMPRESSOR DESIGN 51

4.1 Compressor capacity and volumetric flowrate 52
4.2 Compressor wall thickness 55
4.3 Dynamic balancing of compressor crankshaft 60
4.4 Journal bearing design 64
4.4.1 Journal bearing configuration and force analysis 64
4.4.2 Pressure distribution in a journal bearing 71
4.4.3 Model validation 76
4.4.4 Other design considerations 78
4.4.5 Parametric study 79
4.5 Minimising re-expansion losses in FVC 84
4.6 Vane and valve design 87
4.7 Concluding remarks 89

5 Chapter 5 COMPRESSOR MATHEMATICAL MODEL 91

5.1 Geometric Model 92
5.2 Thermodynamic model 98
5.3 Mass flow model 102

5.4 Performance penalty of re-expansion loss in SVC 104
5.5 Mechanical power loss model 107
5.6 Compressor reed valve & Mathematical model 110
5.6.1 Reed valve model 114
5.6.2 Solution scheme 118
5.6.3 Model validation using FEA 121
5.7 Simulation of the FVC using mathematical model 122
5.7.1 Thermodynamic model predictions 122
5.7.2 Reed valve model predictions 124
5.7.3 Mechanical power loss model predictions 125
5.8 Concluding remarks 126

6 Chapter 6 – COMPRESSOR COMPARATIVE STUDY 127

6.1 Introduction 128
6.2 Trapped gas volume 129
6.3 Simulation setup 131
6.3.1 Step independence test 132
6.3.2 Compressor geometry and boundary conditions 133
6.4 Results and discussion 133
6.4.1 Working chamber volume 133
6.4.2 Reduction in compressor capacity 136
6.4.3 Reduction in volumetric efficiency 138
6.4.4 Input power of FVC and SVC 139
6.5 Sensitivity analysis 140
6.6 Concluding remarks 141

7 Chapter 7 – EXPERIMENTAL STUDY AND VALIDATION 145

7.1 Prototype assembly procedure 146
7.2 Experimental test jig 147
7.3 Experimental procedure 151

7.4 Preliminary tests 152
7.4.1 Dimension inspection 152
7.4.2 Dynamic balance of the compressor driveshaft 155
7.4.3 Valve operation 156
7.5 Comparison of predicted and measured results 159
7.5.1 Mechanical power 159
7.5.2 Mass flow rate 162
7.6 Post-experiment analysis 163
7.7 Concluding remarks 165

8 Chapter 8-CONCLUSIONS AND FUTURE WORK 167
8.1 The 2-in-1 Motor design overview 168
8.2 Compressor design 170
8.3 Simulation studies 171
8.4 Project contributions 173
8.5 Future work 174

Appendix A – DRIVETRAIN ARCHITECTURE & SIMULATION A1
Appendix B – MITSUBISHI I-MIEV AC SYSTEM SPECIFICATIONS B1
Appendix C – MOTOR SPECIFICATIONS AND CHARACTERISTICS C1
Appendix D – MESH INDEPENDENCE TEST D1
References R1

Figure Captions

Figure 1.1 Factors impeding the market penetration of EVs[6] 4
Figure 2.1 Impact of Auxiliary Electrical load on EV's range 11
Figure 2.2 Impact of A/C on i-MiEV's cruise range [16] 12
Figure 2.3 Battery cost percentage of an electric car for various battery types 12
Figure 2.4 Control of traction and compressor drives using independent inverters [9] 13
Figure 2.5 Electrically integrated traction and compressor motors [9] 14
Figure 2.6 Semi-Hermetic compressor with integrated control unit [18] 16
Figure 2.7 Compressor classifications and variants [20] 17
Figure 2.8 Belt driven compressor in a gasoline driven car [21] 18
Figure 2.9 A/C unit of i-MiEV [16] 18
Figure 2.10 Lubricant miscibility chart [23] 20
Figure 2.11 Schematic of a sliding vane compressor [25] 21
Figure 2.12 Schematic view of a screw compressor [32] 22
Figure 2.13 Scroll compressor nomenclature [36] 24
Figure 2.14 Swash plate VDC nomenclature [40] 25
Figure 2.15 Rolling piston compressor nomenclature 26
Figure 2.16 COP of the prototype car at test conditions-A and B [43] 28
Figure 3.1 Integrated drivetrain architecture configuration 36
Figure 3.2 Mode 1: where the drive motor provides tractive power 38
Figure 3.3 Mode 2: where the compressor drive operates the A/C compressor ... 39
Figure 3.4 Mode 3: Boost function 40
Figure 3.5 Mode 4: Air-conditioning during regenerative braking 40
Figure 3.6 Mode 5: Air-conditioning and max charging during regenerative braking 41
Figure 3.7 3D model of the 2-in-1 motor 42
Figure 3.8 Internal clutch mechanism transfers recuperated energy from the traction drive to compressor 43
Figure 3.9 Swing Vane Compressor working principle [94] 46
Figure 3.10 (a) Swing Vane Compressor, (b) Fixed Vane Compressor 47

Figure 3.11 Compressor drive consists of PMSM motor and a planetary gear system..... 48
Figure 4.1 FVC terminologies 54
Figure 4.2 Pressure forces that acts on the compressor end faces 55
Figure 4.3 Actual boundary condition for the front end face of the compressor .. 57
Figure 4.4 Cylinder end wall deflection under uniform internal pressure (a) front face, (b) rear face..... 58
Figure 4.5 Von Misses stresses acting on the cylinder end faces (a) front face, (b) rear face..... 59
Figure 4.6 Dynamic balancing of Eccentric mass in two planes [103]..... 60
Figure 4.7 Placement of the balancing masses results in crank shaft deflection [103]..... 62
Figure 4.8 In-plane counter weight inserted into the eccentric..... 63
Figure 4.9 In-Plane counter weight used to cancel the centrifugal force produced by the eccentric piston..... 63
Figure 4.10 Journal bearing configuration in fixed vane compressor..... 64
Figure 4.11 Free body diagram of the fixed vane compressor..... 65
Figure 4.12 Torsional loads on the fixed vane compressor 68
Figure 4.13 Refrigerant pressure with respect to crank angle..... 70
Figure 4.14 Variation in bearing load with respect to journal angle..... 71
Figure 4.15 Pressure distribution of around a journal bearing [107] 72
Figure 4.16 (a) Oil film pressure and (b) thickness around the journal bearing ... 75
Figure 4.17 Lubricant pressure distribution predicted by CFD and analytical 77
Figure 4.18 Breakdown of hydrodynamic lubrication at negative pressure region [108]..... 78
Figure 4.19 Surface velocity vector plot of a journal..... 82
Figure 4.20 Parametric analysis of key design parameters of a journal bearing... 83
Figure 4.21 (a) Pressure and (b) oil film thickness distribution of the journal bearing..... 85
Figure 4.22 Trapped gas volume in SVC towards the end of compression process 85
Figure 4.23 SVC leakage paths..... 86
Figure 4.24 Comparison between the conventional and new compressor design (a) SVC and (b) New FVC design 87

Figure 4.25 Prototype of the newly designed FVC 87
Figure 4.26 The vane mating surfaces has been grooved to accommodate an O-ring 88
Figure 4.27 Discharge inlet area and reed valve deflection height relationship ... 88
Figure 5.1 Geometric Relationships 92
Figure 5.2 Vane protrusion relationship 94
Figure 5.3 Suction and discharge ports of swing compressors (a) Swing Vane Compressor (b) Fixed Vane Compressor 95
Figure 5.4 Area of a circle segmented by a cord 96
Figure 5.5 FVC discharge port. 96
Figure 5.6 Energy balance diagram of a generic compressor 99
Figure 5.7 Flow through a sharp edged orifice 102
Figure 5.8 FVC discharge port 104
Figure 5.9 Re-expansion loss mechanism in a SVC (a) Suction and compression chambers (b) trapped mass at the end of compression process (c) leakage of trapped mass into suction chamber during the re-expansion stroke. 105
Figure 5.10 Frictional loss in a lip seal as a function of rotational speed and shaft diameter [119] 109
Figure 5.11 Rotary piston compressor assembly nomenclature 110
Figure 5.12 Generic response of a reed valve during discharge phase 111
Figure 5.13 Motion of reed valve with weak stiffness [122] 111
Figure 5.14 Over-compression loss due to stiff discharge valve [24] 112
Figure 5.15 Reed valve over the discharge port 114
Figure 5.16 Element geometry and nodal degrees of freedom 115
Figure 5.17 Valve geometry defined by nodal distribution along x-axis 115
Figure 5.18 Cantilever beam subjected to discreet transverse load 116
Figure 5.19 Flow chart of compressor solver model 120
Figure 5.20 Model validation using a FEA software 121
Figure 5.21 Plots generated by the thermodynamic model 123
Figure 5.22 Plots generated with the reed valve model coupled to the thermodynamic model 125
Figure 5.23 Mechanical losses as a function of angular velocity 125
Figure 6.1 Trapped gas volume in SVC towards the end of compression process 128

Figure 6.2 Refrigerant mass variation with respect to crank angle and trapped mass [126] 129
Figure 6.3 (a) Trapped gas volume in SVC (b) Leakage of trapped gas into the suction chamber 130
Figure 6.4 Compressor discharge location (a) Discharge port located on the cylinder, (b) Discharge port located on the fixed vane. 132
Figure 6.5 Step independence test 133
Figure 6.6 Chamber volume as function of crank angle for (a) SVC and (b) FVC 135
Figure 6.7 Discharge volume in FVC 135
Figure 6.8 Normalised variation of chamber mass with shaft angle 136
Figure 6.9 (a) Temperature and (b) Pressure variation of refrigerant with shaft angle 137
Figure 6.10 Variation of mass as a function of crank angle in a SVC. With and without re-expansion of leakage gas trapped in discharge slot. 138
Figure 6.11 Variation of mass as a function of crank angle in a FVC. With and without re-expansion of leakage gas trapped in discharge slot. 139
Figure 6.12 P-V diagram of the SVC and FVC with re-expansion losses 140
Figure 6.13 Effect of (a) discharge port volume, (b) discharge pressure,(c) operating speed and (d) discharge coefficient on quantity of trapped mass 142
Figure 7.1 Fixed vane compressor module 145
Figure 7.2 Prototype assembly procedure 146
Figure 7.3 A schematic diagram of the experimental setup 147
Figure 7.4 Contactless tachometer for measuring compressor shaft speed 148
Figure 7.5 The experimental setup 148
Figure 7.6 Pressure tank setup 149
Figure 7.7 AC variable speed drive for regulating the compressor speed 150
Figure 7.8 Motor efficiency and power factor curves 151
Figure 7.9 Coordinate measuring machine used to inspect compressor build quality 153
Figure 7.10 Defective piston is replaced with a new piston to ensure the required tolerance are met. 154
Figure 7.11 Vibration with respect to motor speed 155
Figure 7.12 Vane test setup schematic diagram 156

Figure 7.13 (a) Vane test jig assembly, (b) Adhesive sealants prevent leakage between the mating surfaces 157
Figure 7.14 Valve test jig 158
Figure 7.15 Pressure-flow characteristics of the reed valve 158
Figure 7.16 Vane pressure loss 159
Figure 7.17 Viscosity-Temperature relationship of ISO grade lubricants 160
Figure 7.18 Measured and predicted compressor mechanical power 161
Figure 7.19 Measured and predicted compressor discharge mass flow rate 164
Figure 7.20 Compressor condition after experimental investigations (a) Cylinder, (b) Vane bushing, (c) Piston 165
Figure 8.1 2-in-1 motor cut-away view 168
Figure 8.2 Internal clutch mechanism transfers recuperated energy from the traction drive to compressor 170
Figure A.0.1 FBD of a vehicle in a regenerative braking 3
Figure A.0.2 Motor torque-speed curves 4
Figure A.0.3 Variation in inertial, regenerative braking, braking, tractive and drag forces as a function of time 6
Figure A.0.4 Regenerative braking torque generated in (a) a conventional EV and (b) the 2-in-1 motor 7
Figure A.0.5 Variation in the braking forces (F_{reg} and F_{brk}) with respect to time in comparison to the forward inertial force. (a) with a deceleration rate of 0.66g and (b)with a deceleration rate of 0.30g 8
Figure A.0.6 Decreasing the regenerative braking force by varying the transmission ratio 9
Figure A.0.7 The graphical setup in Simulink® for predicting the efficiency improvement 10
Figure A.0.8 Simulated vehicle's (a) velocity (b) regenerative power on ECE 15+EDUC drive cycle 13
Figure A.0.9 Excess regenerative power directed to the battery 13
Figure A.0.10 Percentage savings in battery energy for an electric vehicle driven by 2-in-1 motor for various EU legislative drive cycles. 14
Figure D.0.1 Element count and mesh quality reported by the COMSOL software 1
Figure D.0.2 Mesh independence test results 2

Table Captions

Table 2.1 Thermodynamic properties of R1234yf and R134a Refrigerants [24] 29
Table 3.1 2-in-1 motor operating modes 37
Table 3.2 A comparative study between automobile compressors 45
Table 4.1 Compressor technical requirements 52
Table 4.2 Major compressor dimensions 54
Table 4.3 Journal bearing model boundary conditions 74
Table 4.4 Plain journal bearing operating conditions 76
Table 4.5 Parametric sweep of key parameters governing journal-bearing design 80
Table 4.6 Recommended ISO Viscosity for Machine and Equipment design [115] 80
Table 4.7 Key journal bearing design specifications 84
Table 4.8 List of leakage paths [116] 86
Table 5.1 SVC cycle analysis 105
Table 5.2 Dampening ratio of a reed valve of rolling piston compressor [123] 118
Table 6.1 SVC and FVC geometry and boundary conditions 134
Table 6.2 Power requirements of SVC and FVC with and without re-expansion losses 140
Table 6.3 Variable identified for sensitivity analysis and their corresponding range 141
Table 7.1 Measuring device accuracy 149
Table 7.2 Designed and measured dimensions of the prototype compressor 154
Table 7.3 Localised compressor temperature and lubricant viscosity 160
Table A.0.1 Simulated vehicle parameters 2
Table A.0.2 Regenerative braking with and without the AUX load of 3kW 8
Table A.0.3 EU legislative cycle analysis 12

Dimensional parameters

a	radius ratio (R_p/R_c), acceleration [m/s^2]
A	area [m^2]
b	reed valve width [m]
c	bearing clearance [m]
Cd	discharge coefficient, drag coefficient
D	diameter [m], flexural rigidity [$N\ m^2$]
e	eccentricity [m]
E	Young's modulus [Pa], net energy [J]
F	force [N]
g	gravitation constant – [$9.81 m/s^2$]
h	cylinder height [m], wall thickness [m], fluid thickness [m]
I	moment of inertia [$kg\ m^2$]
L, l	length [m]
m	mass [kg]
$\dot{m}$	mass flow rate [kg/s]
M	moment [Nm], port depth [m]
N	RPM, factor of safety
n	revolutions per second
P	power [W], pressure [Pa]
pf	power factor
Q	heat energy [J], lateral load [N]
R	radius [m]
r	radius [m], transmission ratio, radial position [m]
T	torque [Nm], temperature [K]
t	time [s]
U	fluid velocity field [m/s]
u	internal energy [J/kg]
V	volume [m^3]
v	pisson ratio
v_s	specific volume [m^3/kg]

Greek letters

η	efficiency
θ	crank angle (rad)
ϕ	Integration upper limit (rad)
δ	vane protrusion length (mm)
ω	angular velocity (rad/s)
ζ	dampening ratio
λ	eigen vector
σ	standard deviation, stress (N/m^2)
μ	viscosity ($kg/m \cdot s$), friction coeff.
ρ	density (kg/m^3)
γ	Newmark constant
β	Newmark constant
Φ	mass normalised eigen vector
α	angular acceleration (rad/s^2)
$\varepsilon_1, \varepsilon_2$	clearance [m]

Subscript

0	minimum oil thickness, origin
1	orifices inlet
2	orifices outlet
avg	average
b	bushing (vane)
bf	contact surface between piston and cylinder head
c	cylinder
cf	contact surface between piston and eccentric OR centrifugal force
cv	control volume
d	discharge

w	width [m], lateral deflection [m]
W	work [J]
z	elevation [m]

Superscript

e	element
T	transpose

Matrix notations

C	dampening matrix
C_{ij}	coefficient of flexibility influence
M	mass matrix
U	displacement vector
K	stiffness matrix, flow coefficient

el	electrical power
fl	piston-end face loss
FVC	fixed vane compressor
g	gas
i	inlet
j	journal
jb	journal bearing loss
ls	lip seal loss
p,s	mechanical
min	minimum
o	outlet
p	piston
p,s	piston slipping motion angular velocity
pe	piston-eccentric loss
r	relative angular velocity
s	suction
SVC	Swing Vane Compressor
t	tangential
vd	vane discharge port
vf	vane friction
vn	vane
reading	measurement obtained from instrument at reference conditions
corrected	corrected instrument measurement

Chapter 1
INTRODUCTION

The chapter begins with the importance of Electric Vehicles (EVs) from environmental point of view followed by the difficulties faced by EV in terms of its limitations. Subsequently, the necessity for a climate control unit in EV and the challenges faced is also stated. The focus then shifts towards defining the project's purpose, objective and novelty-which is the design and development of an A/C compressing mechanism for a 2-in-1 motor for EVs.

This section published substantially as :

N. Satheesh Kumar and M. Schier, "Increasing efficiency of ecological vehicles by integrating auxiliary units directly to the traction shaft," *Ecological Vehicles and Renewable Energies (EVER), 2014 Ninth International Conference on*, Monte-Carlo, 2014, pp. 1-6.

1.1 Background

1.1.1 Environmental concern

Temperature rise due to global warming is a concern according to the Intergovernmental Panel on Climate Change (IPCC) [1]. It has been estimated that the global temperature has increased by 0.4 - 0.8^{o} C within the past century [1]. The emission of greenhouse gases (GHG) is one of the main reason that fuels the global warming. The most common GHG includes ozone (O_3), carbon dioxide (CO_2), methane, water vapour and nitric oxide (NO_2). Although natural processes emit these gases, emissions from human related activities are aggravating the concentration levels towards a tipping point [1].

The IPCC has forecasted that emissions from human sources will rise between 25 to 90% by 2030 in the absence of climate policies [1] and will result in sea levels increase to 18 - 60cm. To mitigate the negative effects of global warming, the IPPC has recommended that GHG emissions should be reduced by 50 to 80% below 2000 levels by the end of 2050 in order to control the temperature rise within 2.0-2.4^{o} C [1]. In addition, a universal agreement was made in Conference of Parties in 2015 to cap the global temperature rise to below 2^{o} C [2]. Hence, to attain the target emission levels and temperature, collaborative efforts between various sectors must be undertaken.

The transportation sector accounts for around 5% of global GHG emissions [3], of which, gasoline powered vehicles are the dominant contributors. The introduction of EV is one of the possible means for the transportation sector to meet the increasing demand for personal transportation while minimising the contribution towards GHG emissions.

1.1.2 History of EVs

The first inventor of EV is inconclusive, though it is said that in 1829, a Hungarian named Anyos Jedlik developed the first EV [4]. Robert Anderson from Scotland invented an electric-powered carriage between 1832 - 1839. In addition, numerous other inventors are credited for the invention of the EV [4]. In those days, EVs are preferred over gasoline cars as they were quiet, efficient and able to start with the push of a button (unlike gas cars that required crank). Nevertheless, the appeal for EV was lost in the dawn of the 20th century due to the availability of cheap oil and mass production facilities brought by the industrial revolution. By 1920, the Internal Combustion(IC) engine wiped out the demand for EVs. However, the consequence of embracing IC engines over EVs began to emerge – air pollution. Recently, the volatile oil prices, strong requirements to mitigate carbon emissions and the uncertainty of carbon energy sources has placed the automotive industries under pressure to reconsider EV as a suitable alternative.

1.1.3 Challenges faced by EVs

Though major advancements have enhanced the attractiveness of EVs, scope for improvement are ample. EVs were introduced in commercial marketplace between 1851-1900 [5]. To date, the limited travel range for a given battery charge and high capital costs associated with EV remains as important factors hindering the widespread acceptance of EVs (Figure 1.1). Hence, the main challenge faced by EVs are two folds: come down in cost and improved performance with that of gas-powered vehicles, specifically the cruise range per battery charge.

EV draws its energy from a battery pack or fuel cells to operate electric motor(s) to produce necessary torque and speed for propulsion. In general, the batteries powering the EVs have a poor energy density in comparison to gasoline. Specific energy of 12kWh/kg (43000kJ/kg), whereas an energy storage system based on advanced nickel-metal hydride have a specific energy of 0.1kWh/kg (360kJ/kg) [7].

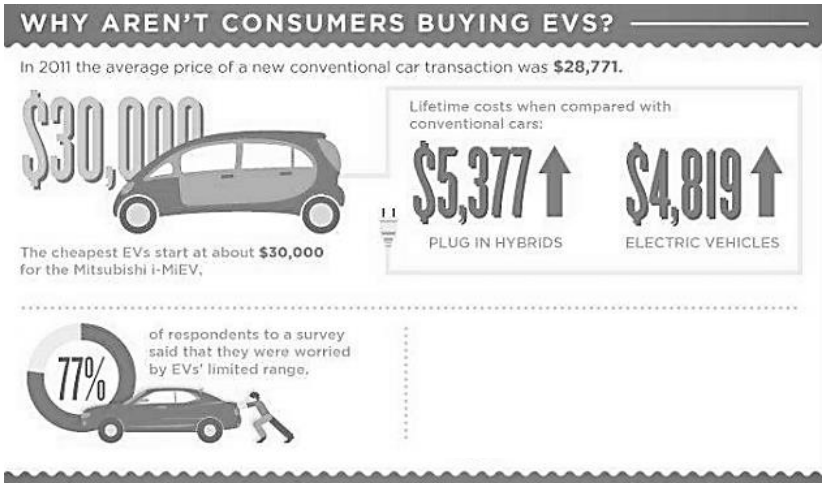

Figure 1.1 Factors impeding the market penetration of EVs[6]

Consequently, batteries powering EVs tend to be bulky and heavy in construction to maximise its energy storing capacity. Owning to the poor energy density of batteries, high power electrical loads from traction and Air-Conditioning (A/C) compressor motors expedites the battery drain, leading to poor cruise range performance.

1.1.4 Electric vehicle cabin climatisation and challenges

To meet the comfort requirements, latest EVs boast a spacious cabin, an upgraded instrument layout and ergonomically designed seats. In addition, consumers expect complete control over the cabin air temperature and in response; an A/C system has become a standard feature in EV.

The primary task of an A/C system is to extract heat from the cabin and rejects it to the surrounding. At the very centre of the A/C system is the compressor that circulates the refrigerant around the refrigeration circuit and creates conditions for heat absorption and rejection at evaporator and condenser respectively. An automobile compressor has to perform these essential tasks over a wide range of operational speeds and ambient temperatures. In addition, an automotive compressor has to meet stringent constraints of weight, size and cost.

An IC engine converts merely 20% of input energy in propelling the vehicle, while an electric motor operates with an efficiency of 78.8% - 92.4% [8]. Regardless of the drive unit type, the inefficiency of the drive system manifest as waste heat. Depending on the effectiveness of the thermal insulation of the cabin, a fraction of wasted heat infiltrates the cabin and adds to the thermal heat loads. Additionally, the cabin also has a poor thermal resistance to heat transfer through solar radiation. Secondly, as the vehicle travels at highway speeds, the convective heat transfer coefficient between the skin of the vehicle and the ambient air rises. This once again weakens the thermal resistance of the cabin, thereby providing another path for heat to transfer into the vehicle. Therefore, the automobile compressor has to operate for an extended period to maintain the cabin temperature.

1.2 Project motivation and purpose

Given the challenges that impend the acceptance of EVs, the motivation of this project is to improve the appeal of EVs by:

- integrating components that are common to A/C compressor and the drive motor to reduce the overall weight and cost through material and component reduction, and
- introducing a mechanism that can better recover the breaking energy so as to improve the cruise range

Hence, in this project, the A/C compressor and its drive motor, and the traction motor are housed together. Doing so will permit the common components such as mounting brackets, cooling mechanism, bearings, electromagnetic shielding to be shared between them. In the regenerative mode of the EV, the main motor also acts a generator to convert the braking energy into electrical energy for storing in battery for future usage. Generally, this braking energy can overwhelm the capacity of the main motor (now acts as generator), during which the excess energy has to be dissipated in brake pads as wasted energy. By incorporating the compressor motor within the same housing of the main motor, the compressor motor can add on to the regenerative capacity of the main motor. This additional regenerative capacity is

expected to further improve the cruise range of the EVs. This new system will be termed as 2-in-1 motor.

This project involves the design of the 2-in-1 motor and then focuses on the detailed study involving design and development of an air-conditioning compressor for the 2-in-1 motor.

1.3 Project Objectives and Scope

The objective of this project is to first conceptualise and design the 2-in-1 motor. It is then followed by detailed study of the compressing mechanisms designed and developed in this project.

The outline of activities in order to meet the project objective is identified as follows.

i. Review the benefits of integrated system design to acknowledge the advantages and disadvantages
ii. To understand the state of the art of existing automotive compressor technology to identify the advantages and disadvantages of the various compressor technologies
iii. Modelling and simulation of 2-in-1 drivetrain architecture to identify its benefits and to approximate the efficiency gains *(refer to appendix A)*
iv. Design a compressing mechanism that is apt for the 2-in-1 motor drivetrain architecture
v. Identify technical requirements of the compressor and formulate mathematical models to facilitate theoretical and parametric analysis of the compressor performance
vi. Design, fabrication, instrumentation and test the performance of the compressor prototype
vii. Compare the measurement and the predictions from the mathematical model to validate the theoretical model

1.4 Dissertation Overview

Chapter 2 reviews the state-of-the art of the electric vehicle climatisation challenges, integrated design concepts and existing compressor designs. In addition, mathematical modelling aspects of compressor are also reviewed.

Chapter 3 focuses on the basic structure of the 2-in-1 motor and discusses its various operational modes. A practical design solution deploying the 2-in-1 motor architecture is introduced. A comparative study is also included to identify a suitable compressing mechanism for the 2-in-1 motor. Chapter 4 details the design process of the selected compressor mechanism and highlights a number of key innovations of the new compressor design, namely in-plane balancing and discharge through vane.

Chapter 5 describes the mathematical formulations to develop an appropriate model to investigate performance characteristics of the proposed compressor design. As such, the geometric equations, thermodynamic, mass flow and valve response models are formulated. A theoretical comparative study is then presented in Chapter 6 to surface the benefits of discharging through vane.

Chapter 7 discusses the experimental setup to investigate the prototype compressor. The experimental findings and critical analysis of the results in relation to the theoretical predications are also presented. Chapter 8 concludes this research project and it also proposes the future direction of the project.

Chapter 2
LITERATURE REVIEW

This chapter lays the background for subsequent chapters by reviewing available literatures to establish the state-of-the art of electric vehicles, integrated compressor design, challenges in automotive air conditioning, compressing mechanisms and compressor mathematical models. An integrated unit serving the dual purpose of providing the traction power and air-conditioning function is yet to be invented. In fact, the first paper exploring the possibility of electronic integration of traction motor and A/C compressor motor was not published until 2007 [9]. *Hence, limited knowledge is available within the open literature which is relevant to the research area explored by this research project.*

2.1 Impact of air conditioning on EV's cruise performance

The first A/C systems were installed in vehicles in the early 1950s [10]. Decades later, in the 1970s and 1980s these proved to be luxurious feature of any vehicle. Today, almost 95% of cars and light trucks are equipped with A/C systems. They have become a standard in most vehicles, adding comfort as well as safety. Aside from cooling, the latest A/C system incorporates an array of features such as de-misting and de-frosting, air filtering and humidity control. In addition, the flexibility to operate the vehicle with closed windows enhances its aerodynamic performance.

On average, an automobile is driven for 250 hours per year [11]. This roughly equates to 115 hours of A/C system operation [12], which corresponds to 45% of the vehicle usage. The power consumption of any vehicle peaks during the usage of the A/C system. For the case of electric vehicles, the increased power consumption leads to low cruise range for a given charge. The A/C system in an EV acts as a parasitic load, as the system draws in energy only when the passenger chooses to turn it on. Such an electrical load is often termed as "off-cycle" electrical load. Other off-cycle loads include wipers, stereo systems, heated seats, head/tail lights, and defrosters. Though these loads tap into the battery power, the A/C system is unique as it requires a considerably larger load. This large electrical load results in rapid depletion of the stored energy. In fact, it is estimated that the use of air conditioning typically decrease the cruise range of electric vehicle by 33% [13].

Farrington and Rugh [14] provided a comprehensive insight on the detrimental impact of auxiliary electrical load on cruise range of electric vehicles. The study simulated a five-passenger EV powered by NiMH battery using ADVISOR (Advanced Vehicle SimulatOR) software [15]. The flexibility of the simulation platform allowed scheduled application of the auxiliary electrical loads based on U.S Environmental Protection Agency certification procedures: FUDS (an urban driving cycle[1]), HWFET (a highway driving cycle), SC03[2] and US06[3]. Figure 2.1

[1] A drive cycle is a series of data points representing vehicle's speed with respect to time
[2] An urban drive cycle with the vehicle A/C unit turned on at a lab temperature of 35^0C
[3] An aggressive drive cycle with abrupt and rapid speed fluctuations

depicts the summary of the simulation results. Considering SC03 drive cycle and an EV operating with 500W of base auxiliary electrical load, an additional 3000W to power the air-conditioning will have its cruise range decreased from 118km to 78km, or by a factor of 36%. The author identified the air-conditioner as the single large electrical load that leads to drastic reductions in vehicle's range. The study concluded that even a marginal improvement in air-conditioning efficiency used in conventional gasoline vehicle would result in a huge reduction in carbon emissions due to the volume of new cars sold each year.

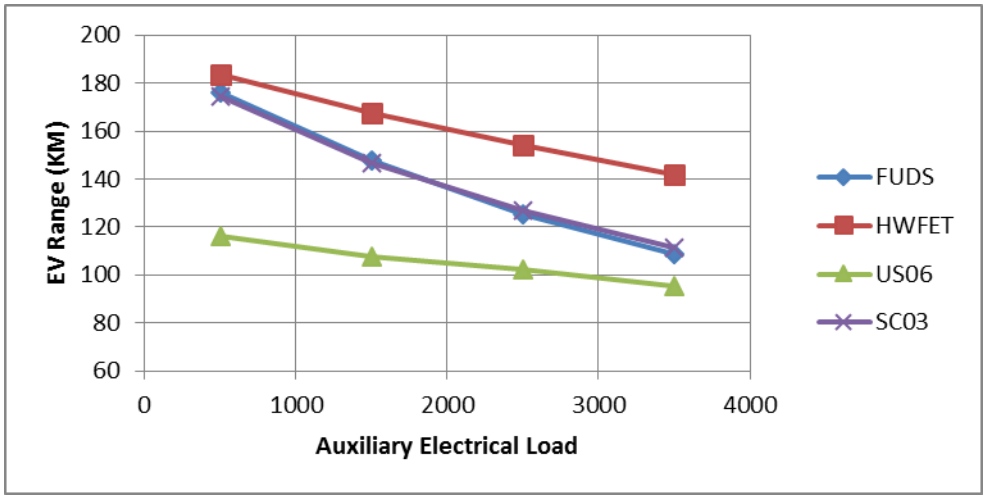

Figure 2.1 Impact of Auxiliary Electrical load on EV's range

In another study, Mitsubishi Motors subjected its recent EV, i-MiEV on number of tests to measure the drop in cruise range due to the operation of A/C [16]. The maximum cruise range of the vehicle was established by conducting the first run with A/C turned off. In the subsequent runs, the A/C unit was operated with moderate and maximum settings to determine its effect on the cruise range. Based on the results shown in Figure 2.2, it can be deduced that cruise range decreases by 30% when A/C is operated with moderate settings and by 48% when operated with maximum settings.

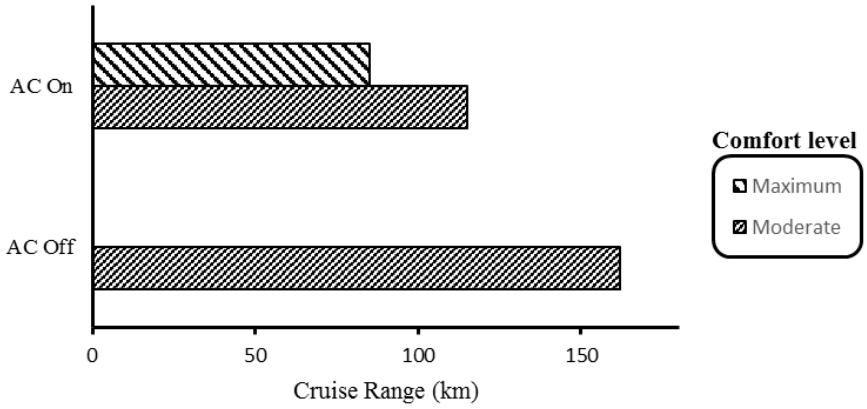

Figure 2.2 Impact of A/C on i-MiEV's cruise range [16]

The poor cruise range is partially due to the existing state of the storage technologies. Batteries are typical used in EVs as an energy storage medium and these batteries tend to have a poor energy density in comparison to gasoline. It might be intuitive to increase the battery size to compensate for its poor energy density. However, nearly one-third of the EV's price stems from the battery cost [17] as shown in Figure 2.3.Therefore, any attempt to increase the storage capacity will add an extra cost and weight to the vehicle, ultimately depreciating its appeal in the market.

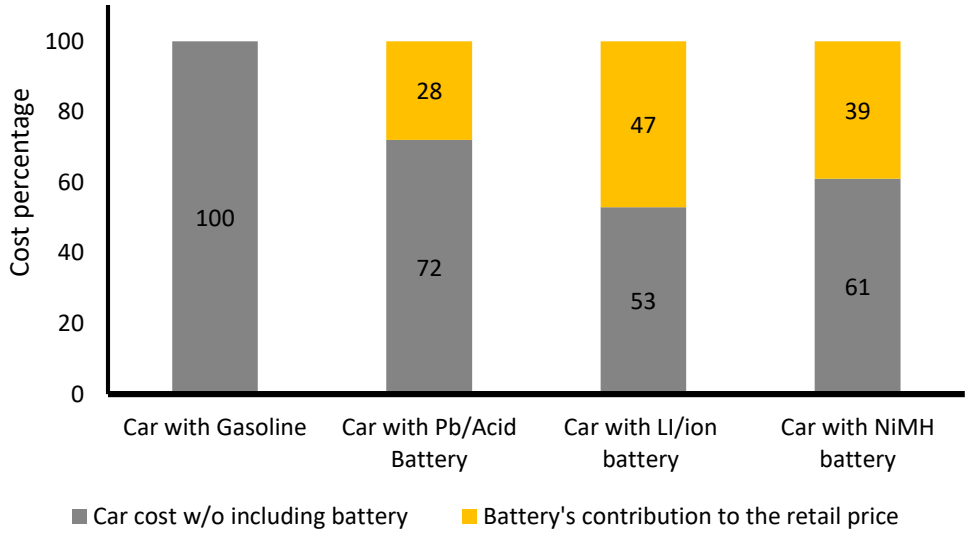

Figure 2.3 Battery cost percentage of an electric car for various battery types

2.2 Review of electronic integration of drive motors

Su et. al. [9] explored the concept of electronic integration of the traction motor with a compressor system as shown in Figure 2.4 as circuit diagram. In a conventional system, independent inverters control the compressor and the drive motor speeds. In this case, two three-phase motors and inverters are required for a trouble-free operation.

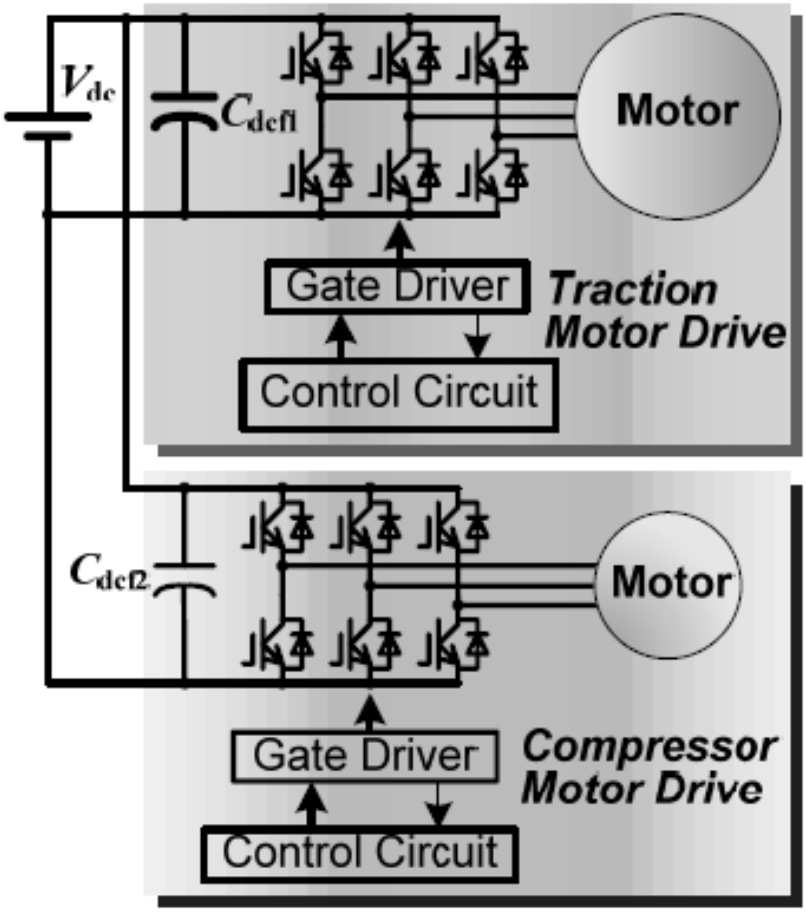

Figure 2.4 Control of traction and compressor drives using independent inverters [9]

The authors [9] also proposed replacing the three-phase unit of the compressor motor with a low-cost two-phase inverter and motor (see Figure 2.5). This configuration decreased the component count, as a two-phase inverter can be constructed using a two-leg inverter and a split-capacitor leg. Moreover, shorter

manufacturing and assembly process of a two-phase motor is cost effective compared to a three-phase counterpart.

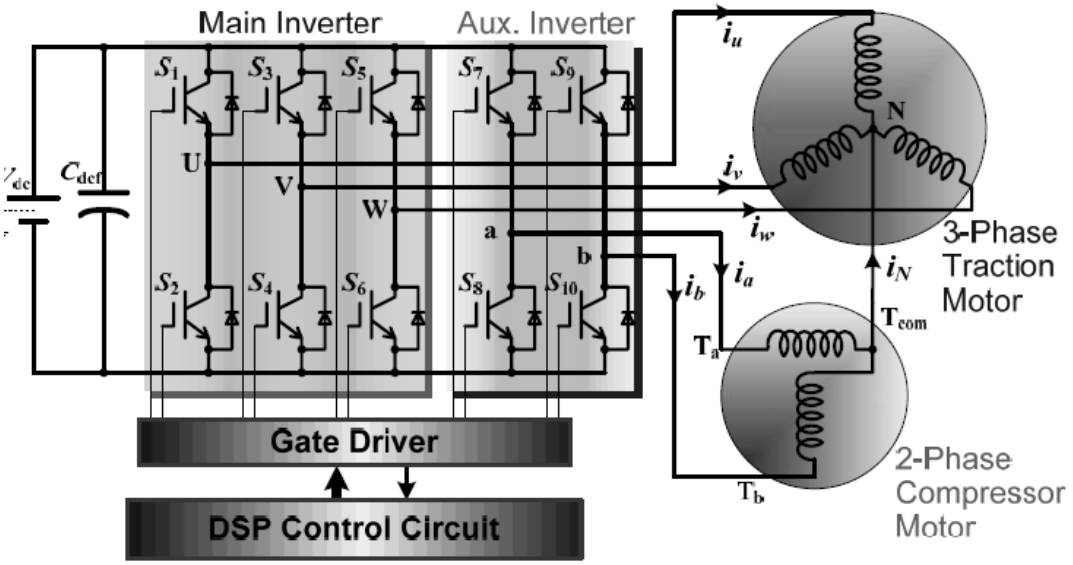

Figure 2.5 Electrically integrated traction and compressor motors [9]

A test was set up to verify the effectiveness of the new circuit design. The experimental results confirmed that the proposed circuit was able to operate the two motors independently without interference. In fact, the system functioned as though independent inverters controlled the traction and compressor motors. Furthermore, the operation of the compressor motor did not overload the main inverter or the traction motor.

As noted in the paper, only electronic integration of the compressor and main drive have been attempted, this resurfaces the project novelty as mechanical integration of these drives is attempted in this PhD research project.

2.3 Review of refrigeration cycle and compressor designs

2.3.1 Compressor classifications

Hermetic, Semi-Hermitic and open are three distinct compressor construction for various types of compressors used for refrigeration and air-conditioning.

1. **Hermetic** – the compressor and the drive motor are assembled and placed inside a sealed casing, to prevent refrigerant leakage. The interface ports such as suction inlet and discharge outlet are located on the external face of the casing. The drive motor is designed to operate without any external aid and cooled by the compressed refrigerant discharged from the compressor. The sealed casing cannot be opened as there are no user serviceable parts. Typical application includes household refrigeration and air conditioning.

2. **Semi-Hermetic** – similar to the Hermit compressor, both the compressor and the drive motor are enclosed in sealed casing. The casing of semi-hermetic compressor can be opened to replace components for maintenance and repair. Therefore these compressors outperform hermetic compressors in terms of longevity, reparability and reliability.

3. **Open** – These are compressors without any built-in driving mechanism, hence some form of external drive has to be coupled with the compressor. In general, this type of compressor is used in gasoline powered passenger vehicles.

The current industrial trend for EV application favours the usage of semi-hermetic compressors with an integrated inverter and electronics control as shown in Figure 2.6 [18], [19]. Other design variations use a top-mounted electronic control unit that is a part of the motor housing. The advantages of integrating the compressor drive and the electronic control unit into a single housing include:

- Sharing of a cooling system for the electronics control.
- Elimination of external cabling to connect the control electronics unit with the compressor motor.

- A combined housing for the electronics and the compressor
- Weight and space saving
- Reduced parts count and increased reliability

These advantages are attractive for the automotive industry as the compressor operate at higher efficiency, improved reliability and decreases the manufacturing cost.

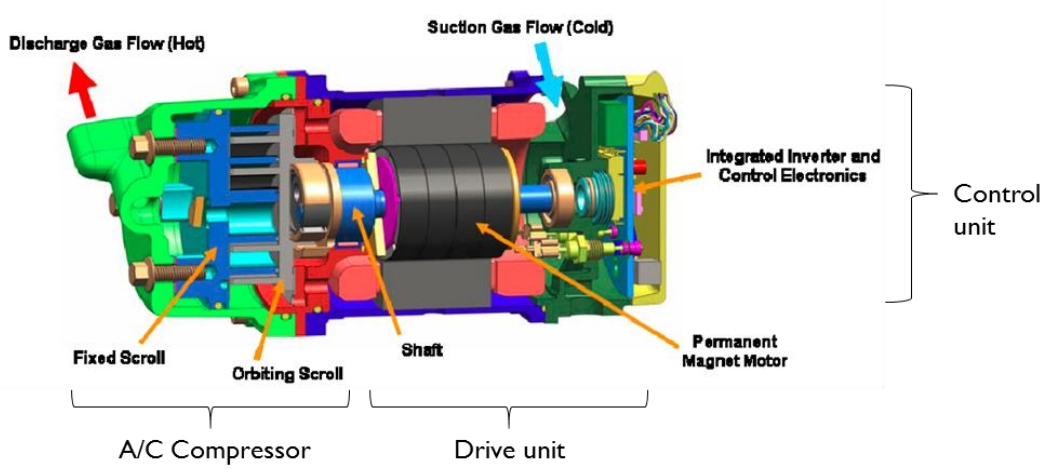

Figure 2.6 Semi-Hermetic compressor with integrated control unit [18]

2.3.2 Compressor variants

Figure 2.7 provides an overview of compressor technology, classified into two distinct categories: positive displacement and dynamic. In positive displacement compressors, regardless of the compressor type, the pressure rise occurs through the reduction of working volume. The reciprocating compressor is well suited for applications requiring low refrigerant flow rates and high discharge pressures. On the other hand, an axial compressor is appropriate for applications requiring high refrigerant flow rate but low discharge pressures. The rotary and centrifugal compressors provide a balanced compromise between discharge flow rate and pressure [20]. The reciprocating and the rotary compressors are most common for automotive application.

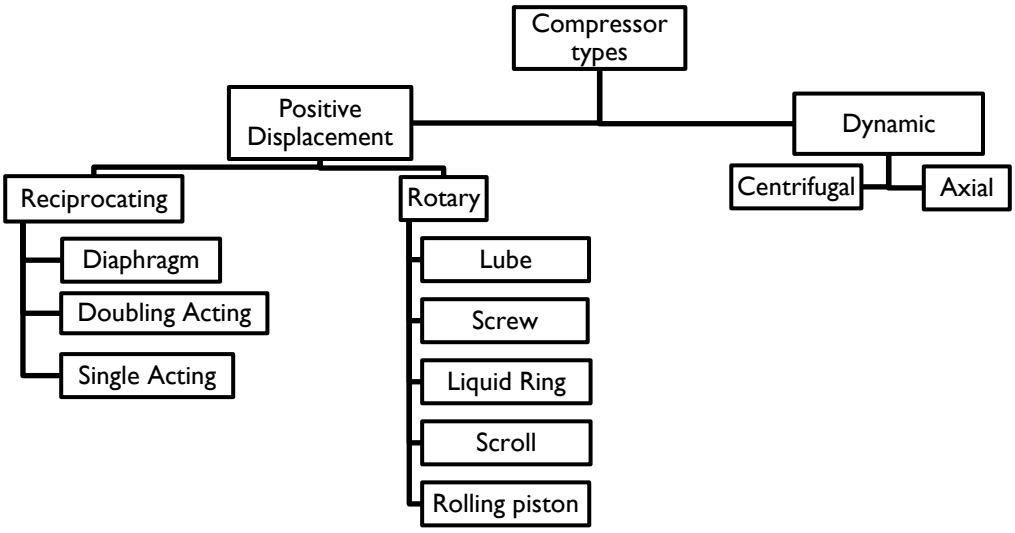

Figure 2.7 Compressor classifications and variants [20]

2.3.3 Capacity control

Compressor-capacity control refers to the system that matches the compressed-refrigerant output to the system-refrigerant demand. The efficiency of the air-conditioning system improves when the compressor is operating close to the designed load. There are various means to control the compressor capacity; these include (1) Bypass control (2) Start-stop control, (3) Inlet Valve unloading control (4) Speed variation control and (5) Inlet size variation control.

An automotive air conditioning system utilizes either the fixed or variable capacity compressors. In a gasoline driven vehicle, these compressors are belt driven by engine (Figure 2.8); hence, the operating speed is proportional to that of the engine. A fixed capacity compressor cycles on and off through an electromagnetic clutch to meet the cooling load demands. This could result in large pressure fluctuations and frequent switching could increase the wear of the compressor and its clutch. In contrast, a variable capacity compressor such as the swash-plate compressor is able to vary its output capacity while operating at engine speed. Noticeable deterioration

in vehicle performance is a norm for belt driven compressors as the compressor consumes a fraction of the power developed by the engine.

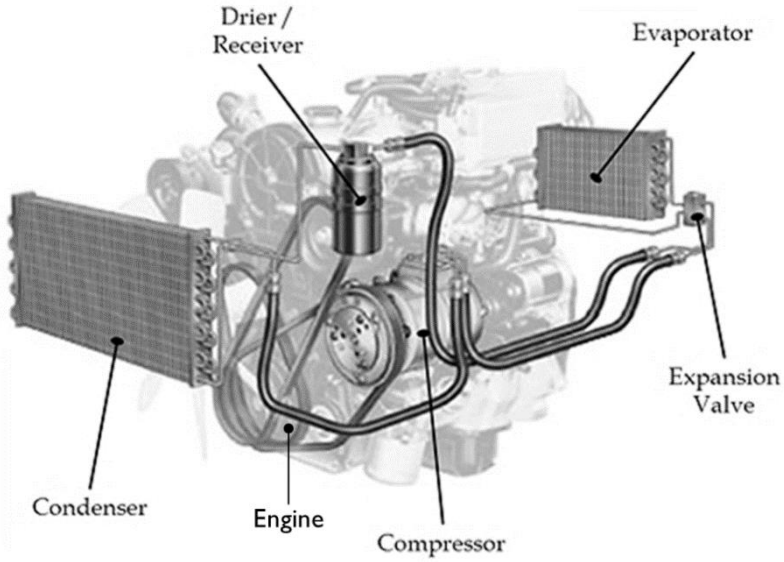

Figure 2.8 Belt driven compressor in a gasoline driven car [21]

Figure 2.9 show the A/C unit of Mitsubishi's electric vehicle, i-MiEV. The system consists of a scroll compressor with an integrated oil separator, inverter and motor drive. The use of independent electric motor provides an easy control over the compressor capacity through speed variation. In addition, the vehicles acceleration and uphill driving performance remains unaffected while the compressor is in operation.

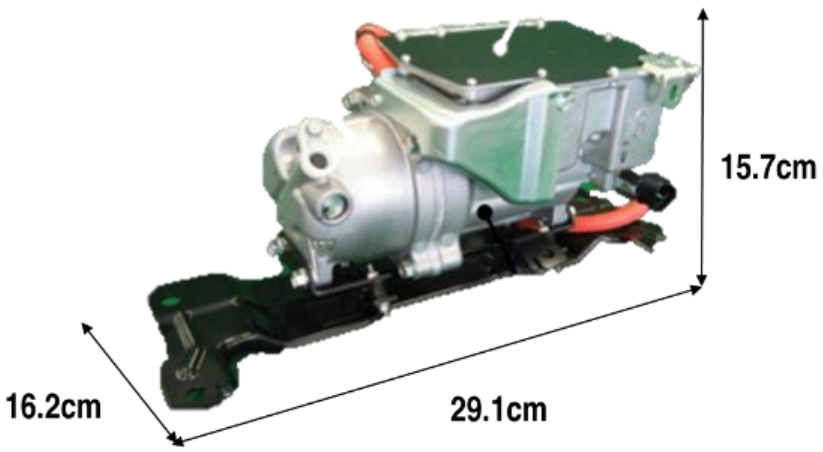

Figure 2.9 A/C unit of i-MiEV [16]

2.3.4 Compressor lubrication

A proper choice of lubricating oil is a necessity in the overall reliability and efficiency of the compressor. Lubrication of the moving parts not only minimises friction but also facilitates heat transfer from the bearing surfaces, it protects against corrosion and seals the clearances to reduce the internal leakage of high pressure refrigerants [22]. The choice of lubricant depends on the compatibility and the desired miscibility with the refrigerant fluid. Improper lubrication choice or inadequacy of the lubrication can decrease the reliability of the compressor and can lead to a complete seizure of the compressor.

Miscibility refers to the ability of the lubricating oil to mix with the refrigerant to form a homogeneous mixture. Some refrigeration systems are fitted with oil-separators to segregate the lubrication oil from the refrigerant-lubricant blend. In such cases, a lubricant that is immiscible or has low miscibility with selected refrigerant is a preferred choice. Meanwhile, miscible lubricants are apt for air conditioning systems without oil-separators. The miscibility and viscosity of the lubricant are important to ensure that the refrigerant-lubricant blend maintains a single phase as it passes through the evaporator. The selected lubricant should have sufficient miscibility at the evaporator temperature to prevent the possibility of separation from the refrigerant-lubricant blend. In addition, the lubricant should have a low viscosity at evaporator temperature to ensure the blend passes through the evaporator without entrapment.

The miscibility chart (Figure 2.10) relates the phase separation temperature with the percentage of refrigerant-lubricant blend. In the immiscible regions defined by the upper and lower bound curves, only a fraction of the lubricant is able to mix with the refrigerant. Increasing the phase separation temperature between the upper and lower bound curve produces a homogeneous refrigerant-lubricant mixture. The miscibility chart is unique for a given refrigerant-lubricant combination and read based on evaporator operating temperature and percentage of lubricant carried in the refrigerant-lubricant blend.

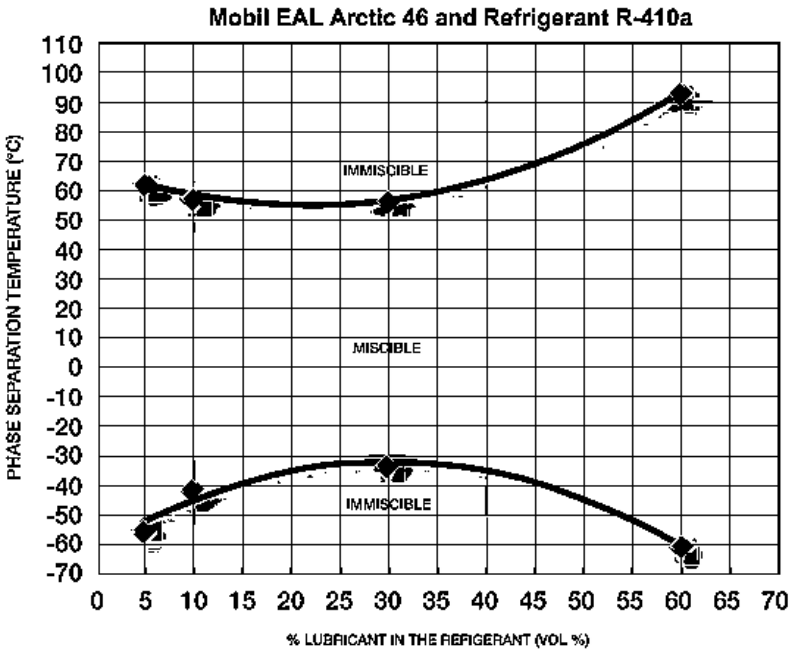

Figure 2.10 Lubricant miscibility chart [23]

The compressor discharge temperature is another primary parameter used in the selection of compressor lubrication oil. The selected oil should have sufficient viscosity over the operating temperature to avoid any metal-to-metal contact. This is necessary to prevent abrasive wear of the moving parts and to enhance the heat transfer out of bearing surfaces. The minimum acceptable oil viscosity is recognised as about 36 SUS [24]. Any further reduction in viscosity results in oil film to being squeezed out of bearing surfaces, consequently resulting in abrasion and metal bonding.

The solubility of the lubricant is an important parameter affecting the oil viscosity at high temperature and pressure. The majority of petroleum based compressor lubricant will absorb the refrigerant to some extent. The high temperature and pressure enhances the absorption of the lubricant, leading to a decrease in lubricant viscosity. The actual absorption characteristics can only be found through extensive and time-consuming laboratory tests that closely replicate the operating conditions. Nevertheless, selecting an oil having 5 to 10 SUS [24] higher viscosity can mitigate the gas dilution effect.

2.3.5 Automobile air-conditioner compressors

Air conditioning compressors are used in automobiles to drive the climatisation system of a vehicle. There are basically five basic type of compressors suited for automobile application. This section provides an introduction of these compressor variants and its operating principles.

2.3.5.1 Sliding vane compressor

A schematic of a sliding vane compressor [25] is shown in Figure 2.11. In this compressor, the rotor is eccentrically placed in stationary cylinder with the tip of the vanes being kept in sliding contact with the inner cylinder wall. The space surrounded by the inner cylinder wall, the rotor and any two adjacent vanes forms the working chamber.

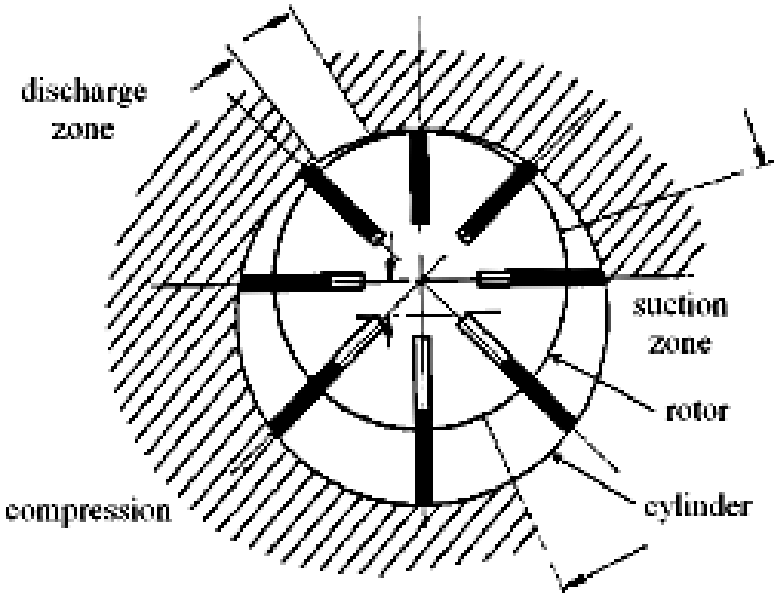

Figure 2.11 Schematic of a sliding vane compressor [25]

This type of compressor suffered from chattering at low operation speed as the vane tip is repeatedly detached and pushed back against inner cylinder wall [26] and results in impact fatigue. Its volumetric efficiency also suffered from internal leakage and thus requires an appropriate constant vane slot back pressure [27]. It is

a valve-less system which favours its reliability as well as volume efficiency [25] with minimum noise and vibration. Compressor fitted with forward inclination angle of 5° enhanced specific capacity however does not have real advantages over increased manufacturing cost associated with inclined vanes [28]. Moreover it also suffer from friction and wear and require periodic maintenance [29]–[31] which increases the operational cost.

2.3.5.2 Screw compressor

Screw compressor is a rotary type positive displacement compressor as shown schematically in Figure 2.12. It has two intermeshing helical rotors, where the lobe (male rotor) meshing into corresponding flute (female rotor) and form the working chamber in between.

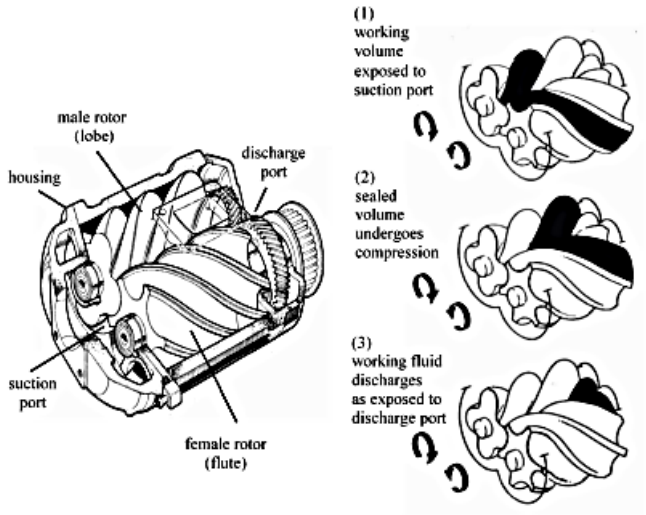

Figure 2.12 Schematic view of a screw compressor [32]

It is also a valve-less system with built-in volume ratio. The operation of screw compressor takes place in four consecutive phases [32]: (i) the pair of lobe and flute starts to un-mesh during suction resulting a space and the gas is drawn through suction port till the trapped pocket of working fluid is isolated from suction and discharge port; (ii) the pocket of working fluid is being transferred during transfer phase; (iii)subsequently, mesh point moves axially towards discharge port and the

volume of trapped working fluid reduces gradually to allow the pressure to increase; and lastly (iv) at the moment of pre-determined built-in volume ratio, the pocket of compressed working fluid is released through the discharge port. Fujiwara et al. [32] claimed that the torque requirement and volumetric efficiency decreases with an increases in intermeshing rotors clearance due to leakage through the clearances. Tighter clearance can reduce leakages, however suffers from increased viscous loss and diminished mechanical efficiency. Thus the compressor has inborn potential in reliability since it involves only two purely rotational rotors without any valves [33], [34].

2.3.5.3 Scroll compressor

The scroll compressor was invented by Léon Creux at the beginning of the 20th century [35]. However, due to tight tolerance requirements, the production of the scroll compressor was delayed till 1970s. Ever since its successful application, the scroll compressor has gained popularity as it contained fewer moving parts, lower noise levels, superior efficiency and higher reliability [36]. Mitsubishi's i-MiEV — uses a scroll compressor for its air-conditioning system [16].

A scroll compressor consists of two spiral scrolls – a fixed and an orbiting scroll as shown in Figure 2.13. The fixed scroll is secured to the body of the compressor, thereby being held rigidity in space. The eccentric placement of the orbiting scroll in relation to the crankshaft creates an orbital motion of the scroll. The orbital motion creates a series of gas pockets between the two scrolls. On the outward portion of the scroll, the pocket draws in refrigerant and pushes the refrigerant towards the centre due to the rotation of the disk. As the gas moves through the progressively smaller inner pockets, the temperature and pressure increases to discharge conditions. The compressed refrigerant exits the compressor from the centrepoint of the fixed scroll. These compressors are very efficient and quiet but represent a significant challenge due to precision manufacturing requirements.

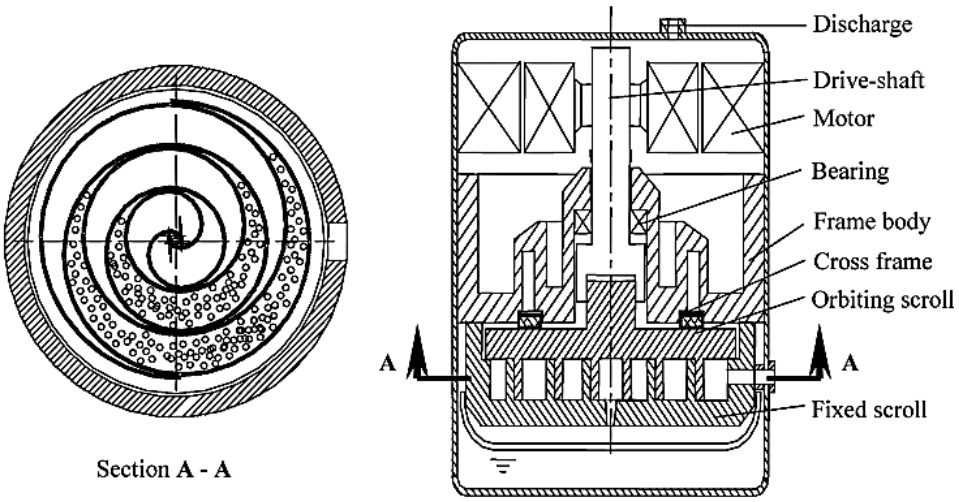

Figure 2.13 Scroll compressor nomenclature [36]

2.3.5.4 Swash and wobble plate compressors

The piston type variable displacement compressor (VDC) dynamically alters the piston stroke length to vary its capacity based on the cooling demands. The usage of a variable displacement compressor improves comfort in the passenger compartment as drastic temperature fluctuations are eliminated while increasing the fuel economy of the vehicle [37]–[39]. There are two types of VDCs: wobble plate and swash plate (Figure 2.14). Tian et. al. [40] explained that in the wobble plate VDC, a piston rod connects the wobble plate and piston. An adjustment of the inclination angle of the wobble plate varies the piston stroke length thereby altering the compressor displacement capacity. However, a swash plate VDC eliminates the need for a piston rod by directly communicating with the piston. In practice, swash plate VDC is preferred over wobble plate VDC owing to fewer components and simpler construction.

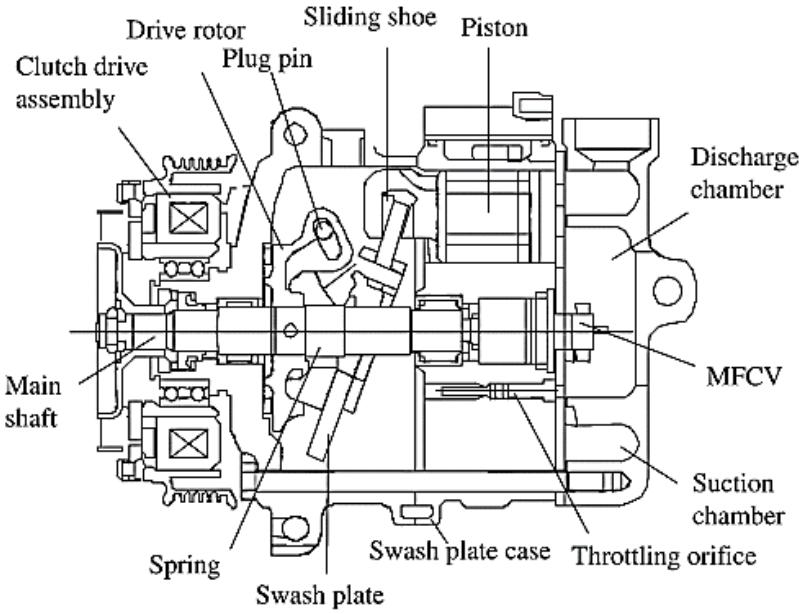

Figure 2.14 Swash plate VDC nomenclature [40]

2.3.5.5 Rolling piston compressor

A rolling piston compressor consists of a cylinder, spring-loaded vane, suction and discharge ports and a piston eccentrically mounted to the crankshaft as shown in Figure 2.15. During operation, the two volumes confined by the cylinder inner surface, roller contact point and the vane change in size, leading to the compression of the refrigerant. The vane acts as a separator between the two volumes.

A complete cycle consists of two revolutions of the motor. During the first revolution, the refrigerant enters the rolling piston through the suction port and fills the suction chamber. During the second rotation, progressive compression of the refrigerant takes place in the compression chamber. A reed valve placed over the discharge port seals the compression chamber and facilitates pressure building. The reed valve opens and releases the compressed refrigerant once the refrigerant pressure exceeds that of the discharge pressure. Although scroll, wobble plate, swash plate and rolling piston compressors are widely used in the automotive industry, in this project, the rolling piston compressors are preferred over the others owing to its simpler construction. Rolling piston compressors offer the best

combination of efficiency, lower component count, ease of manufacturing and controllability.

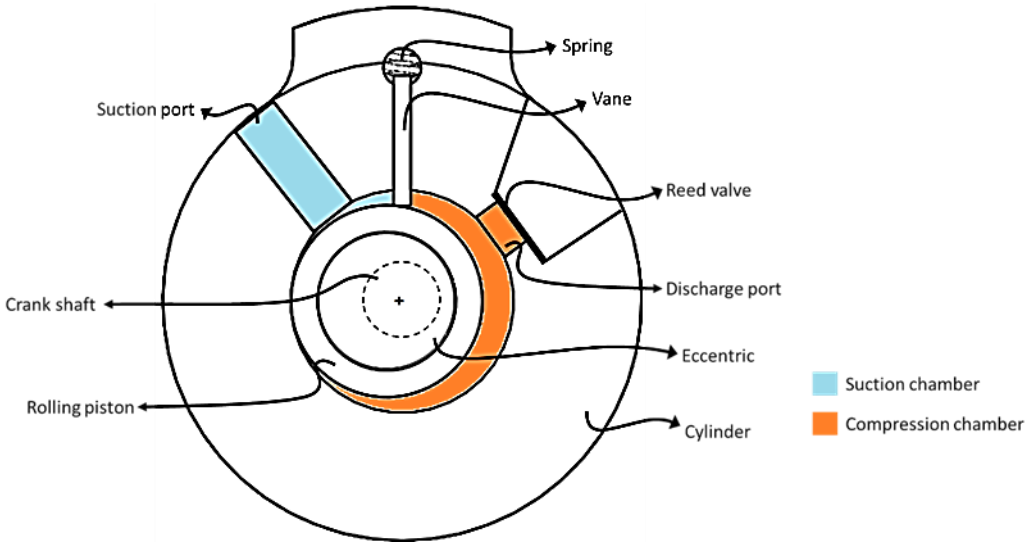

Figure 2.15 Rolling piston compressor nomenclature

One of the major disadvantage associated with rotary piston compressor is large frictional and leakage losses incurred by the sliding vane tip as it rubs over the piston. Both frictional and leakage losses negatively affect the cooling capacity and volumetric efficiency of the compressor. To address this issue, a new variant of the rotary piston compressor was introduced by Daikin in 1994 and is commonly known as "Swing Vane Compressor (SVC)" [41]. The SVC is similar to rolling piston compressor, except for the fact that the vane is rigidly attached to the piston body, thereby eliminates all leakage and frictional losses between the vane tip and the piston. Consequently, the new design variant has a higher efficiency in the range of 2% - 9% [42] as compared to the conventional rolling piston compressor.

2.3.6 Refrigerants for automobile compressors

A suitable refrigerant for a given application is selected based on the operating conditions, thermodynamic characteristics and properties, safety consideration and cost. A refrigerant can be classified into one of the following ASHRAE classifications:

- R717 – Ammonia
- R1234yf – Tetrafluoropropene
- R234ze
- R600a – Isobutane
- R774 – Carbon dioxide (CO_2)
- R134a, R404a, R507 – Hydrofluorocarbons (HFC)

The Montreal Protocol (in 1989) completely banned the usage of CFC for all applications due to ozone depletion potential. After 1994, R134a (also known as 1,1,1,2-Tetrafluoroethan, or HFC-134a) was used as an alternative. R134a is proved as an important factor in combatting ozone layer depletion and greenhouse emissions. Nevertheless, even a trace amount of leakage of R134a is detrimental to the environment due to its high global-warming potential[4] (GWP). R134a has a GWP of 1430; consequently, an emission of 1 gram of R134a is equivalent to emitting 1430 grams of CO_2. Therefore, R134a was eventually phased out.

In early to mid 90s, concerns over climate change have escalated in recent years, which prompted the consideration of CO_2 (commonly known as R774) as a replacement for R134a. In fact, relevant European legislations have already been passed to encourage the industry to favour the usage of R774 [43]. Nevertheless, usage of natural refrigerant such as CO_2 is not new within the industry. Until 1950, air conditioning units based on CO_2 was widely used in the marine installation owing to high safety, natural availability and economical production cost. However, the appeal of CO_2 refrigerant was lost in favour of hydrocarbons due to increased power consumption, detrimental impact on refrigeration capacity at high ambient temperature and failure of compressor manufacturers to follow the trends in compressor design.

In 1993 Lorentzen and Pettersen [43] carried out experimental measurements on a prototype car to access the difference in coefficient of performance (COP) between

[4] Global-warming potential (GWP) is a relative measurement of the heat trapping capacity of greenhouse gases. The measurement compares the heat trapping capacity of greenhouse gas in question with that of CO_2. Carbon dioxide has a GWP of one; hence, a gas having the same mass as CO_2 with a GWP 72 (Methane) indicates that it is 72 times more effective in trapping heat when compared with CO_2.

CO_2 and synthetic refrigerant-CFC12 at two test conditions (A and B as shown in Figure 2.16). The test result showed that CO_2 mimics the performance potential of CFC12 and outperforms the standard CFC12 system at high ambient air temperature. The authors identified four reasons for the observed improvements in the COP of the system through the usage of CO_2. Namely, (1) enhanced internal heat exchange, (2) improved heat transfer characteristics of the evaporator, (3) increased compressor performance due to reduction in pressure ratio and (4) a closer approach to ambient temperature at the condenser outlet. In summary, their study conclusively showed that CO_2 is a practical refrigerant for automobile application that is capable of combating environmental concerns associated with the air-conditioning systems.

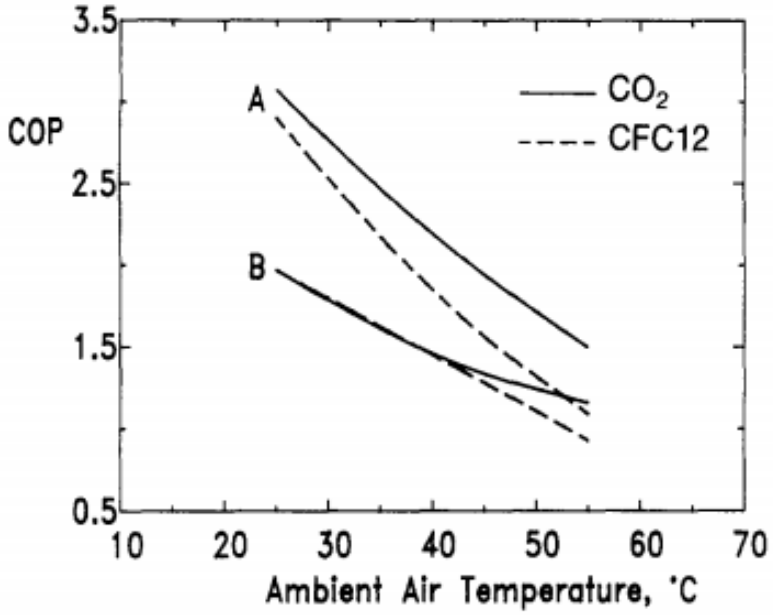

Figure 2.16 COP of the prototype car at test conditions-A and B [43]

Due to the drastic difference in operational conditions of CO_2, the refrigerant R1234yf has been introduced as a drop-in replacement for HFC-134a and has been seen as a viable replacement for HFC-134a. Unlike HFC-134a, R1234yf has a low GWP of four [24] as compared to 1430 for HFC-134a. Moreover, the urgency to replace HFC-134a has been raised after the European Union (EU) banned it for all new air conditioner models effective from January 1, 2011. Additionally, legislations have been passed by the EU which require all automotive air

conditioners to have a global warming potential lower than 150 by 2017. Henceforth switching to R1234yf is a possible means to meet such requirements.

R1234yf has similar performance and thermodynamic characteristics to R134a as shown in Table 2.1. Comparison of the attributes indicates that both refrigerants share very similar molar mass, critical temperature and pressure, thereby suggesting R1234yf is a viable substitute for R134a.

Table 2.1 Thermodynamic properties of R1234yf and R134a Refrigerants [24]

Thermodynamic Property	**R1234yf**	**R134a**
Chemical Formula	$C_3F_4H_2$	CF_3CH_2F
Molar Mass (kg/kmol)	114.04	102.03
Boiling Point at 1 atm (K)	243.70	247.08
Freezing Point (K)	Unknown	169.85
Critical Temperature (K)	367.85	374.21
Critical Pressure (MPa)	3.38	4.06
Critical Density (kg/m^3)	478.01	511.90
Sat. Vapour density (kg/m^3)	12.296	9.8164
Latent heat of vaporisation (kJ/kg)	169.81	206.40
Saturated pressure@-10.6^{o}c (kPa)	216.92	195.90
Saturated pressure @ 54.4 (kPa)	1469.8	1444.5

Ooi [44] accessed the performance characteristics of a rolling piston compressor with R1234yf as a working fluid. In this study, the author simulated a rolling piston compressor with a displacement volume of 32cm^3 operating at 2875rev/min. The simulation revealed that the pressure-volume (PV) plot was similar for both R1234yf and R134a. It was concluded that there were negligible variations in energy requirements when switching from R134a to R1234yf. The simulation also suggested that R134a gives a better performance characteristic (COP and cooling capacity) when operated under high condensing and low evaporating temperatures. Nevertheless, as the condensing temperature decreased, the usage of R1234yf resulted in a superior compressor performance. The study reported a moderate difference in cooling capacity of approximately 5% and a moderate difference in COP off around 10% between these refrigerants.

In a separate study, Pamela et. al. [45] conducted a performance comparison between R134a and R1234yf using a thermodynamic model of a heat exchanger. The simulated heat exchanger model revealed that both refrigerants have similar performance characteristics for a given outlet refrigerant temperature and heat load. However, a variation of around 40% was observed in pressure losses in the heat exchanger and pipes between these refrigerants, and thus different design were suggested based on refrigerant choice. This led to the conclusion that a system originally designed to work with R134a should not be operated with R1234yf without any design modification. The authors recommended that prior to switching to R1234yf for an existing system based on R134a, a comprehensive analysis is necessary to identify performance variations.

2.4 Review of compressor mathematical models

A comprehensive theoretical models to evaluate the compressor performance may include geometry, thermodynamics, kinematics, compressor dynamics, valve dynamic, internal leakage of working fluid, heat transfer inside working chamber and compressor lubrication. These models will be briefly discussed.

2.4.1 Geometric model

Geometry model describes the variation of the working chamber volume with time as compressor operates. In the case of a positive displacement compressor, it is this volume changes which causes the operation of the compressor cycle. The rate of change of the volume dictates the dimensions of suction and discharge ports among other parameters such as heat transfer and pressure rise in the chamber. The later indirectly affecting the bearing design.

2.4.2 Thermodynamic model

Thermodynamics model describes the process of working fluid in a compressor operation and reveals variations of pressure, temperature and mass inside the

compressor working chamber. In a simplified model, working fluid behaviour can be modelled as polytropic process [46] or as ideal gas behaviour [47]. The use of idea gas equation of state in the first law model is evident in early literature published by Karll [48], but it has been reported to be inadequate to evaluate basic compressor cycle by Prakash and Singh [49]. The use of real gas behaviour offer close agreement against experimental findings [50]–[52]. As reported by Sun and Ren [53], the use of first law of thermodynamics and real gas equations offer better results, particularly on working chamber pressure and displacements of suction and discharge valve. Ooi and Wong [54] reported about 10% discrepancy when compared with available experimental data by the use of first law of thermodynamics and real gas equations.

A comprehensive real gas description of working fluid behaviour is now available in commercial package and can be used with compressor simulation studies. Undoubtedly, applications of first law of thermodynamics and real gas equation of state are now the way to model the process of working fluid in the research of various refrigeration compressors [55] whereas the use of ideal gas equation is still employed purely for convenience [56].

2.4.3 Heat transfer model

Heat transfer between the working fluid and the surrounding working chamber is an important aspect as it affects pressure variation inside the working chamber. Though there are a number of heat transfer correlations available in the open literature, however most of these were derived for reciprocating engine in 70s. In-chamber heat transfer have influence on volumetric efficiency and indicate work of a compressor [57]. In addition, Prasad [58] pointed out that the importance of temperature as it affects dimensional stability and integrity of the components.

Development of in-chamber convective heat transfer correlation ceases after late 80s and available convective heat transfer correlations contributed by early researchers were frequently applied in energy analysis of hermetic compressors with good agreement against experimental findings with discrepancies mostly less than 10% [59]–[64]. In general, heat transfer should be considered for a

comprehensive simulation of thermodynamic process in the working chamber of a compressor by adopting empirical correlations [36], [65]–[67].

2.4.4 Valve model

Valve performance plays an important role which dictates the working fluid flow in compressor and thus requires to simulate accurately. Reed valve experiences a complex motion due to fluid-structure interaction and often suffers from fatigue failure due to repetitive nature of operation [68], [69]. Between 70s to 80s, a number of relatively simple numerical mathematical models have been developed to describe the interaction between compressor valve and working fluid based on non-linear differential equation and most of the available models are based on to some degree on the pioneer analysis by Costagliola et al. [70], [71]. Early study by Wambsganss and Cohen [72] concluded that single degree of freedom approximation is not sufficient to represent valve reed dynamics in a high speed compressor and effect of valve restriction is large at low values of compressor pressure ratio, as all of the aforementioned models are semi-analytical in nature due to the incorporation of several empirical coefficients. These shortcomings lead to the development of analytical studies based on different numerical approaches [73], [74] with good comparsion against measured results. This simulation studies were further developed with the help of finite element method (FEM) and computational fluid dynamics (CFD) techniques [75], [76]. Fagotti et al. [77] emphasized the flexibility in finite element approach by incorporating variable width for the valve reed.

A more recent CFD techniques emphasize the effect of fluid structure interaction [74], [78], [79]. Thus a more comprehensive and more realistic modelling for valve performance and valve displacement behaviour, analysis of impact and stress, effective flow and force areas, failure mechanism, fluid flow visualization and others are now possible.

2.4.5 Leakage model

Internal leakages of working fluid decrease the volumetric efficiency of the compressor and thus, cooling capacity and coefficient of performance are affected [80][81]. In the case of leakage flow through the clearance gap between the rotor and the stator of a rotary compressor, it can be modelled as gas flow driven by pressure difference through a convergent-divergent nozzle under consideration of ideal gas properties for simplicity, constant flow area and upstream pressure are approximated as an average of suction and discharge pressure [82]–[84]. Among various available models, oil-refrigerant mixture leakage flow model is the most appropriate model to predict realistic internal leakage flow as claimed by various researchers [85]–[87].

2.4.6 Lubrication model

Lubricants are essential in compressor operation as they lubricate the rubbing surfaces to prevent excessive wear and thus improves reliability and mechanical performances. Lubricants also serve to seal the gap and cool the compressor. Earlier analysis on lubrication performance focuses on individual flow path, for example, flow through journal bearing and flow through spiral groove and later it was extended to analysis for the entire flow systems. Oil supply into various elements in vertical [88][89] and horizontal [90] rolling piston compressor under steady state conditions has been studied by employing equivalent electric circuit network together with the effect of journal bearing groove shape and inclination angle. In more recent studies, computational fluid dynamics [90]–[92] has been employed for more dynamic studies.

2.5 Concluding remarks

Literature shows that the mechanical integration of the compressor and electrical drive motors is yet to be attempted. The electrical integration of these drives offers a number of advantages, which includes fewer component count, compact size and lower production cost.

There are several compressor design variants developed for automotive industry and it is evident that the current trend favours a compressor that involves fewer component count and simpler geometries. Rotary compressors are a promising lead as opposed to reciprocating and swash plate compressor owning to its superiority in terms of geometrical simplicity, fewer parts, good efficiency, noise and vibration.

Literature also reveals that the air conditioning compressor is a significant electrical load in EVs. The cruise range of an EV can decrease by 22 to 48% [16] depending on the A/C usage. Therefore, it is imperative to find means to improve its efficiency through design changes and optimisation studies. With the advent of modern computers, theoretical assessment can be executed through comprehensive mathematical models. These models can expedite the possibilities of a more efficient compressor or even a new compressor design.

Chapter 3

2-in-1 MOTOR DESIGN AND COMPRESSOR SELECTION

In this chapter a new 2-in-1 motor has been introduced. This new design integrates the main driving motor of the EV with the A/C compressor and its drive motor. The chapter also describes various operational modes of this unit. It is then followed by the introduction to the motor design to highlight other advantages associated with this new 2-in-1 design. Following that, various compressor design variants are examined to identify the most suitable compressing mechanism that is apt for the 2-in-1 motor's new drivetrain.

***The design discussed in this section has been presented and awarded with Best Originality Award, 2014 by Teco GreenTech, an international design competition held yearly in Taiwan.** This competition draws close to 150 participants from universities including UCLA, Boston University, the University of Tokyo, Waseda University, Lomonosov Moscow State University, National University of Singapore, Peking University, and National Tsing Hua University.*

3.1 2-in-1 Motor Structure

Figure 3.1 shows the basic structure of the newly invented 2-in-1 motor concept in this research project [93].The unit consists of an A/C compressor, a compressor and its drive motors, an electrical clutch, planetary gear unit and a valve. The drive motor is the prime mover, which is connected to the vehicle's wheels via gearbox. This motor also functions as a generator during the regenerative braking process. The compressor motor, the planetary gear and the A/C compressor are located on a concentric shaft where one shaft is housed within a hollow shaft. This enables the compressor motor to operate independently of the main drive motor and transmits its power to the compressor via a planetary gear.

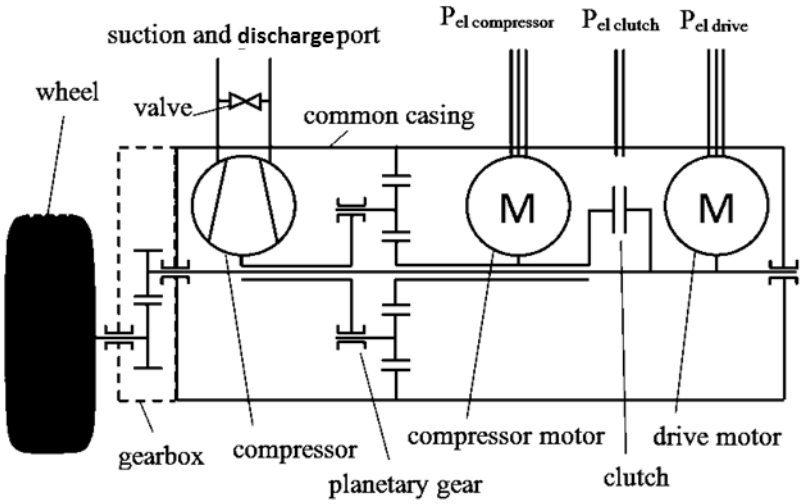

Figure 3.1 Integrated drivetrain architecture configuration

The planetary gear serves the function to ensure the compressor operates within its operating speed range. The electromagnetic clutch placed between the motors enable the mechanical power transfer between the compressor and drive motors. The valve located between the suction and discharge port of the compressor acts as a bypass valve to short the air-conditioning circuit when the compressor motor is used to supplement the main motor to provide additional power to the EV. Note that in Figure 3.1, $P_{el\ compressor}$, $P_{el\ clutch}$ *and* $P_{el\ drive}$ are the respective electrical supplies to the compressor, clutch and the drive motor.

3.2 Operating modes for 2-in-1 motor

The 2-in-1 motor drivetrain architecture makes it possible to use both motors in a parallel hybrid mode, where the drive motor for the compressor and the main drive motor can both supply tractive power to the EV. This structure facilitates six possible operating modes as listed in Table 3.1. Both of these motors can operate as generator when needed during regenerative mode. The clutch can be operated (opened or closed) to facilitate power transfer between the concentric shafts and the air-conditioning circuit can be "bypassed" if necessary. The six driving modes shown are described below.

Table 3.1 2-in-1 motor operating modes

Mode No.	Function mode	Drive motor mode	Compr. motor mode	Clutch mode	Compr. mode
1	Drive only	Motor	-	Open	-
2	Air-conditioning only	-	Motor	Open	On
3	Boost	Motor	Motor	Closed	Shorted
4	Air-conditioning by recuperation	-	-	Closed	On
5	Air-conditioning by recup. and max. charging	Generator	Generator	Closed	On
6	Drive and air-conditioning indepentently	Motor	Motor	Open	On

Mode 1: Drive only

In this mode, the 2-in-1 motor operates in the drive only mode (shown in Figure 3.2) when the air-conditioner is off. This situation occurs when the cabin has attained the desired temperature set by the passenger or when the air conditioner is turned off. In this mode, the drive motor receives electrical power $P_{el\ drive}$ to generate

the tractive power necessary to operate the vehicle as shown by the blue arrows in the figure, while the clutch and the compressor motor remain inactive.

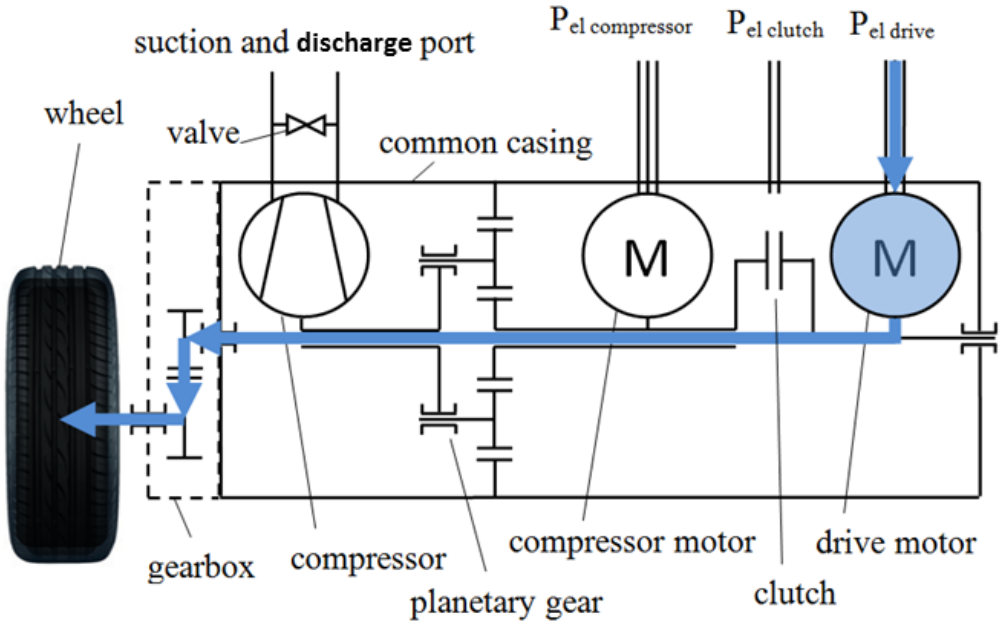

Figure 3.2 Mode 1: where the drive motor provides tractive power

Mode 2: Air-conditioner only

In this mode, only the air-conditioner is being turned on and the car is standstill as shown in the energy flow figure in Figure 3.3. In this condition, the compressor motor receives $P_{el\ compressor}$ from the electrical supply and operates the air-conditioning compressor at the desired speed. Since mode 1 and 2 operate independent of each other, when both modes operate together it forms mode 6, which is not explicitly shown in the figure.

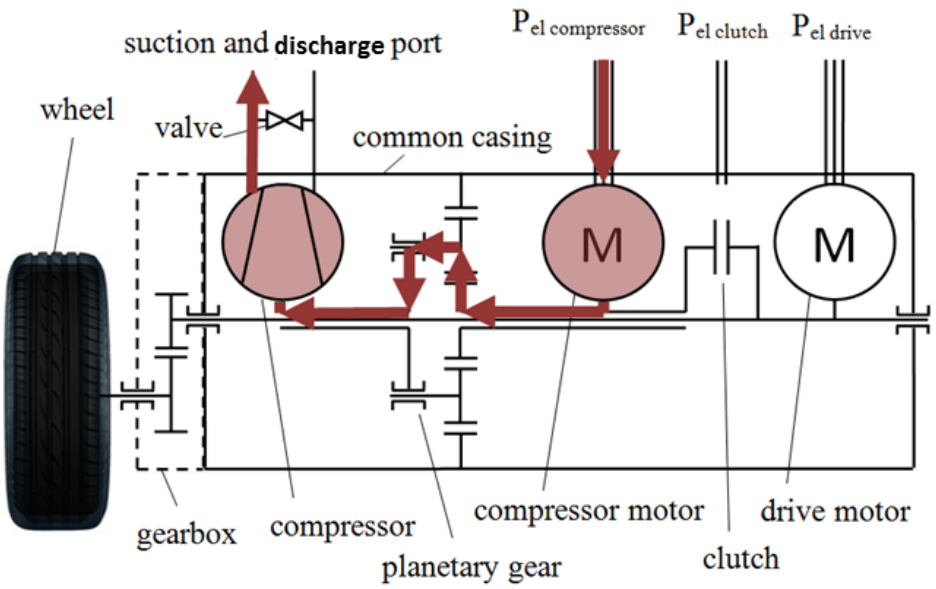

Figure 3.3 Mode 2: where the compressor drive operates the A/C compressor

Mode 3: Boost function

In this mode, the 2-in-1 motor has the capability to use the both motors to generate tractive power for the vehicle as shown in Figure 3.4. This facilitates the vehicle to accelerate faster or overcome steep upward slopes without the need for a large drive motor. Since the compressor is mechanically coupled to the compressor motor, the valve located between the suction and discharge ports of the compressor can be operated to short or bypass the air-conditioning circuit and hence unloads the A/C compressor from the compressor motor.

Meanwhile, the electromagnetic clutch is energised using $P_{el\ clutch}$ to facilitate the power transfer from compressor drive shaft to the vehicle drive shaft to provide additional driving torque to the wheels. The momentary loss of power to air-conditioning circuit will probably go unnoticed if the duration is not too long as the air in the cabin acts a large thermal capacitor.

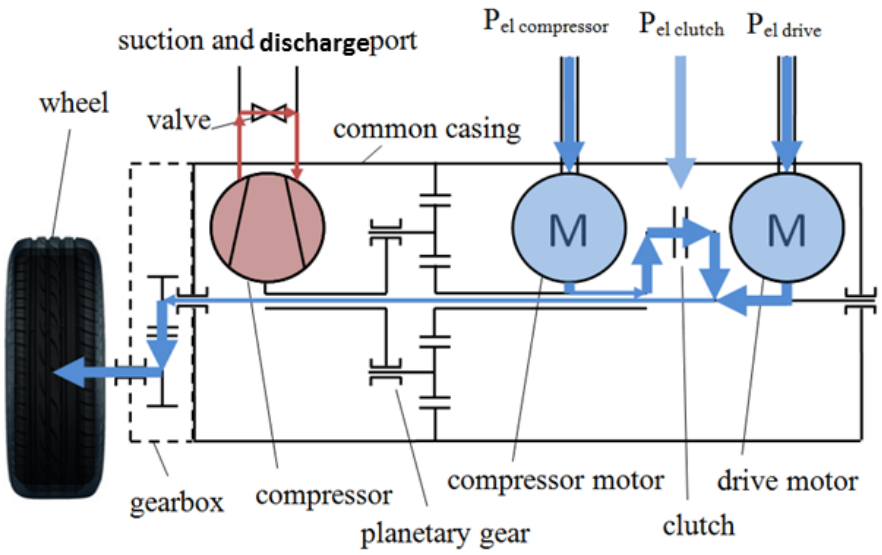

Figure 3.4 Mode 3: Boost function

Mode 4: Air-conditioning during regenerative braking

This mode describes the main application of the 2-in-1 motor system, where the power to operate the A/C compressor is provided by the vehicle during braking events. In this mode, both the compressor and the drive motors are disconnected from the electrical supply, while the electromagnetic clutch is energized. When braking, the otherwise wasted kinetic energy of the vehicle is recovered and directed to the A/C compressor via the drive shaft and the clutch mechanism.

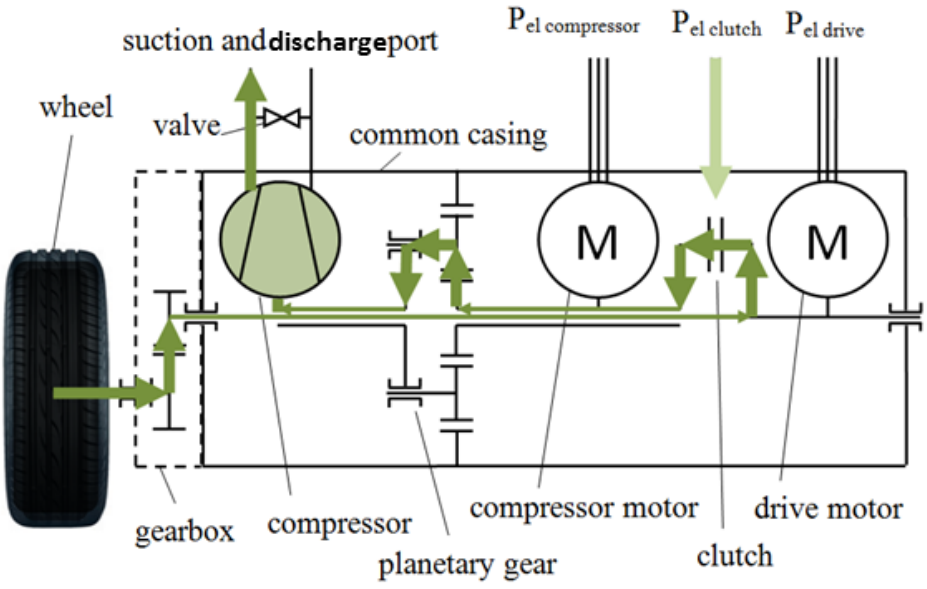

Figure 3.5 Mode 4: Air-conditioning during regenerative braking

Mode 5: Air-conditioning by regenerative braking and max charging

In this mode, the 2-in-1 motor offers a novel solution to minimise energy wasted in the brake pads by enabling the compressor motor to act as a generator to facilitate power recovery as show in Figure 3.6. This permits the use of a smaller drive motor while enhancing the recovering power during regenerative braking. In addition, the A/C compressor can remain loaded (to meet air-conditioning requirements) to facilitate a large power to be recovered during abrupt braking events. This not only boosts the electrical vehicle range, but also decreases the wear on the brake pads. A rigorous estimate on the cruise-range extension capability of the 2-in-1 motor is presented in appendix A. Based on the simulation results, the 2-in-1 motor is expected to improve the cruise range by 3.2%.

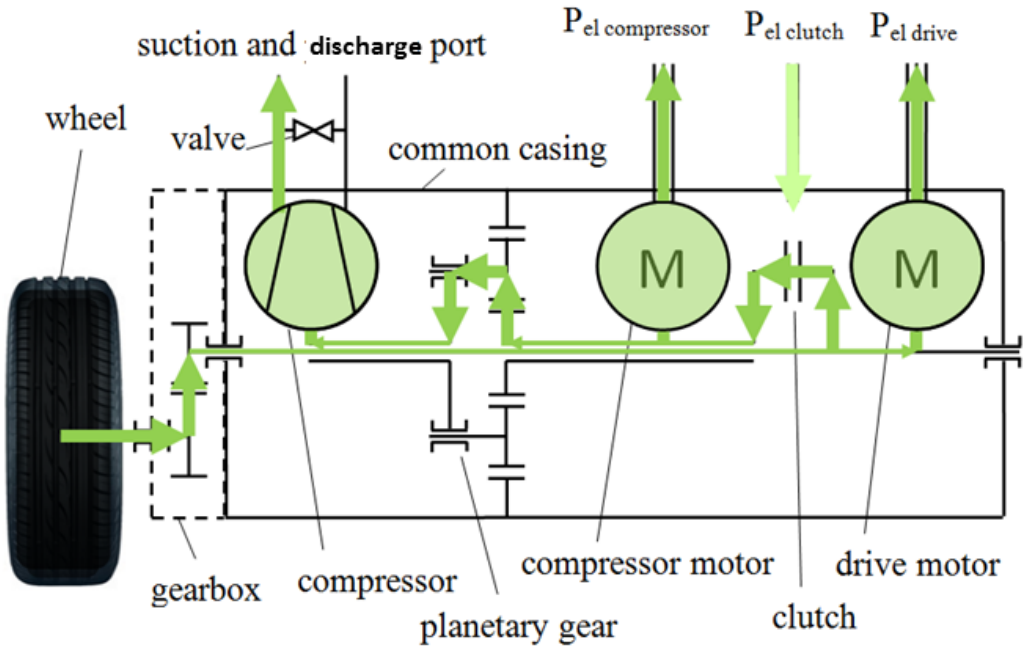

Figure 3.6 Mode 5: Air-conditioning and max charging during regenerative braking

Mode 6: Drive and Air-conditioning operate independently

Mode 6 is a combination of mode 1 and 2 as mentioned under mode 2.

3.3 2-in-1 Motor design

After considering the operational modes mentioned in section 3.2, one potential implementation of the new 2-in-1 motor structure is shown in Figure 3.7. Note that Figure 3.7 shows the possible embodiment encompasses all the possible modes of operation, without going through detailed engineering calculations. The detailed component of each part is show in respective engineering drawings, which are presented in *Appendix E*. These drawings have been submitted to the patent office in Germany for a patent application [93].

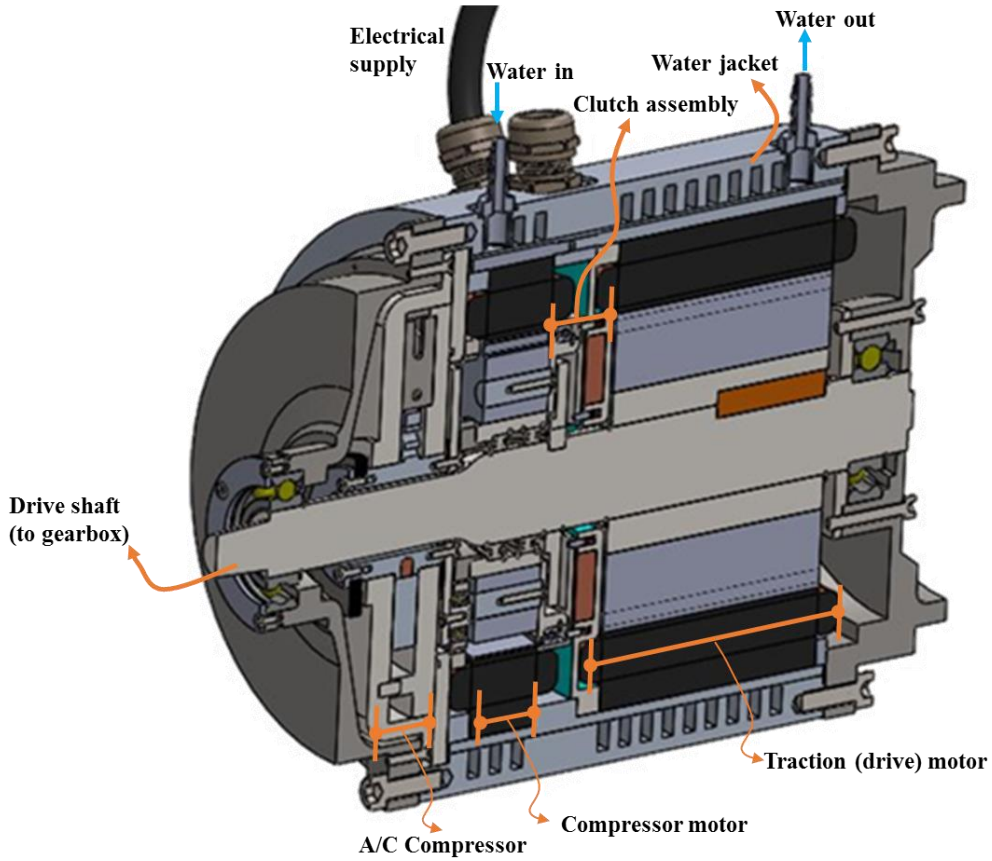

Patent: Europe A 63 630 j [93]

Figure 3.7 3D model of the 2-in-1 motor

An electromagnetic clutch, shown in Figure 3.8 is placed between the compressor and traction rotors to physically connect the traction and compressor motors during braking events. It is intended that the 2-in-1 motor to have a compact configuration, hence it is proposed to use two high power density Permanent Magnet Synchronous

Motors (PMSM) to generate the necessary torque for operating the compressor and providing tractive power to operate the vehicle. It is foreseeable that there will be heat generation from these motors and hence water jacket is used to enclose the motor for heat removal purpose. It is expected that the cooling water can be obtained from the vehicle's battery thermal management system.

The housing of the 2-in-1 motor designed to have the following additional benefits:

i. mounting bracket, cooling mechanism (water jacket), inverter housing, bearings and other components common for both motors can be shared, hence resulted in lowering material cost and weight savings,
ii. streamlined and compact configuration of the compressor and the motor saves spaces, and
iii. easier management of housing seals, performance and electromagnetic compatibility

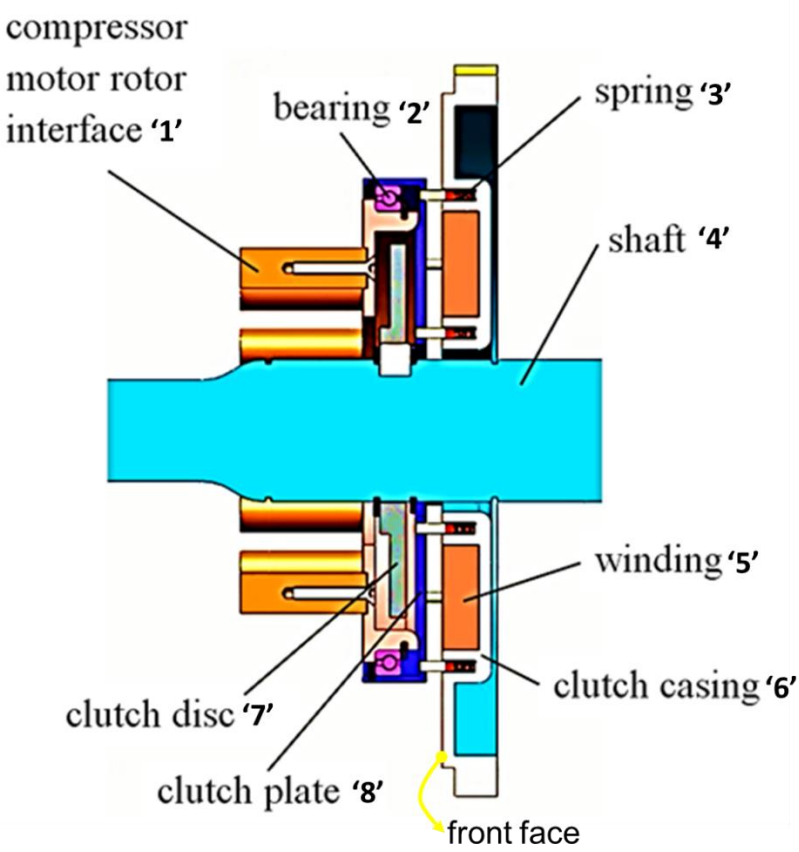

Figure 3.8 Internal clutch mechanism transfers recuperated energy from the traction drive to compressor

The electromagnetic clutch (see Figure 3.8) located between the drive and the compressor motor consists of a fixed clutch casing ***'6'*** that houses the electrical winding ***'5'*** and springs ***'3'*** circumferentially located on its front face. A clutch disc ***'7'*** is mounted on the traction drive shaft ***'4'***. The compressor motor rotor interface rods ***'1'*** are inserted into compressor rotor during assembly. When energized, the clutch casing ***'6'*** becomes magnetized and attracts the clutch plate ***'8'***. This in-turn pulls the compressor motor rotor interface rods ***'1'*** towards the clutch disc ***'7'***. When the compressor motor rotor interface ***'1'*** comes in contact with the clutch disc ***'7'***, the friction between these components couples the shaft ***'4'*** with the compressor rotor to facilitate power transfer. When the clutch is de-energized, the springs ***'3'*** located in the clutch casing ***'6'*** pushes the clutch plate ***'8'*** to its original position to disconnect the compressor from the traction shaft ***'4'***.

3.4 Compressor selection

This section compares various compressor variants to identify an appropriate compressing mechanism to be integrated with the 2-in-1 motor design. In general, an automotive compressor is required to meet the following requirements [94]: variable cooling capacity, high efficiency, compact, light weight, low vibration and low noise operation. Section 2.5.5 discussed three common compressor technologies apt for automobile application, namely the: (1) Scroll, (2) Swash plate and (3) Rolling piston compressor. Each compressor type has its own unique performance characteristics, advantages, and disadvantages. For example, the scroll compressor has quieter operating characteristics and high efficiency, but is plagued by high manufacturing costs and design complexity. Table 3.2 provides a more comprehensive comparison between the various types of automobile compressor types.

Table 3.2 A comparative study between automobile compressors

Compressor	**Advantages**	**Disadvantages**
Scroll [10], [94]–[96]	-Efficient -Low noise -Compact -Lightweight -Low vibration -Fewer parts count -No valves	-High manufacturing cost -Not repairable -Capacity control through stacking compressors -Complex structure
Swash plate [10], [40], [94]	-Smooth capacity control -Low vibration -High pressure ratio -Bulky	-High parts count -High moving parts -Complex design
Rolling Piston [86], [97]–[99]	-Simplest design -Few moving parts -Compact -Lightweight -Low cost -High efficiency -High performance -High reliability	-Operates at high RPM -Moderate vibration -High Frictional losses at high rotational speed

A suitable compressor can be selected based on the merits listed in Table 3.2. Ease of integration with the proposed motor design is the most important consideration. The limitation of axial space within the motor housing excludes the possibility of using the swash plate compressors due to the latter's bulky construction. Though the scroll compressor has a compact design, the high manufacturing cost and complexity in design means that the more favourable choice would be the rolling piston mechanism.

The rolling piston compressor is widely favoured by the industry due to its simple design, high reliability, and efficiency [99]. As compared to swash or wobble plate compressors, the rolling piston compressor has nearly 50% fewer parts than the former, thereby facilitating the easier fabrication of the compressor and decreased weight and cost. However, the rolling piston compressor experiences high frictional losses between sliding contacts when operated at high speeds. Significant frictional losses occur due to the contact of the vane tip with the rolling piston. This results in loss of compressor power, decrease in compression ratio [29], [100] and a decrease in overall performance.

A Swing Vane Compressor (SVC) is a variant of the rolling piston compressor. In a SVC, one end of the vane is rigidly fixed to the rolling piston while the other end is connected to the cylinder via a hinge joint as shown in Figure 3.9. It is similar to that of the rolling piston compressor; the cylinder axis coincides with the crankshaft, while the piston axis coincides with the eccentric axis. The piston rotates tangentially along the inner surface of the cylinder, creating two crescent-shaped volumes separated by the vane. The volume that communicates with the suction port is referred to as the "suction chamber" while the volume that communicates with the discharge port is known as the "compression chamber". The rotation of the rolling piston results in cyclical changes in these volumes leading to suction and compression of the working fluid. In general, the SVC has a lower frictional loss under similar operating conditions as compared with the conventional rolling piston compressor [94] as the contact friction between the vane and the piston is completely eliminated.

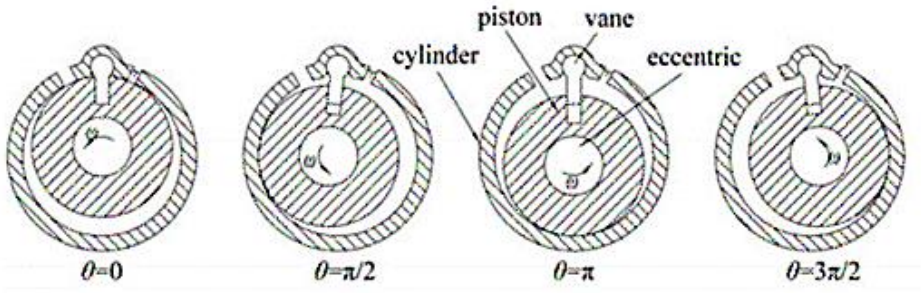

Figure 3.9 Swing Vane Compressor working principle [94]

Ooi [101] further enhanced the efficiency of the SVC by replacing the oscillating vane with a rigid vane as shown in Figure 3.10(b), the latter is called the Fixed Vane Compressor (FVC). Due to the pressure difference between the suction and compression chamber, a strong contact force occurs between the vane bushing and the oscillating vane in a conventional SVC (Figure 3.10 (a)). However, in the case of FVC, where the vane is fixed rigidly to the cylinder. Therefore, the contact force between the vane bushing and the rigid vane is no longer a function of differential pressure acting on the exposed vane surfaces. Thus, the novelty in FVC mechanism minimises the frictional losses between the vane and the bushing. In addition, FVC allows the driving shaft to pass through its centre, which is needed in the 2-in-1

motor design. Therefore, the FVC is chosen as the candidate for the 2-in-1 motor A/C compressor.

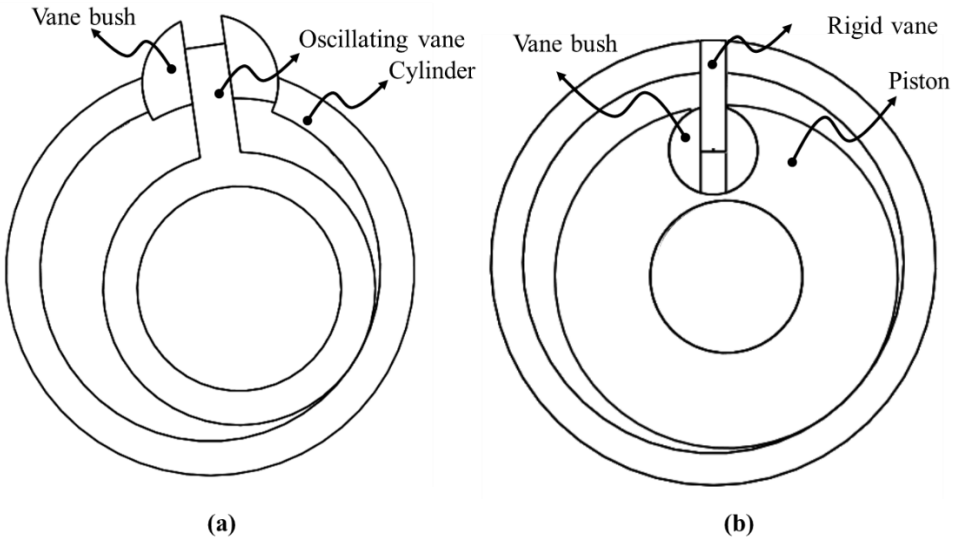

Figure 3.10 (a) Swing Vane Compressor, (b) Fixed Vane Compressor

3.5 Compressor drive

The compressor is driven by a Permanent Magnet Synchronous Motor (PMSM) as shown in Figure 3.11. This particular motor is compact, efficient but operates at high RPM. However, the rolling piston compressor typically operates at around 3000RPM. Therefore, a planetary gear system has to be introduced to ensure that the compressor operates at a slower speed. In the planetary gear system, the sun gear is driven by the compressor drive motor with the ring gear being held stationary. The torque to the compressor is delivered by the planetary gears. The sun gear has 60 teeth while each planet gear has 25 teeth. This configuration produces a 2.3:1 gear ratio thereby stepping down the speed of the compressor motor by a factor of 2.3.

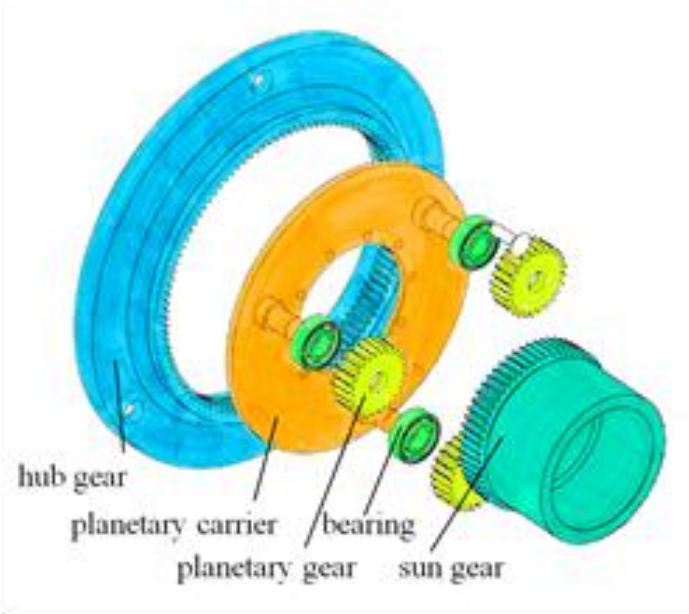

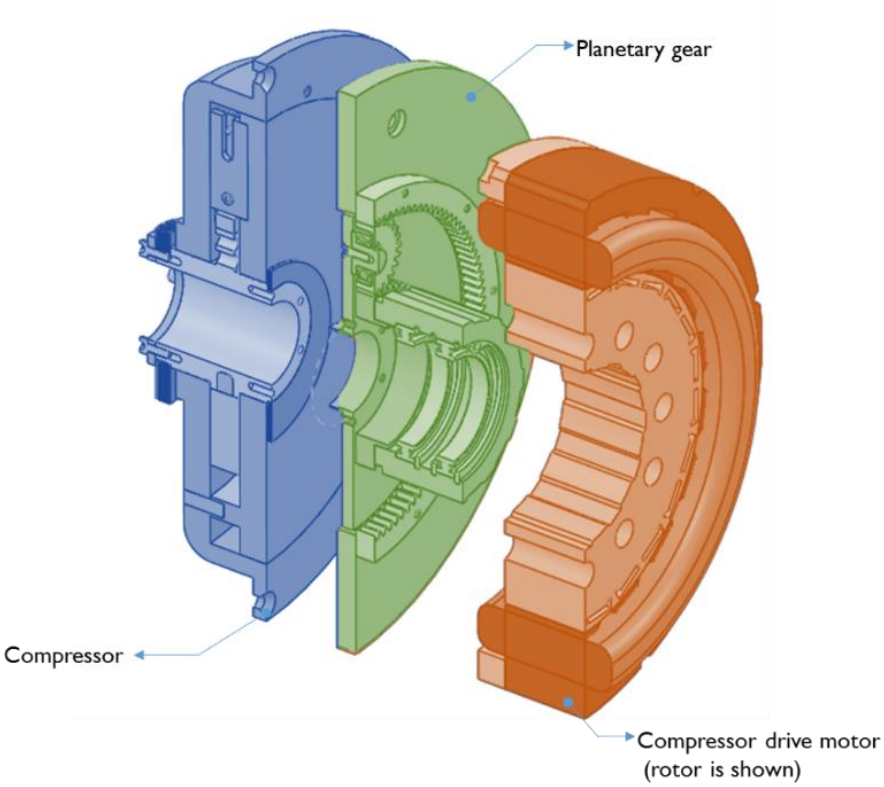

Figure 3.11 Compressor drive consists of PMSM motor and a planetary gear system

3.6 Concluding remarks

The basic structure and the operational modes of the 2-in-1 motor was introduced in this chapter. In summary, the 2-in-1 motor has the flexibility to operate in six different modes according to the need of the drive situations. Apart from performance gains, the 2-in-1 motor has the potential to reduce the manufacturing cost of the EV as it shares components which are common between the compressor and the drive motors.

A comparative study on various compressor designs was conducted to identify the most suitable compressing mechanism that suits the 2-in-1 motor drive train architecture. A fixed vane compressing mechanism was chosen for the compressor design which is integrated into the 2-in-1 motor structure.

Chapter 4
COMPRESSOR DESIGN

The detailed design of a possible embodiment of the 2-in-1 motor has been presented and discussed in chapter 3. A close examination of all the components that make up the 2-in-1 motor reveals that the modified compressing mechanism is the most unique mechanism that is newly introduced in this 2-in-1 motor design since, the motor designs are well established. Hence, the focus of this research project subsequently is on detailed design and analysis as well as prototyping test of the A/C compressor. This chapter describes the calculation of the key dimensions of the compressor to meet its design intent and requirements.

4.1 Compressor capacity and volumetric flowrate

Section 3.4 explains the choice of the Fixed Vane Compressor mechanism. Therefore, this chapter presents the detailed design of this compressor.

The intention of the 2-in-1 motor is to be used in a compact EV. Hence, EV such as i-MiEV (Mitsubishi Motors) or Leaf (Nissan) can be used as reference to establish design parameters related to the air-conditioning systems, including compressor. Here, i-MiEV has been chosen as a reference as the relevant data was readily available [16].

The specifications of the air-conditioning unit used in the i-MiEV can be found in *appendix B.* Based on this information, the compressor design data are established and presented in Table 4.1. The operating conditions are in accordance with the ASHRAE standard for compressor characterization (ASHRAE, 2008).

Table 4.1 Compressor technical requirements

Parameter	**Value**
Displacement Capacity per cycle (1 cycle = 2 Rev.)	25 cc
Maximum operating speed	3000 RPM
Evaporator load (Based on medium size vehicle)	5.275 kW
COP	2.5 to 3
Compressor Power Requirement	2 to 1.75 kW
Refrigerant	R1234yf
Maximum pressure	18 bar
Evaporating temperature	7.2° C
Degree of superheat	27.8° C
Condensing temperature	65° C
Degree of subcool	8° C

The compressor geometrical dimensions can be calculated from the technical requirements listed in Table 4.1. For a rolling piston compressor with a cylinder height h_c, the displacement capacity is calculated by subtracting the rolling piston and vane volume from the cylinder volume

$$V_{displacement} = h_c\left(\frac{\pi}{4}(D_c^2 - D_p^2) - w_{vn}l_{vn}\right) \tag{4.1}$$

where w_{vn} and l_{vn} are the width and the length of the vane respectively. The relevant compressor terminology can be found in Figure 4.1.

Piston diameter can be expressed in terms of cylinder diameter and eccentricity, e as

$$D_p = D_c - 2e \tag{4.2}$$

Substituting Eq. (4.2) into Eq. (4.1) yields

$$V_{displacement} = h_c\left(\frac{\pi}{4}(D_c^2 - (D_c - 2\mathrm{e})^2) - w_{vn}l_{vn}\right) \tag{4.3}$$

The eccentricity, e is taken as [102]

$$e = 0.09D_c \tag{4.4}$$

With this relationship, Eq. (4.3) becomes

$$V_{displacement} = h_c\left(\frac{\pi}{4}(D_c^2 - (D_c - 2(0.09D_c))^2) - w_{vn}l_{vn}\right) \tag{4.5}$$

where the minimum required vane length, $l_{vn,min}$ can be expressed as function of eccentricity and the cylinder diameter

$$l_{vn,\min} = +\sqrt{\left(\frac{D_c}{2}\right)^2 + 2e\left(\frac{D_c}{2}\right) + e^2} - \left(\frac{D_c}{2}\right) \tag{4.6}$$

The practical vane length should ensure that the vane has sufficient length to remain within the vane bushing throughout the compressor cycle. Therefore, in this design, the practical vane length is taken as

$$l_{vn,practical} = l_{vn,\min} + R_{bush} \tag{4.7}$$

The displacement volumetric rate of the compressor is

$$\dot{V} = \frac{V_{displacement}N}{60} \tag{4.8}$$

It can be noted from Eq. (4.5) that the compressor displacement volume is proportional to the square of the cylinder diameter. Therefore, a large increase in displacement volume can be achieved by a marginal increase in the cylinder diameter as compared to the cylinder length. By fixing the cylinder height and vane width based on physical constrains, Eq. (4.5) and (4.8) can be solved to determine the compressor diameter such that it meets the desired capacity and volumetric flow rate for a given operating speed. The major dimensions of the FVC which meets the specified requirements are listed in Table 4.2.

Table 4.2 Major compressor dimensions

Parameter	**Value (mm)**
Cylinder diameter	122
Cylinder height	11
Piston diameter	111
Eccentricity	5.5
Vane width	14
Vane length	33.5

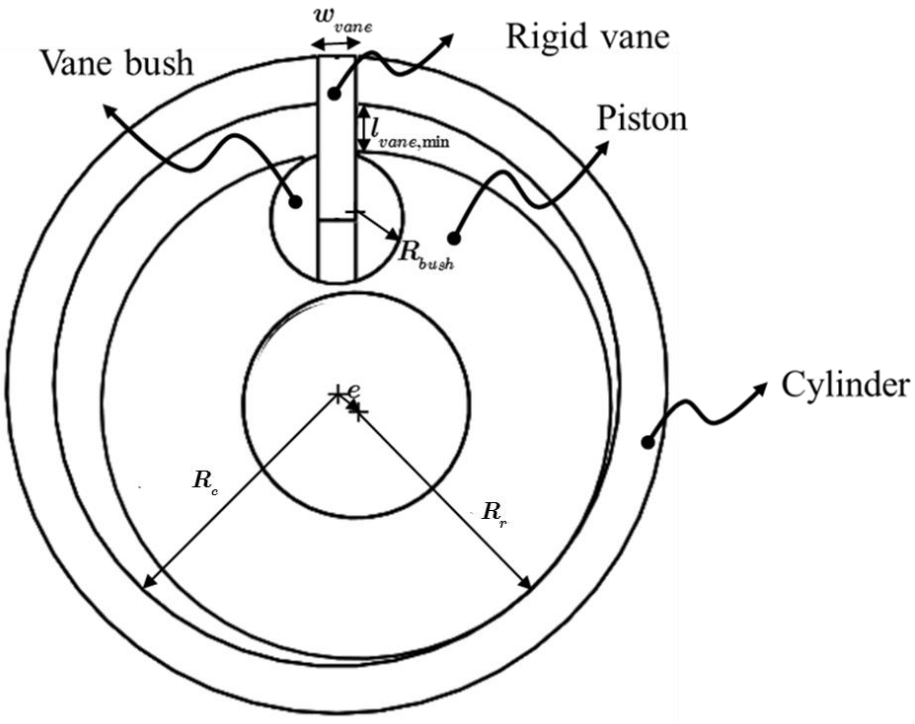

Figure 4.1 FVC terminologies

4.2 Compressor wall thickness

The saturated pressure corresponds to the condensing temperature of 65 ^{o}C for R1234yf is 1834.8 kPa (~18 bar). For safety, the compressor casing will be designed to withstand at least three times this operating pressure. The compressor casing can be modelled as a simple pressure vessel for simplicity. A pressure vessel is a closed container designed to hold gases or liquids at a pressure substantially different from the ambient. The tensile forces that develop within the pressure vessel walls acts against the pressure exerted by the pressurised fluids. Therefore, the wall thickness of the pressure vessel should be designed to withstand the operating stresses. The computation of the cylinder wall thickness consists of two parts: (1) the axial cylinder wall thickness and (2) the radial cylinder wall thickness.

Axial cylinder wall thickness

The end faces of the cylinder can be modelled as circular plate subjected to uniform pressure load, *P* as shown in Figure 4.2. Since the end faces of the cylinder is rigidly attached to the longitudinal portion, the circumferential boundary of the end faces can be modelled as a fixed support that resists angular deformation.

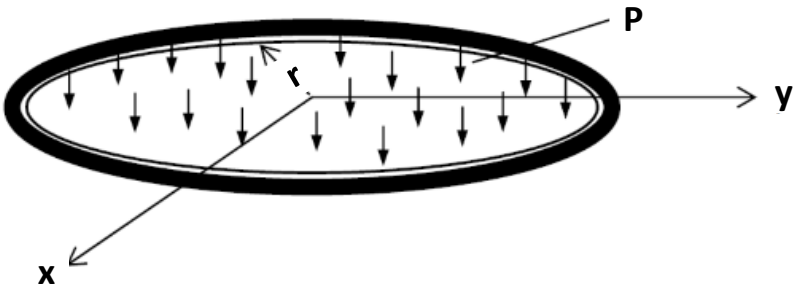

Figure 4.2 Pressure forces that acts on the compressor end faces

The partial differential equation describing the deflection of the flat plate reads:

$$\frac{d^2w}{dx^4} = -\frac{P}{D} \tag{4.9}$$

where D $= Eh^3/12(1-v^2)$

Since the ends are clamped rigidly, slop and deflection are zero at the boundary. Mathematically, it can be defined as

$$w = 0, \frac{\partial w}{\partial x} = 0, \frac{\partial w}{\partial y} = 0 \tag{4.10}$$

Assuming the deflection can be described by a function:

$$w = c(x^2 + y^2 - r^2)^2 \tag{4.11}$$

Substituting Eq. (4.11) and boundary conditions listed in Eq. (4.10) into Eq. (4.9) yields

$$c = -\frac{P}{64D} \tag{4.12}$$

Substituting Eq.(4.12) in (4.11), the magnitude of the maximum deflection at the plate centre is

$$|w| = \frac{P}{64D} r^4 \tag{4.13}$$

The maximum stress in the plate occurs at the outer fixed edge can be obtained using:

$$\sigma_{\max} = \frac{3P}{4}\left(\frac{r}{h}\right)^2 \tag{4.14}$$

The compressor end faces also serve as a journal bearing as shown in Figure 4.3. Therefore, the initial design analysis was performed assuming that the wall thickness is equal to that the length of the front and rear journal bearings; which was calculated to be 10.5mm using the journal bearing model (to be discussed in next section). Though the analytical method is ought to provide an accurate analysis on the adequacy of the wall thickness, the simplifications that the circumferential boundary remains rigid does not represent the actual boundary conditions experienced by the end faces. For example, the fixed end of the front end face is away from the pressure application point as shown in Figure 4.3. Therefore, a more

comprehensive finite element analysis was performed to compare the analytical predictions with the numerical solutions.

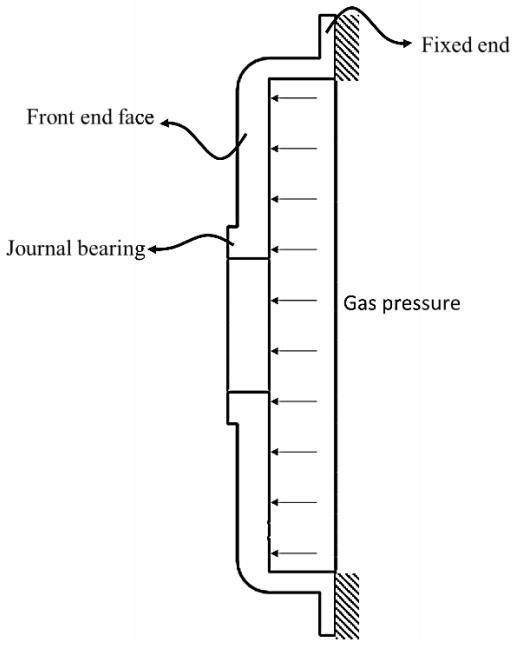

Figure 4.3 Actual boundary condition for the front end face of the compressor

Figure 4.4 compares the deflection of the front and rear end faces predicted by analytical and FEA method. For the both end faces, it is apparent that the analytical solutions tend to over predict the deflection. This is probably because analytical solution ignores the presence of the journal bore at the plate centre where no pressure load acts. Since the FEA provides a more comprehensive representation of pressure load, it can be expected that the total expansion of the end faces $(\Delta\delta)$ is a mere 0.137mm, which is less than 1.5% of the wall thickness.

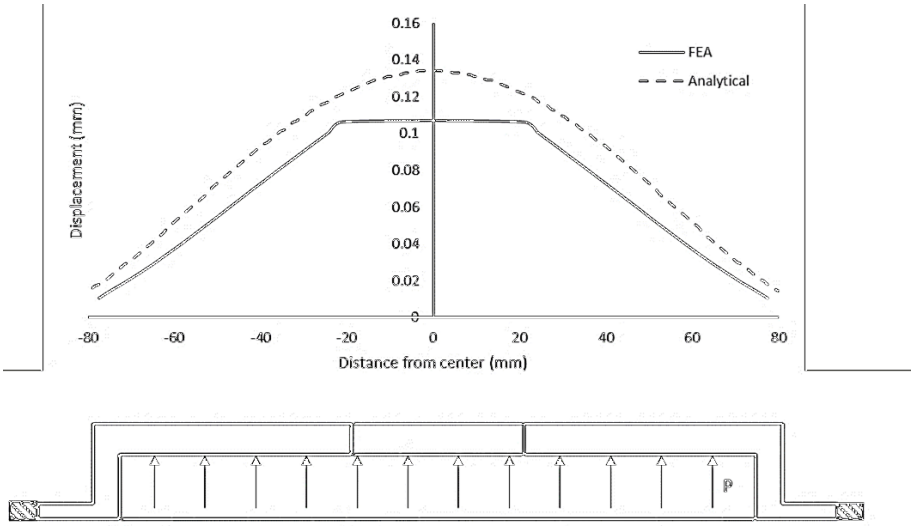

(a)

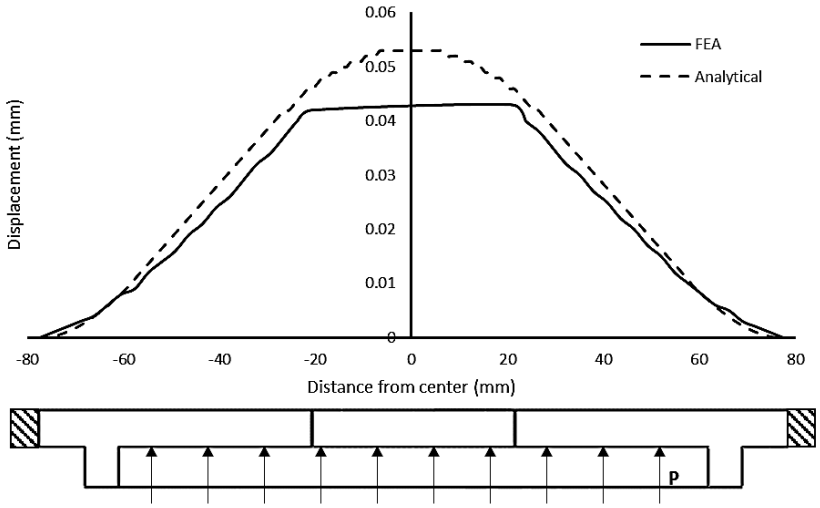

(b)

Figure 4.4 Cylinder end wall deflection under uniform internal pressure (a) front face, (b) rear face

Substituting material and geometrical parameters into Eq. (4.14) predicts that the maximum stress in the cylinder end faces to be approximately 128MPa. Once again, FEA was performed to visualise the stress distribution due to the uniform pressure load acting on the end faces as shown in Figure 4.5. Based on the FEA, the maximum von Misses stress was calculated as 105MPa. The cylinder will be manufactured out of stainless steel having a yield strength of 315MPa. Based on the maximum stress reading and the material yield strength, the factor of safety is calculated to be 3.

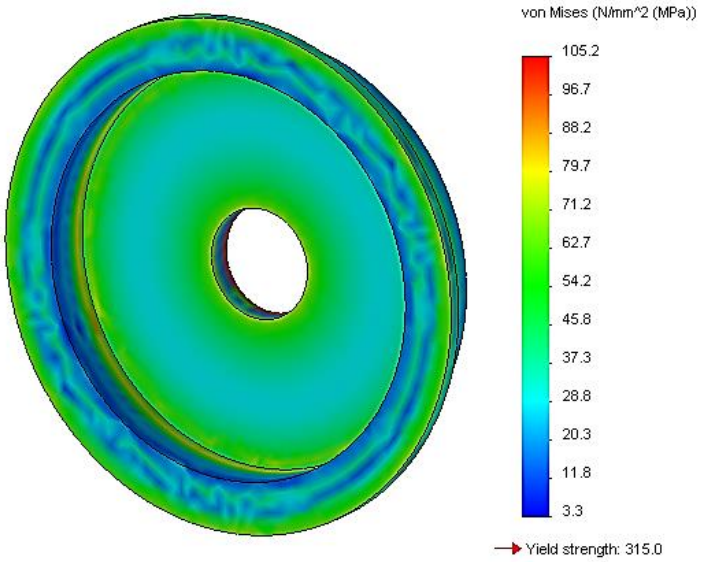

(a)

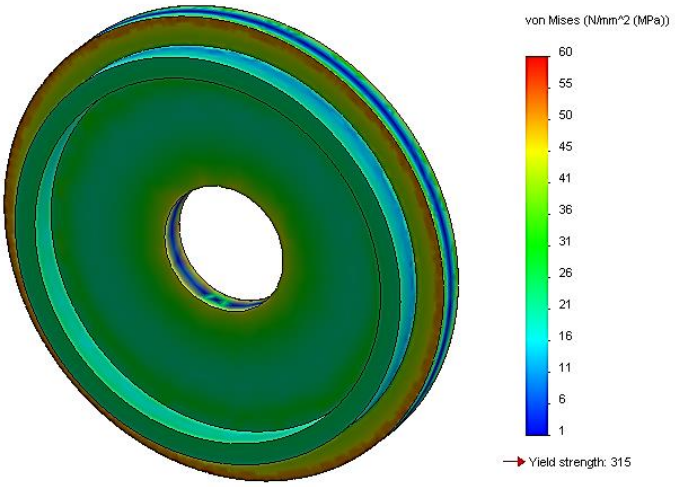

(b)

Figure 4.5 Von Misses stresses acting on the cylinder end faces (a) front face, (b) rear face

Radial cylinder wall thickness

The minimum wall thickness along the radial direction can be easily calculated using the pressure vessel method for thin walled cylinders. Thin wall assumption is valid as the wall thickness is usually significantly smaller than the cylinder diameter. A thin walled cylinder with end faces subjected to internal pressure experiences both the longitudinal (σ_l) and hoop (σ_h) stresses. These stresses can be calculated using Eqs. (4.15) and (4.16).

$$\sigma_l = \frac{P \cdot r}{2h} \tag{4.15}$$

$$\sigma_h = \frac{P \cdot r}{h} \tag{4.16}$$

Comparing Eqs. (4.15) and (4.16), it can be noted that the hoop stress is twice that of the longitudinal stress and thus will be used for determining the minimum radial wall thickness. By including a factor of safety, *N* and solving Eq. (4.16) for minimum cylinder wall thickness, *h* yields

$$h = \frac{N \cdot P \cdot r}{\sigma_h} \tag{4.17}$$

Substituting the hop stress (σ_h) with the material yield strength, the minimum wall thickness was found as 1.7mm. Since the cylinder diameter is nearly 50 times larger than the calculated wall thickness, the thin wall assumption is valid.

4.3 Dynamic balancing of compressor crankshaft

In a conventional rolling piston and SVC, the centrifugal force generated by the eccentric rolling piston (m_3) in position l_3 on the crankshaft is dynamically balanced by using two balancing masses (m_1 and m_2) placed on balancing planes at positions l_1 and l_2 as shown in Figure 4.6.

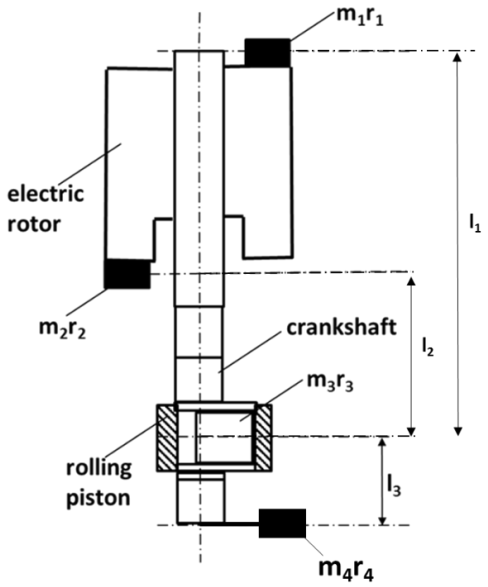

Figure 4.6 Dynamic balancing of Eccentric mass in two planes [103]

The balance in forces is achieved when:

$$m_2 r_2 = m_3 r_3 + m_1 r_1 + m_4 r_4 \tag{4.18}$$

where r is the distance to the centroid of the mass measured from the shaft rotating axis.

Taking moments about the plane containing mass 3 yields

$$l_2 m_2 r_2 + l_3 m_4 r_4 = l_1 m_1 r_1 \tag{4.19}$$

where l is the distance to the mass measured from the plane.

In theory the use of three balancing masses to balance the crank shaft seems a perfect solution, however, it is impossible to achieve perfect dynamic balance as the balancing weight neither accounts for the flexibility of the crankshaft nor the journal bearing housings. Moreover, this method gives no consideration for the possibility of variations in the balancing masses in a large scale production. These variations typical include material density, mounting position of the balancing masses from datum, manufacturing tolerances [103] and defects such as voids. In addition, there will be variation in the rotor dimensions between individual electric motors.

The placement of balancing masses on the crankshaft results in unwanted crankshaft deflection as shown in Figure 4.7. As observed, these deflections are the largest at the locations of the eccentric rotating piston and the balancing masses. This deflection ultimately results in increased mechanical vibration leading to rotor-stator rubs, failure in spot welds [104], higher bearing load and increased crank shaft fatigue. In practise, individual compressor assembly has to be balanced using a trial and error technique to minimise the amplitude of vibrations at the operating speed range. This eventually results in increased production time and cost.

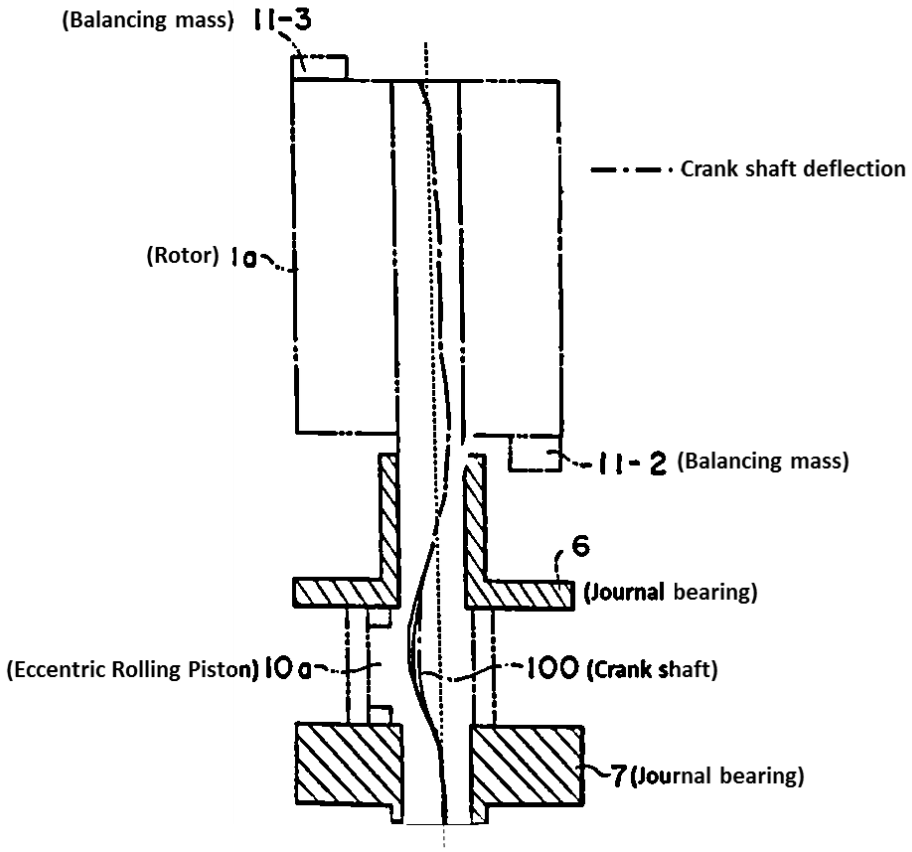

Figure 4.7 Placement of the balancing masses results in crank shaft deflection [103]

The newly designed compressor utilizes an in-plane counterweight to cancel the centrifugal force produced by eccentric rotating piston. This is achieved by producing the eccentric rotating piston using a metal with low density (such as aluminium) and the in-plane counter weight with a material having a much higher density (such as copper). Holes can be further drilled into the eccentric rotating piston to reduce the mass of the in-plane counter weight. During assembly, the in-plane counterweight is simply inserted into the eccentric as shown in Figure 4.8.

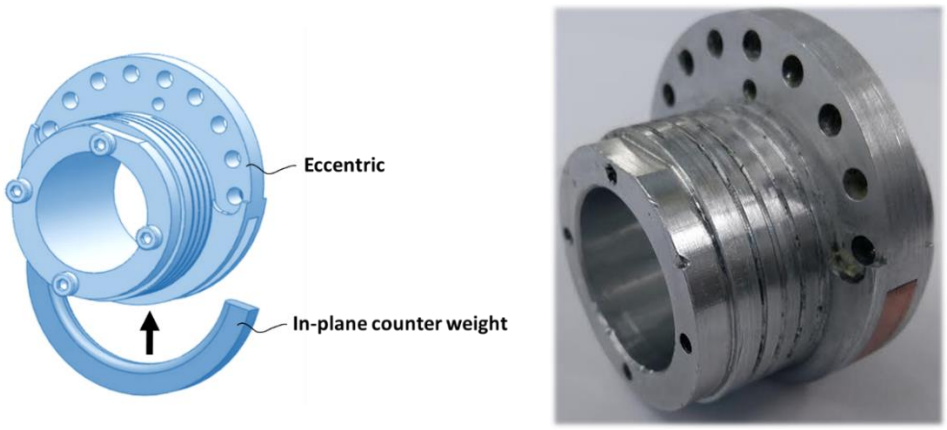

Figure 4.8 In-plane counter weight inserted into the eccentric

This approach is ought to produce a simpler design and a smoother compressor operation due to drastic reduction in the crankshaft deflection. Moreover, the new design is much tolerant to variation in large-scale production as any crank shaft deflection caused by imbalance is confined between the journal bearings as shown Figure 4.9.

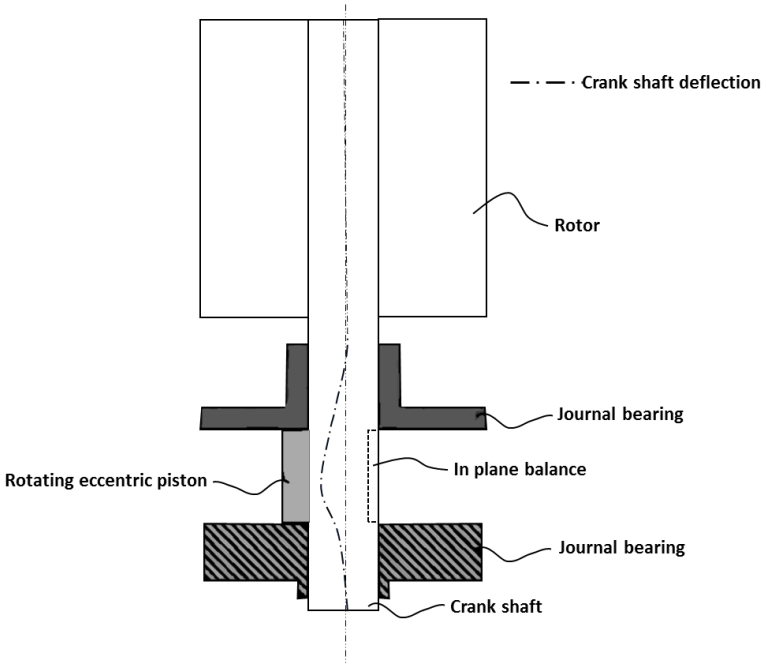

Figure 4.9 In-Plane counter weight used to cancel the centrifugal force produced by the eccentric piston

4.4 Journal bearing design

A journal bearing consists of a shaft housed within a metal sleeve or shell which is supported by hydrodynamic lubrication during operation. There are no rolling elements in these bearings since this is a plain bearing. This section focuses on systematic design and analysis of journal bearing that supports the compressor drive shaft on either ends. The design procedure of a journal bearing starts by defining the L/D ratio, oil film thickness and clearance. Thereafter, a design analysis is performed to verify if the bearing is able to operate under anticipated loading condition.

4.4.1 Journal bearing configuration and force analysis

The front and aft journal bearings of the compressor design is shown in Figure 4.10. In this arrangement, the rolling piston is simply-supported by bearings located in both ends. Therefore, the loads exerted by the piston on the journal is equally shared between the bearings.

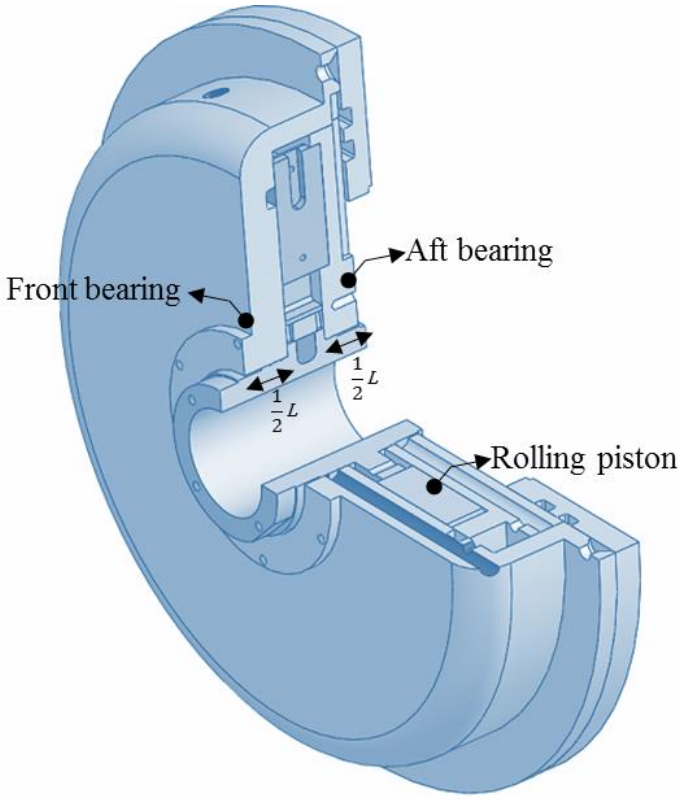

Figure 4.10 Journal bearing configuration in fixed vane compressor

Figure 4.11 shows the main forces that acts on a fixed vane compressor during a compression cycle. The key loads include (1) vane contact and frictional forces, (2) piston centrifugal force and (3) gas compression force. Each of these forces will be modelled to calculate the magnitude and the argument of the resultant force, which is subsequently transmitted to the journal.

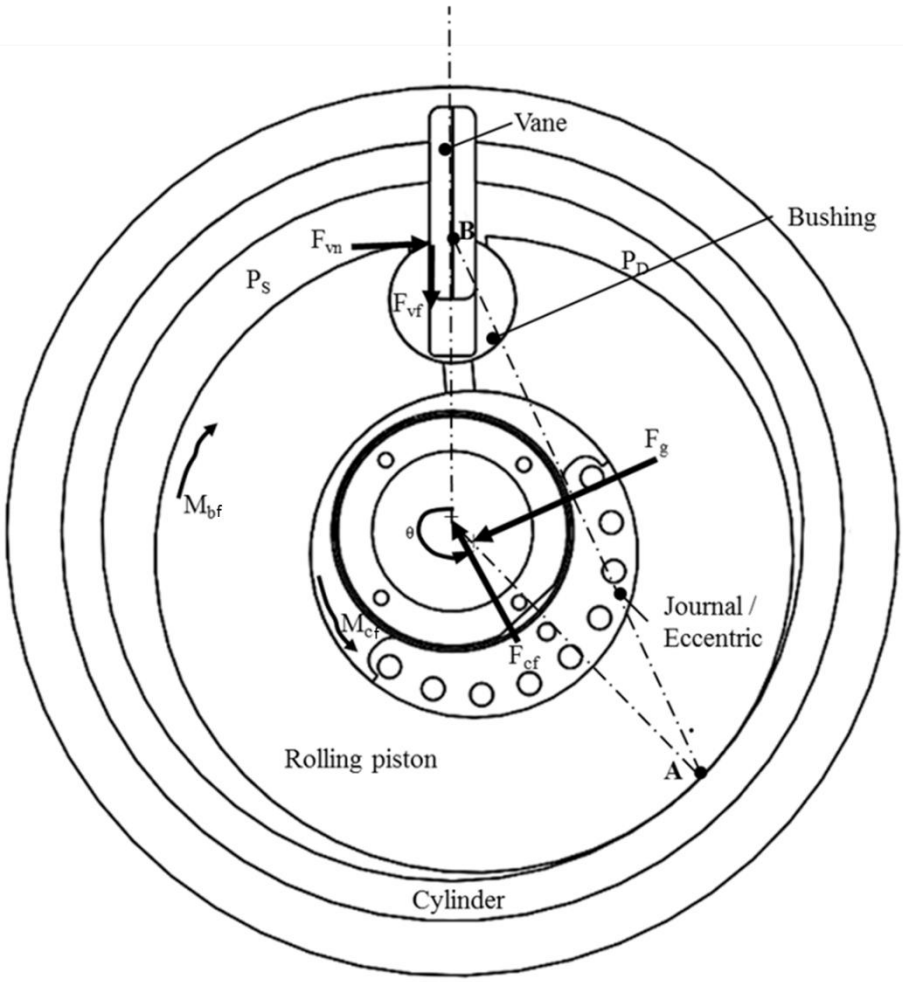

Figure 4.11 Free body diagram of the fixed vane compressor

Vane contact and frictional force

The vane contact force, F_{vn} can be evaluated by applying torque equilibrium about the rolling piston centre assuming there is a small clearance between the rolling piston and the inner cylinder wall [97]

$$I_0 \cdot \alpha_0 = M_{cf} - F_{vn} R_p - M_{bf} \tag{4.20}$$

where I_0 represents the net rotational inertial of the piston, eccentric and the crankshaft assembly. The net rotational inertia can be expressed as

$$I_0 = \left(\frac{1}{2} m_r \left(R_r^2 + R_e^2 \right) - \frac{m_b}{2} R_b^2 - m_b l_b^2 \right) + \frac{1}{2} m_e R_e^2 + \frac{1}{2} m_{rs} R_{rs}^2 \tag{4.21}$$

where e is the eccentricity of piston about the axis of rotation and l is the radial location of the vane bushing measured from rolling piston centre.

Assuming the eccentric remain concentric to the rolling piston and the radial clearance between the piston and eccentric is known to be δ. The bearing moment per face at the contact surface between the piston and the eccentric, M_{cf} can be modelled as viscous drag between two concentric cylinders (i.e piston and the eccentric) [82]

$$M_{cf} = \frac{2\pi\mu R_e^3 h_c \omega_r}{\delta} \tag{4.22}$$

where the relative angular velocity, ω_r is simply the difference between the crankshaft, ω and the piston ω_p [82]

$$\omega_r = \omega - \omega_p \tag{4.23}$$

Neglecting the vane bushing, the frictional moment between the piston and the cylinder head per face, M_{bf} can be modelled using viscous drag formula between two rotating disks [82]

$$M_{bf} = \frac{\pi\mu\omega_p}{2\varepsilon_2} (R_p^4 - R_c^4) \tag{4.24}$$

ε_2 represents the axial clearance between cylinder and eccentric.

Therefore, the vane contact force F_{vn} can be evaluated using Eq. (4.25)

$$F_{vn} = \frac{M_{cf} - M_{bf} - I_p \alpha_p}{R_r} \tag{4.25}$$

The vane contact force is assumed to act perpendicular to the vane side face through the compression cycle due to pure sliding motion of the vane bushing. A frictional force develops along the longitudinal axis of the vane due the vane contact force. The vane contact frictional force is given by

$$F_{vf} = \mu_{vf} F_{vn} \tag{4.26}$$

The coefficient of frictional, μ_{vf} can be taken as 0.15 [105] for metal-to-metal contact between the vane and the bushing.

Centrifugal force

The centrifugal force, F_{cf} that acts on the crankshaft due to piston-eccentric assembly is given by

$$F_{cf} = m_e \cdot e \cdot \omega_e^2 + m_p \cdot e \cdot \omega_{p,s}^2 \tag{4.27}$$

where $\omega_{p,s}$ is the angular velocity of the piston due to slipping motion

The centrifugal force contribution from the eccentric can be excluded as it has been dynamically balanced using an in-plane counter balance as discussed in previous section. As defined in Eq. (4.27), the eccentric and the piston has an independent angular velocity. This is because, the eccentric has a pure rotational motion about the crankshaft axis, while the piston experiences a slipping motion relative to crankshaft axis.

The angular velocity of the rolling piston, $\omega_{p,s}$ due to slipping motion of the roller relative to the cylinder can be determined by studying the torsional loads that acts on the piston-eccentric assembly (identified in Figure 4.12). Under equilibrium conditions, the torque produced by the piston-cylinder head friction should be equal to piston-eccentric frictional force.

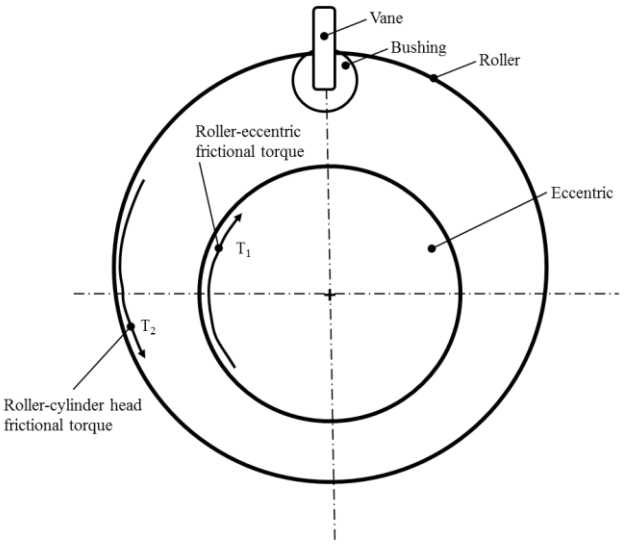

Figure 4.12 Torsional loads on the fixed vane compressor

The roller-eccentric frictional torque, T_1 is given by [106]

$$T_1 = \frac{2\pi\mu R_e^3 h_c \omega_{p,s}}{\delta} \tag{4.28}$$

where δ is the radial clearance between the roller and eccentric.

Likewise, the roller-cylinder head frictional torque, T_2 is given by [106]

$$T_2 = \frac{\pi}{\varepsilon_1}\mu\left[\omega\left(1-\frac{1}{a}\right)+\omega_{p,s}\right]\cdot(\mathrm{R}_p^4 - R_e^4) \tag{4.29}$$

where ε_1 represents the axial clearance between cylinder and roller.

Equating Eq.(4.28) and Eq. (4.29) yields

$$\frac{\pi}{\varepsilon_1}\mu\left[\omega\left(1-\frac{1}{a}\right)+\omega_{p,s}\right]\cdot(\mathrm{R}_p^4 - R_e^4) = \frac{2\pi\mu R_e^3 h_c}{\delta}\left[\frac{\omega}{a}-\omega_{p,s}\right] \tag{4.30}$$

Solving for the angular velocity of the rolling piston due to slipping motion, $\omega_{p,s}$

$$\omega_{p,s} = \frac{\dfrac{\omega}{a}\left[\dfrac{2R_e^3 h_c}{\delta} - \dfrac{(a-1)}{\varepsilon_1}R_p^4\right]}{\left[\dfrac{2R_e^3}{\delta} + \dfrac{R_r^4 - R_e^4}{\varepsilon_1}\right]} \tag{4.31}$$

The argument of the centrifugal force is simply the crankshaft angle

$$\measuredangle F_{cf} = \theta$$

Gas compression force

The refrigerant pressure in the working chamber of the compressor varies w.r.t to the crankshaft angle as shown in Figure 4.13. This setups a differential pressure between the suction and compression chambers. The differential pressure acts on the rolling piston giving rise to the gas compression force. The gas compression force, F_g is given by

$$F_g = h_c(P_{cv}(\theta) - P_s)\overline{\mathrm{AB}} \tag{4.32}$$

where length $\overline{AB}$ (identified in Figure 4.11) can be found using geometric relationships and is given by

$$\overline{AB} = \sqrt{2r_p^2\left[1-\cos\left(\theta+\frac{3}{2}\pi-\sin^{-1}\left(\frac{e\cos\theta}{r_p}\right)\right)\right]} \tag{4.33}$$

The argument of the gas compression force is given by

$$\measuredangle\vec{F}_g = \frac{\theta}{2}+\frac{1}{2}\sin^{-1}\frac{e\cos\theta}{r_p}+\frac{\pi}{4} \tag{4.34}$$

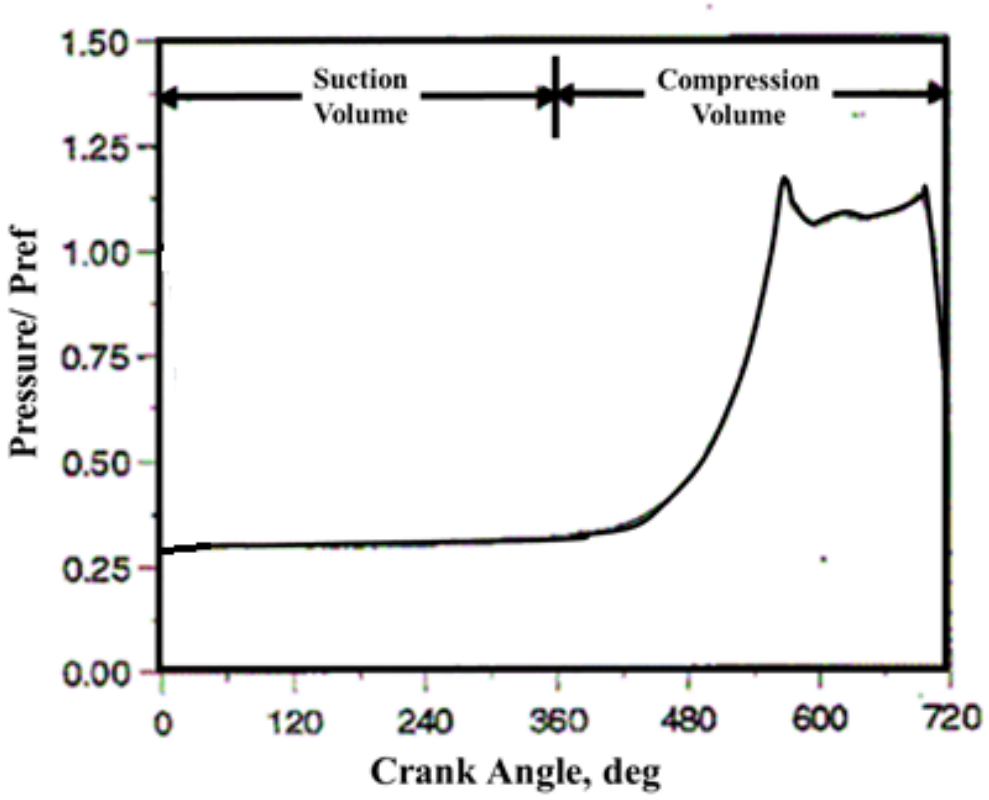

Figure 4.13 Refrigerant pressure with respect to crank angle.

The net resultant force that acts on the piston is given by the vector addition of the centrifugal and gas pressure forces as stated in Eq. (4.35)

$$\vec{F}_{net} = \vec{F}_{cf} + \vec{F}_{g} = F_{cf} \measuredangle \vec{F}_{cf} + F_{g} \measuredangle \vec{F}_{g} \tag{4.35}$$

The variation of resultant force during the compression stroke is shown in Figure 4.14 for the compression geometry specified in Table 4.2. Based on the plot, an initial resultant force of about 200N acts on the journal bearing at the start of the suction stroke. The centrifugal force and the vane contact and frictional forces contribute majority of this initial load. Thereafter, the gas compression forces increase which results in the peak resultant load of about 2kN towards the end of the compression cycle.

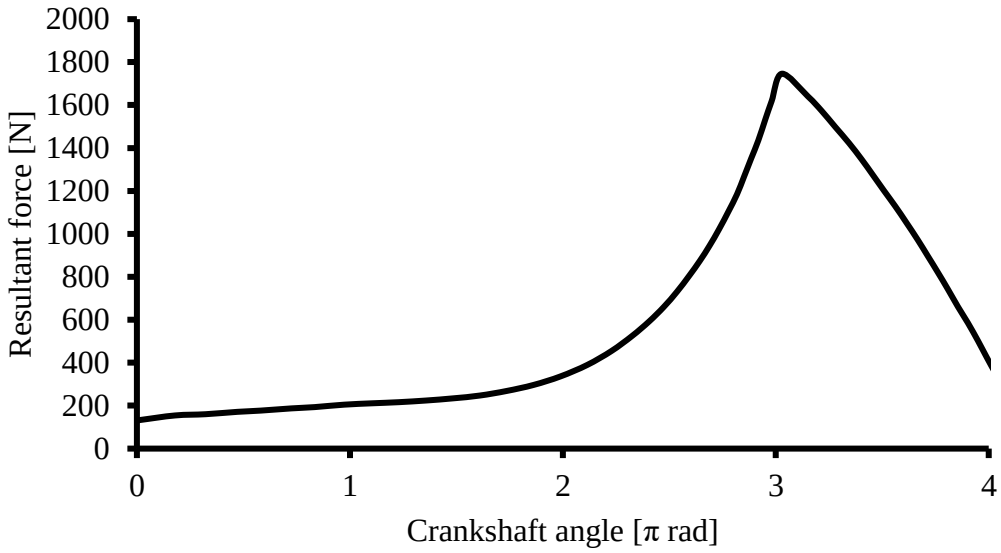

Figure 4.14 Variation in bearing load with respect to journal angle

4.4.2 Pressure distribution in a journal bearing

With reference to Figure 4.15, it can be observed that the resultant force, W_r is supported by the journal and transmitted to the bearing through a thin fluid film. The lubricant film acts a medium to absorb vibration and support the dynamic load while preventing metal-to-metal contact. Due to fluctuations in the resultant load, the journal, suspended over a thin film of lubricant exhibits an orbital motion along the longitudinal axis. This motion relocates the journal within bearing clearance, *c* such that centre of journal is a distance *e* away from the bearing centre.

The motion of the journal during compression cycle leads to variation in fluid film pressure, *p* and thickness, *h*. It is important for the bearing designer to be able to predict both the film pressure distribution and thickness of fluid film to prevent abrasive wear of the journal, self-excited vibration and to improve the reliability.

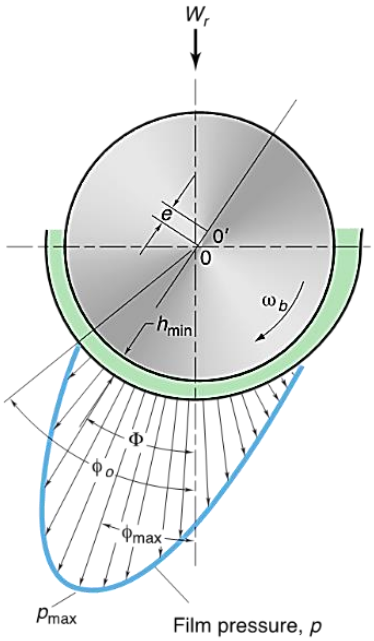

Figure 4.15 Pressure distribution of around a journal bearing [107]

Reynolds equation, a partial differential equation governing the pressure gradient of thin viscous film over a flat plate can be used to model the pressure distribution of the fluid film in journal the bearing. Reynolds equation as shown in Eq. (4.36) is valid for a Newtonian fluid that exhibits low Reynolds number, thin fluid film thickness and negligibly pressure variation across the film thickness.

$$\frac{\partial}{\partial x}\left(\frac{\rho h^3}{12\mu}\frac{\partial P}{\partial x}\right)+\frac{\partial}{\partial y}\left(\frac{\rho h^3}{12\mu}\frac{\partial P}{\partial x}\right)=\frac{1}{2}\frac{\partial}{\partial x}[\rho(\mathrm{U}_a+U_b)h] - \rho U_b\frac{\partial h}{\partial x}+\rho(w_b-w_a)+h\frac{\partial \rho}{\partial t} \tag{4.36}$$

where *U* represents the fluid flow velocity.

The pressure terms on the left hand side of the Reynolds equation motivates a flow due to pressure gradient, which is known as Poiseuille flow. The first term on the right hand side contributes to the flow due to shear, which is known as Couette flow; the second term generates a flow due to geometric squeeze; while the third term encourages the flow due to normal squeeze and the last term indicates the time-variant expansion. The flow characteristics within a journal bearing with zero eccentricity ratio *(e/c)* and subjected to a load, can be modelled as Couette flow

between parallel plates. The Couette flow term on Reynolds equation can be expanded into Eq. (4.37)

$$\frac{1}{2}\frac{\partial}{\partial x}[\rho(\mathrm{U}_a+U_b)h]=\frac{1}{2}\begin{bmatrix}\rho h\dfrac{\partial(U_a+U_b)}{\partial x}+\\ \rho(U_a+U_b)\dfrac{\partial h}{\partial x}+h(U_a+U_b)\dfrac{\partial \rho}{\partial x}\end{bmatrix} \tag{4.37}$$

The first term on the right hand side of Eq. (4.37) represents the bearing material stretch and hence can be ignored as journal bearings are produced from rigid material. The second term describes the distribution of the physical wedge which results in the desired pressure distribution in the journal bearing. In practice, for a journal bearing to exhibit positive load bearing capacity, the physical wedge must be a converging gap, thereby requiring the term $\partial h/\partial x$ to be negative. The last term describes the density distribution of the physical wedge and can be often excluded from analysis for lightly loaded journal bearings or if the lubricant is incompressible.

Therefore, for a rigid journal bearing lubricated with an incompressible fluid operating at steady- state, the Reynolds equation can be simplified to

$$\frac{\partial}{\partial x}\left(\frac{\rho h^3}{12\mu}\frac{\partial P}{\partial x}\right)+\frac{\partial}{\partial y}\left(\frac{\rho h^3}{12\mu}\frac{\partial P}{\partial x}\right)=\frac{1}{2}\rho(U_a-U_b)\frac{\partial h}{\partial x}+\rho(w_b-w_a) \tag{4.38}$$

where w_a and w_b are the bounding body velocities in x and y respectively.

Special simplifications are required to find a closed form solution of the simplified Reynolds equation. The solution of the simplified partial differential equation then provides the desired pressure distribution around a journal bearing. These special approximations often lead to an infinitely short or long journal bearing pressure distribution model. The infinitely short journal bearing approximation is valid for situation where the diameter of the bearing is very much larger than the length. In this circumstance, the flow due to rotational motion is assumed to be negligible compared to the flow along the bearing sides. On the other hand, the infinitely long journal bearing is appropriate for situation where the bearing diameter is much

smaller in comparison to the bearing length. In this condition, the flow along the side of the bearing is assumed to be negligible as compared to the flow due the rotational motion.

In practice, journal bearings are neither infinitely long nor short. Therefore, CFD can be employed to accurately capture the 3D pressure distribution of the journal bearing. COMSOL CFD analysis was used to capture the pressure distribution in a journal bearing by providing the geometrical dimensions of the bearing, oil inlet temperature and viscosity. The COMSOL CFD analysis is based on thin-film flow lubrication simulations. The CFD solver generates the pressure distribution in the lubricant of the journal bearing by solving Reynolds equation on the surface wetted by the lubricant around the journal. The CFD program uses converging and diverging lubricant thickness to calculate the journal eccentricity within the bearing clearance.

The CFD analysis computes the minimum oil film thickness and average oil film pressure around the journal – the key parameters that aid journal bearing design. Based on the boundary conditions listed in Table 4.3, the pressure distribution and the fluid film thickness predicted by the model is shown in Figure 4.16(a) and (b) respectively. The accompanying polar plots reveals the pressure and oil film thickness distribution at the mid-section of the journal bearing.

The results plotted in Figure 4.16(a) shows the existence of negative pressure in oil film. This is physically impossible, as oil film cannot withstand negative pressure (tensile force). Therefore, these pockets of negative pressure distribution can be ignored for practical reasons.

Table 4.3 Journal bearing model boundary conditions

Type	Locations	Expressions	Purpose
Pressure	z = 0 and z = L	$P_{gauge} = 0$	Pressure at journal ends is assumed to be equal to ambient pressure
Velocity	Outer walls	$u = -\omega \cdot R_j \cdot \sin(\theta)$ $v = \omega \cdot R_j \cdot \cos(\theta)$	x and y components of the journal velocity

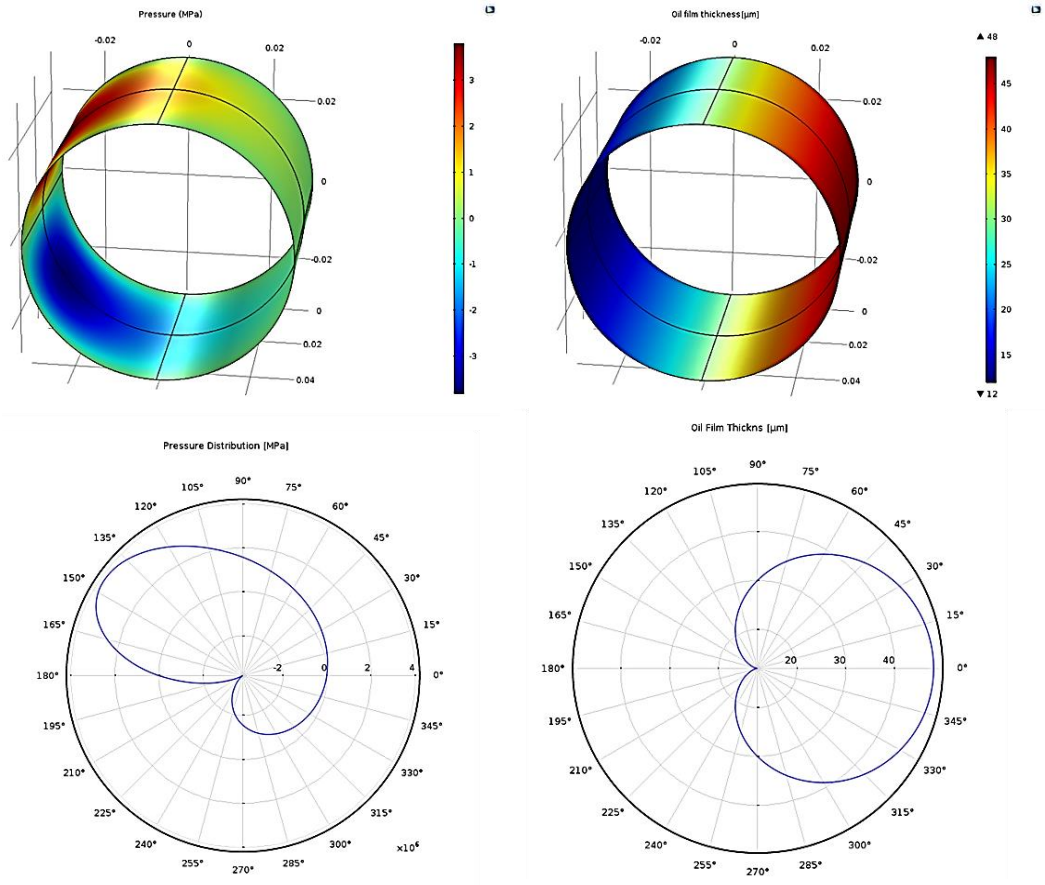

(a) **(b)**

Figure 4.16 (a) Oil film pressure and (b) thickness around the journal bearing

For a hydrodynamically lubricated journal bearing, the average frictional factor due to resulting pressure distribution is given by Petroff equation:

$$f_{j,avg} = 2\pi^2 \mu \frac{n}{P_{avg}} \frac{r_j}{c} \tag{4.39}$$

where r_j represents the journal radius and n denotes the angular speed of journal in rev/s. From above equation, it is noted that the frictional factor is proportional journal radius, therefore it is advantages to minimize journal diameter.

A surface integral of the pressure distribution yields the load carrying capacity of the bearing. This then can be used to find the optimum bearing clearance c, and fluid film thickness, h. However, such a procedure is not recommended, as there are other design considerations that has been taken into account to ensure practical

operation of the journal bearing. These design considerations are discussed in the section 4.4.4.

4.4.3 Model validation

The CFD model can be validated by comparing the predicted pressure distribution against the pressure distribution obtained from analytical method for an idealized bearing. A mesh independence test has been conducted prior to the model validation study to ensure that the results generated by the COMSOL software is independent of mesh settings. The results of this study can be found in appendix D. Consider an infinitely long journal bearing shown in Figure 4.15 operating conditions listed in Table 4.4. The pressure distribution of the lubricant film is given by [108]:

$$P_\theta = \frac{6\mu U_t r_j}{c^2} \frac{n(2+\varepsilon\cos\theta)\sin\theta}{(2+\varepsilon^2)(1+\varepsilon\cos\theta)^2} \tag{4.40}$$

where the tangential velocity of fluid film at the journal surface, U_t is given by

$$U_t = \omega r_j \tag{4.41}$$

Table 4.4 Plain journal bearing operating conditions

Parameter	Value
Journal radius	1.5cm
Speed	2000 RPM
Radial clearance	0.002cm
Lubricant viscosity	0.025Pa s
Eccentricity ratio	0.8

The pressure distribution of the lubricant predicted by the CFD and analytical model is shown in Figure 4.17. The negative pressure distribution beyond 180^0 degrees predicted by both methods merely means that the hydrodynamic lubrication does not exists in this region as shown in Figure 4.18. The polar pressure plot of lubricant around the journal shown in Figure 4.18 illustrates that the cavitation pressure manifests at the divergent region of lubrication film and can be ignored for practical purpose if the negative pressure is higher than the lubricant vapour pressure.

Both the analytical and CFD model predicts a single peak pressure along the circumference of the journal bearing. This peak pressure occurs at the location of minimum lubricant thickness and is due the geometry of the journal and how the lubricant expands and contracts around boundary of the journal shaft. It is also noted that the CFD model prediction is close to the analytical solution of an idealized plain journal bearing. Only a marginal difference in magnitude of peak pressure varies between both methods and this could be attributed to the software approximations, infinitely long bearing assumption used in the analytical method and the mesh quality. Therefore, this validates the accuracy of the CFD model.

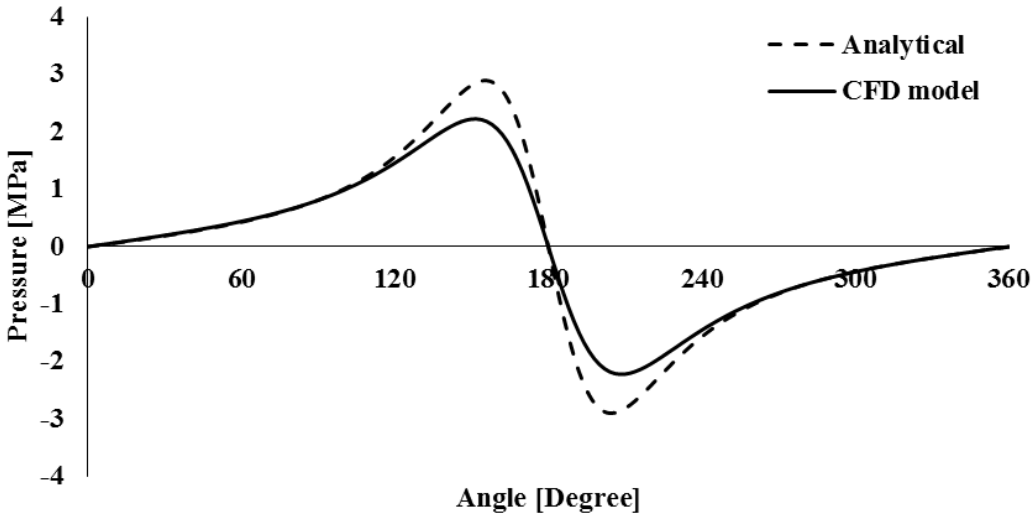

Figure 4.17 Lubricant pressure distribution predicted by CFD and analytical Methods

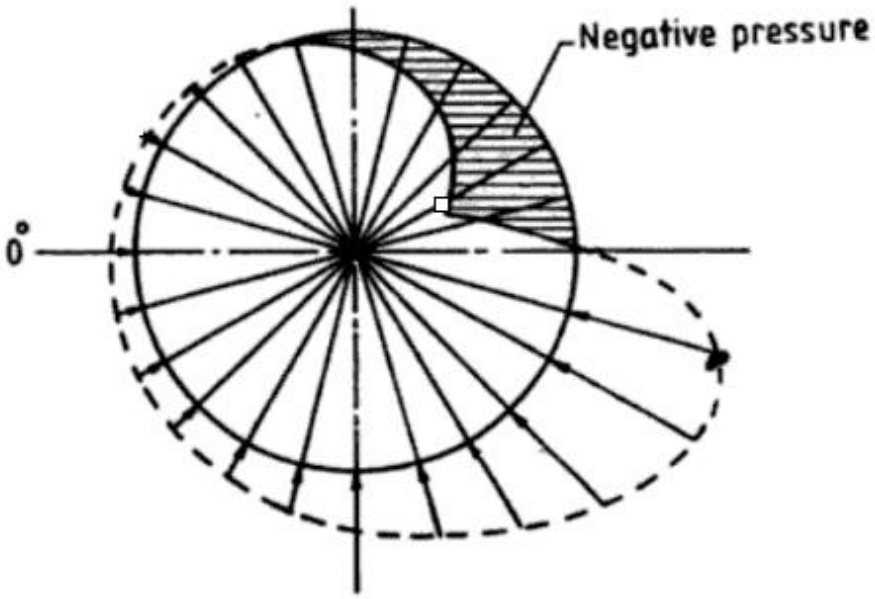

Figure 4.18 Breakdown of hydrodynamic lubrication at negative pressure region [108]

4.4.4 Other design considerations

4.4.4.1 Oil film thickness

In practise, it is recommended that the minimum oil film thickness should be higher than the surface roughness of the journal. Thicker oil film thickness allows the bearing to handle vibration and to compensate for reduction in lubricant viscosity due to an increase in fluid film temperature [109]. Literature review also suggests that the smallest h_{min} should at least be greater than or equal to ten times the combined surface roughness of journal [109]. Trumpler et. al. [110] suggests the following correlation to determine the minimum oil film thickness provided the surface roughness (peak-to-valley) does not exceeds 5μm.

$$h_{0,\min} \geq 0.005 + 0.00004D \tag{4.42}$$

In the case of dynamic loading, it is desirable to peg the oil film thickness at least three times larger than that calculated for static loading [111]. Therefore, the desirable oil film thickness for dynamic loading is given by

$$h_{0,dyn} = 3h_0 = 3(0.005 + 0.00004D) \tag{4.43}$$

In general, the minimum oil film thickness should be as generous as possible to account for variations in manufacturing process, surface finish, stack up tolerance and to minimize frictional losses. Moreover, it is cost effective to have a large fluid film thickness rather than a having a stringent surface finish requirements.

4.4.4.2 Bearing clearance, machining tolerance and eccentricity ratio

The bearing clearance, *c*, defines the load carrying capacity of the journal bearing. Based on empirical guidelines, designers are recommended to select a c/R_j of about 0.001 for high precision journal bearing with a shaft diameter of 25 to 150mm [111]. In addition tolerance fits H6/f6, H8/f8, H7/f7, H6/d6, H6/e6 are recommended for the journal bearing bore and the shaft diameter respectively [112]. To minimize the possibility of self-excited vibration, designers are recommended to ensure that the journal bearings operate at a steady state eccentric ratios (journal eccentricity/radial clearance) of about 0.6 – 0.7 [113].

4.4.4.3 Bearing length

One of the important design decision is the selection of the *L/D* ratio. Based on hydrodynamic lubrication theory, lubricating a long bearing results in high load capacity in comparison to a shorter bearing. However, usage of a long bearing increases the risk of bearing failure due to shaft misalignment. Therefore, short bearings with a shaft length to diameter ratio (L/D) of 0.25 to 0.75 are often recommended [109].

4.4.5 Parametric study

A steady state analysis of the CFD based journal-bearing model is carried out to understand the effect of key parameters on bearing power loss, minimum fluid film thickness and load carrying capacity. The data to use for the parametric sweep is listed in Table 4.5. The influence of each parameter is studied by varying the parameter of interest between the minimum and maximum range while holding

other parameters at the nominal value. The desired L/D ration was achieved by pegging the diameter at 30mm (arbitrary value), while varying the length as necessary. The dimeter is held constant as the frictional losses of the journal bearing is sensitive to diametrical variations as compared to the variations in bearing length.

Table 4.5 Parametric sweep of key parameters governing journal-bearing design

Parameters	**Minimum**	**Maximum**	**Nominal**
L/D ratio	0.25	0.75	0.50
RPM	2000	3500	2750
Eccentricity ratio	0.50	0.80	0.65

Based on the design guidelines suggested by Weiksner (reproduced in Table 4.6),an oil with ISO viscosity grade classification of 68 (R-POE 68)[5] will be used for journal bearing lubrication. It is anticipate that the oil reservoir temperature could attain temperatures as high as 98.3^0C during steady state operation [114]. As such the inlet oil temperature is taken to be 100^0C throughout the analysis. The density variation within the bearing due to temperature rise is modelled using Eq. (4.44).

$$\rho_{oil} = 0.89 - 0.00063(T_{oil} - 15.6) \tag{4.44}$$

ISO Viscosity Grade Classification	**Machine or Equipment Description**
32	Hydraulics, lightly loaded slideways
46	Hydraulics, rotary screw compressors
68	Vertical motors, turbines, journal bearings, pumps
100	Reciprocating air compressors, angle drives, conveyors
150	Gear reducers, screw conveyors, feeders
220	Turbine drives, cooling tower drives, heavily loaded slideways
320	Gear reducers
460	Exhausters, vacuum pumps, large conveyor drives
680	Gear drives

Table 4.6 Recommended ISO Viscosity for Machine and Equipment design [115]

[5] Based on manufacture's specification, the oil viscosity is established to be 6.23e-2 $\mathrm{Pa \cdot s}$ at 40^0C and 8.02e-3 $\mathrm{Pa \cdot s}$ at 100^0C.

Effect of L/D ratio

The effect of L/D ratio on the frictional power loss, load carrying capacity and fluid film thickness is shown in Figure 4.20(a). The simulation revealed that the L/D ratio had negligible effect on the fluid film thickness, therefore h_{min} remained relatively constant at 10μm regardless of variation in L/D ratio. Increasing the L/D ratio has a positive effect on the load bearing capacity. This is an expected outcome as a larger L/D ratio is able to shoulder heavier loads due to increase in load bearing surface area. However, the bearing frictional power loss increases linearly with increasing L/D ratio. The larger L/D ratio results in increasing the journal wetted surface area, thereby contributing to frictional losses. Therefore, for a lightly loaded bearing, its advantages to minimize the L/D ratio. However, excessively small L/D ratio degrades the dampening performance of the bearing thereby contributes self-excited vibration.

Effect of RPM

With reference to Figure 4.20(b), increasing the angular velocity of the journal leads to a linear increase in load carrying capacity and frictional power loss. The change in minimum fluid film thickness, h_{min} w.r.t increasing angular velocity was found to be negligible within the RPM range. Therefore, it is appropriate to assume that the h_{min} remains constant if the bearing operates within a narrow angular speed range. It is interesting to note that the load bearing capacity of the journal increases with angular velocity. This observation can be explained by observing the velocity vector plot shown in Figure 4.19. As the speed increases, the no-slip boundary condition on the journal surface results in dragging a larger amount of oil flow into the convergent bearing region there by enhancing the film pressure to support a larger load.

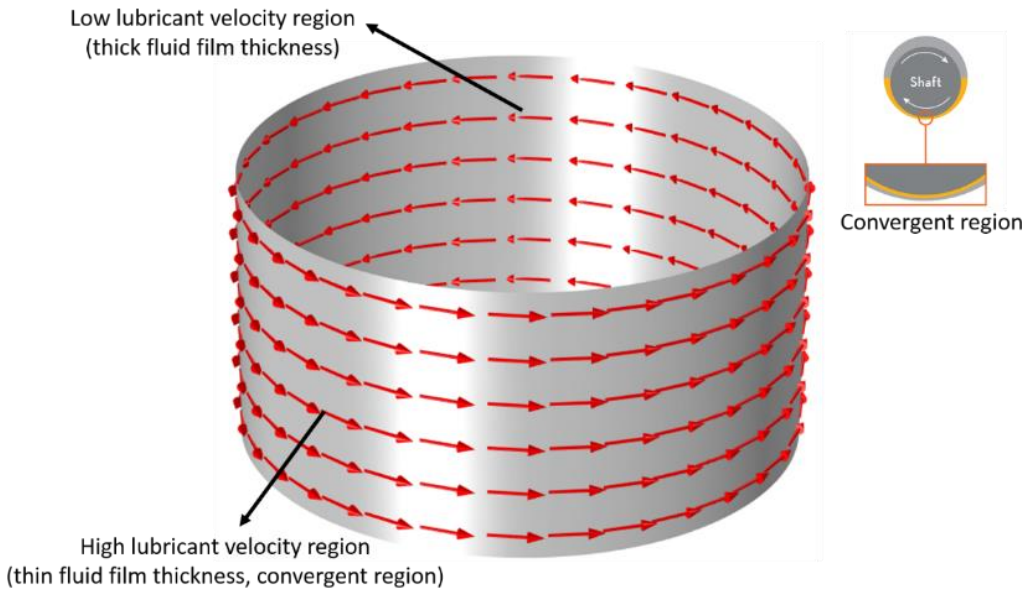

Figure 4.19 Surface velocity vector plot of a journal

Effect of Eccentricity ratio

Eccentricity ratio, i.e journal eccentricity/radial clearance has an effect on the load bearing capacity and fluid film thickness. As Figure 4.20(c) indicates, a larger eccentricity ratio, results in a thinner oil film thickness while the load bearing capacity appears to increase. However, this higher eccentricity ratio situation will increase the risk of metal-to-metal contact due to smaller radial clearance, *c*. On the other hand, if the eccentricity is too small (journal nearly concentric with the bearing), the machine could easily become unstable as excessive fluid film thickness can contribute to poor bearing stiffness.

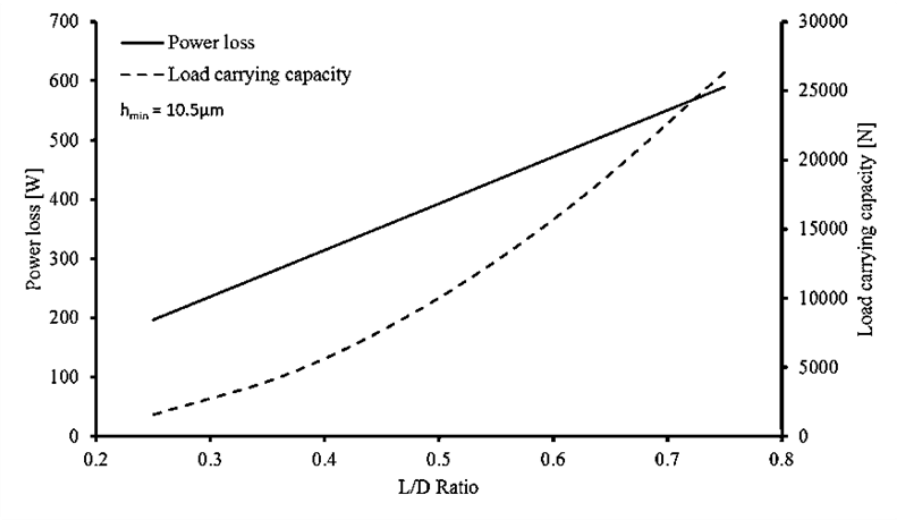

(a)

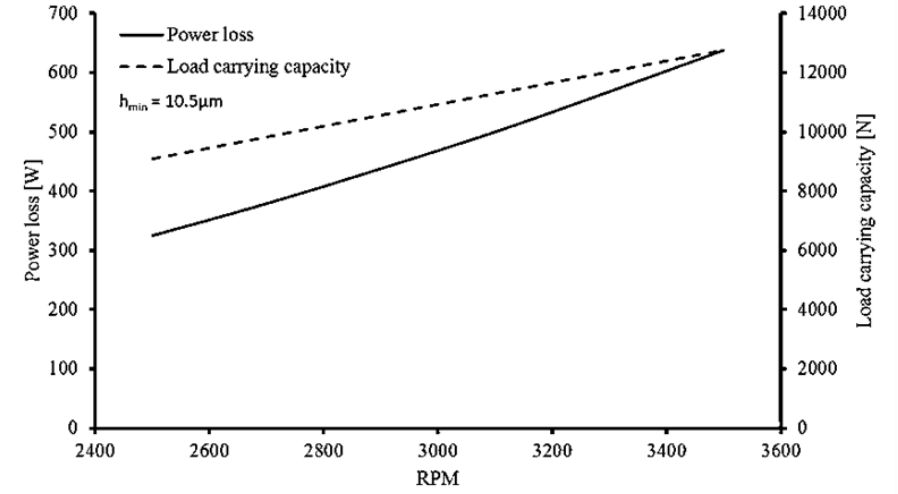

(b)

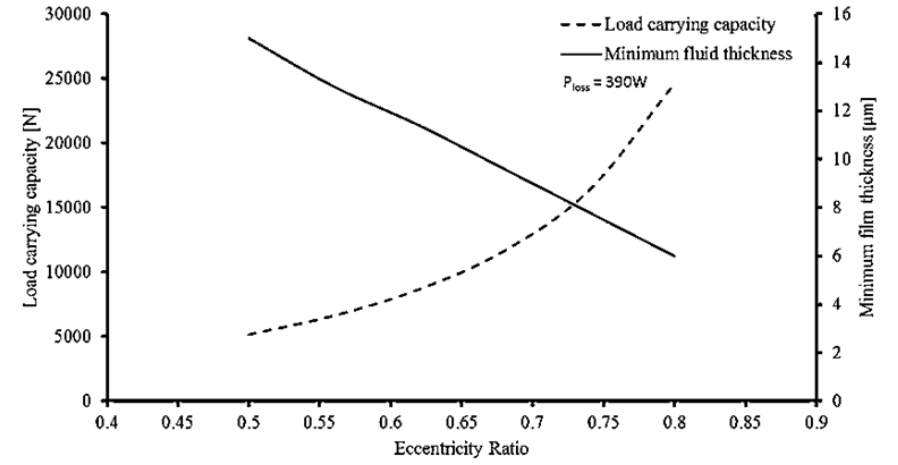

(c)

Figure 4.20 Parametric analysis of key design parameters of a journal bearing

Radial clearance

The relationship between the fluid film thickness, radial clearance and eccentricity ratio is given by

$$h_{\min} = c(1-\varepsilon) \tag{4.45}$$

For a given loading conditions and bearing length, the minimum oil film thickness is governed by the surface finish and the diameter of the journal bearing. The journal can be manufactured using turning process and a surface finish of 1μm can be achieved without much difficulty. Since it is recommended that the minimum oil film thickness is at least 10 times surface finish of the journal, the appropriate radial clearance can be calculated to be 25μm using Eq.(4.45). Table 4.7 list the summary of key parameters governing the journal bearing design.

Table 4.7 Key journal bearing design specifications

Parameter	**Value**
L/D	0.5
Eccentricity ratio, ε	0.6
Radial clearance, *c*	25μm
Lubricant	POE 68
Surface finish	≤ 1μm
Maximum oil inlet temperature	100^0C

The pressure and film thickness distribution of the journal bearing with specification listed in Table 4.7 is shown in Figure 4.21. This bearing is expected operate with a minimum oil film thickness of 10μm with a load carrying capacity of 5kN and experience a frictional loss of 600W at 3500RPM.

4.5 Minimising re-expansion losses in FVC

In a SVC design, the discharge port is located on the cylinder wall; therefore, the rolling piston compresses the gas can only discharge the compressed gas up to the point when the discharge port is passed. Any undischarged gas remains trapped (see Figure 4.22) and eventually leaks back into the suction chamber, resulting in re-expansion loss. The current FVC design also suffers from similar re-expansion loss.

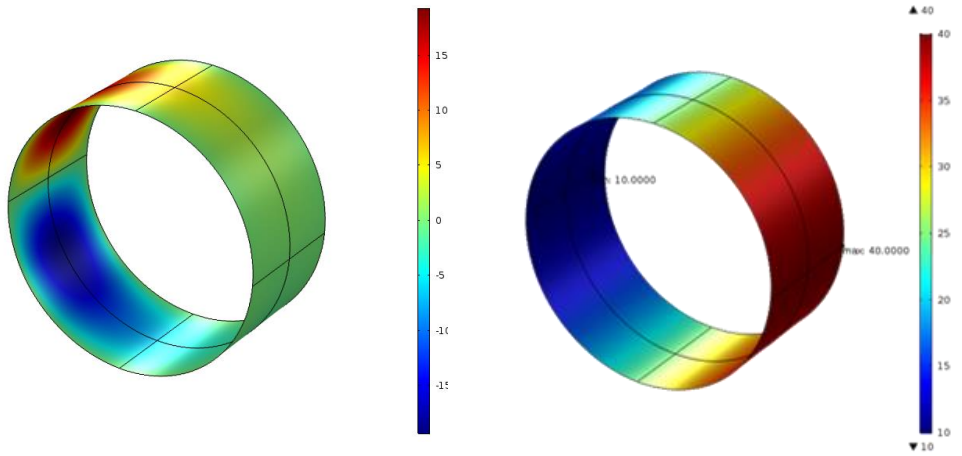

(a) **(b)**

Figure 4.21 (a) Pressure and (b) oil film thickness distribution of the journal bearing

Various researchers [86], [87], [116], [117] have performed rigorous analyses of the leakage paths presented in Table 4.8. Nevertheless, practically none of these researchers considered the re-expansion loss as form of internal leakage. However, Reed W.A [117] described the re-expansion mechanism as an internal leakage as it results in decreasing the gas delivering capacity of the compressor (leakage path 7 in Figure 4.23) . Reed W.A [117] identified the discharge port as an additional volume which is capable of trapping compressed refrigerant at the end of discharge process. Reed W.A [117] added that a significant quantity of gaseous refrigerant remains in the confines of the discharge port that subsequently discharges into the working chamber due to the large pressure difference between the refrigerant contained in these two volumes.

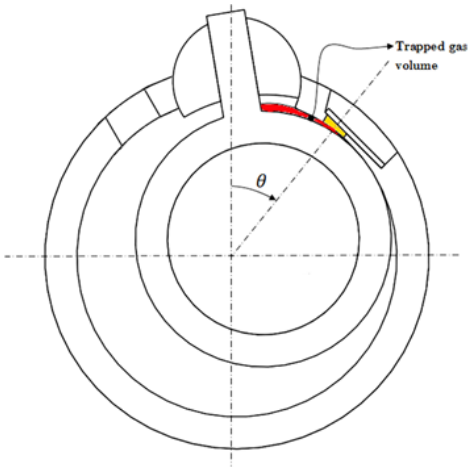

Figure 4.22 Trapped gas volume in SVC towards the end of compression process

Table 4.8 List of leakage paths [116]

No.	Leakage Path
1	Radial gap between the piston and cylinder wall separating the compressor and suction volumes
2	Axial gap between each piston end face and cylinder end wall separating the compression chamber from high pressure oil
3	Axial gap between each piston end face and cylinder end wall separating the suction chamber from high pressure oil
4	Axial gap between each vane side face and cylinder end wall separating the suction and compression chambers
5	Clearance between the vane and vane port separating the compression chamber from high pressure fluid
6	Clearance between the vane and vane port separating suction chamber from high pressure fluid
7	Overflow of the trapped compressed gas from the discharge port

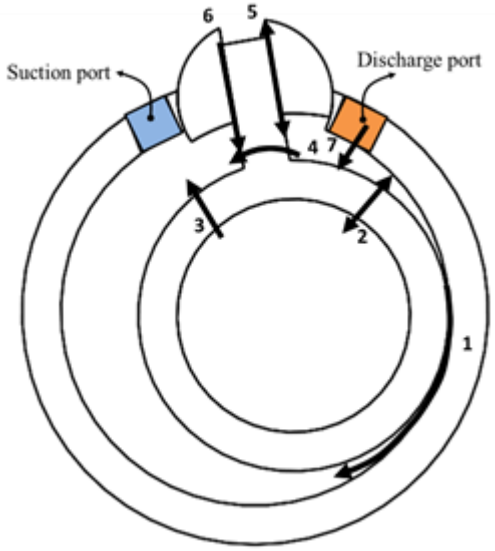

Figure 4.23 SVC leakage paths

The new FVC compressor design explored in this research project minimises re-expansion losses by relocated the discharge slot from the compressor wall (as in the case of SVC) to the fixed vane as depicted in Figure 4.24. In the conventional design, the piston can only facilitate the discharge of the compressed gas up to the discharge port. In contrast, the new FVC design minimizes the quantity of trapped gas at the end of compression process as the piston naturally forces the compressed gas though the vane until the end of compression the process. The prototype of the newly designed FVC is shown in Figure 4.25.

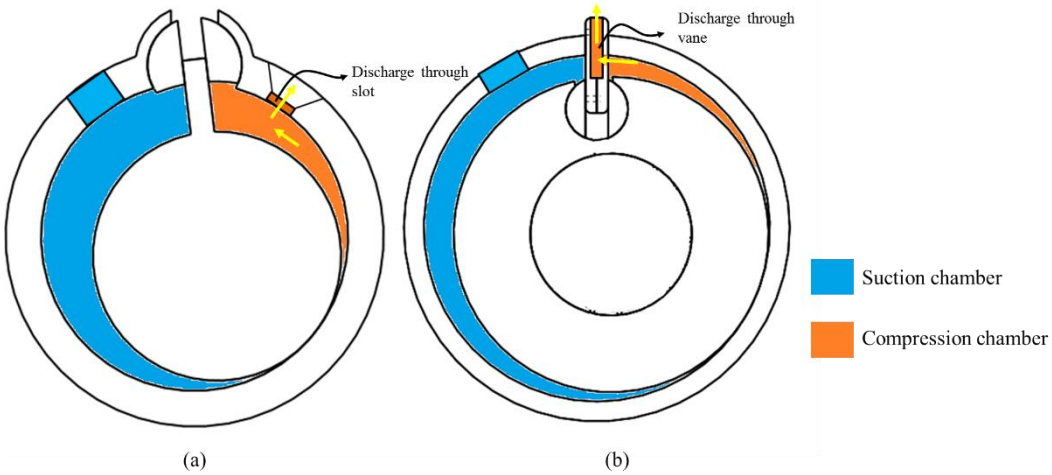

Figure 4.24 Comparison between the conventional and new compressor design (a) SVC and (b) New FVC design

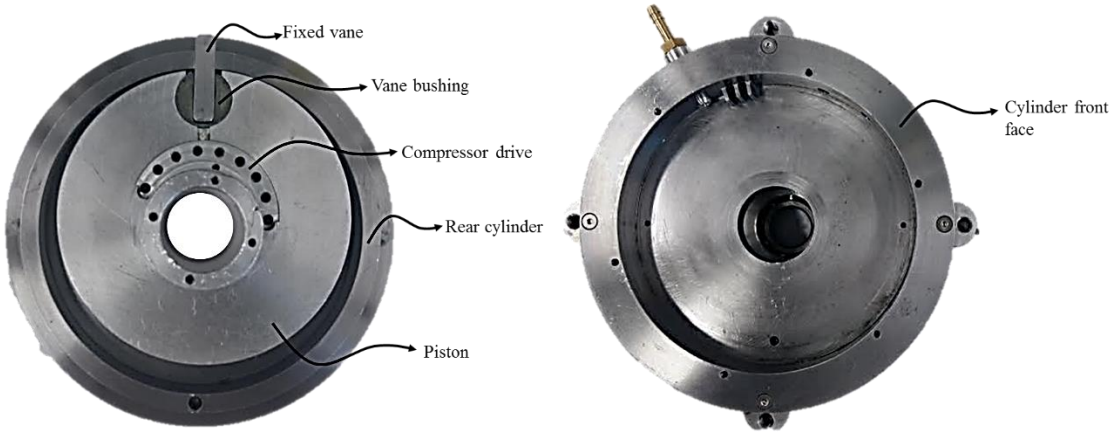

Figure 4.25 Prototype of the newly designed FVC

4.6 Vane and valve design

The reed valve is housed inside the fixed vane as shown in Figure 4.24(b). The reed valve with a thickness of 0.5mm is manufactured from Sandvik razor blade steel as it is known to have high fatigue endurance limits and high tensile strength. As shown in Figure 4.26, the inner matting surface of the vane has been grooved to accommodate O-rings to prevent leakage flow.

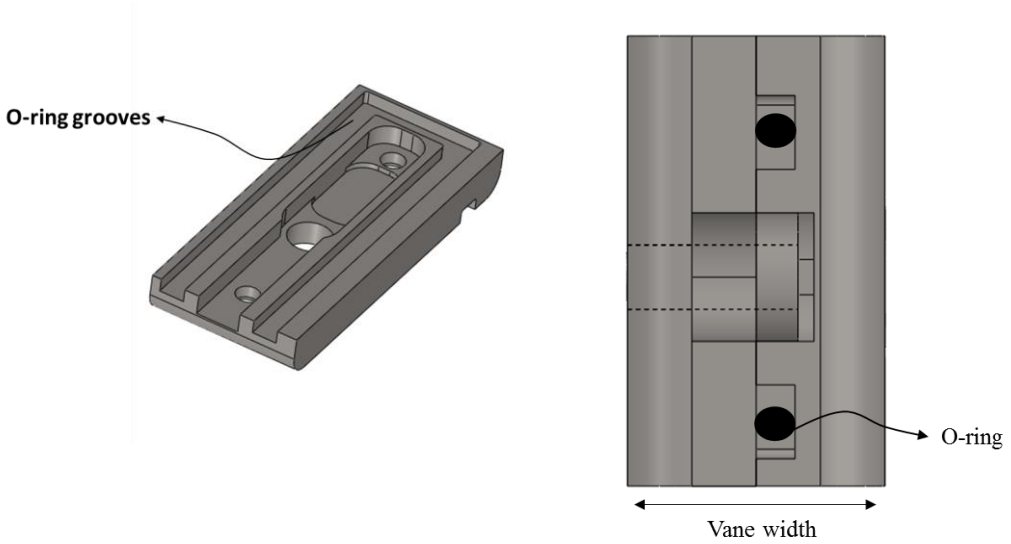

Right half of the vane Vane assembly top view

Figure 4.26 The vane mating surfaces has been grooved to accommodate an O-ring

The vane width has to be sufficient to accommodate the maximum reed valve deflection, $h_{d,max.}$ With reference to Figure 4.27, the maximum reed valve deflection is obtained by equating the discharge inlet flow area to the discharge outlet flow area as shown:

$$\left(\frac{\pi D^2}{4}\right)_{\text{discharge inlet}} = \left(\pi D h_d\right)_{\text{discharge outlet}} \tag{4.46}$$

$$h_{d,\max} = \frac{D}{4} \tag{4.47}$$

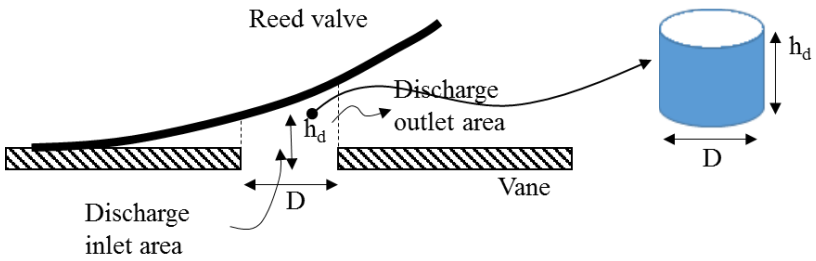

Figure 4.27 Discharge inlet area and reed valve deflection height relationship

4.7 Concluding remarks

The compressor technical specifications and details of compressor design have been presented in this chapter. The compressor design includes a passive in-plane balancing weight to achieve dynamic balancing of the crankshaft. The journal bearings of the compressor have been designed using an accurate CFD model to predict the steady-state pressure distribution, load carrying capacity, power loss and oil film thickness. The key design innovation of the compressor is its ability to discharge through the fixed vane to reduce re-expansion leakage losses.

Chapter 5
COMPRESSOR MATHEMATICAL MODEL

This chapter formulates the geometric, thermodynamic, mass flow, reed valve and power loss models describing the Swing Vane Compressor (SVC) and the Fixed Vane Compressor (FVC) designs. The geometric model describes the change in working chamber volume as a function of shaft angle. The change in working chamber volume is used by the thermodynamic model to compute the refrigerant's state properties such as the temperature and pressure. Meanwhile, the mass flow model captures the refrigerant flow through the compressor suction and discharge ports. The resulting model is coupled with valve response and power loss models to create a mathematical representation of the SVC and FVC designs to facilitate parametric analysis.

5.1 Geometric Model

This section formulates the geometric model to describe the change in working chamber volume as a function of crank angle, θ. With reference to Figure 5.1, applying the cosine rule yields the following geometric relationship between the cylinder radius R_c, piston radius R_r, the eccentricity e is

$$R_p^2 = e^2 + R^2 - 2eR\cos(\theta - \phi) \tag{5.1}$$

$$R_c = R_p + e \tag{5.2}$$

Substituting Eq. (5.1) in Eq. (5.2) and solving for R yields

$$R = R_c(1-a)\cos(\theta-\phi) + \sqrt{R_c^2(1-a)^2\cos^2(\theta-\phi) + R_c^2(2a-1)} \tag{5.3}$$

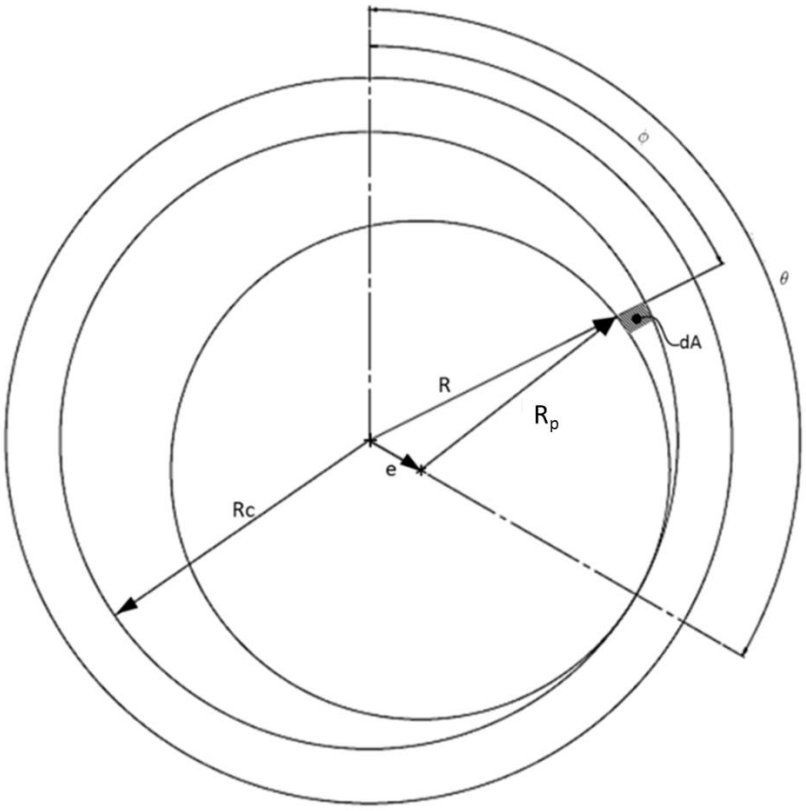

Figure 5.1 Geometric Relationships

The area element (dA) between the cylinder and the piston is given by:

$$dA = \frac{1}{2}(R_c^2 - R^2)d\theta \tag{5.4}$$

Substituting Eq. (5.3) in (5.4) and integrating from ϕ=0° to the point of contact of the piston with the cylinder, $\phi = \theta$ yields the trapped area

$$A_{cv}(\theta) = \frac{R_c^2}{2}\left[\begin{array}{l}(1-a^2)\theta - \dfrac{(1-a)^2}{2}\sin(2\theta) - a^2\sin^{-1}[(\dfrac{1}{a}-1)\sin\theta] - \\ a(1-a)\sin\theta\sqrt{1-\left(\dfrac{1}{a}-1\right)^2(\sin\theta)^2}\end{array}\right] \tag{5.5}$$

The working chamber volume as function of angular position, θ is given by

$$V_{cv}(\theta) = h_c\int_0^{\theta_{cv}} A_{cv}\,d\theta_{cv} \tag{5.6}$$

where h_{cyl} is the cylinder height of the working chamber.

Subtracting the volume occupied by the vane with width, w and height h_c yields the working chamber volume as function of crank angle:

$$V_{cv}^{'}(\theta) = V_{cv}(\theta) - \frac{th_c\delta}{2} = hA(\theta) - \frac{wh_c\delta(\theta)}{2} \tag{5.7}$$

where δ is the vane protrusion length identified in Figure 5.2.

The vane protrusion length, δ is obtained from the geometric relationship defined using the cosine rule:

$$R_p^2 = (R_c - \delta)^2 + e^2 - 2(R_c - \delta)e\cos(\theta) \tag{5.8}$$

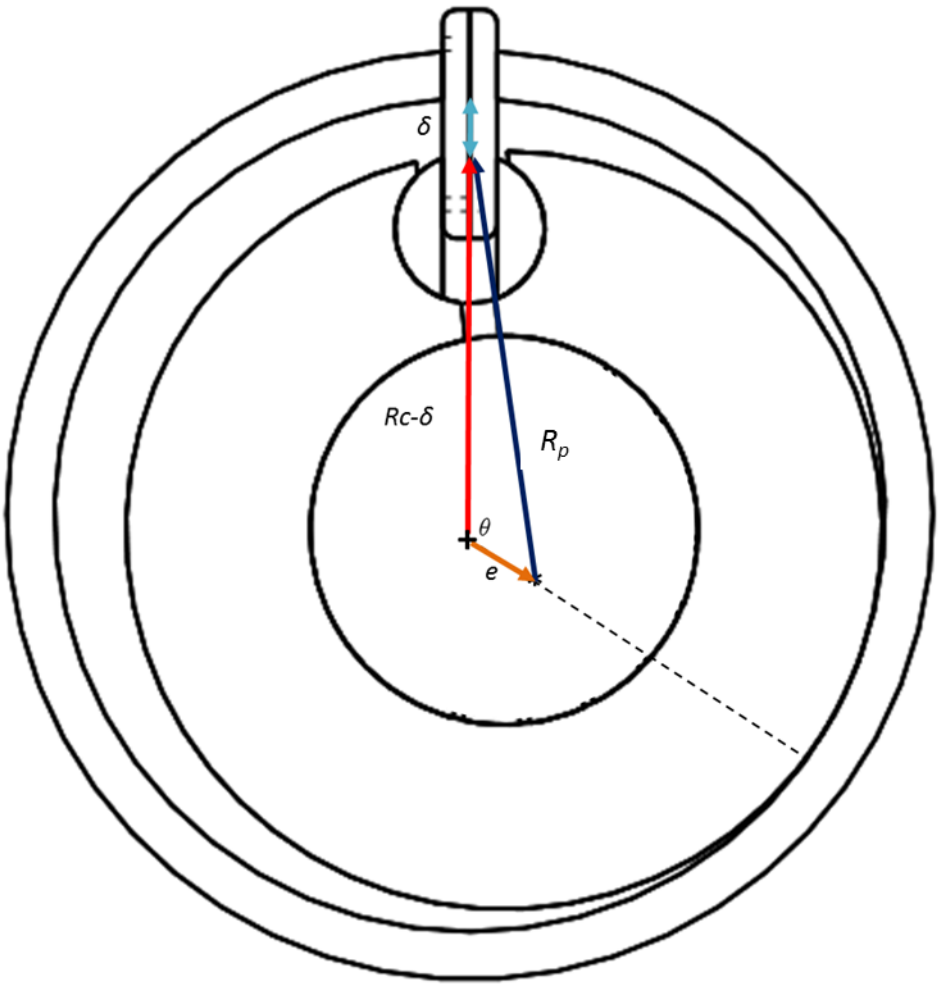

Figure 5.2 Vane protrusion relationship

Solving for δ:

$$\delta(\theta) = R_c - e \cdot \cos(\theta) - \sqrt{R_p^2 + \left(e^2 \cos(\theta)\right)^2 - e^2} \qquad (5.9)$$

Figure 5.3 highlights the suction and discharge ports of the SVC and the newly designed FVC. Note that in both compressor designs, the discharge port is covered by a reed valve. Researchers often ignore the volume introduced by these ports as part of working chamber volume. However, the comparative study between the SVC and FVC requires the inclusion of these volumes.

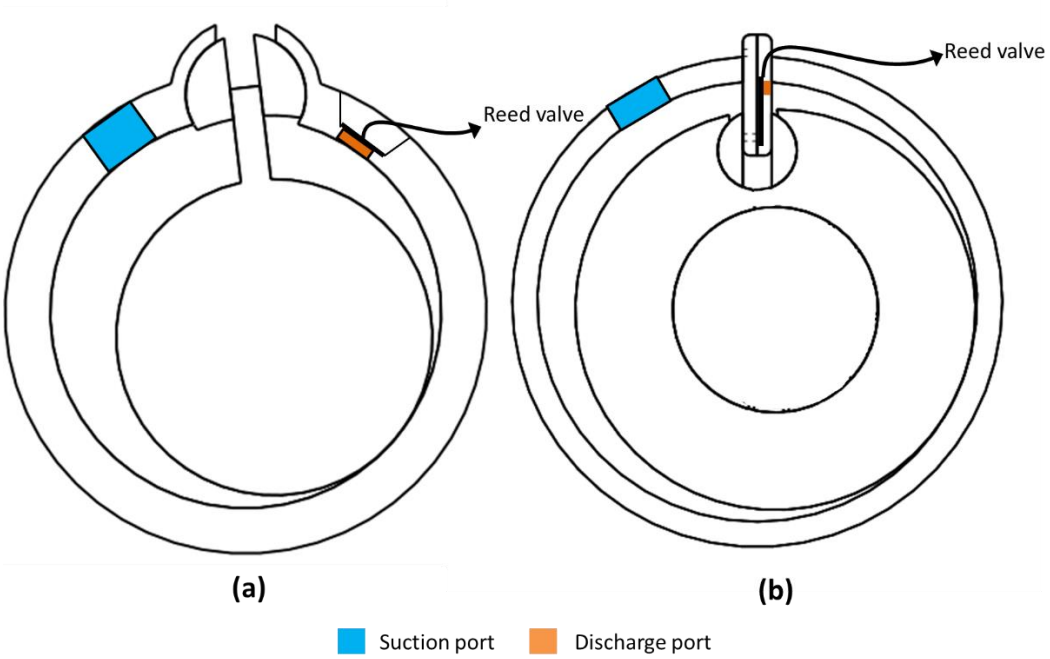

Figure 5.3 Suction and discharge ports of swing compressors (a) Swing Vane Compressor (b) Fixed Vane Compressor

For the SVC, the suction and discharge port volumes are given by Eq. (5.10) and (5.11) respectively.

$$V_s = \frac{\pi D_s^2}{4} M_s \tag{5.10}$$

$$V_{d,SVC} = \frac{\pi D_d^2}{4} M_d \tag{5.11}$$

For FVC, the suction port volume is also obtained from Eq (5.10). But the discharge port volume is a function of crank angle. This is because the discharge port, with radius R_{vd} can be partially covered by the vane bushing towards the end of the compression stroke (see Figure 5.5). Therefore, the area of discharge port that remains open towards the end of the compression stroke can be calculated using area of a circle segmented by a cord as shown in

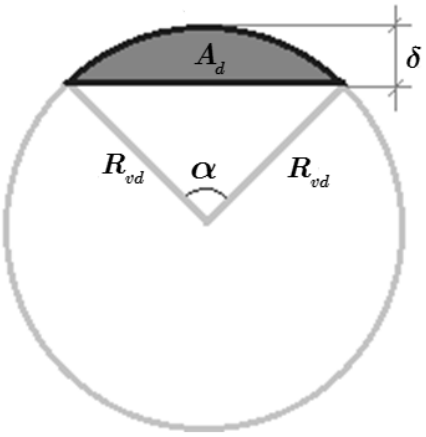

Figure 5.4 Area of a circle segmented by a cord

$$A_d = \frac{1}{2} R_{vd}^2 (\alpha - \sin\alpha) \tag{5.12}$$

where $\alpha = 2\cos^{-1}(1-\delta/R_{vd})$.

Therefore, for a discharge port having a diameter of D_{vd} and a depth M_{vd}, the discharge port volume is given by

$$V_{d,FVC} = \min\left(\frac{\pi D_{vd}^2}{4}, A_d\right) M_{vd} \tag{5.13}$$

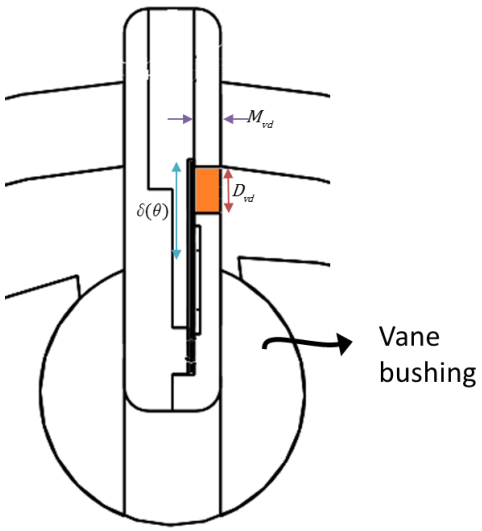

Figure 5.5 FVC discharge port.

Inclusion of the suction and discharge port volume requires piecewise definition of the working chamber volume based on crank angle as given by Eq. (5.14).

$$V_{cv}^{'}(\theta) = hA(\theta) - \frac{wh\delta(\theta)}{2} + V_s \text{ for } 0^0 \le \theta \le \left(360^0 + \theta_s\right)$$
$$V_{cv}^{'}(\theta) = hA(\theta) - \frac{wh\delta(\theta)}{2} + V_d \text{ for } \left(360^0 + \theta_s\right) \le \theta \le 720^0 \quad (5.14)$$

where θ_s represents the angular location of suction port.

The characteristics of the motor can be included to provide the working chamber volume as a function of time. Assuming the compressor motor operates at constant angular velocity, the crankshaft angle can be described as a function of time

$$\theta(t) = \omega \cdot t \quad (5.15)$$

where ω, represents the angular velocity of the compressor motor

The specific volume and the refrigerant mass is related by

$$v_s = \frac{V_{cv}}{m_{cv}} \quad (5.16)$$

The derivative of the specific volume with respect to crank angle is

$$\frac{dv_s}{d\theta} = \frac{1}{m_{cv}}\left(\frac{dV_{cv}}{d\theta} - \frac{V_{cv}}{m_{cv}}\frac{dm_{cv}}{d\theta}\right) \quad (5.17)$$

The term $dV_{cv} / d\theta$ can be obtained by differentiating Eq. (5.14)

$$\frac{dV_{cv}^{'}}{d\theta}=\frac{-R_c^2\cdot h_c}{2}\left[\begin{array}{l}\cos(2\theta)\cdot(a-1)^2+a^2+\dfrac{a^2\cdot\cos(\theta)\cdot\left(\dfrac{1}{a}-1\right)}{\sqrt{1-\sin^2(\theta)\cdot\left(\dfrac{1}{a}-1\right)^2}}\\ -a\cdot\cos(\theta)\cdot\sqrt{1-\sin^2(\theta)\cdot\left(\dfrac{1}{a}-1\right)^2}\cdot(a-1)+\\ \dfrac{a\cdot\cos(\theta)\cdot\sin^2(\theta)\cdot(a-1)\cdot\left(\dfrac{1}{a}-1\right)^2}{\sqrt{1-\sin^2(\theta)\cdot\left(\dfrac{1}{a}-1\right)^2}}-1\end{array}\right]$$

$$-\frac{1}{2}h_c\cdot t\left(e\cdot\sin(\theta)+\frac{e^2\cdot\cos(\theta)\cdot\sin(\theta)}{\sqrt{R_r^2+e^2\cdot\cos^2(\theta)-\mathrm{e}^2}}\right) \tag{5.18}$$

The term $dm_{cv}/d\theta$ can be obtained from the conservation of mass equation.

$$\frac{dm_{cv}}{d\theta}=\sum\frac{dm_i}{d\theta}-\sum\frac{dm_o}{d\theta} \tag{5.19}$$

5.2 Thermodynamic model

The thermodynamic model used to predict the refrigerant state properties *(T_c, P_c)* in the working chamber is developed in this section. Figure 5.6 shows the energy balance diagram of a generic compressor. Applying first law of thermodynamics to the identified control volume yields

$$\frac{dQ_{cv}}{dt}-\frac{dW_{cv}}{dt}=\frac{d}{dt}\int_{cv}E\rho dV+\int_{cs}E\rho\vec{V}\cdot\vec{A} \tag{5.20}$$

where *E* represented the sum of kinetic, potential and internal energy. Since changes in kinetic and potential energy is insignificant, the Eq. (5.20) can be simplified as

$$\frac{dQ_{cv}}{dt}-\frac{dW_{cv}}{dt}=\frac{d}{dt}\int_{cv}u\rho dV+\int_{cs}u\rho\vec{V}\cdot\vec{A} \tag{5.21}$$

Applying work flow concept, Eq. (5.21) can be expressed as

$$\frac{dQ_{cv}}{dt} - \frac{dW_{cv}}{dt} = \frac{d}{dt}\int_{cv} u\rho dV + \frac{d}{dt}\int_{cs} h\rho\vec{V}\cdot\vec{A} \qquad (5.22)$$

The second term on the left side of Eq. (5.22) represents the work done on the control volume due to volumetric changes. This work can be expressed as

$$\frac{dW_{cv}}{dt} = P_{cv}\frac{dV_{cv}}{dt} \qquad (5.23)$$

Assuming that the compressor is perfectly sealed and fluid enters and exits the compressor only through the inlet and outlet ports respectively, Eq. (5.22) can be simplified as

$$\frac{dQ_{cv}}{dt} + \frac{dm_i}{dt}h_i = \frac{dW_{cv}}{dt} + \frac{dm_o}{dt}h_o + \frac{d(m_{cv}u_{cv})}{dt} \qquad (5.24)$$

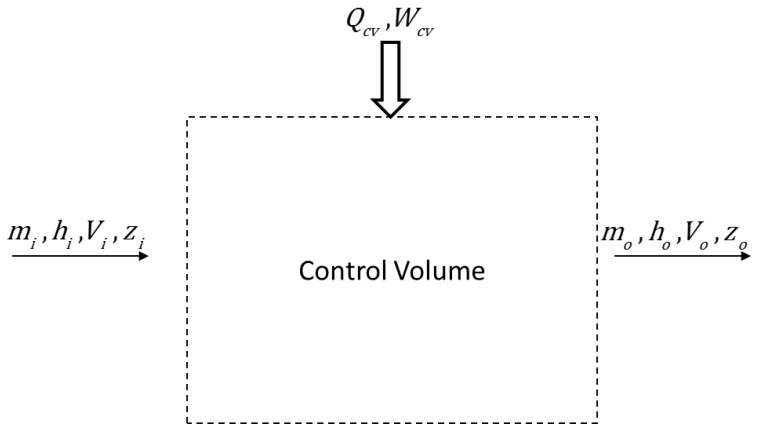

Figure 5.6 Energy balance diagram of a generic compressor

Eq.(5.19) can be expressed as a derivative of time by

$$\frac{dm_{cv}}{dt} = \sum\frac{dm_i}{dt} - \sum\frac{dm_o}{dt} \qquad (5.25)$$

The summation sign in Eq. (5.25) can be dropped since the flow is assumed to enter and exit the control volume strictly through the inlet and outlet ports.

The last term in Eq. (5.24) can be expanded by applying the chain rule

$$\frac{d}{dt}(m_{cv}u_{cv}) = m_{cv}\frac{du_{cv}}{dt} + u_{cv}\frac{dm_{cv}}{dt} \tag{5.26}$$

The internal energy of the working chamber (u_{cv}) can be obtained from the enthalpy definition:

$$u_{cv} = h_{cv} - P_{cv}v_s \tag{5.27}$$

Differentiating Eq.(5.27) w.r.t time and substituting in Eq. (5.26)

$$\frac{d(mu)_{cv}}{dt} = m_{cv}\frac{dh_{cv}}{dt} - P_{cv}\frac{dV_{cv}}{dt} - V_{cv}\frac{dP_{cv}}{dt} + h_{cv}\frac{dm_{cv}}{dt} \tag{5.28}$$

Substituting Eq. (5.25) and (5.28) in (5.24) and rearranging the terms:

$$\frac{dh_{cv}}{dt} = \frac{1}{m_{cv}}\left[\frac{dQ_{cv}}{dt} + \frac{dm_i}{dt}(h_i - h_{cv}) - \frac{dm_o}{dt}(h_o - h_{cv}) + V_{cv}\frac{dP_{cv}}{dt}\right] \tag{5.29}$$

For the constant angular velocity of the crank, differentiation of Eq. (5.15) results in

$$d\theta = \omega \cdot dt \tag{5.30}$$

Thus Eq. (5.29) can be articulated in terms of the crank angle as

$$\frac{dh_{cv}}{d\theta} = \frac{1}{m_{cv}\cdot\omega}\left[\frac{dQ_{cv}}{d\theta} + \frac{dm_i}{d\theta}(h_i - h_{cv}) - \frac{dm_o}{d\theta}(h_o - h_{cv}) + V_{cv}\frac{dP_{cv}}{d\theta}\right] \tag{5.31}$$

In general, the specific enthalpy is a function of two parameters of the three thermodynamic properties (pressure, temperature and specific volume). It is convenient to express the enthalpy as function of specific volume and temperature, therefore

$$\frac{dh_{cv}}{d\theta} = \left(\frac{\partial h_{cv}}{\partial T}\right)_{v_s}\frac{dT_{cv}}{d\theta} + \left(\frac{\partial h_{cv}}{\partial v_s}\right)\frac{dv_s}{d\theta} \tag{5.32}$$

Combing Eq. (5.31) with (5.32) yields

$$\left(\frac{\partial h_{cv}}{\partial T}\right)_{v_s}\frac{dT_{cv}}{d\theta}+\left(\frac{\partial h_{cv}}{\partial v_s}\right)\frac{\partial v_s}{\partial \theta}=\frac{1}{m_{cv}}\left[\begin{array}{l}\dfrac{dQ_{cv}}{d\theta}+\sum\dfrac{dm_i}{d\theta}\left(h_i-h_{cv}\right)- \\ \\ \sum\dfrac{dm_o}{d\theta}\left(h_o-h_{cv}\right)+V_{cv}\dfrac{dP_{cv}}{d\theta}\end{array}\right] \tag{5.33}$$

The pressure and temperature variation with respect to crank angle are the two unknowns in Eq.(5.33). The derivative of the specific volume and mass flow rate are obtained from Eq. (5.17) and (5.19) respectively. An electronic database containing refrigerant properties at various states (such as RefProp [3]) can be used to provide the values of thermodynamic derivatives.

The unknown pressure derivative appearing Eq. (5.33) can be obtained by assuming that the pressure is a function of temperature and specific volume: $P_{cv}(T_{cv},v_s)$. Differentiating the assumed pressure function with respect to crank angle:

$$\frac{dP_{cv}}{d\theta}=\left(\frac{\partial P_{cv}}{\partial T_{cv}}\right)_{v_s}\frac{dT_{cv}}{d\theta}+\left(\frac{\partial P_{cv}}{\partial v_s}\right)_{T}\frac{dv_s}{d\theta} \tag{5.34}$$

Substitution of Eq. (5.34) in (5.33) and solving for the temperature derivative yields

$$\frac{dT_{cv}}{d\theta}=\frac{\dfrac{1}{m_{cv}}\left[\dfrac{dQ_{cv}}{d\theta}+\dfrac{dm_i}{d\theta}\left(h_i-h_{cv}\right)-\dfrac{dm_o}{d\theta}\left(h_o-h_{cv}\right)+\dfrac{dv_s}{d\theta}\left[v_{cv}\left(\dfrac{\partial p_{cv}}{\partial v_s}\right)_T-\left(\dfrac{\partial h_{cv}}{\partial v_{cv}}\right)_T\right]\right]}{\left[\left(\dfrac{\partial h_{cv}}{\partial T_{cv}}\right)_{v_s}-v_{cv}\left(\dfrac{\partial p_{cv}}{\partial T_{cv}}\right)_{v_s}\right]} \tag{5.35}$$

The Runge-Kutta integration technique can be used to solve Eq. (5.34) and (5.35) simultaneously to determine the pressure and temperature variation within with respect to crank angle. Likewise, the pressure and temperature variation with respect to time can be obtained by multiplying these equation with the inverse of motor angular velocity.

The power required for compression can be calculated from

$$\dot{W}_{cv}=n\int P_{cv}dV \tag{5.36}$$

where *n* is the number of cycle per second.

5.3 Mass flow model

This section models the flow of refrigerant through the compressor suction and discharge ports. The mass flow rate through the inlet and outlet ports can be modelled as a one-dimensional steady flow through an orifice. Such a practice is common in the mathematical modelling of the rotary piston compressor.

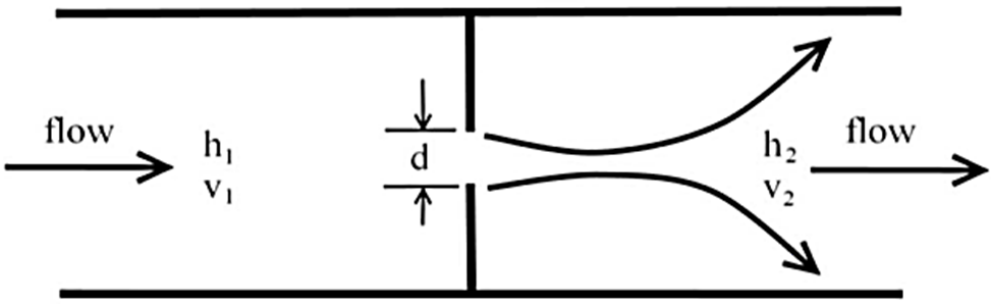

Figure 5.7 Flow through a sharp edged orifice

The steady state energy equation applied between points *1* and *2* in Figure 5.7 yields

$$h_1 + \frac{V_1^2}{2} + z_1 g = h_2 + \frac{V_2^2}{2} + z_2 g \tag{5.37}$$

Neglecting potential variation between points *1* and *2* and assuming stagnant condition at the inlet; the flow velocity at point *2* can be obtained from

$$V_2 = \sqrt{2(h_1 - h_2)} \tag{5.38}$$

The discharge velocity in Eq. (5.38) is based on isentropic flow through the valve. However, in reality, the flow is non-isentropic. The non-isentropic phenomenon can be accounted for through the introduction of an isentropic efficiency:

$$V_2 = \eta_{valve} \sqrt{2(h_1 - h_{2s})} \tag{5.39}$$

Therefore, the mass flow rate through the valve can be obtained from

$$\frac{dm_2}{dt} = \eta_{valve} K A_{orif} \rho_2 \sqrt{2(h_1 - h_{2s})} \tag{5.40}$$

where *K* denotes the flow coefficient and represents the flow losses between points *1* and *2*. For ease of computation, the flow coefficient and the isentropic efficiency can be combined into a single parameter, C_d

$$\frac{dm_2}{dt} = C_d A_2 \rho_2 \sqrt{2(h_1 - h_{2s})} \tag{5.41}$$

The orifice area for the suction port is given by

$$A_{2,s} = \frac{\pi D_s^2}{4} \tag{5.42}$$

The orifice area for the discharge port is varies between the compressor models. A SVC discharges through a cylindrical discharge port. In this case, the discharge orifice area is given by:

$$A_{2,\mathrm{d,model1}} = \frac{\pi \cdot D_\mathrm{d}^2}{4} \tag{5.43}$$

On the other hand, the FVC discharges through the discharge port located on the vane (see Figure 5.8). In this case, the discharge area is a function of crank angle as there is a possibility for the vane bushing to partially cover the discharge port towards the end of the compression stroke. Therefore, the discharge area is given by:

$$A_{2,\mathrm{d,model2}} = \min\left(\frac{\pi D_{vd}^2}{4}, A_d \right) \tag{5.44}$$

where the area A_d is defined by Eq. (5.12)

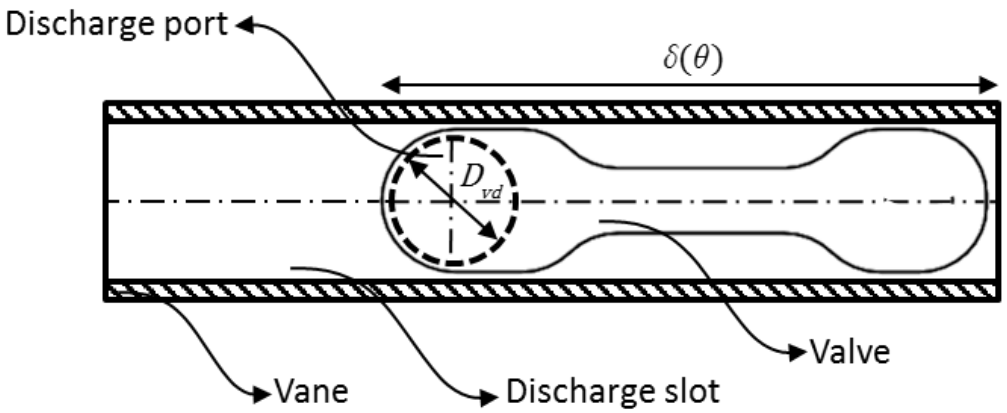

Figure 5.8 FVC discharge port

5.4 Performance penalty of re-expansion loss in SVC

Equations derived in this section is required for evaluating the losses associated with trapped discharge gas leaking into the suction chamber (re-expansion loss) for the SVC model. The suction and compression chambers of the SVC has been identified in Figure 5.9. The suction and discharge ports are located at θ_s and θ_d positions respectively. The centre line through the vane defines 0^0, 360^0 and 720^0 degree positions of the shaft. A complete cycle consists of two revolutions and comprises of four distinct process defined based on the angular position of the crankshaft (see Table 5.1).

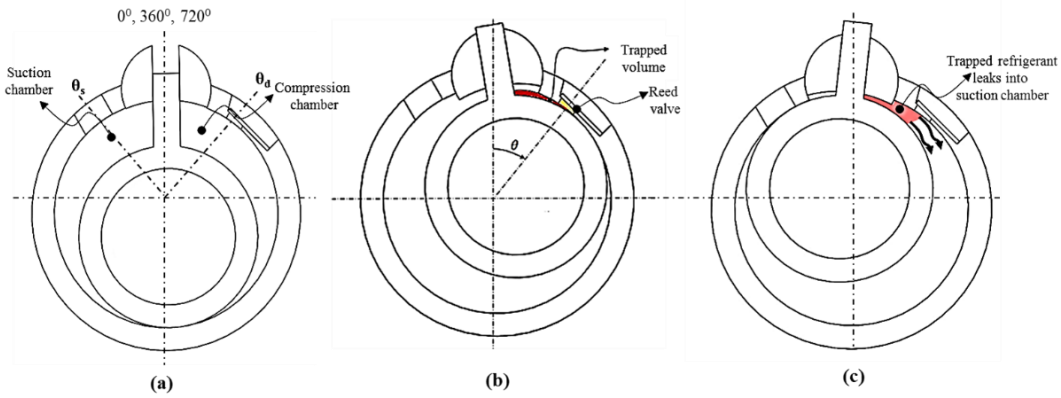

Figure 5.9 Re-expansion loss mechanism in a SVC (a) Suction and compression chambers (b) trapped mass at the end of compression process (c) leakage of trapped mass into suction chamber during the re-expansion stroke.

Table 5.1 SVC cycle analysis

	Shaft angular position			
Process No.	**Start**	**End**	**Process**	**Description**
1	0^0	θ_s	-	Working chamber volume corresponds to the dead volume introduced by the clearances between various components.
2	θ_s	360^0	Suction and compression	Refrigerant drawn into the suction chamber, while the refrigerant induced in previous cycle is compressed in the compression chamber
3	θ_d	θ_s	Re-expansion	Refrigerant contained in the suction chamber expands and the refrigerant in the trapped volume leaks into the suction chamber.
4	$360^0+\theta_s$	720^0	Compression and discharge	The refrigerant mixture is compressed and discharged through the discharge port.

Process 1: The working chamber volume in the compressor is contributed by the clearances and tolerances between various mating components. There is no appreciable change in the chamber volume as piston rotates from 0^0 to θ_s.

Process 2: The motion of the piston sweeping past the suction port initiates the induction of refrigerant into the suction chamber. As the piston rotates further, the increasing chamber volume draws in more refrigerant into the suction chamber – a process that continues until the piston completes the first revolution. Meanwhile, there is a corresponding reduction in the compression chamber volume, which results compressing the refrigerant drawn in previous cycle. As the pressure in the compression chamber exceeds the discharge pressure, the reed valve placed over the discharge port opens to release the gas. However, the piston can only force gas out of the compression chamber up to the location of the discharge port. Once the

piston sweeps past the discharge port, the gas remaining the compression chamber becomes trapped in the volume identified in Figure 5.9(b).

Process 3: As the piston rotates from the discharge port to the suction port, the refrigerant in the suction chamber expands future while the refrigerant trapped at the end of discharge process leaks into the suction chamber as shown in Figure 5.9 (c). This result in the mixing of the compressed refrigerant with the refrigerant contained in the suction chamber, resulting in re-expansion losses.

Process 4: The refrigerant mixture is compressed and discharged through the discharge port at the end of second revolution. This process once again trapes a small quantity of refrigerant and the cycle repeats.

The quantity of mass trapped in the volume identified in Figure 5.9 (b) is given by

$$m_{trapped} = V_d \cdot \rho \tag{5.45}$$

The volume of trapped gas is given by

$$V_d = \frac{R_c^2 h_c}{2}\left[\begin{array}{l}(1-a^2)\theta_d - \dfrac{(1-a)^2}{2}\sin(2\theta_d) - a^2\sin^{-1}[(\dfrac{1}{a}-1)\sin\theta_d] - \\ a(1-a)\sin\theta_d\sqrt{1-\left(\dfrac{1}{a}-1\right)^2\left(\sin\theta_d\right)^2}\end{array}\right] \tag{5.46}$$

It might be tempting to assume that the density of the trapped mass is a function of discharge conditions. However, this is not the case, as the enthalpy of the compressed gas within the discharge port has to exceed the enthalpy at the discharge boundary to motivate a positive mass flow out of the discharge port. Hence, the compressed gas discharges at a pressure and temperature slightly higher than that specified in the discharge conditions. Therefore, a preliminary simulation with re-expansion effects supressed has to be performed to determine the density of the trapped gas at the discharge condition.

Assuming the discharge condition of the control volume is known, the enthalpy of the trapped mass is

$$h_{trapped} = f(\mathrm{T_{d,cv}}, \mathrm{P_{d,cv}}) \tag{5.47}$$

It is valid to assume that the mixing occurs instantaneously due the large pressure difference between the trapped refrigerant and the suction chamber. Since there is no reed valve over the suction port, the sudden release of trapped mass will result in a back-flow of the refrigerant through the suction port. This prevents any pressure rise within the suction chamber, therefore the mixing process can be modelled as an isobaric event. The enthalpy of the resulting mixture is given by

$$h_{mixture} = \frac{m_s h_s + m_{trapped} h_{cv}}{m_s + m_{trapped}} \tag{5.48}$$

The release of trapped refrigerant during the re-expansion process results in an instantaneous increase in the mass contained in the suction chamber. The total mass contained in the chamber after the release of trapped refrigerant is

$$m_{cv,total} = m_{cv} + m_{trapped} \tag{5.49}$$

5.5 Mechanical power loss model

The mechanical power supplied to the compressor shaft provides the power to compression the refrigerant and to overcome various frictional losses. These frictional losses include the piston end-face loss (P_{fl}), piston-eccentric loss (P_{pe}), lip seal loss (P_{ls}) and journal bearing loss (P_{jb}).

The clearance space between the rolling piston side face and the cylinder wall is assumed to be filled with lubricant. Assuming negligible radial velocity in comparison to the tangential velocity, the frictional power loss due to viscous drag as the piston-eccentric assembly rubs against the cylinder walls can be obtained from the following equation [82]

$$P_{fl} = \frac{\pi\mu\omega_r^2}{\varepsilon_1}\left(R_p^4 - R_e^4\right)\cdot\omega + \frac{\pi\mu\omega^2}{2\varepsilon_2}\left(2R_e^4 - R_s^4\right) \tag{5.50}$$

where ε_1 represents the axial clearance between cylinder and the piston, while ε_2 represents the axial clearance between cylinder and eccentric and ω_r represents the piston angular velocity obtained from Eq. (4.31). The axial clearances, ε_1 and ε_2 can be assumed to be equal for most cases [118].

As discussed in section 4.4.1, there exists a relative motion between the eccentric and the piston, which gives rise to piston-eccentric loss, P_{pe}. Assuming the radial clearance space between the piton and eccentric is filled with lubricant, the piston eccentric assembly can be modelled as a journal bearing. Assuming the centrifugal force due to eccentric mounting of the roller to be negligible [118], the frictional loss is purely due to viscous drag generated by the relative motion between two concentric cylinders (piston and eccentric) separated by a concentric lubricating film. This vicious drag can be obtained from the following relationship [82]

$$P_{pe} = \frac{2\pi\mu h_c R_e^3 \omega_r^2}{\delta} \tag{5.51}$$

Lip seals are installed in the both ends of the compressor drive shaft to prevent leakage of compressed refrigerant through the clearance between the crankshaft and the casing The power loss due to the lip seals P_{ls} can be obtained from the manufacture catalogue (reproduced in Figure 5.10).

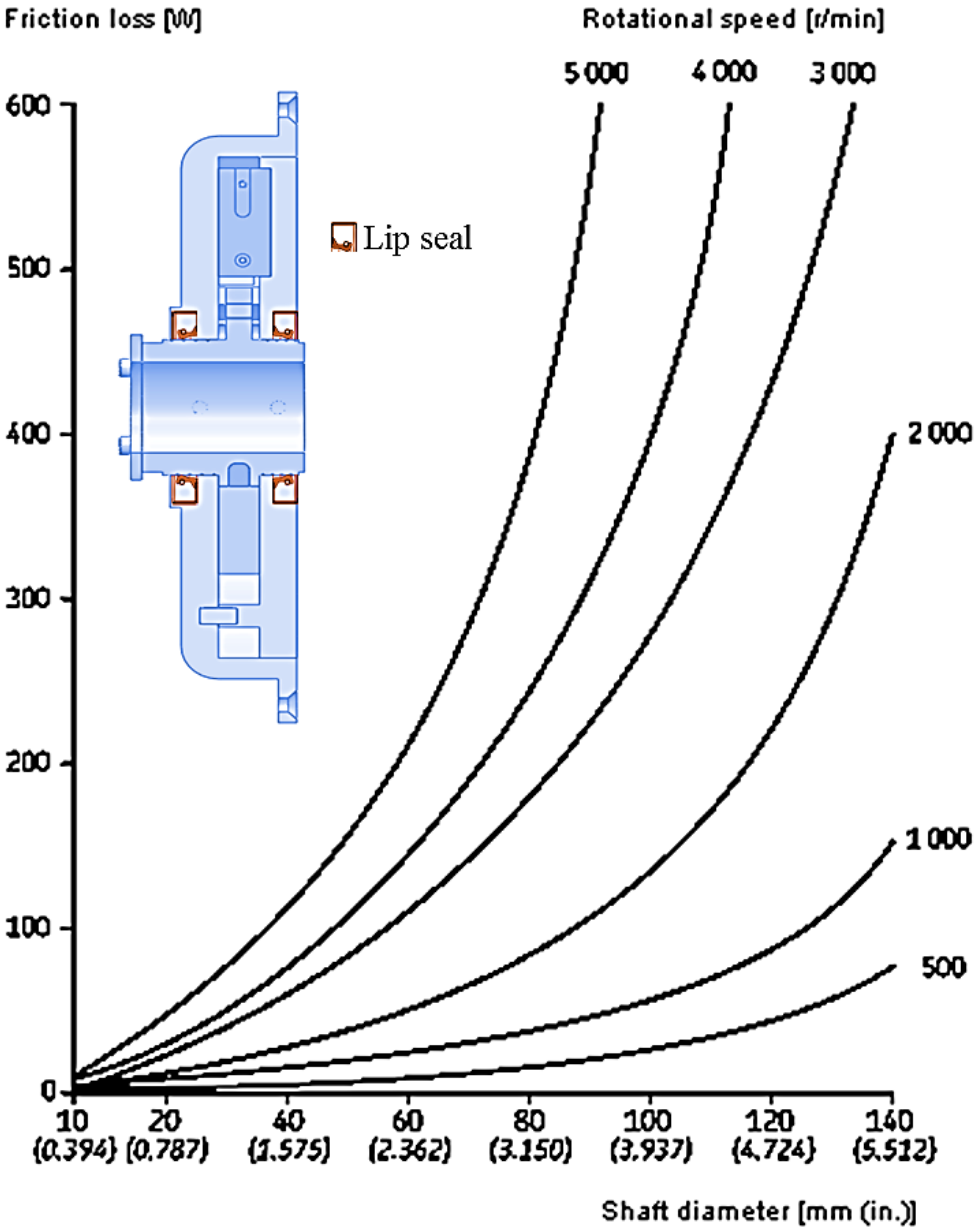

Figure 5.10 Frictional loss in a lip seal as a function of rotational speed and shaft diameter [119]

To aid modelling in a computer program purpose, the lip seal losses has been expressed a function of 2nd order polynomial function for a shaft given diameter. The power loss in the journal bearing, P_{jb} is obtained from COMSOL model discussed in section 4.4.

5.6 Compressor reed valve & Mathematical model

As identified in Figure 5.11, a Swing Vane Compressor assembly consists of casing, a drive motor, journal bearings, compressor, suction and discharge interfaces. A reed valve covers the discharge port of the compressor to facilitate the compression process. The valve prevents the premature release of the refrigerant in the compression chamber, whilst preventing the back flow of refrigerant from the discharge port. A valve stop prevents excessive deformation of the reed valve by constraining its displacement range.

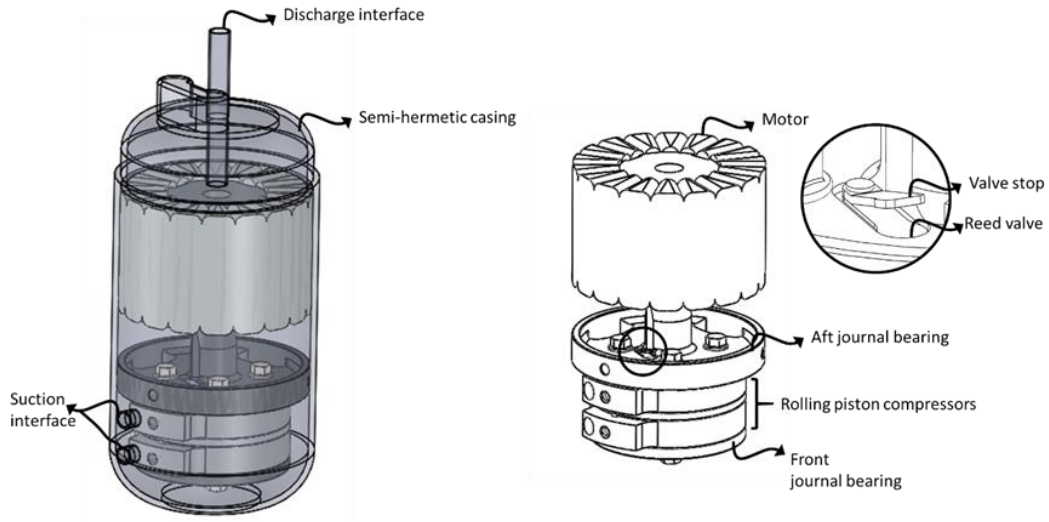

Figure 5.11 Rotary piston compressor assembly nomenclature

A reed valve is often referred as an automatic or self-acting valve, as the pressure difference is all that is required to open and close it. The compressor valve has a direct influence on the compressor's efficiency, noise characteristics, and reliability. Therefore, the simulation the of valve motion as a function of crank angle has been of interest during the design phase [120].

Figure 5.12 depicts the generic response of a reed valve during discharge phase. As observed in the response figure, owing to the inertia as well as stiffness of the material, the valve neither opens instantaneously at the start of discharge process, nor closes instantaneously at the end. The actual response of a reed valve is a

complex two-way fluid structure interaction involving large deflections, and is affected by parameters such as dampening coefficient, valve thickness, elasticity of the reed valve material, inertia, discharge coefficient, and viscous forces experienced during the discharge phase [121].

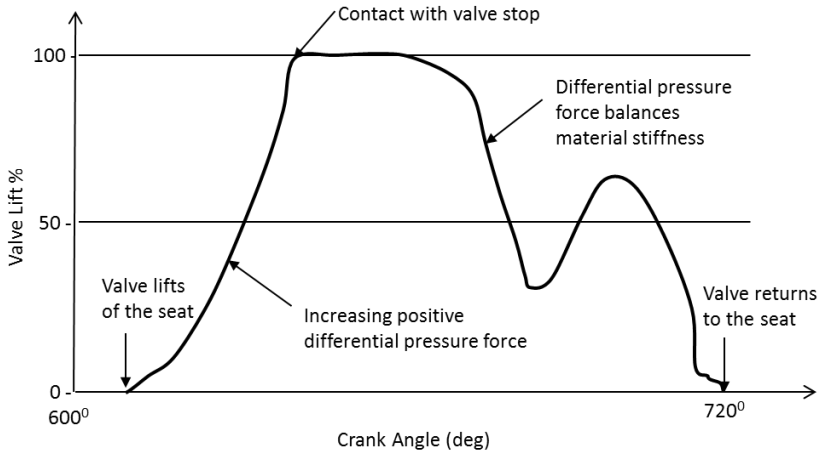

Figure 5.12 Generic response of a reed valve during discharge phase

The usage of a reed valve with weak stiffness will result large displacement of the valve during the discharge process as observed Figure 5.13. This ultimately decrease the reliability of the valve and could lead to failure due to fatigue. Moreover, it may not provide adequate sealing of the discharge port during compression stroke.

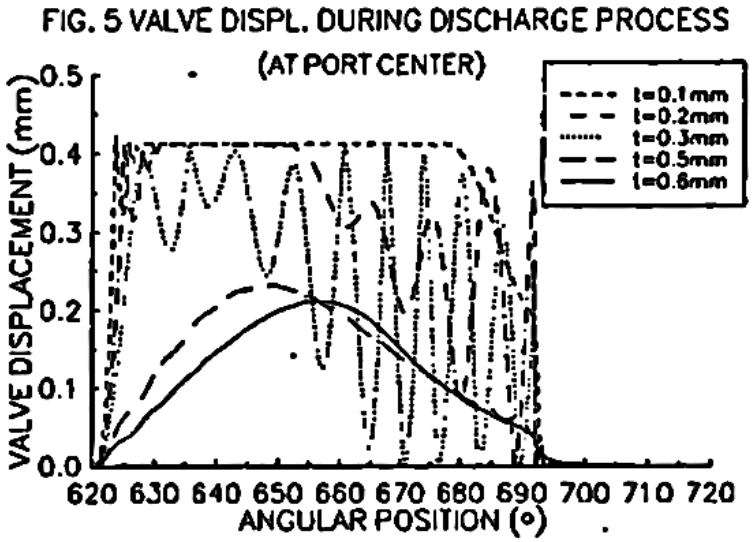

Figure 5.13 Motion of reed valve with weak stiffness [122]

When a reed valve with high stiffness is used, the pressure within the compression chamber have to rise higher than what is normally required. If the stiffness is excessive, pressure oscillations will appear above and below the discharge pressure throughout the discharge stroke as shown in Figure 5.14. This results in over compression losses, increases the high-pressure flow losses in vicinity of the valve and pulsations in the refrigerant flow rate. The gas pulsation enhances the flow turbulence resulting increased compressor noise level [122].

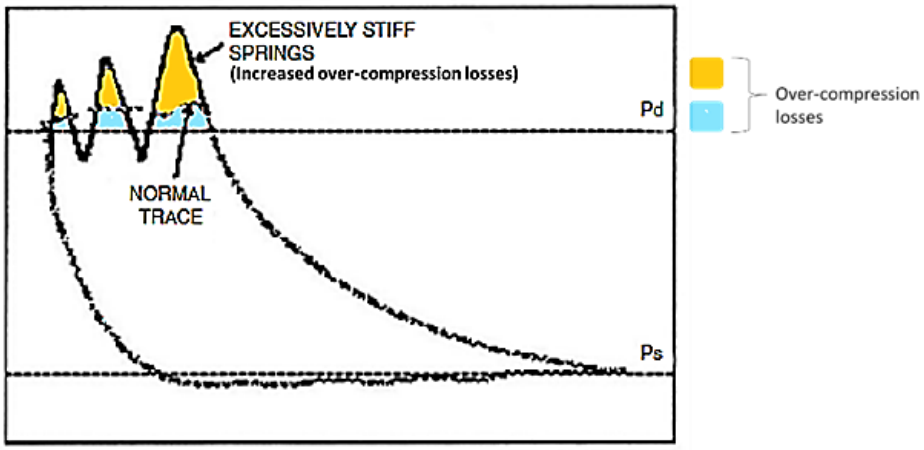

Figure 5.14 Over-compression loss due to stiff discharge valve [24]

The single-degree freedom lumped parameter reed valve model is by far the simplest mathematical model [123]. However, such a simplified analysis compromises the accuracy and fidelity of the output. Piechna [124] performed a dynamic analysis of the reed valve based on the Finite Element Method (FEM). But the valve geometry was restricted to rectangular shapes. Fabian Fagotti improved the FEM reed valve analysis by accommodating various valve geometries and other characteristics [77]. However, the model relied on experimental measurements to obtain the dampening matrix. In fact, the dampening matrix was used as a parameter to provide a fit between model prediction and the experimental data.

Ooi [122] modelled the reed valve as an Euler beam with a rectangular cross-section and a circular disk attached at the end. He approximated the first two mode shapes using shape functions, and used Rayleigh's quotient to determine the natural frequency. The deficiency with this approach is that one of the shape functions did

not satisfy the natural boundary condition at the clamped end. The model analysed the valve motion for a dampening ratio in the range of 0.1 to 1.0. In recent years, several researchers [37-39] have resorted to two-way fluid structure analysis in the Computer Fluid Dynamics (CFD) package to predict the complex non-linear motion of the reed valve. However, these analyses are time-consuming, and transient coupled two-way fluid structure interactions are challenging to replicate in CFD [40], due to large deflections of reed valve geometry.

The single-degree freedom lumped parameter reed valve model is by far the simplest mathematical model [123]. However, such a simplified analysis compromises the accuracy and fidelity of the output. Piechna et. al. [124] performed a dynamic analysis of the reed valve based on Finite Element Method (FEM) with rectangular shaped valves. Fabian Fagotti et. al. [77] improved the FEM reed valve analysis by accommodating various valve geometries and other characteristics. However, the model relied on experimental measurements to obtain the dampening matrix. In fact, the dampening matrix was used as a parameter to provide a fit between model prediction and the experimental data.

Ooi [122] modelled the reed valve as a Euler beam with a rectangular cross-section and a circular disk attached at the end. The author approximated the first two mode shapes by using shape functions, and used Rayleigh's quotient to determine the natural frequency. The drawback with this approach is that one of the shape functions did not satisfy the natural boundary condition at the clamped end. The model analysed the valve motion for a dampening ratio in the range of 0.1 to 1.0. But experimental measurements from other literature reported that the rolling piston reed valve operates with dampening ratio of 0.03 to 0.05 [123].

In recent years, several researchers [37-39] have resorted to two-way fluid structure analysis in the Computational Fluid Dynamics (CFD) computational codes to predict the complex non-linear motion of the reed valve. However, these analyses are time-consuming, and transient coupled two-way fluid structure interactions are challenging to replicate in CFD [40], due to large deflections of reed valve geometry.

5.6.1 Reed valve model

Figure 5.15 depicts a reed valve, with thickness *t* positioned above the discharge port. The reed valve's upper face is open to the discharge pressure, P_d while the lower face communicates with the compressor chamber pressure, P_{cv}. The force due to differential pressure acting on the reed valve can be calculated using Eq. (5.52). This force is assumed to act perpendicular and through the centre of the reed valve discharge opening.

$$F(t) = A_d \cdot (P_{cv}(t) - P_d) \tag{5.52}$$

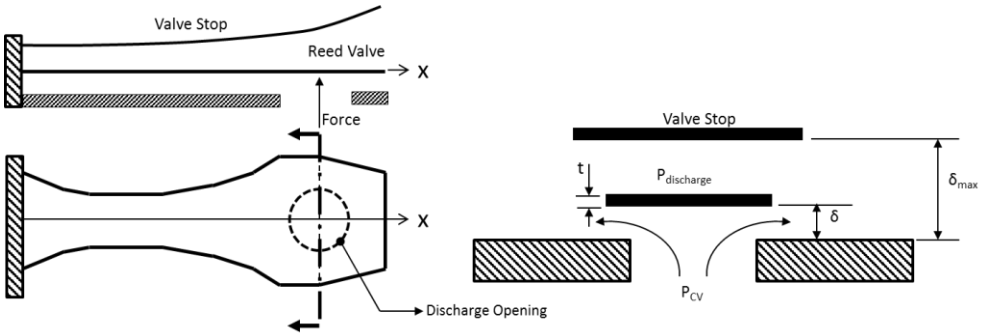

Figure 5.15 Reed valve over the discharge port

The thermofluid model provides the instantaneous pressure in the compressor chamber, *Pcv*. Given the discharge pressure, the reed valve model is able to predict the response of the valve by using the equation of motion for a structural finite element system expressed in Eq. (5.53)

$$[M]\{\ddot{U}\} + [C\{\dot{U}\} + [K]\{U\} = \{F(t)\} \tag{5.53}$$

This chapter models the reed valve based on a two-node, finite element representation of an Euler beam as shown in Figure 5.16. Each element has two degrees of freedom, as the nodes are constrained to lateral motion. As shown Figure 5.17, the nodal position along the horizontal axis defines the valve geometry. The global stiffness *K*, mass *M* and dampening matrix *C* can be constructed given the valve thickness and Young's modulus.

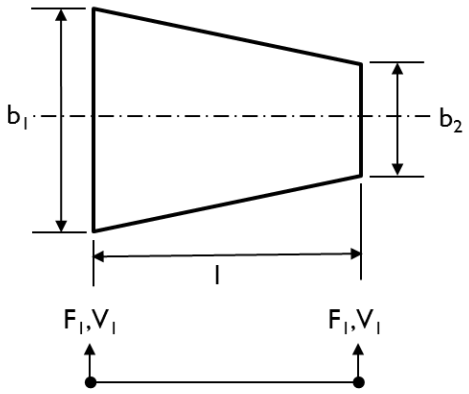

Figure 5.16 Element geometry and nodal degrees of freedom

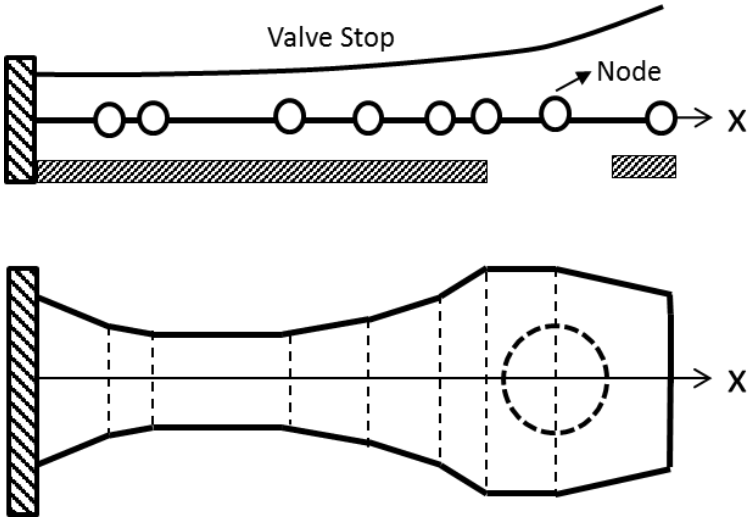

Figure 5.17 Valve geometry defined by nodal distribution along x-axis

Stiffness matrix

There are two possible ways to construct the stiffness matrix, *K*. The first method involves discretising the reed valve into Euler beam elements having a finite length. The stiffness matrix for each element can be constructed based on the local coordinate system. Combing the local stiffness matrix based on the global coordinate system yields the global stiffness matrix. An alternative approach based

on influence coefficients allows the direct computation of the global stiffness matrix, thereby eliminating the need to calculate the local stiffness matrix, as well as the assembly of the global stiffness matrix.

Consider a cantilever beam subjected to lateral loads (Q) at discreet points along its length (Figure 5.18). The deflections at these discreet points, *q* is characterized by:

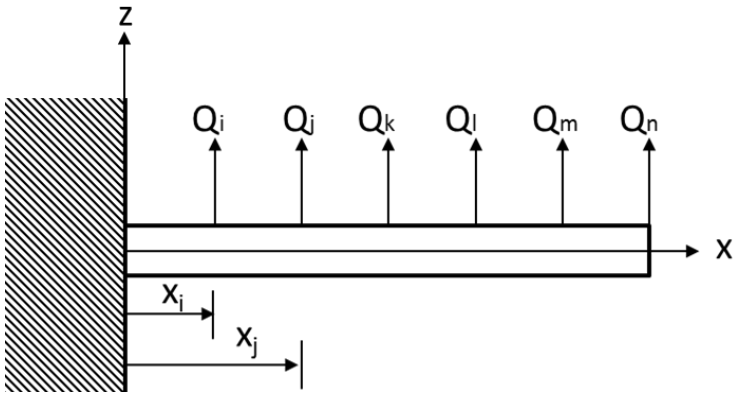

Figure 5.18 Cantilever beam subjected to discreet transverse load

$$\begin{bmatrix} q_1 \\ q_2 \\ q_3 \\ q_4 \\ q_5 \\ q_6 \end{bmatrix} = \begin{bmatrix} C_{11} & C_{12} & C_{13} & C_{14} & C_{15} & C_{16} \\ C_{21} & C_{22} & \cdots & \cdots & \cdots & \cdots \\ \vdots & & \ddots & & & \vdots \\ \vdots & & & \ddots & & \vdots \\ \vdots & & & & \ddots & \vdots \\ C_{61} & \cdots & \cdots & \cdots & \cdots & C_{66} \end{bmatrix} \begin{bmatrix} Q_1 \\ Q_2 \\ Q_3 \\ Q_4 \\ Q_5 \\ Q_6 \end{bmatrix}$$

where C_{ij} represents the flexibility influence coefficient.

The flexibility influence coefficient, C_{ij} correlates the deflection, *q* at i^{th} location as a result of the application of unit load *Q* at j^{th} node. Maxwell's theorem of reciprocal deflection specifies that the flexibility influence coefficient matrix is symmetric. Assuming constant Young's modulus (E) and second moment of area (I) between nodes i and j, the individual elements of influence coefficient matrix can be obtained from

$$C_{ij} = \frac{1}{E \cdot I}\left(\frac{x_i^2 x_j}{2} - \frac{x_i^3}{6}\right) \quad for\ x_i \le x_j \tag{5.54}$$

Inverting the flexibility influence coefficient matrix yields the global stiffness matrix.

$$[K] = [C]^{-1} \tag{5.55}$$

Mass matrix

The mass matrix can be constructed by using either a consistent or a lumped mass matrix. The lumped mass matrix was selected as it is a sparse matrix with diagonal elements, thereby requiring less storage space and computational time. For a two-node bar element, the lumped mass matrix is described by

$$[\mathrm{M}^{\mathrm{e}}]_{lumped} = \frac{\rho AL}{2}\begin{bmatrix} 1 & 0 \\ 0 & 1 \end{bmatrix} \tag{5.56}$$

Dampening matrix

Unlike the stiffness and mass matrix, the dampening matrix cannot be obtained from valve dimensions or material properties[125]. Nevertheless, for linear systems, the dampening matrix can be calculated from its modal damping ratios. Considering the first two modes of valve deflection, the dampening matrix can be constructed from Rayleigh's dampening equation:

$$[C] = a_0[M] + a_1[K] \tag{5.57}$$

Assuming the same dampening ratios, ζ for the first two modes, Eq.(5.58) yields the factors a_0 and a_1

$$a_0 = \zeta\frac{2\omega_1\omega_2}{\omega_1 + \omega_2} \qquad a_1 = \zeta\frac{2}{\omega_1 + \omega_2} \tag{5.58}$$

where ω_1 and ω_2 represent the natural frequency of first and second modes, respectively. The natural frequency of the first two modes can be obtained by solving Eq. (5.59).

$$\det([K]-\lambda_i[M])=0 \tag{5.59}$$

Dampening ratio

Glen et. al. [123] conducted experiments to measure the dampening ratio of a reed valve used in a rolling piston compressor. Their study measured the sensitivity of the dampening ratio to factors such as the clamping torque, valve preload force and lubricant viscosity. Experimental data published by the study has been reproduced in Table 5.1 Analysis of the data reveals that the reed valve is an under dampened system having a dampening ratio of 1% to 5%. For the purpose of simulation, one can assume a dampening ratio in the range of 0.03 to 0.05 [123]. Thereafter, simulation results have to be compared with experimental measurements to ascertain the actual value.

Table 5.2 Dampening ratio of a reed valve of rolling piston compressor [123]

Design factor		**Dampening Ratio - ζ**	σ_ζ
Torque (N-m)	2.26	0.0307	0.009
	2.83	0.0333	0.013
	3.39	0.0368	0.007
Preload (N)	0	0.0216	0.000
	0.111	0.0457	0.005
	0.334	0.0413	0.002
Viscosity	0.002 (dry air)	0.0489	0.005
	45 (light oil)	0.0502	0.008
	190 (AB300)	0.0457	0.005

5.6.2 Solution scheme

The global stiffness, mass and damping matrix can be substituted into Eq. (5.53) to predict the response of reed valve to a time varying pressure force, *F(t)*. The reed valve model is coupled to the thermofluid model as depicted in flowchart presented

in Figure 5.19. The solver initiates the thermofluid model with the inputs such as compressor geometry and boundary conditions at the suction and discharge ports. Since the first revolution of the crankshaft corresponds to suction stroke, the reed valve model is bypassed to speed up the execution.

During compression stroke, the solver monitors whether the chamber pressure exceeds that of the discharge pressure. If the chamber pressure exceeds the discharge pressure, the reed valve model is triggered to calculate the displacement of the reed valve due to the differential pressure forces. The reed valve model uses linear Newmark scheme to solve the governing equation as it provides an unconditional stability for any time step. Once the nodal displacements are computed for the given time step, the reed valve model outputs the effective flow area of discharge port. This parameter is then used by Eq. (5.41) to compute the variation in mass flowrate due to displacement of the reed valve.

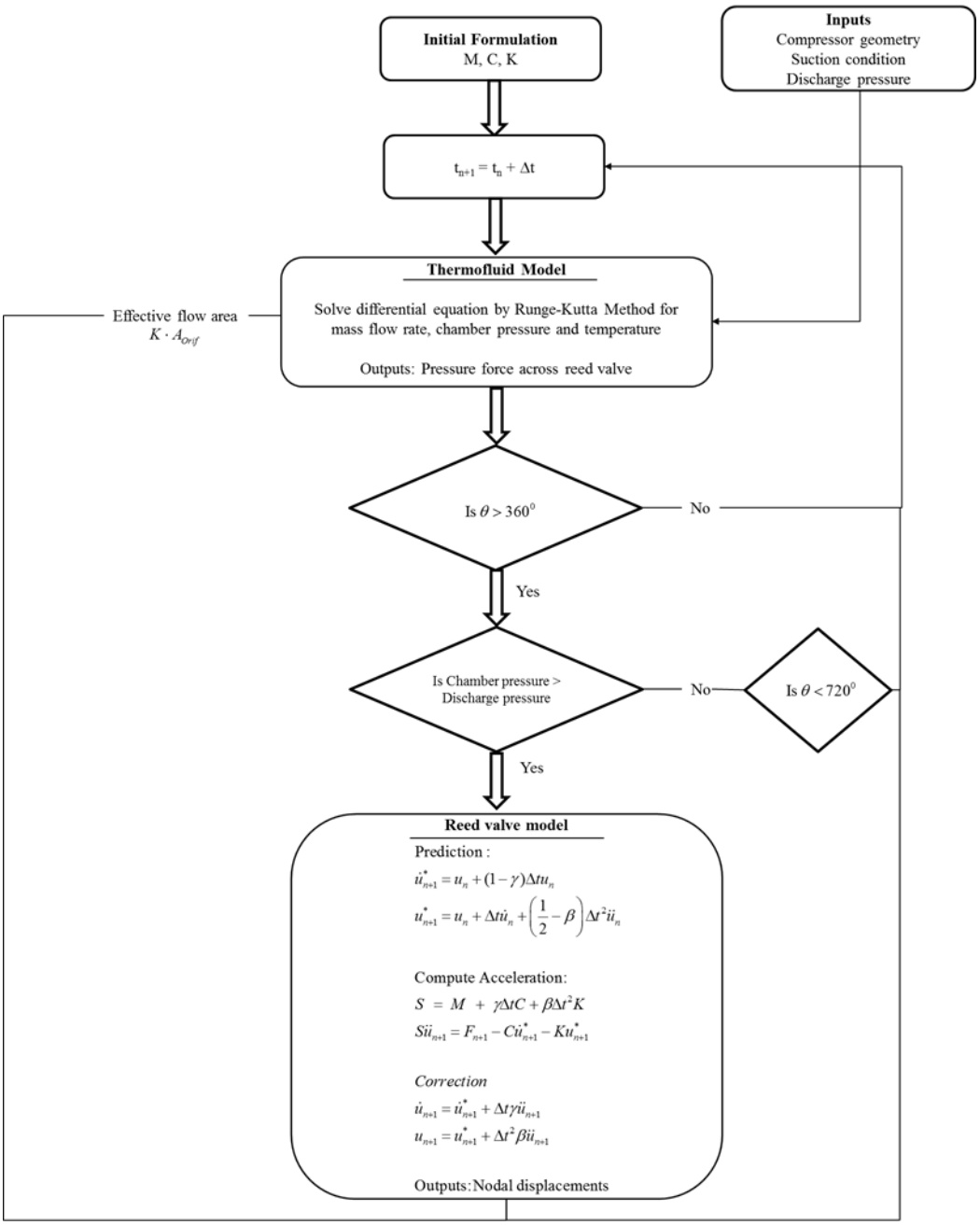

M	Mass matrix	u	Displacement
K	Stiffness matrix	$\dot{u}$	Velocity
C	Dampening matrix	$\ddot{u}$	Acceleration
F	Force matrix	S	Forcing function
t	Time	n	Solver step
		Δ	Small increment

* γ and β are solver constants taken to be $\frac{1}{2}$ and $\frac{1}{6}$ respectively [125]

Figure 5.19 Flow chart of compressor solver model

5.6.3 Model validation using FEA

The accuracy of the mathematical model is verified by comparing the displacement predicted by a Finite Element Analysis (FEA) software to that predicted by the model (Figure 5.20). The displacement plot generated by the FEA is continuous and smooth as it uses large number of nodes, while the mathematical model outputs discreet displacements at sparsely spaced nodes.

The discharge port is located at 30mm from the clamped end. The displacement at this position is predicted to be 0.91mm by the FEA while the displacement calculated the model is approximately 0.63mm. Using the FEA as reference, this corresponds to an error of 32%. This error is attributable to the simplified geometry used by the mathematical model and due to dampening matrix obtained from empirical methods. Though it is possible to reduce the error by increasing the node density, doing so will result in increased computation time and complexity.

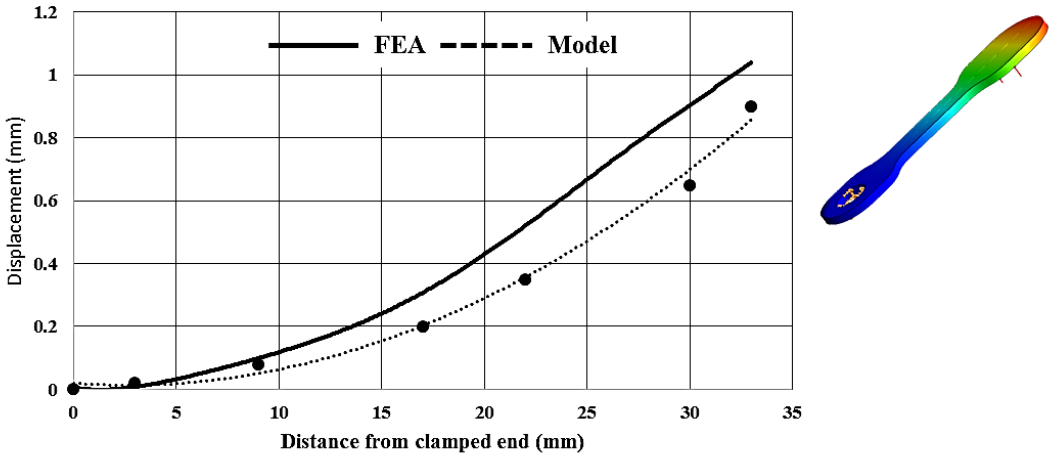

Figure 5.20 Model validation using a FEA software

5.7 Simulation of the FVC using mathematical model

The section discusses the prediction made by the mathematical model for compressor design parameters generated in chapter 4.

5.7.1 Thermodynamic model predictions

The mathematical model receives basic inputs such as the compressor geometry, refrigerant choice and boundary conditions and predicts various state properties such as temperature, pressure and mass as a function of crank angle. Figure 5.21 shows the plots generated by the model for the compressor parameters defined in Table 4.1 and Table 4.2 for compressor operating with an ideal reed valve.

Analysis of the plot shown in Figure 5.11 reveals that the temperature and pressure is nearly constant with respect to crank angle up to 500º. However, there is a rapid variation in the mass entrained into the suction chamber during this period. Therefore, it is evident that the pressure and temperature is nearly constant during the suction process. Therefore, the only purpose of the suction process is to maximise the mass drawn into the compression chamber. Note that the mass variation plot starts with a non-zero value due to the initial mass that is trapped in the clearance volume of the compressor. The mass variation plot ends with a non-zero value due the mass that is trapped in the discharge port towards the end of compression process. A more rigorous analysis of this will be presented in chapter 6.

The PV plot generated by the model can be used to predict the work energy that is required to compress the refrigerant from suction pressure to discharge pressure. The compression power requirements are then easily obtained by dividing the compression work energy by the angular velocity of the compressor.

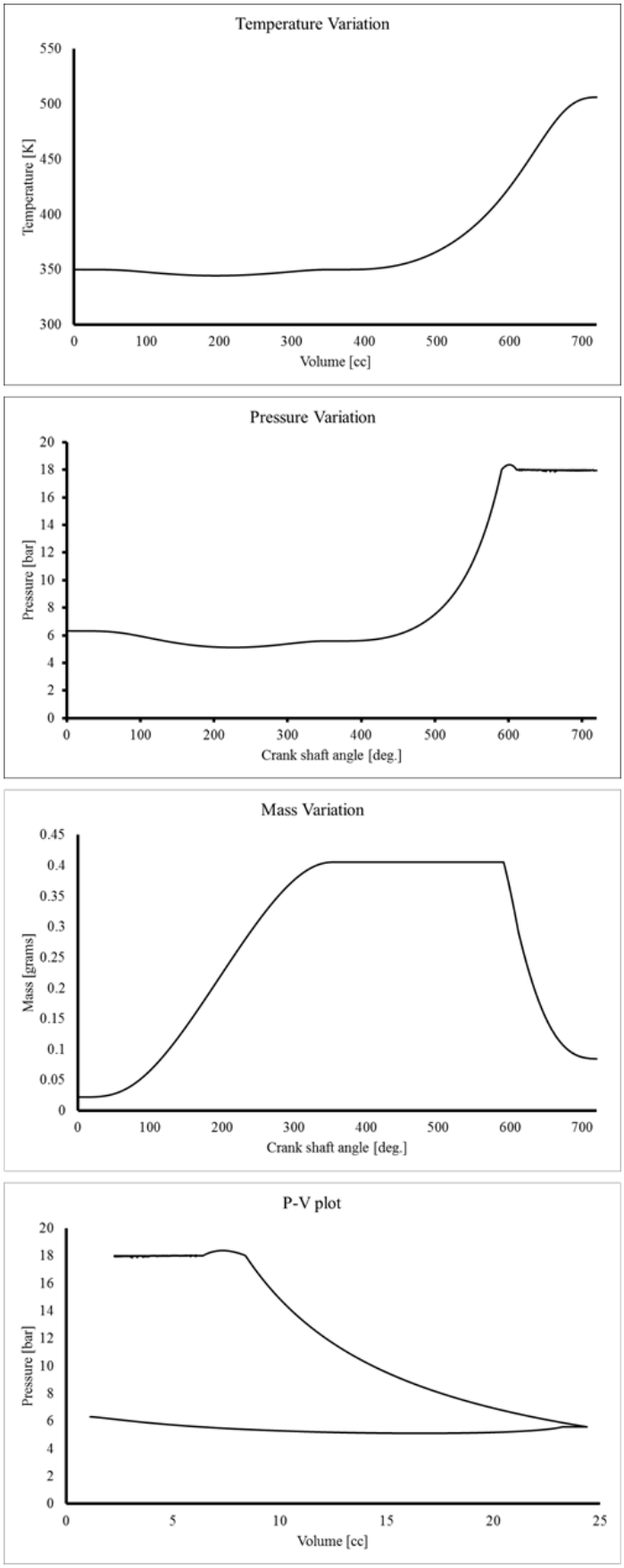

Figure 5.21 Plots generated by the thermodynamic model

5.7.2 Reed valve model predictions

The plots in Figure 5.22 shows the pressure, mass and PV plots with the reed valve model coupled with the thermodynamic model. The reed valve young's modulus was varied between 20700 MPa to 21300 MPa to identify its effect on the pressure, mass and PV plots. In general, increasing the reed valve stiffness delays the discharge port opening, thereby contributing to overcompression loss and unwated heating of the mass contained within the compression chamber. While decreasing the reed valve stiffness results in rapid movement of reed valve tip towards the end of discharge process, which may contribute to reed valve fatigue.

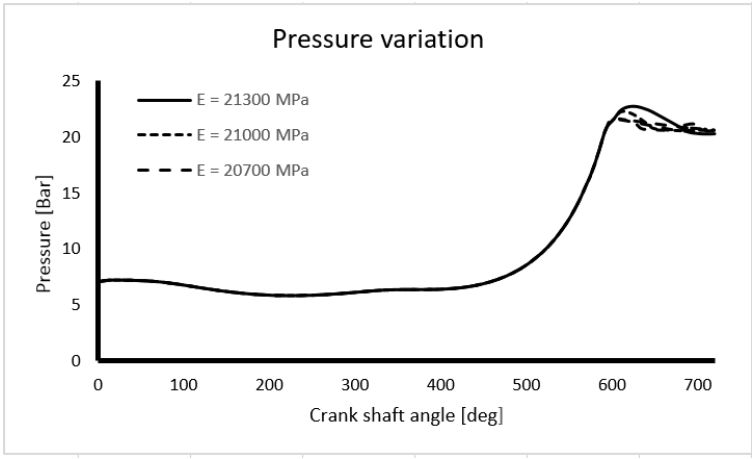

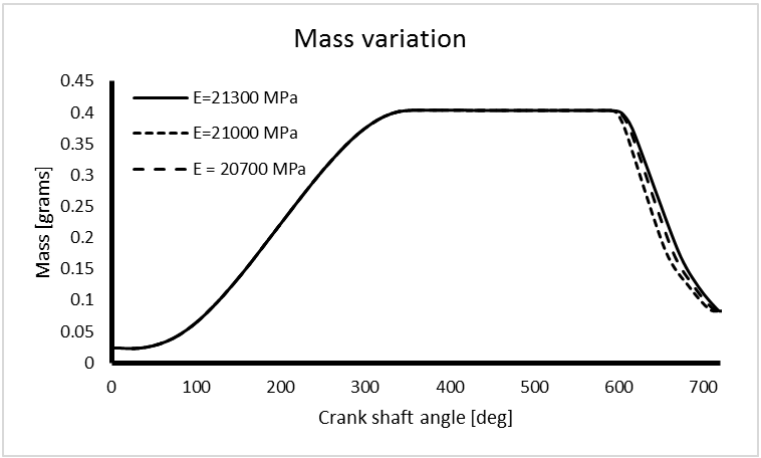

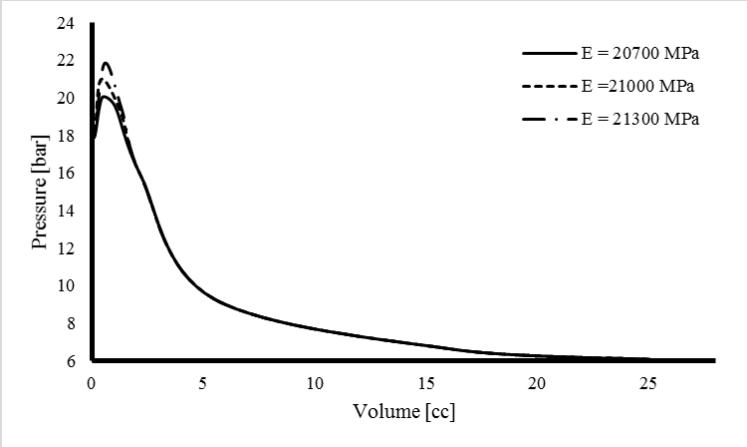

Figure 5.22 Plots generated with the reed valve model coupled to the thermodynamic model

5.7.3 Mechanical power loss model predictions

The key mechanical power losses occur at the lip seals, between the roller, eccentric and the cylinder side walls. These losses are purely a function of angular velocity of the compressor and its variation with respect to compressor speed is shown in Figure 5.23. Based on the plot, it is evident that the lip seal is the major component that contributes to mechanical power loss at low speeds (0 to 150rad/s). Thereafter, the friction loss between the roller and eccentric increase rapidly outweighs the contribution by lip seals and frictional loss occurring at the cylinder side walls.

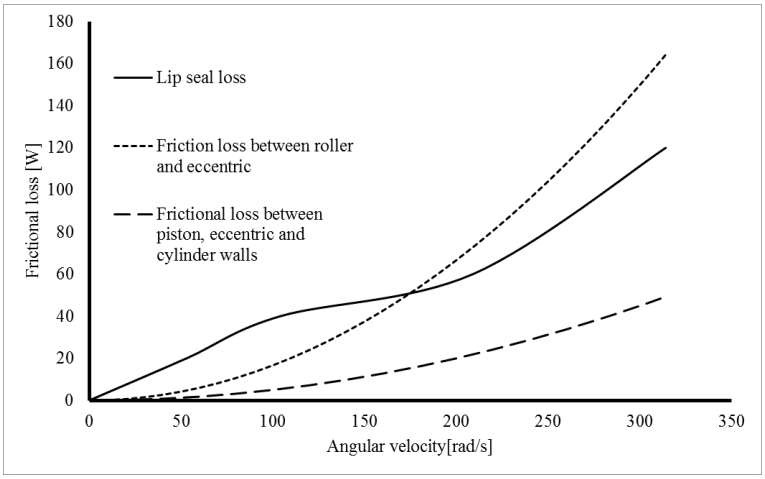

Figure 5.23 Mechanical losses as a function of angular velocity

5.8 Concluding remarks

The geometric, thermodynamic, mass flow, power loss and valve mathematical models of the swing and fixed vane compressors are formulated in this chapter. The geometric model provides the variation in chamber volume with respect to shaft angle. The thermodynamic model coupled with the geometric model predicts the pressure and temperature of the refrigerant during the suction and compression stroke. The valve model regulates the peak pressure of the compressor by predicting reed valve response to the differential pressure that acts across its face. The subsequent chapter will use the models to predict and compare the performance of the swing and fixed vane compressors.

Chapter 6
COMPRESSOR COMPARATIVE STUDY

This chapter simulates the Swing Vane Compressor (SVC) and the newly designed Fixed Vane Compressor (FVC) using theoretical models developed in chapter 5 to compare their performance characteristics. Both compressors are simulated under idealised conditions, hence assumed to be adiabatic and frictionless. The focus of this chapter is to theoretically investigate the benefit locating the discharge port on the fixed vane rather than on the cylinder wall.

6.1 Introduction

The major disadvantage associated with rotary piston compressor is the frictional and leakage losses incurred by the sliding vane tip as it rubs over the piston. Both the frictional and leakage losses reduces the cooling capacity and volumetric efficiency of the compressor. To address this issue, a new variant of the rotary piston compressor was introduced by Daikin, named "Swing Vane Compressor" (SVC) in 1994 [41]. The SVC is similar to rotary compressor, except for the fact that the vane is rigidly attached to the piston body, thereby eliminating all leakage and frictional losses between the vane tip and the piston. Consequently, the new design variant has a higher efficiency in the range of 2% - 9% [42] as compared to the conventional rotary piston compressor.

Though, SVC effectively eliminates the frictional and leakage losses at the vane tip, it still experiences re-expansion losses due the entrapment of compressed refrigerant towards the end of discharge process (see Figure 6.1). In a SVC design, the discharge port is located on the cylinder wall; therefore, the rolling piston can only facilitate the discharge of the compressed gas up to the discharge port. Any undischarged gas remains trapped and eventually leaks back into the suction chamber, resulting in re-expansion loss.

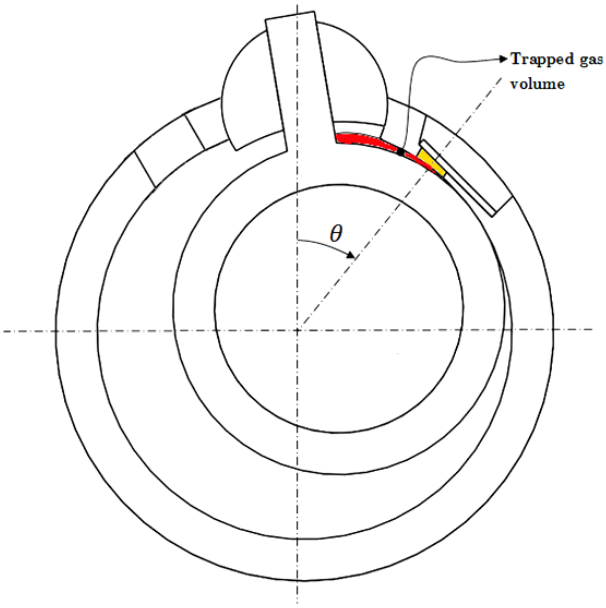

Figure 6.1 Trapped gas volume in SVC towards the end of compression process

6.2 Trapped gas volume

Park [126] analysed the transient performance characteristics of the rolling piston compressor. The study analysed the variations in gas pressure, work done and refrigerant mass in the working chamber with respected to crank angle from compressor start-up till to steady state ($t \rightarrow t+\delta t$). Figure 6.2 shows the variation in refrigeration mass with respect to crank angle. The figure highlights that for a given cycle, the cylinder achieves its maximum capacity at 360^0. The large compressor capacity observed during the start-up process is attributed to high evaporating pressure and a small compression ratio. The residual refrigerant mass contained in the working chamber at the end of the compression process represents the trapped refrigerant mass due to internal leakages contributed by the compressor clearance volume.

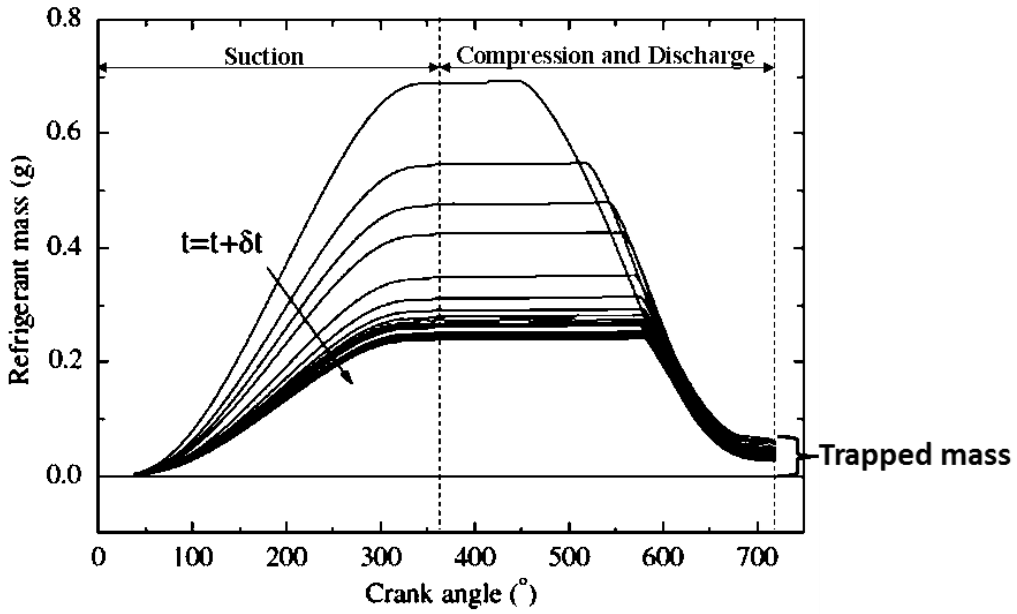

Figure 6.2 Refrigerant mass variation with respect to crank angle and trapped mass [126]

The trapped mass identified in Figure 6.2 remains undelivered by the compressor. The main objective of this study is to surface the benefits of the newly designed FVC, where the location of the discharge port is expected to minimise the quantity of the trapped mass. In a SVC design, the discharge port is located on the cylinder wall; hence, the rolling piston can only facilitate the discharge of the compressed

gas up to the discharge port as identified in Figure 6.3(a). Any undischarged gas remains trapped and eventually leaks back into the suction chamber as shown in Figure 6.3(b).

The volume of the trapped gas can be calculated using Eq.(6.1). Readers are directed to section 5.1 for detailed derivation.

$$V_{trapped} = \frac{R_c^2 \cdot h_c}{2}\left[\begin{array}{l}(1-a^2)\theta_d - \frac{(1-a)^2}{2}\sin(2\theta_d) - a^2\sin^{-1}[(\frac{1}{a}-1)\sin\theta_d] - \\ a(1-a)\sin\theta\sqrt{1-\left(\frac{1}{a}-1\right)^2(\sin\theta_d)^2}\end{array}\right] \quad (6.1)$$

where θ_d is the angular location of the discharge port

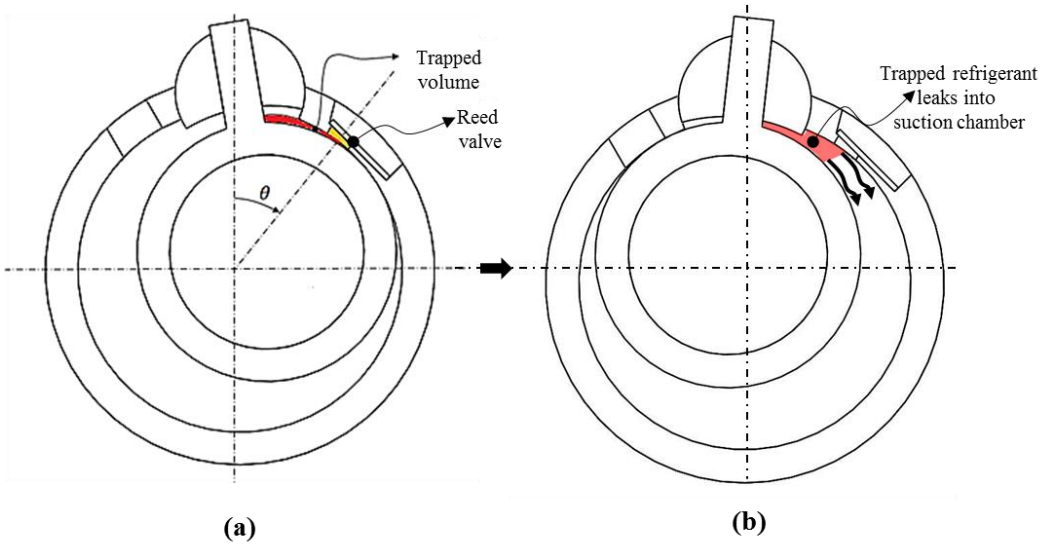

Figure 6.3 (a) Trapped gas volume in SVC (b) Leakage of trapped gas into the suction chamber

6.3 Simulation setup

Figure 6.4 compares the location of the discharge port of the SVC and FVC designs. It can be noted that the discharge port of the newly designed FVC is located on the fixed vane. By locating the discharge port on the fixed vane, the new FVC design eliminates discharge gas from being trapped towards the end of the compression process.

For the purpose of this study, a computer model based on MATLAB [127] programming language is used to solve the compressor mathematical models of the SVC and FVC derived in chapter 5. REFPROP [128] refrigerant database provides the necessary thermodynamic state properties of the working fluid. The program is initialised with initial conditions (i.e. suction and discharge pressure pressure, temperature etc.) and key compressor dimensions (i.e cylinder diameter, reed valve thickness, port dimensions etc.). The differential governing equations are solved using Runge-Kutta numerical integration technic and Newmark scheme for solving the reed valve displacement.

The centre line through the fixed vane defines 0^0, 360^0 and 720^0 degree positions of the shaft as shown in Figure 6.4(a). The simulation starts at 0^0 and progresses through two full revolutions. The first revolution corresponds to the suction process, while the second revolution corresponds to the compression and discharge processes. During the simulation, the thermodynamics model, refer to chapter 5, Figure 5.19 calculates the pressure and temperature variation in the suction and compression chamber. During the compression process (360^0 to 720^0), the program computes the pressure difference across the reed valve and activates the valve dynamics model should the compression chamber pressure exceed the discharge pressure. The simulation assumes that the trapped gas in the SVC is reintroduced into the suction chamber when the rolling piston sweeps past the discharge port.

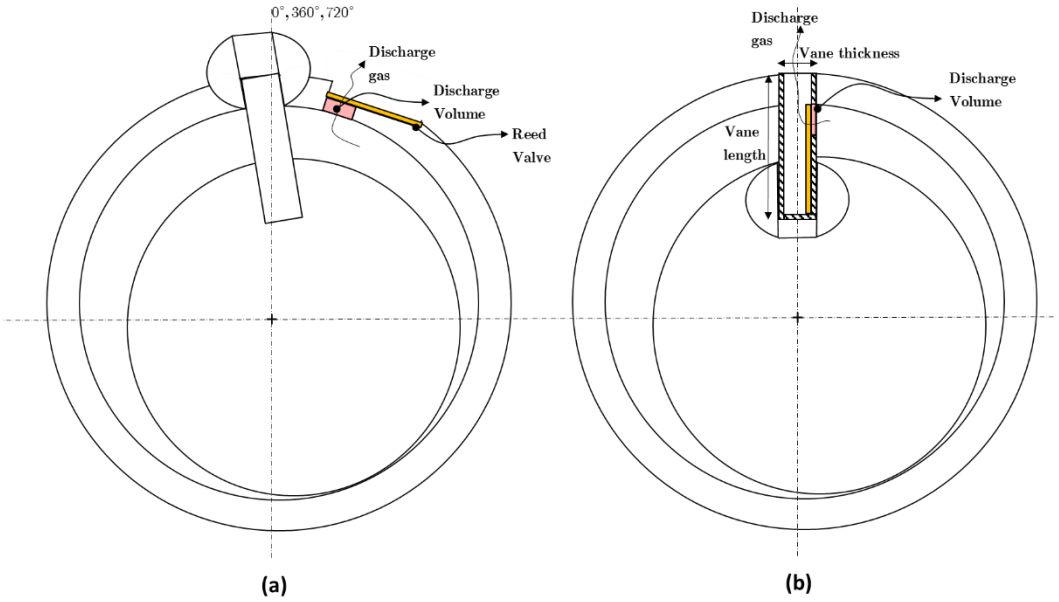

Figure 6.4 Compressor discharge location (a) Discharge port located on the cylinder, (b) Discharge port located on the fixed vane.

6.3.1 Step independence test

Numerical solutions are sensitive to step size, hence a step independence test is prudent to deduce the optimum number of steps that provides a compromise between accuracy and computation effort. The convergence of power required to operate the compressor can be used as a gauge for the step independence test. The initial simulation was executed with 500 steps for a complete cycle (consisting of two revolutions). Thereafter, the number of steps was increased by an increment of 500.

Figure 6.5 shows the convergence of input power with increasing step quantity. The percentage change in the input power attained by increasing the number of steps is superimposed for added clarity. The input power is used as the converging criteria because it is derived variable consisting of several basic parameters such as mass flow, enthalpy, speed etc. As observed in the figure, increasing the number of steps from 500 to 1000 results in a drastic reduction in percentage change. Thereafter, even a large increment in steps quantity yielded a marginal improvement in percentage change, suggesting the convergence of measured parameter. Increasing

the step number beyond 2000 resulted in a lengthy execution time. Hence, subsequent simulations in this chapter was performed with 2000 steps.

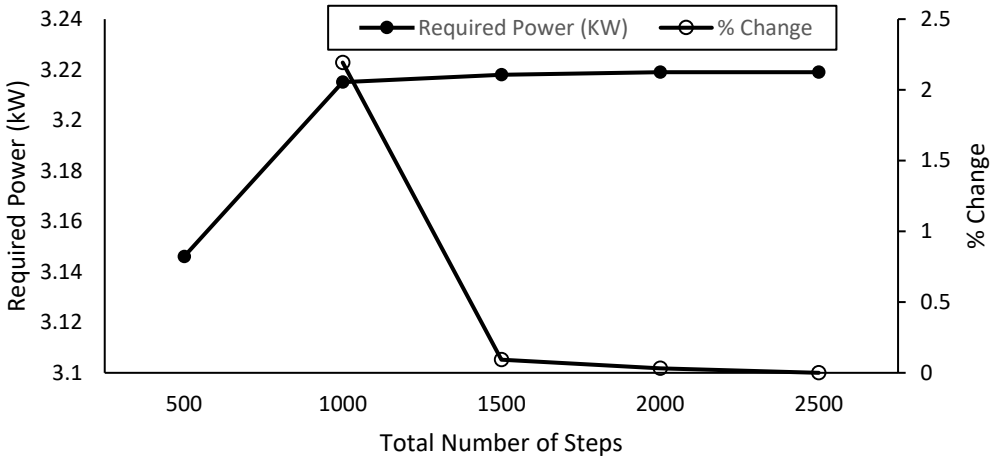

Figure 6.5 Step independence test

6.3.2 Compressor geometry and boundary conditions

The boundary conditions, refrigerant fluid and key compressor dimensions used for the simulation are listed in Table 6.1. Note the volume of the discharge port is identical for both the SVC and the FVC compressor to facilitate a fair comparison. The flow resistance, C_d at the suction and discharge ports is arbitrarily fixed at 0.95 [129]. In addition all leakage effects in the compressor will be excluded in the analysis to surface the benefits of discharging through the fixed vane.

6.4 Results and discussion

6.4.1 Working chamber volume

Figure 6.6 shows the variation in the chamber volume with respect to shaft rotation for SVC and FVC. For both compressor models, the non-zero volume at 0^0 location corresponds to the compressor clearance volume contributed by the mechanical clearance and tolerance, which is assumed to be a small fraction of the suction port volume [129].

Table 6.1 SVC and FVC geometry and boundary conditions

Boundary Conditions	
Suction temperature	251 K (1.4 bar)
Discharge temperature	355 K (19 bar)
Compressor Dimensions	
Capacity	30 cc
Refrigerant	R134a
Operating speed	3000 rpm
Cylinder inner diameter	200 mm
Cylinder height	100 mm
Piston diameter	150 mm
Eccentricity radius	25 mm
Vane height	100 mm
Vane thickness	10 mm
Vane length	25 mm
Suction Port Dimensions and Parameters	
Port diameter	8 mm
Port length	10 mm
Port location (θ_s)	15^0
Discharge coefficient (C_d)	0.95
Discharge Port Dimensions and Parameters	
Port diameter	3.2 mm
Port length	3.1 mm
Port location (θ_d)	345^0
Discharge coefficient (C_d)	0.95

The working chamber volume begins to rise when the piston sweeps past the suction port in the first revolution and peaks at 360°, resulting in the suction of the working fluid. During the second revolution, the working chamber volume progressively decreases, resulting in the compression of the working fluid. The chamber volume at the end of compression process corresponds to the compressor's trapped volume.

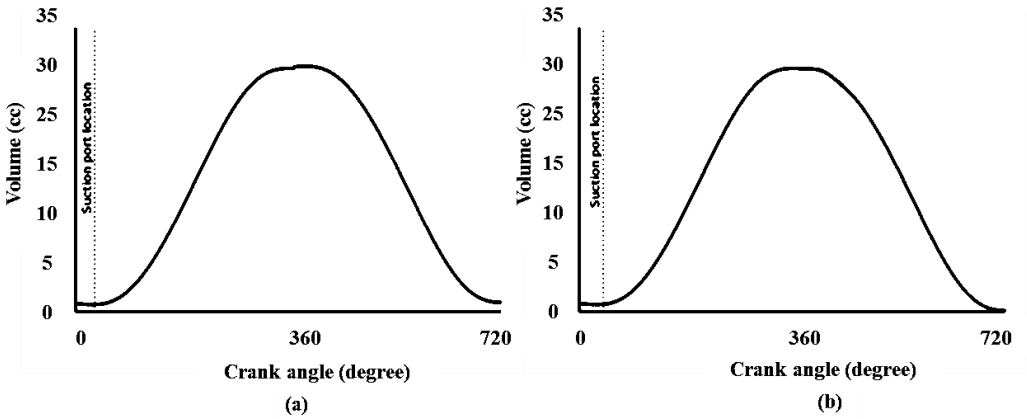

Figure 6.6 Chamber volume as function of crank angle for (a) SVC and (b) FVC

Based on the plot the SVC has a comparatively higher trapped volume as compared FVC due to the location of the discharge port. The FVC has negligible trapped volume as the piston naturally forces all the compressed gas through the discharge port located on the vane side face. The minuscule non-zero chamber volume at the end of the compression process in the case of FVC corresponds to the discharge port volume as identified in Figure 6.7.

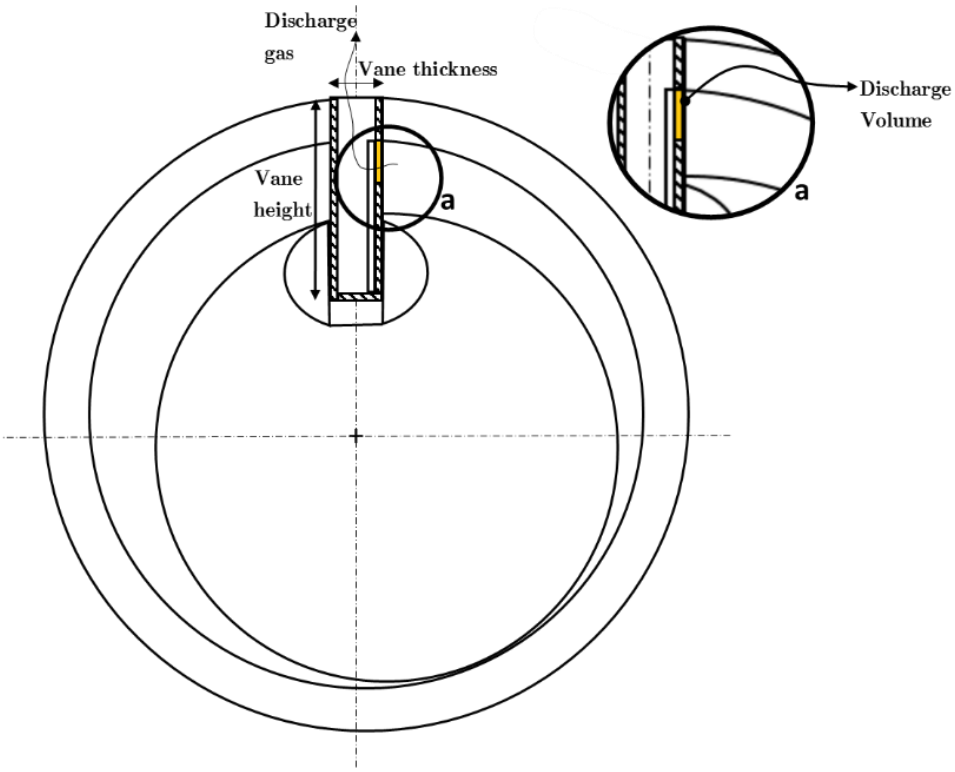

Figure 6.7 Discharge volume in FVC

6.4.2 Reduction in compressor capacity

Figure 6.8 shows the normalised plot depicting the variation in chamber mass in the simulated SVC for two cases: with and without re-expansion losses. For the case without re-expansion loss, the suction process begins at 15^0 and completes at 375^0, during which the refrigerant quantity gradually increase from zero to the maximum compressor capacity. The compression process occurs between 375^0 to approximately 680^0, during which the refrigerant is progressively compressed to discharge pressure. Once the compression chamber pressure exceeds the discharge pressure, the reed valve covering the discharge port opens and releases the compressed refrigerant. However at the end of the discharge process, a fraction of the refrigerant is trapped inside the compressor volume confined by the vane, cylinder, rolling piston and the reed valve (see Figure 6.3(a)). In the simulated case, nearly 26% of the mass drawn into the SVC has been trapped at the end of compression process (mass at 720^0).

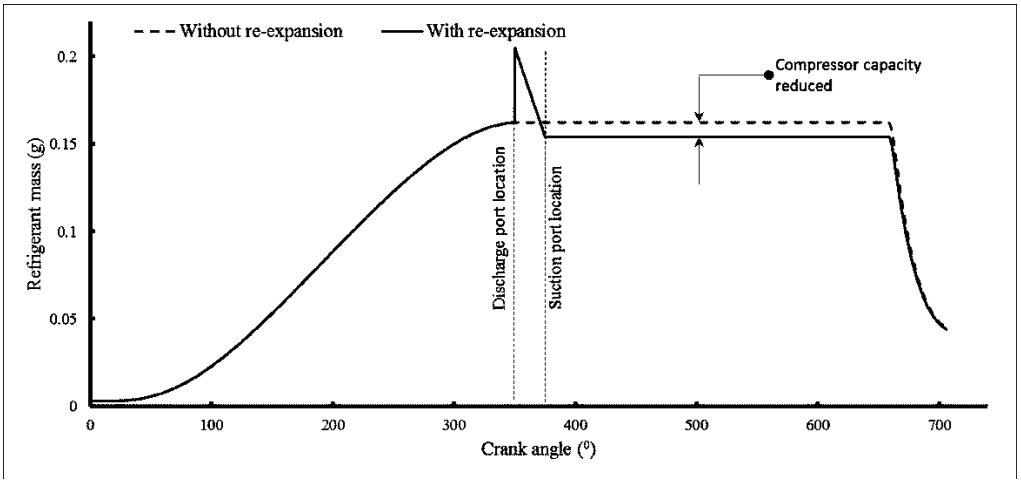

Figure 6.8 Normalised variation of chamber mass with shaft angle

The suction process considering re-expansion loss is similar to the previous case. However, in this case, when the piston sweeps past the discharge port, the trapped mass from the previous cycle leaks into the suction chamber. This explains the sharp spike observed in the chamber mass variation at the discharge port location.. The direct injection of the trapped refrigerant into the suction chamber immediately displaces the gas drawn in during the suction stroke, which results in the expulsion

of the suction gas through the suction port. This displacement of the suction gas continues until the piston rotates past the suction port.

As observed in Figure 6.8, the net effect of the re-expansion of the trapped gas in the suction chamber results in the reduction in compressor capacity. This reduction in compressor capacity occurs through three mechanisms. The first mechanism is due to the released trapped gas occupying a finite volume in the suction chamber, thereby displacing the gas drawn in during the suction stroke. The second mechanism is initiated by the high enthalpy content of the trapped refrigerant. When the trapped refrigerant mixes with the suction gas, the mixture temperature rises (Figure 6.9 (a)) abruptly and hence the density decreases. Since the mixing process occurs at isobaric condition and the cylinder volume remains fixed during the process, the decrease in mixture density will result in the ejection of mass through the suction port. As observed in Figure 6.9 (b), the expulsion of the suction gas results in decreasing the refrigerant pressure shortly after the mixing process. The third mechanism is the direct reduction in compressor capacity, as the trapped refrigerant remains undelivered by the compressor. Additionally, from energy point of view, the re-compression and re-expansion of the trapped mass in the discharge port results in wasted energy.

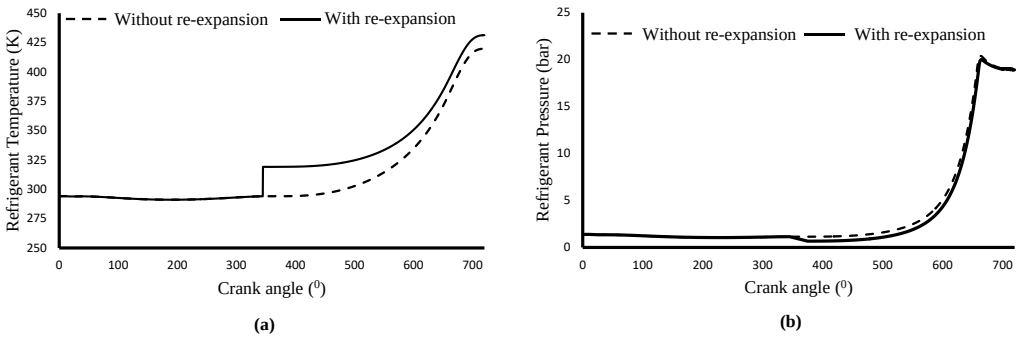

Figure 6.9 (a) Temperature and (b) Pressure variation of refrigerant with shaft angle

However, the FVC design with the discharge port located on the vane will not experience an appreciable re-expansion loss as the rolling piston naturally forces all the compressed gas through the discharge port towards the end of compression process.

6.4.3 Reduction in volumetric efficiency

Figure 6.10 depicts the refrigerant mass variation as function of shaft angle in a SVC. Recall that the suction port is located at 15^0 while the discharge port is located at 345^0. The suction chamber attains the maximum capacity when the piston revisits the suction port at 375^0. Meanwhile, the mass trapped in the discharge slot leaks into the suction chamber when the piston sweeps past the discharge port at 345^0. With reference to the plot, for the case without re-expansion, suction chamber drew in 0.154grams of mass of which 0.040grams was trapped at the completion of discharge process. An ideal SVC would have discharged the entire 0.154grams of the refrigerant.

In the case with re-expansion loss, the step change in mass at 345^o corresponds to leakage of trapped mass into the suction chamber (0.040grams was released). The introduction of trapped mass resulted in heating and displacing the suction mass, thereby decreasing the capacity of the suction chamber to 0.149grams. Based on these figures, it is possible to calculate that the compressor volumetric efficiency of the SVC is 73.8% and 82.4% with and without re-expansion losses respectively. In addition, the compressor capacity has be decreased by 3.2% due to the re-expansion losses. It appears that the volumetric efficiency of the compressor has increased due to the re-expansion of trapped gases. However, this is misleading because the quantity of the incoming mass is reduced, which the base for calculating the volumetric efficiency.

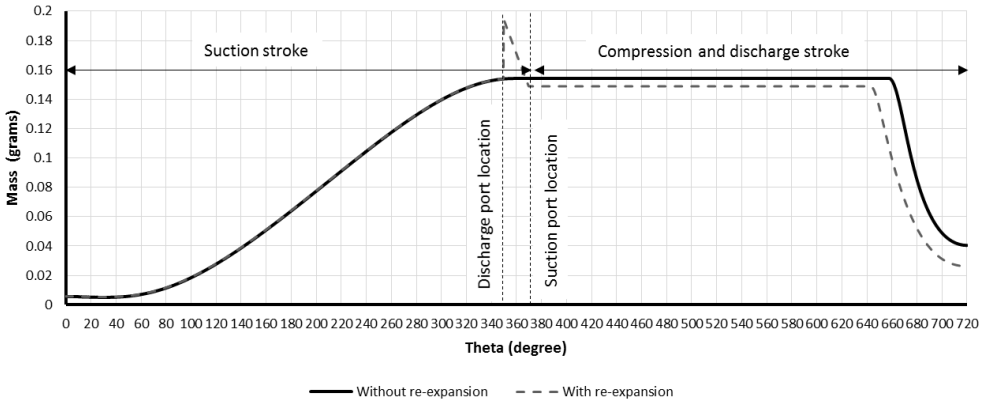

Figure 6.10 Variation of mass as a function of crank angle in a SVC. With and without re-expansion of leakage gas trapped in discharge slot.

Figure 6.11 provides a similar plot for the newly designed FVC. In the case without re-expansion, the FVC drew in 0.154 grams of refrigerant into the suction chamber and traps a meniscal mass at the end of the compression process (due to minuscule discharge port volume). Therefore, the proposed FVC design with the discharge port located on the vane side is an effective solution for minimising re-expansion losses.

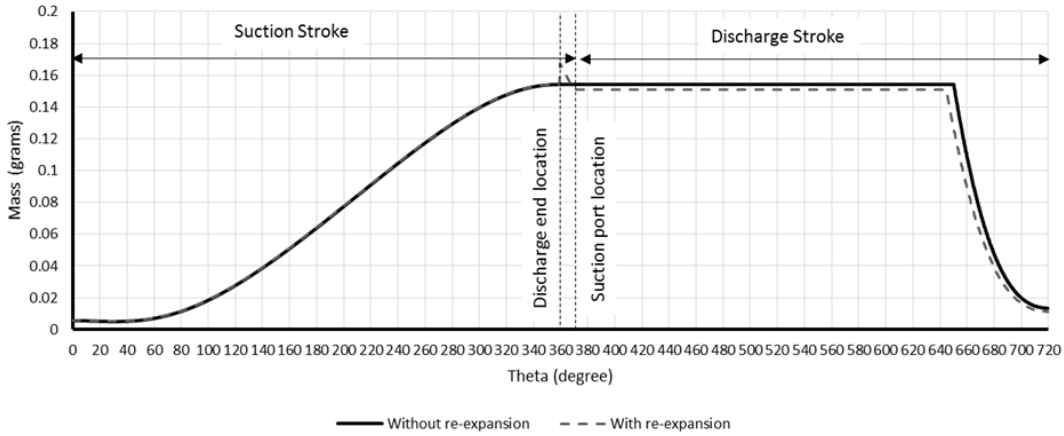

Figure 6.11 Variation of mass as a function of crank angle in a FVC. With and without re-expansion of leakage gas trapped in discharge slot.

For both SVC and FVC, it appears that the volumetric efficiency of the compressor has increased due to the re-expansion of trapped gases. However, this is misleading because the quantity of the incoming mass is reduced, which the base for calculating the volumetric efficiency.

6.4.4 Input power of FVC and SVC

The power required to operate a given compressor can be calculated by evaluating the area enclosed by the pressure-volume plot. Accounting for re-expansion losses, Figure 6.12 shows the P-V diagram for FVC and SVC compressor models. Based on the larger footprint of SVC over FVC, one can deduce that FVC operates with lower power requirements.

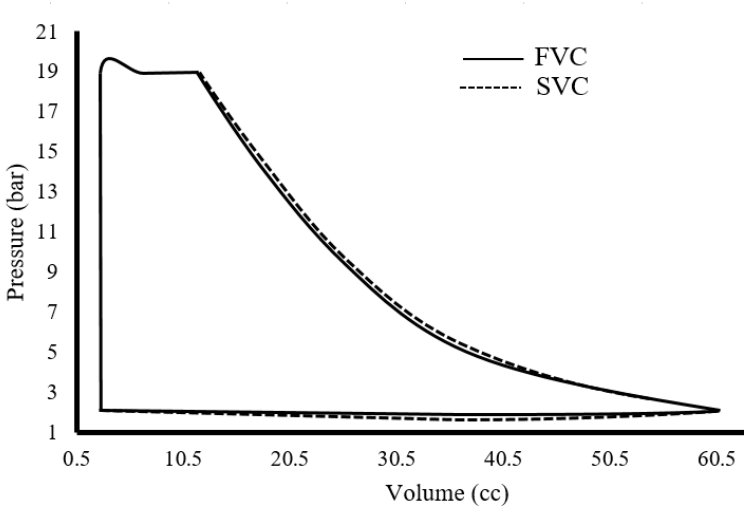

Figure 6.12 P-V diagram of the SVC and FVC with re-expansion losses

Table 6.2 provides a quantitative comparison on the power requirements to operate the FVC and SVC with and without accounting for the re-expansion losses. Based on the complied results, it can be noted that SVC has a smaller power requirements in comparison to the FVC with re-expansion losses ignored. This observation is due the fact that work is not performed on the quantity of trapped mass in the SVC towards the end of the discharge process. However, accounting for re-expansion losses, it has been established that the newly designed FVC decreases the power requirements by 6.4 %.

Table 6.2 Power requirements of SVC and FVC with and without re-expansion losses

Configuration		Power input (kW)	Practical compressor % savings
SVC	without re-expansion	2.2	N/A
	with re-expansion	3.5	6.4%
FVC	with re-expansion	3.3	

6.5 Sensitivity analysis

A sensitivity study was conducted on SVC model to evaluate influence of key design or operating variables on the quantity of trapped refrigerant gas. Variables such as the discharge pressure, entrapment volume, compressor-operating speed and the port discharge coefficient were selected for this study. The identified variables were varied in five intervals between the median of the range listed in

Table 6.3. Note that entrapment volume is expressed as the percentage of chamber volume.

Table 6.3 Variable identified for sensitivity analysis and their corresponding range

Variable	Upper	Lower	Median
Discharge port volume	3.0%	1.0%	2.0%
Discharge pressure	25bar	13bar	19bar
Operating speed	4000RPM	1800RPM	2900RPM
Discharge coefficient	0.90	0.75	0.825

Figure 6.13 shows the normalised refrigerant mass variation plot for each the variable. As expected, the entrapment volume has a significant impact in the quantity of trapped mass. A mere 2% increase in the entrapment volume resulted in 30% increase in the trapped mass quantity. The compressor discharge pressure was also found to have a significant impact on the quantity of the trapped mass. During the study, the discharge pressure was increased from 13 bar to 25 bar in five equal increments, which produced a 19% increase in the quantity of trapped mass. Since the discharge pressure has direct consequence of the density of the trapped refrigerant, a higher discharge pressure will certainly result in packing more mass for a given discharge port volume. Both the RPM and discharge coefficient found have a negligible impact in the quantity of trapped mass.

6.6 Concluding remarks

The paper analysed the implications of the re-expansion losses in a SVC. At the end of the compression process, a significant amount of gaseous refrigerant is trapped in the volume confined by the cylinder, vane, reed valve and the piston, which eventually expands and mixes into the suction chamber. The subsequent consequences of this mixing process was analysed using mathematical models.

The simulation identified the mixing of trapped gas with the suction gas is equivalent to heat addition to the suction gas, which is known-to negatively affect both the compressor capacity and efficiency. While the reduction in efficiency can be attributed to the wastage of energy in compressing the trapped gas over and over

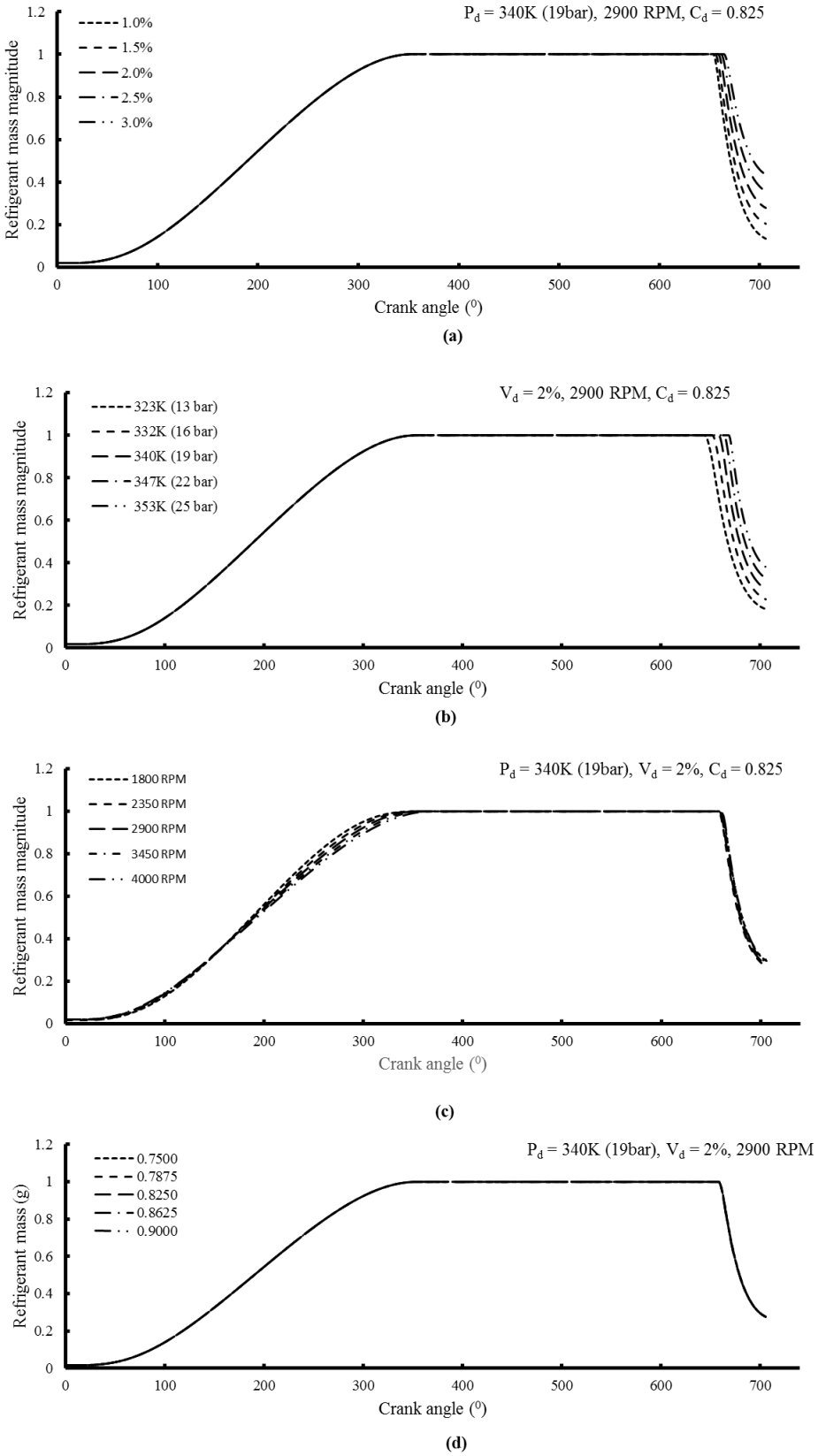

Figure 6.13 Effect of (a) discharge port volume, (b) discharge pressure,(c) operating speed and (d) discharge coefficient on quantity of trapped mass

again. In a simulated SVC, a 3.2% drop in compressor capacity was observed due to the mixing of trapped discharge gas with the suction gas. The proposed FVC design with the discharge port located on the fixed vane is shown to operate with an efficiency 6% higher than the SVC as re-expansion losses are greatly reduced.

A parametric study was conducted to identify critical design variables contributing to quantity of trapped mass. The study identified that the quantity of trapped mass is most sensitive to the entrapment volume and discharge pressure. A 2% rise in the entrapment volume results in 30% increase in the quantity of trapped mass. Meanwhile a 12 bar increase in the discharge pressure results in 19% increase in the quantity of trapped mass.

Chapter 7

Experimental Study and Validation

A prototype of the fixed vane compressor (Figure 7.1) was manufactured to conduct experimental analysis and to validate the accuracy of the aforementioned mathematical models. This chapters starts by presenting the experimental test jig and key preparation activities prior to experimental analysis. Following that, experimental procedure is discussed and the experimental data is compared with the model predictions. The dry weight of the compressor module is measured to be 6.4kg.

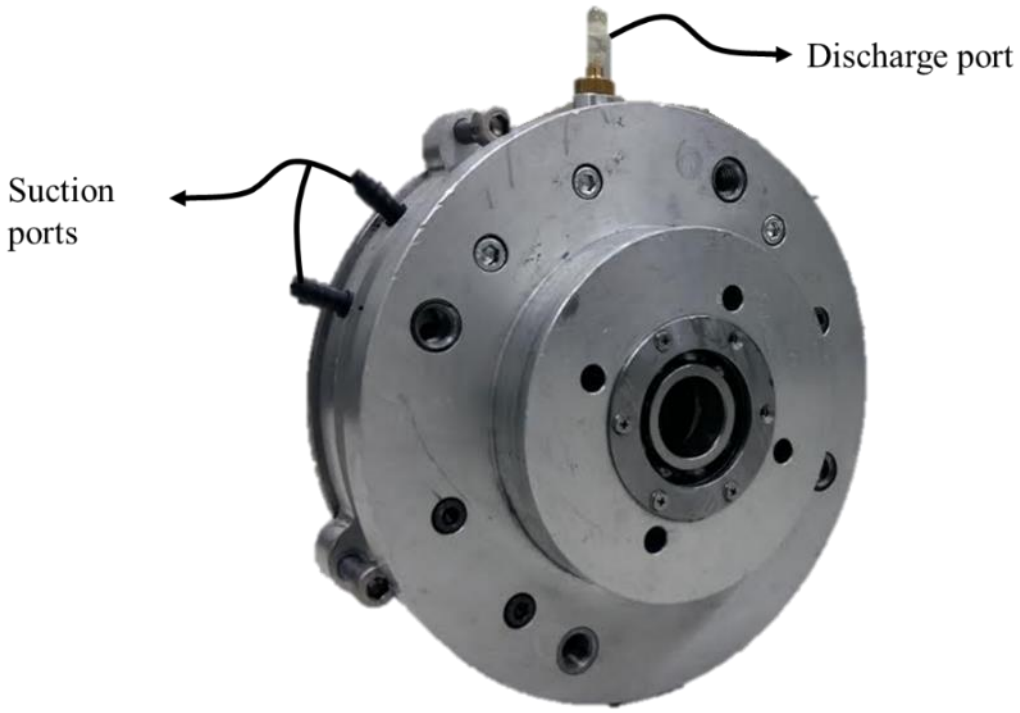

Figure 7.1 Fixed vane compressor module

7.1 Prototype assembly procedure

The assembly procedure of the newly designed FVC is shown in Figure 7.2. The vane has to be assembled prior assembling the rest of the prototype. The vane assembly consists of the vane right half **'1',** vane left half **'2'** and the valve **'3'**. The valve **'3'** head is oriented over the discharge port located on the vane side face and sandwiched between the **'1'** and **'2'** using countersunk machine screws.

The in-plane counterweight **'9'** is inserted into the compressor drive **'5'** to complete the compressor drive sub-assembly. Following that, the compressor drive sub-assembly and the vane bushing **'7'** is inserted into the rolling piston **'6'**. This assembly is then placed over the cylinder **'4'** along with the vane assembly. The front cover **'8'** is placed over the cylinder **'4'** to complete the assembly procedure.

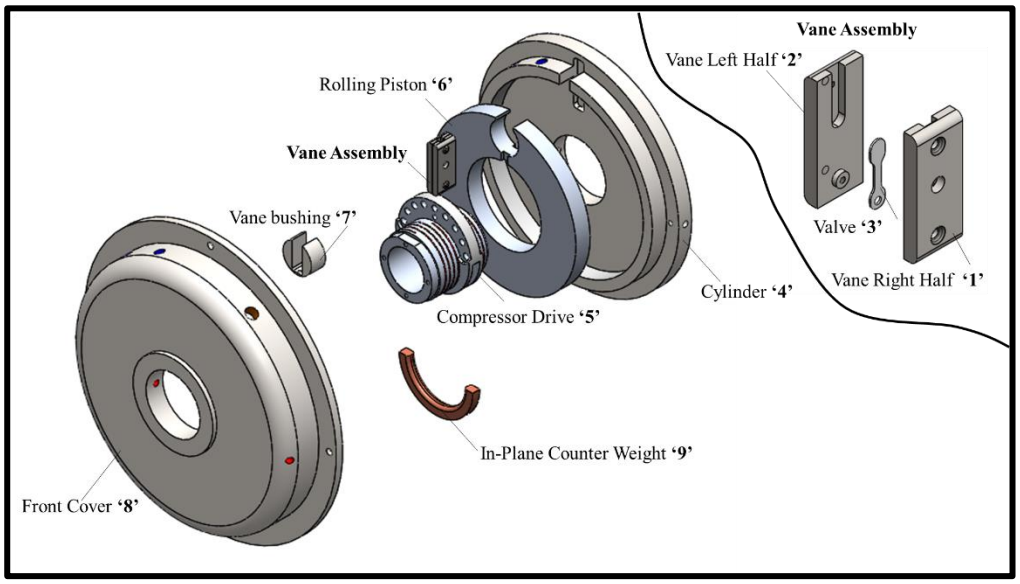

Figure 7.2 Prototype assembly procedure

7.2 Experimental test jig

The experiments are designed to assess the performance of the prototype compressor, specifically the power consumption and refrigerant flow rate. For simplicity, air is used as the working fluid. The schematic diagram of the main experimental setup is shown in Figure 7.3. The compressor is coupled to the 4kW induction motor through a flexible shaft coupling *(refer to appendix C for motor specifications)*. The motor is controlled using a frequency-based speed controlling inverter. The quantities such as pressure, flowrate and temperature are measured using analog instruments.

All moving and mating parts such as the vane bushing, journal bearing, piston side faces were coated with Teflon based lubricant prior to the experiment. In addition, the compressor was feed with a compressor oil with a viscosity grade of 100 (ISO). The flow rate is measured using gas flow meter, while the compressor RPM is measured using contactless tachometer shown in Figure 7.4. The connection to the constant pressure source is shown in Figure 7.6. The compressor external temperature is captured using a thermal imaging camera. The accuracies of measuring devices are listed in Table 7.1.

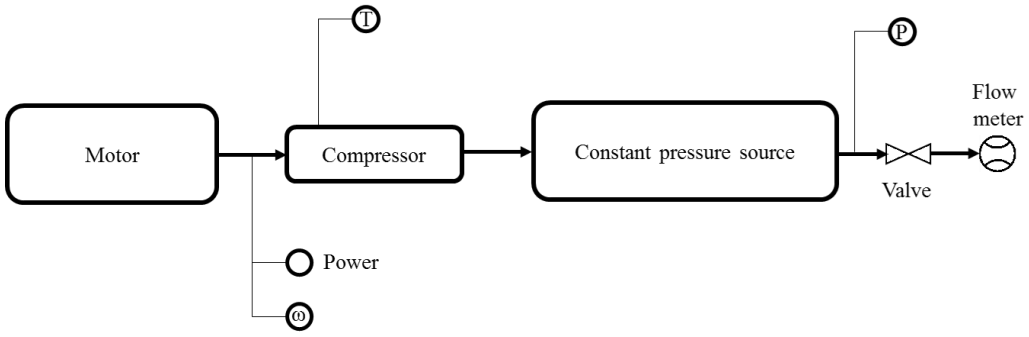

Figure 7.3 A schematic diagram of the experimental setup

Figure 7.4 Contactless tachometer for measuring compressor shaft speed

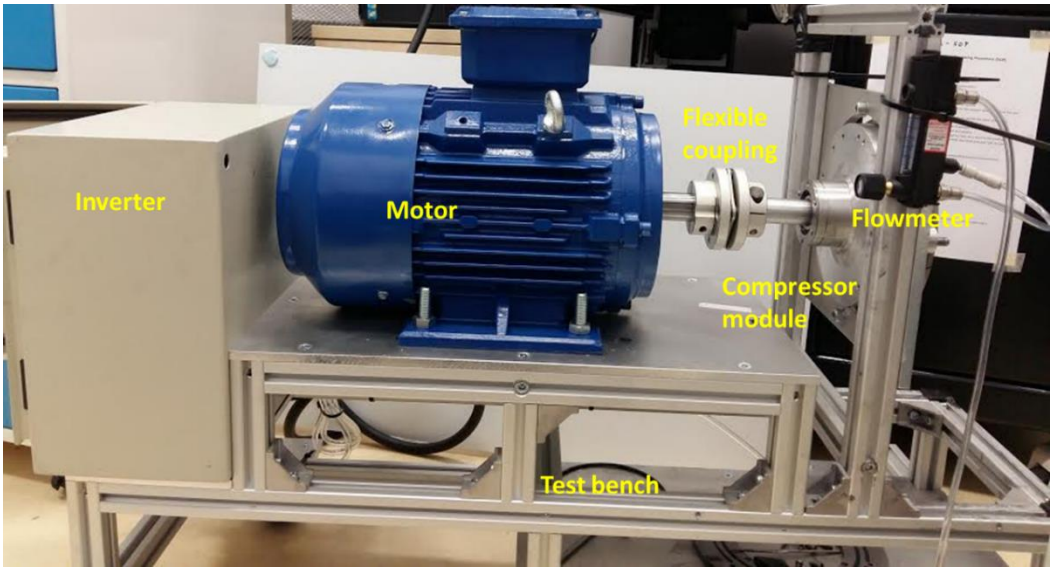

Figure 7.5 The experimental setup

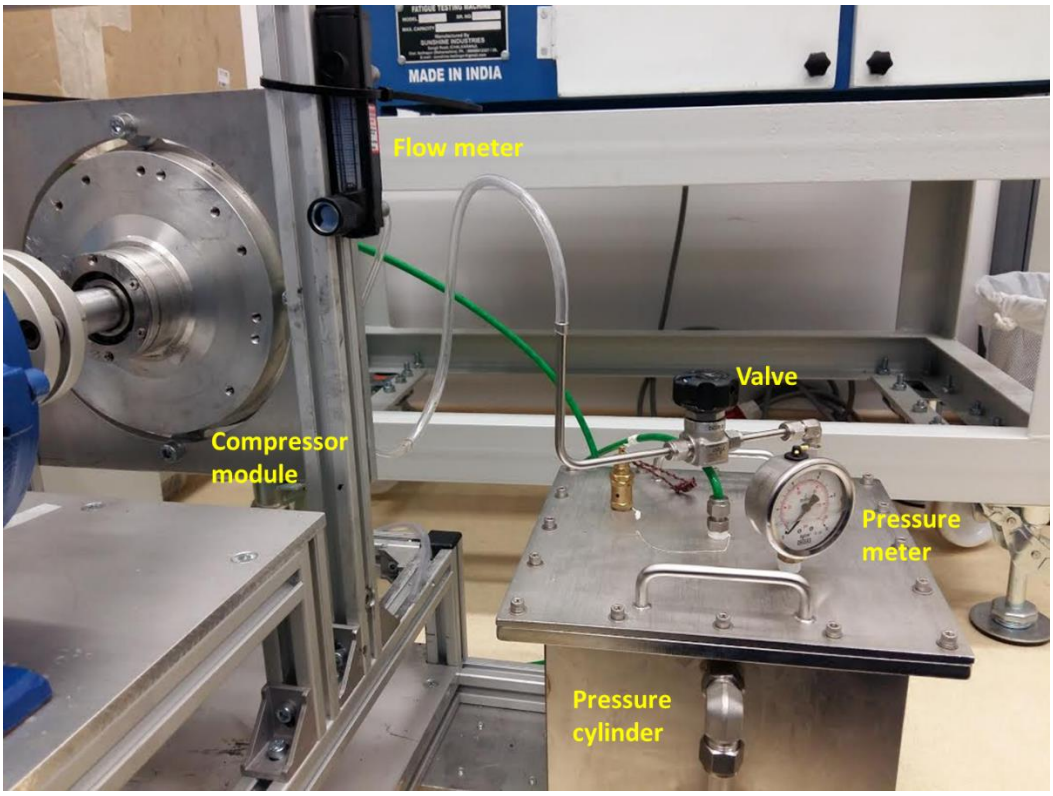

Figure 7.6 Pressure tank setup

Table 7.1 Measuring device accuracy

Instrument	Accuracy
Power	±0.2W
Gas flow meter	±4% of reading
Contactless tachometer	±0.05% of reading
Thermal imaging camera	± 2^0C
Pressure meter	±1.6% Full Scale Deflection

The compressor shaft speed is regulated using a three-phase inverter shown in Figure 7.7. The inverter varies the voltage and current to produce the desired synchronous speed. However, due to the slip, the shaft speed will be lower than the selected synchronous speed. Therefore, output from the tachometer is used measure the actual shaft speed.

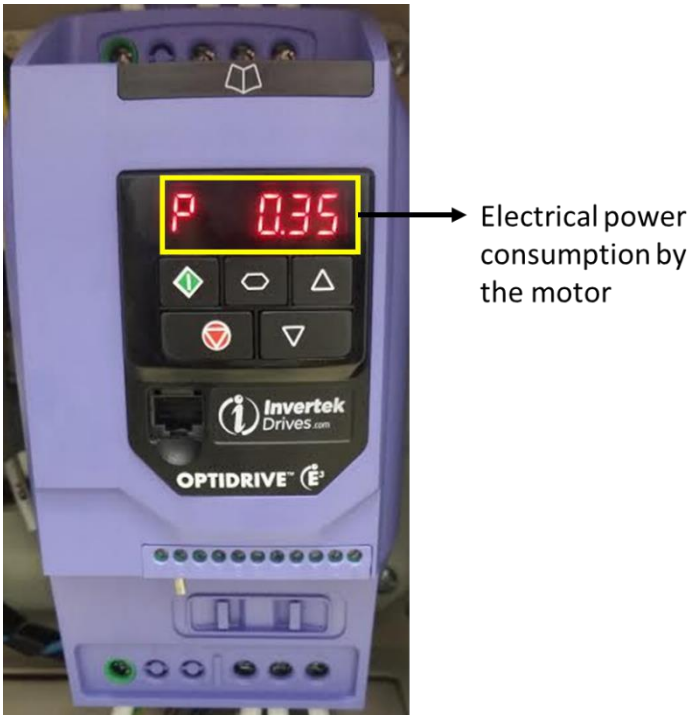

Figure 7.7 AC variable speed drive for regulating the compressor speed

The electrical power input to the motor, $\dot{W}_e$ is displayed in the inverter as shown in Figure 7.7. The mechanical power input to the compressor, $\dot{W}_m$ can be obtained from Eq. (7.1). The power factor, *pf* and the motor efficiency, η is obtained from the motor catalogue (reproduced in Figure 7.8). Following that, the mechanical torque, T_m supplied to the compressor can be obtained from Eq. (7.2). The angular velocity of the shaft, ω is read from the contactless tachometer.

$$\dot{W}_m = \dot{W}_e \cdot pf \cdot \eta \tag{7.1}$$

$$T_m = \dot{W}_m / \omega \tag{7.2}$$

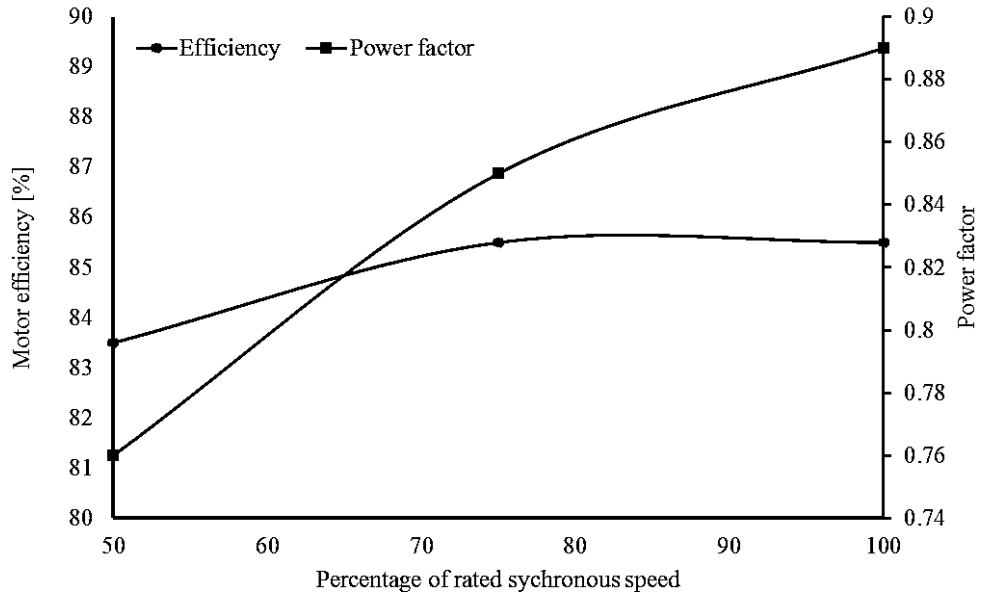

Figure 7.8 Motor efficiency and power factor curves

7.3 Experimental procedure

Parameters such as the mechanical power input to the compressor, the shaft speed, discharge pressure, discharge temperature and the volumetric flow rate of air are measured during the experiment. All data points are collected during steady state operation. The compressor was tested to the maximum limit of the variable speed drive, which is 50Hz in this case. The general experimental procedures adopted throughout the study are as follows:

i. The compressor is started from rest and the speed is gradually increased to 900rpm at a constant rate of acceleration. Thereafter, the compressor is operated at this speed for a period of five minutes to warm up the compressor.

ii. The compressor is then ramped up to the desired test speed at a constant rate of acceleration. Upon attaining the desired speed, the operating conditions are maintained for a period of five minutes to stabilized the RPM, pressure and flow rates. The steady-state condition is verified by observing small

fluctuations of the measured readings. Thereafter necessary readings are obtained from the appropriate instruments.

iii. Once the measurements at a desired test speed is recorded, the compressor is throttled back to 900 rpm for a brief period. Following that, the compressor speed is once again ramped up to the desired test speed and the measurements are re-recorded. This process is repeated for three times to obtain an average value of the measurement and the standard deviation.

iv. The discharge pressure for a give test RPM is controlled by regulating the the valve shown in Figure 7.6. Higher discharge pressure at a given RPM is thus obtained by restricting the flow through the valve.

v. Once the necessary data is collected, the compressor is powered down to 900 rpm and a fresh supply of lubricant is feed. Following that, the discharge pressure is released by turning the flow regulator valve to fully open positon. The VSD is then disconnected from the power supply once the pressure meter registers zero gauge pressure.

7.4 Preliminary tests

With the experimental test bed and measuring instruments set up, few preliminary tests were conducted on the prototype FVC to evaluate the overall compressor build quality. The results obtained from the preliminary tests are discussed in the following sections.

7.4.1 Dimension inspection

The build quality of the compressor is largely dependent on the dimensional accuracy of the compressor components. The dimensional tolerance of the fabricated components plays a large part in determining the success of the entire compressor assembly. For example, the compressor drive shaft has to be smaller

than the bearing inner race diameter to facilitate the assembly process and the spacing between these mating components dictate the bearing clearance.

The fabricated compressor components received from the workshop was cleaned thoroughly using alcohol to remove all traces of coolant, oil and dirt particles. Following that, the critical dimensions of the compressor components was measured using the Coordinate Measuring Machine (see Figure 7.9), digital micrometre and Vernier. The dimensions were recorded at room temperature and multiple measurements were made using micrometre and Vernier to minimize human error. The crucial dimensions measured from these instruments are listed in Table 7.2.

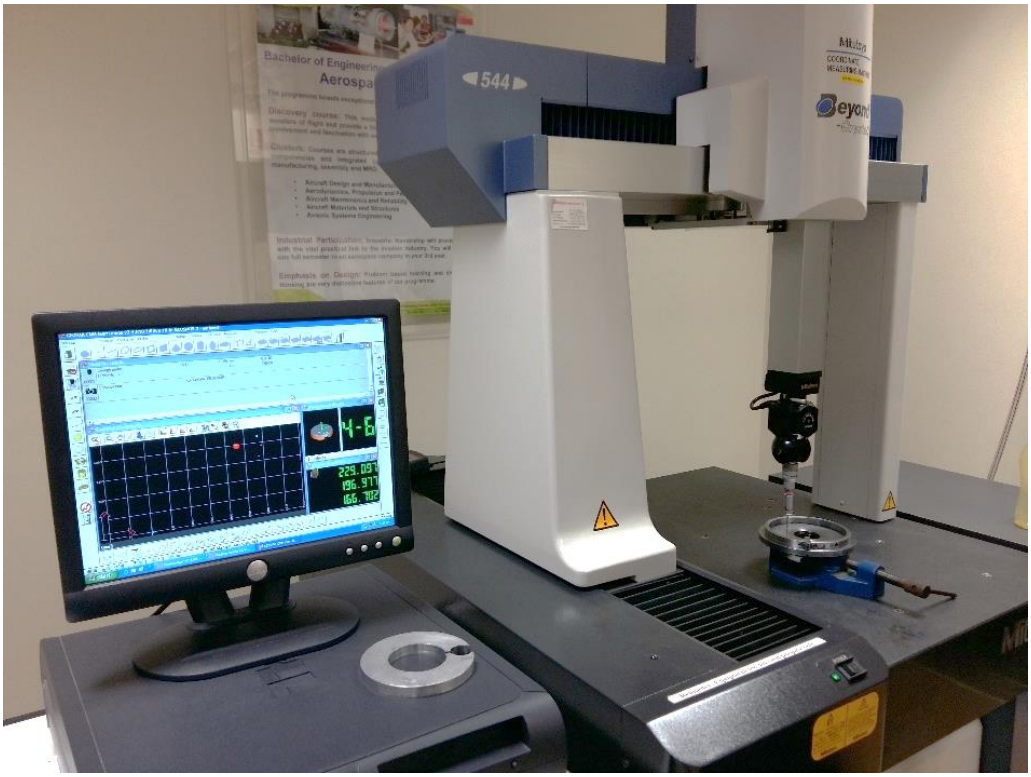

Figure 7.9 Coordinate measuring machine used to inspect compressor build quality

Table 7.2 Designed and measured dimensions of the prototype compressor

Component	Designed value	Measured value	Error (%)
Cylinder inner dia.	122	122.05	0.04
Cylinder height	11	10.97	-0.27
Cylinder-drive shaft dia.	42	42.11	0.26
Vane bushing dia.	22	21.59	-1.86
Vane bushing thickness	11	10.75	-2.27
Piston dia.	111	110.05	-0.86
Piston-eccentric dia.	57	56.58	-0.74
Piston height	11	11.19	1.73
Vane length	33.5	33.42	-0.24
Vane thickness	14	13.93	-0.50
Vane width	8	7.82	-2.25

In general, the fabrication accuracy of the compressor would have been acceptable if it isn't for the large deviation between the piston intendent diameter and the actual measurement. This deviation is expected to cause a large radial clearance between the piston and the cylinder wall, potentially contributing to radial leakage as it creates a narrow passage between the suction and compression chamber (item one in Table 4.8). Therefore, a new piston was manufactured to replace the poorly manufactured piston as shown in Figure 7.10.

Figure 7.10 Defective piston is replaced with a new piston to ensure the required tolerance are met.

7.4.2 Dynamic balance of the compressor driveshaft

It is of at most importance to ensure the dynamic balance of the compressor driveshaft assembly to prevent unnecessary centrifugal forces from acting on the journal bearing. Unwanted centrifugal loads deteriorate the bearing performance and may contribute to a complete compressor failure due to excessive vibration.
During design phase, the Centre of Gravity (CG) of the compressor driveshaft is shifted to coincide with the centre of the rotating axis using in-plane counter weight. However, during manufacturing stage, minute variations in material design, imperfection and tolerances could shift the CG from the desired location. Therefore, all rotating components have to be pre-inspected carefully prior to operation.

During the preliminary examination, the compressor driveshaft assembly was positioned over a flatbed. The assembly is then rotated to various angular positions and it is observed that it is able to remain in rest at any orientation.
Following the visual inspection, the compressor driveshaft balance was studied using an accelerometer mounted on top flange of the motor. The accelerometer measures the vibration amplitude of the structure (motor and compressor) in terms of unit *g*. The peek vibration amplitude measured within the expected operating speed range of the compressor is shown in the Figure 7.11. Note that a surface vibration of 1*g* corresponds to the scenario in which an object placed on top will start to lift off. The vibration test provided a quantitative confirmation that the compressor drive shaft is dynamically balanced and experiences a low vibration amplitude.

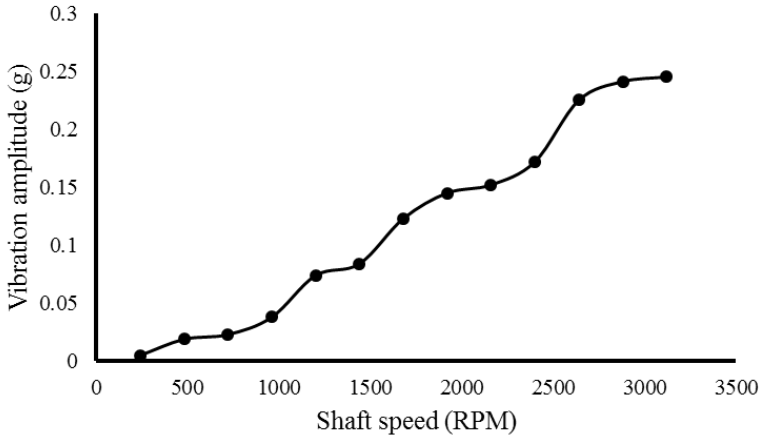

Figure 7.11 Vibration with respect to motor speed

7.4.3 Valve operation

The pressure-flow characteristics of the reed valve assembly is useful to study the leakage loss, pressure losses and to verify if it operates as intended. A reed valve can be modelled as a transistor operating either in forward or reverse region. The operation of the reed valve in reverse region represents the leakage flow from the discharge chamber to the cylinder. Meanwhile the operation of the valve in forward region represents the flow from the cylinder to the discharge chamber. An ideal reed valve will have infinite resistance to flow under reverse region and a zero resistance to flow in forward region.

A vane test bench was setup to access the leakage and pressure losses occurring the reed valve. The results presented here after will be limited to the maximum supply line pressure of 8 bars available in the laboratory. The schematic diagram of test jig is shown in Figure 7.12. The test jig comprises of two pairs of pressure and flow meters, with one pair placed in the flow outlet and another in the inlet. The difference in the pressure meter P_2 and P_1 represents the pressure loss across the vane assembly while the difference between the flow meters Q_2 and Q_1 represents the leakage loss in the vane assembly.

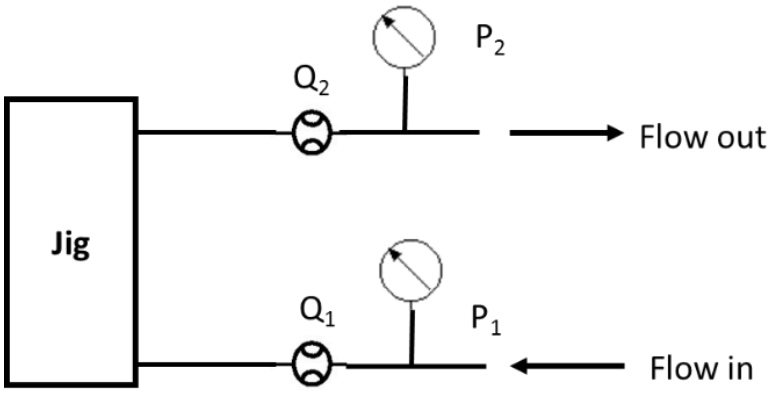

Figure 7.12 Vane test setup schematic diagram

The vane is sandwiched between walls of the test jig as shown in Figure 7.13(a). The mating surfaces between the jig and the vane is coated with adhesive sealants and grease to prevent leakage losses between the vane-jig matting surfaces as identified in Figure 7.13(b). The reverse region of the valve is characterised by the

connecting the pressure and flow meter to the flow inlet port while supplying compressed air through the flow outlet port and vice versa for characterising the forward region.

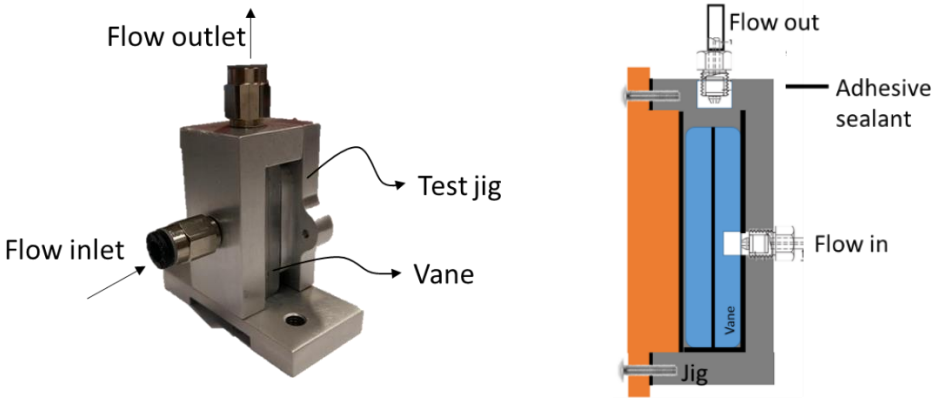

(a) Vane test jig assembly

(b) Adhesive sealants applied between the vane-jig mating surfaces.

Figure 7.13 (a) Vane test jig assembly, (b) Adhesive sealants prevent leakage between the mating surfaces

The pressure-flow characteristics of the reed valve in forward and reverse region is obtained from the vane test jig shown in Figure 7.14 and the experimental result is shown in Figure 7.15. Ideally, a steeper response in the forward region and a flatter response in reverse region is preferred. The reed valve operates as expected in the forward region, but appears to be suffering from leakage losses in reverse region. It can be noted that the reed valve leakage in reverse region is nearly constant till 0.6MPa and increases sharply beyond that (identified as breakdown pressure). This could be due to lack of sealant between the reed valve and the discharge port mating surface. The pressure loss across the vane assembly is shown in Figure 7.16. The pressure loss across the vane assembly is relatively constant up to 3LPM and increases sharply thereafter. However, for practical purpose, the pressure loss across the vane can be assumed to be constant as the discharge flow rate of the compressor is much smaller than the test range.

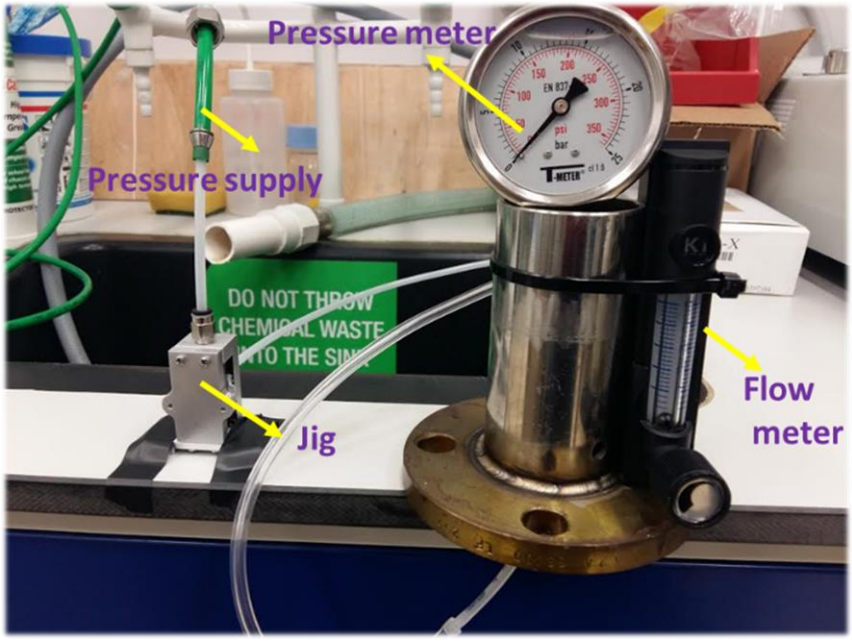

Figure 7.14 Valve test jig

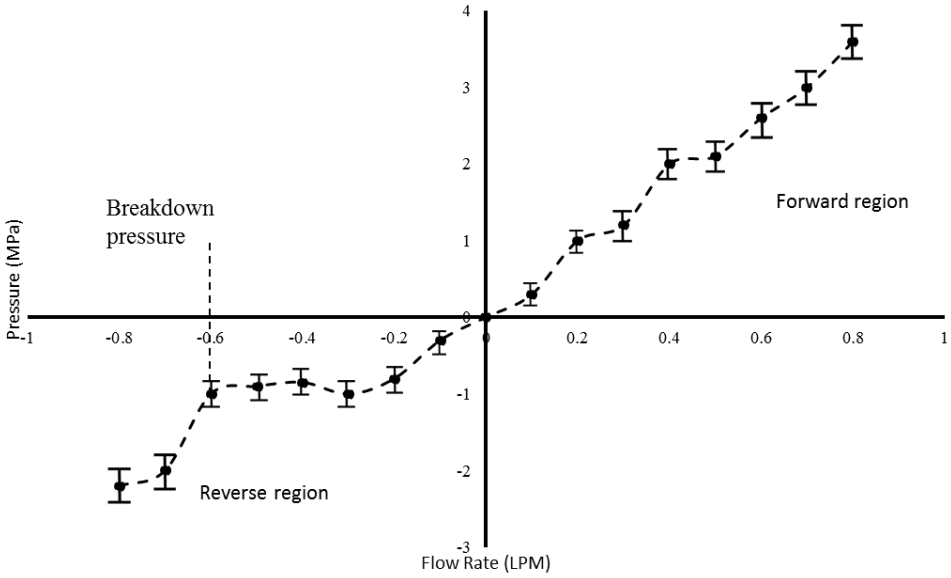

Figure 7.15 Pressure-flow characteristics of the reed valve

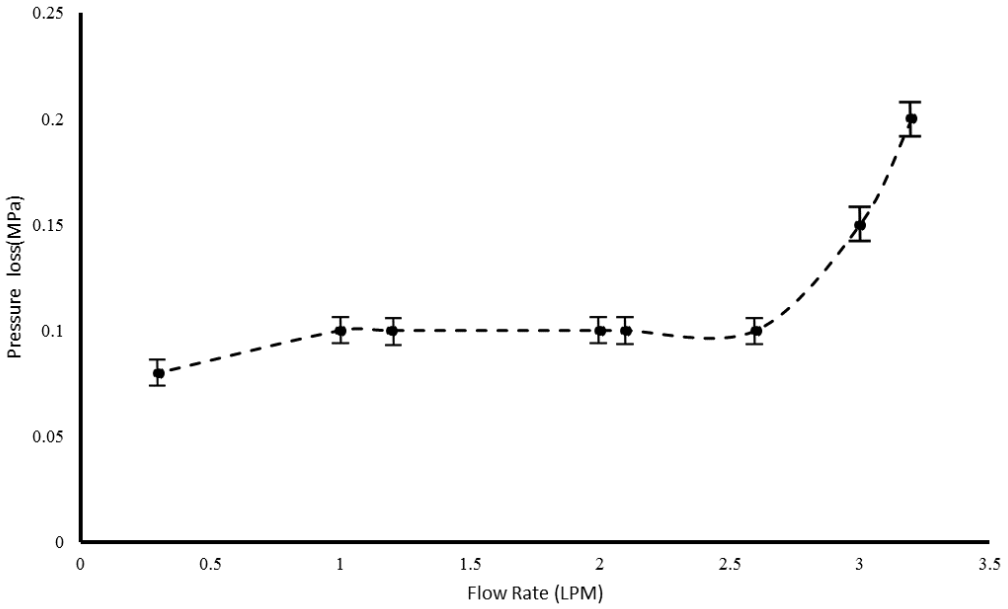

Figure 7.16 Vane pressure loss

7.5 Comparison of predicted and measured results

7.5.1 Mechanical power

The mechanical power requirements for operating the compressor at four discreet discharge pressures is shown in Figure 7.18. Note that the compressor discharge pressure has been limited to 3 bar as severe leakage was observed beyond this pressure. In general, the mechanical power consumption increases with the rotational speed and discharge pressure. The mechanical power supplied to the compressor consists of the compression power and various other mechanical power losses modelled in section 5.5. The predicted power consumption of the compressor largely depends on the operating speed and oil viscosity. The relationship between oil viscosity and temperature for various oil grades is shown in Figure 7.17. In general, the oil viscosity decreases exponential as the temperature increases.

Oil with ISO viscosity grade of 100 was used as the compressor oil. The expected operating speed range of the compressor is between 2250 to 3000 rpm. This range is divided into four equal groups with an interval of 250 rpm. Table 7.3 lists the measured temperature and the estimated lubricant viscosity at key compressor locations. Under steady state, temperature at these locations is assumed uniform

due to high thermal conductivity of metals. By using localised temperature and oil viscosity, the predicted mechanical power is in general within 10% of the measured mechanical power. However, there is a large discrepancy between the predicted and measured mechanical power at 3 bars. This is largely due to heavy leakage experienced within the compressor.

Table 7.3 Localised compressor temperature and lubricant viscosity

Speed (rpm)	Front journal bearing		Aft journal bearing		Cylinder wall	
	Temp. ^{0}C	Vis. 10^{-2} Pa-s	Temp. ^{0}C	Vis. 10^{-2} Pa-s	Temp. ^{0}C	Vis. 10^{-2} Pa-s
2250	89	4.1	83	4.8	68	7.6
2500	91	4.0	90	4.0	74	6.9
2750	94	3.7	94	3.7	89	4.1
3000	98	2.1	97	2.7	98	2.1

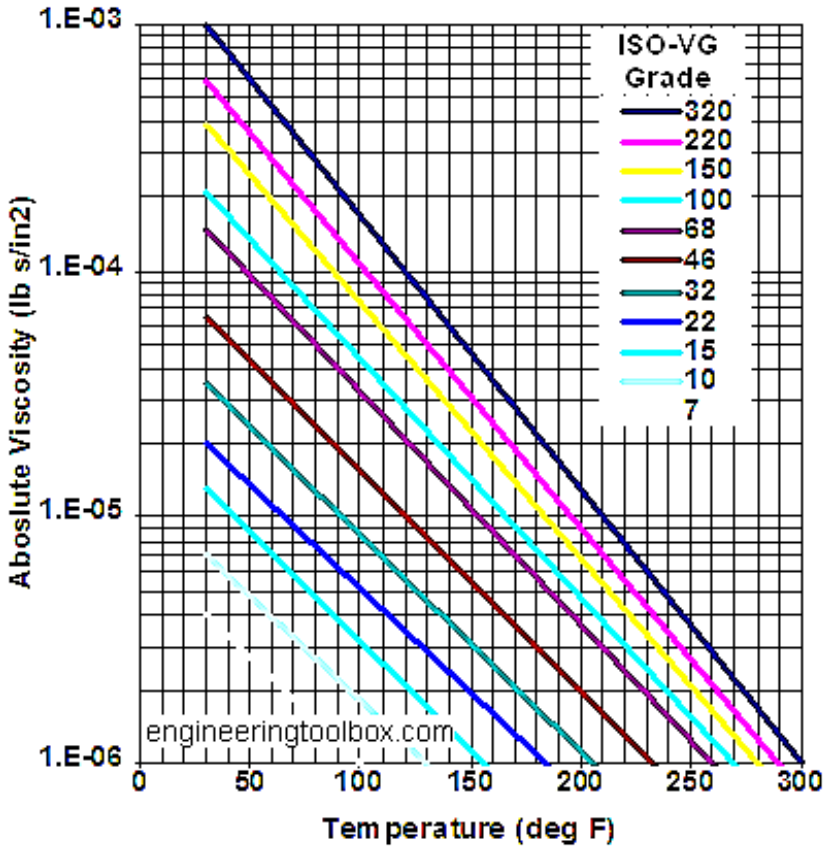

Figure 7.17 Viscosity-Temperature relationship of ISO grade lubricants

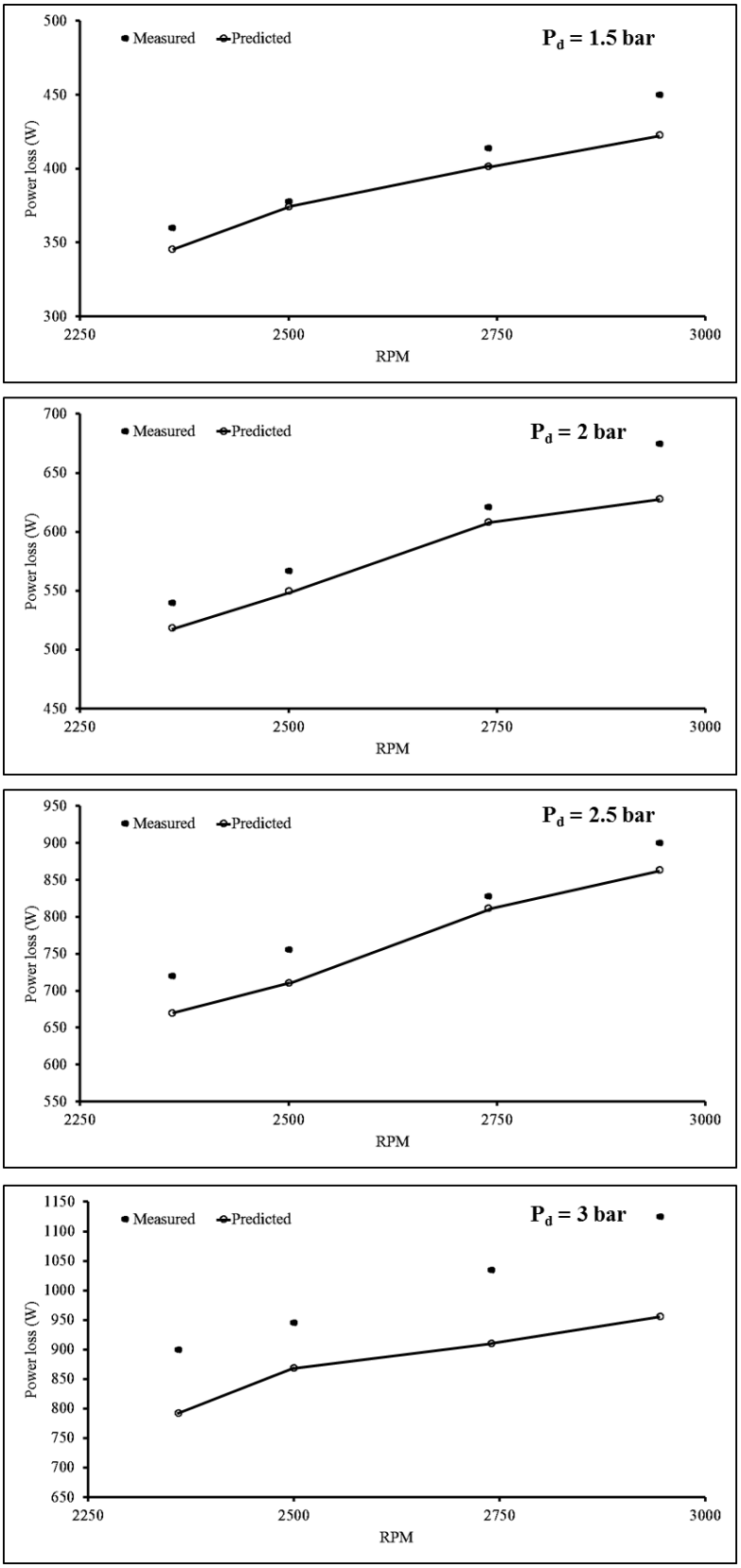

Figure 7.18 Measured and predicted compressor mechanical power [6]

[6] The uncertainty range has been excluded from the plot as the power measurement instrument has a high accuracy of ±0.2W.

7.5.2 Mass flow rate

The mass flow rate from the compressor is measured using a rotameter. Following precautions are observed to ensure the accuracy of the measurements:

1. Since the rotameter uses a ball float, all readings were read from the ball center.
2. The rotameter is mounted vertically to the jig in a manner such that the external and internal vibrations are minimized.
3. Special care was taken to insure that the inlet and outlet tube connections to the rotameter are kept straight to prevent unwanted flow restrictions.

The float in the rotameter is calibrated to the maximum design temperature and pressure. Hence, the measured flowrate has to be corrected to account for pressure and temperature measured from the experimental process. The corrected flow rate is given by Eq. (7.3). The resulting mass flowrate is then calculated using Eq. (7.4)
.

$$Q_{corrected} = Q_{reading}\left(\frac{P_{reading}}{P_{design}} \cdot \frac{T_{design}}{T_{reading}}\right) \tag{7.3}$$

$$\dot{m} = Q_{corrected}\frac{P_{reading}}{RT_{reading}} \tag{7.4}$$

Figure 7.19 shows the recorded mass flow rate of air with respect to rotational speed. In general, the discharge mass flow rate increases with higher discharge pressure and crankshaft speed. The observation conforms to expectation as increasing the discharge pressure results in higher discharge density while increasing the shaft speed results in higher displacement rate.

In general, there is a large disagreement between the predicted and measured mass flowrates, much of which can be attributed to leakage flow. This discrepancy is largest at lower rotational speed and higher discharge pressure. This is an expected outcome as leakage flow is largely is motivated by the pressure difference between the chambers. At higher discharge pressure of 3 bar, the leakage flow is observed to be excessive thereby resulting in a large deviation from the prediction.

The large discrepancy between the prediction and measurement is likely due to the lack of leakage flow model. The leakage flow is a complex phenomenon, therefore requires extensive number of models to capture its characteristics accurately. Apart from the obvious leakage from the high-pressure chamber to lower-pressure chamber, leakage flow may also occur in form of single-phase oil flow with dissolved gas or two-phase oil-gas mixture. The leakage flow is also sensitive to dimensional tolerance, surface finish, clearance, operating speed, pressure ratio and lubricant properties.

7.6 Post-experiment analysis

The prototype and the test-jig was disassembled after the experimental test runs lasting nearly a month. This section discusses the state of the prototype and test jig observed through visual inspection.

Upon disassembly of the compressor assembly, the lubricant was observed to remain within the confines of the compressor cylinder walls. This indicated the effectiveness of O-rings that seals the mating surfaces. Thereafter, the compressor was cleaned using alcohol. Figure 7.20 shows the state of the compressor cylinder, vane bushing and the piston after all removing all traces of oil. Visual inspection revealed number of circular scratch marks on the surface of cylinder and the piston faces. These marks are indicative of lack of lubrication between these mating surfaces, which may be the cause of severe leakage observed at higher discharge pressures.

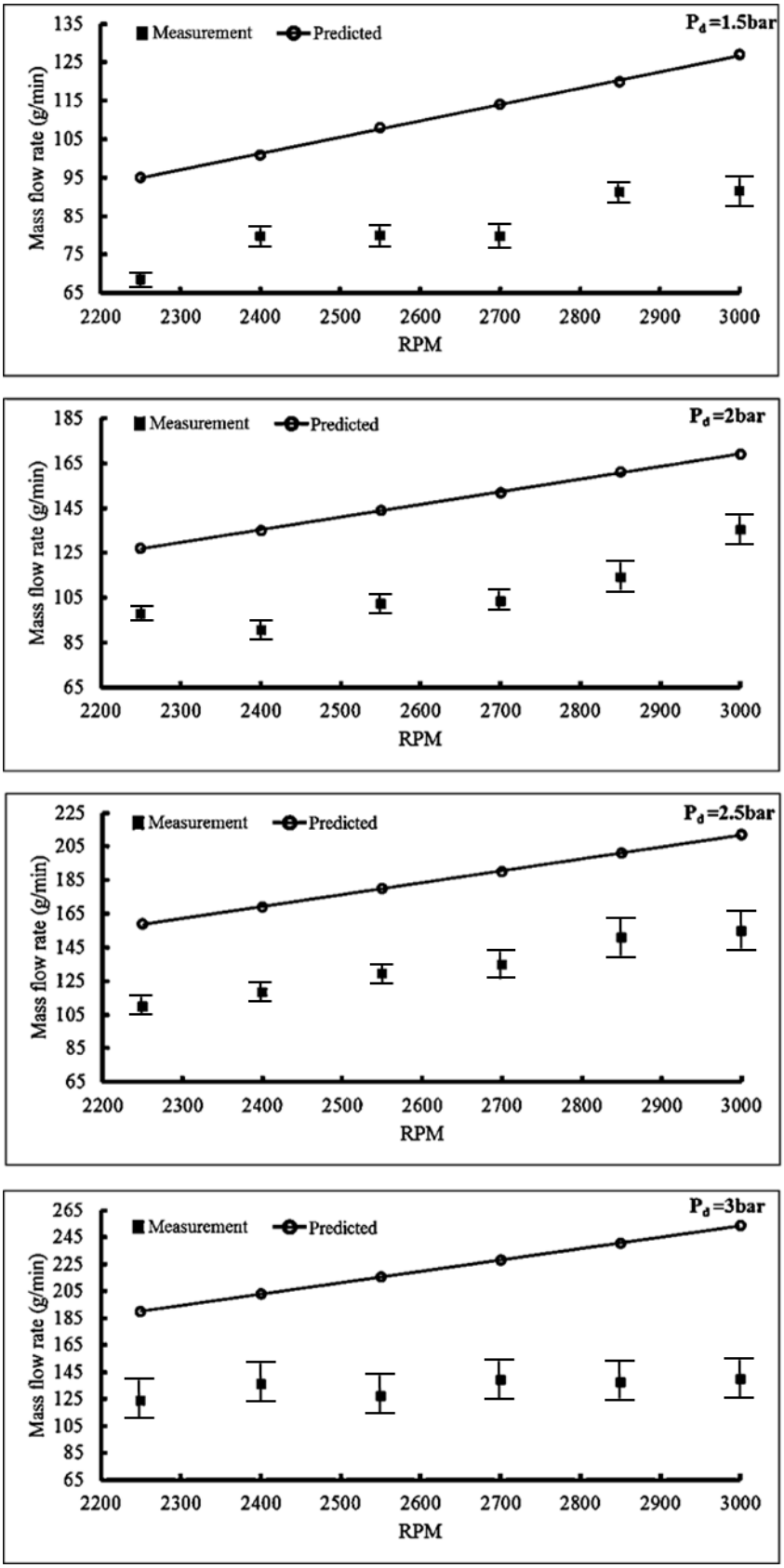

Figure 7.19 Measured and predicted compressor discharge mass flow rate

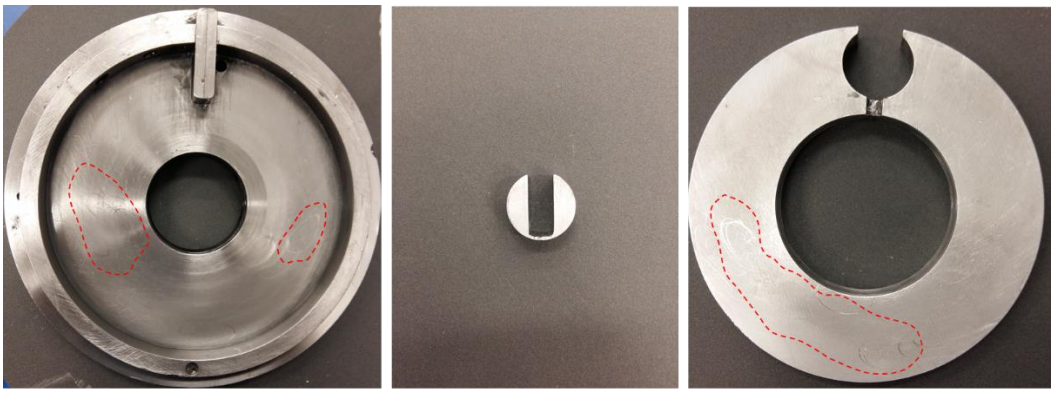

Figure 7.20 Compressor condition after experimental investigations (a) Cylinder, (b) Vane bushing, (c) Piston

The shaft and the interface between the shaft and lip seal were closely examined. The absence of oil mark beyond the shaft-lip seal interface indicated the effectiveness of the lip seals. In general, the crankshaft did not exhibit any form of wear and tear. Following that, the reed valve was disassembled to inspect its health. The examination revealed that valve housing to be extensively flooded with oil and dirt. Future designs of the reed valve should take this observation in consideration as excessive presence of lubricant and dirt could deteriorate the sealing ability of the reed valve.

7.7 Concluding remarks

There is a strong agreement between the predicted and measured mechanical power requirements. In fact, the discrepancy is generally below 10% between the measured and predicted parameters. However, the compressor experienced severe leakage, resulting in poor correlation between predicted and measured mass flow-rate. The leakage within the compressor is mainly due to tolerance between mating parts. This leakage can be reduced by operating the compressor at higher operating speed and manufacturing the components with higher precision.

Chapter 8

Conclusions and future work

This research project designed, developed and tested a new Fixed Vane Compressor design, specifically developed to facilitate the construction of a 2-in-1 motor for Electric Vehicles. This chapter concludes with design overview of the 2-in-1 motor, the compressor design, simulation models and experimental studies. In addition, the contribution of this research project and future work are also discussed in this chapter.

8.1 The 2-in-1 Motor design overview

The invention combines the Air-Conditioning (A/C) compressor, compressor and the drive motors of the Electric Vehicle (EV) into a single two-plate package. The 2-in-1 motor design is the first to use concentric shafts to achieve coaxial placement of the compressor and traction drives. This arrangement provides the flexibility to independently control the torque-speed of the motors without any mechanical interference. Hence, the A/C compressor can be operated at full capacity even while the vehicle is at a complete standstill. An electromagnetic clutch is placed between the compressor and traction rotors to physically connect the traction and compressor motors during braking events. This facilitates the direct utilization of the vehicle's kinetic energy to operate the A/C compressor thereby minimising energy conversion losses.

The 2-in-1 motor, shown in Figure 8.1 employs two high power permeant magnet motors to generate the necessary torque for driving the A/C compressor and providing tractive power to operate the vehicle. These motors are enclosed inside a water jacket to ensure that sufficient cooling during operation. The cooling water can be obtained from the vehicle's battery thermal management system.

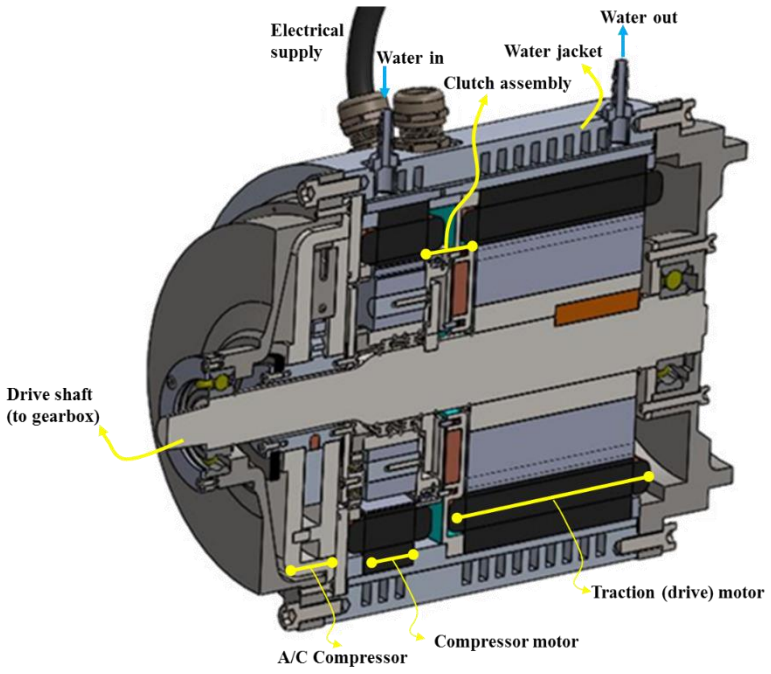

Figure 8.1 2-in-1 motor cut-away view

The advantages of the 2-in-1 motor design includes:

Advantage 1- Cost and Space Savings

Since the A/C compressor and traction motors are combined into a single housing, components that are common to these motors can be shared. These include motor casing, sealing devices, cooling mechanism, and the electronic drive controls and housing. This reduction in parts count decreases the manufacturing cost, weight and the bulk of the overall system. The drop in parts count also improves the overall reliability as the system complexity is reduced. The elimination of a mounting bracket, casing and inverter housing for the A/C unit also reduces the carbon footprint in the production of EVs as the associated material processing is eliminated.

Advantage 2 - Increased Cruise Range

In conventional drive-train architecture, the A/C compressor motor is not able to use the energy generated from the recuperation event directly. Instead, the recuperated energy have to be directed to the battery for it to be available for subsequent usage by the compressor motor. However, in each step, the energy must be converted from one form to another, either from mechanical to electrical or electrical to chemical or vice versa. These energy conversion steps bleeds away the available recuperated energy due to inherent nature of energy conversion process *(refer to appendix A for a detailed discussion).*

By combining the traction and compressor motors into a single unit, the 2-in-1 motor minimises energy conversion losses incurred by A/C compressor motor. This is achieved by an electromagnetic clutch (see Figure 8.2) which physically connects the traction and compressor motors during breaking events. This clutch facilitates the immediate utilization of recovered kinetic energy to power the A/C compressor. As the energy flow path is short-circuited, a fraction of the recuperated energy can be immediately used to drive the A/C compressor without the need for energy conversions. Based on simulations, and conservative estimates, the elimination of

energy conversion is expected to further boost the cruise range of EVs by an additional 3%.

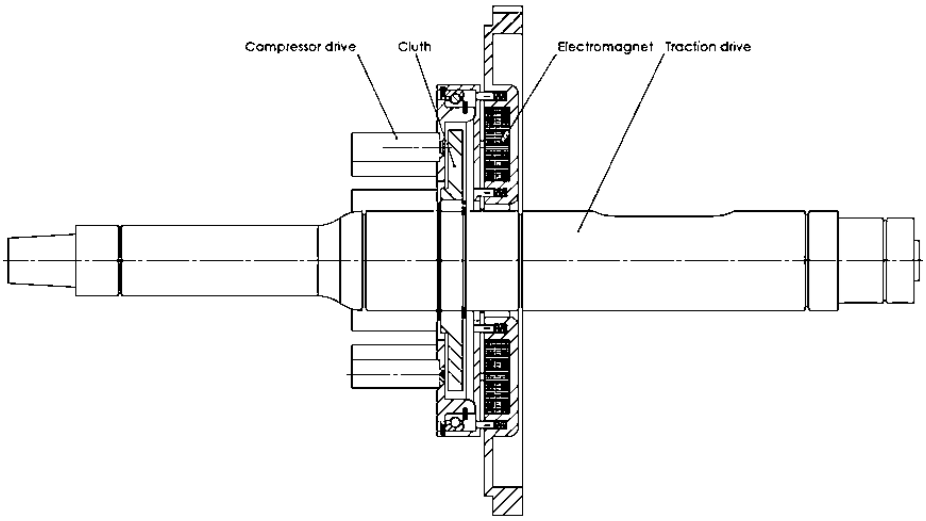

Figure 8.2 Internal clutch mechanism transfers recuperated energy from the traction drive to compressor

Advantage 3 - Increased Regenerative Power and torque

In a conventional EV, the traction motor generates all of the regenerative braking torque. Thus brakes have to be applied should the braking event generates a power that is larger than the rated capacity of the motor - which results in energy wastage. However, in the case of the invention, the generative braking torque will be higher, because the A/C compressor load and the compressor motor can act in unison with the traction drive during the braking events. Likewise, the compressor motor can supplement the drive motor should there be a need for additional torque to facilitate rapid acceleration or climb stepper gradients.

8.2 Compressor design

Various positive displacement compressor designs apt for automotive application have been reviewed. Meticulous attention have been given to each compressor variant to understand its working principal, its limitations and more importantly, its suitability for the proposed 2-in-1 motor. The design and development of a Fixed

Vane Compressor (FVC) which discharges through the vane has been the main focus of this research project.

A conventional Swing Vane Compressor (SVC) has an oscillating vane while the FVC has its vane rigidity held against cylinder wall. This reduces the frictional losses between the vane bushing and the vane as the contact force between these components are no longer a function of pressure difference acting on the exposed vane surfaces. This design is future enhanced by discharging the compressed refrigerant through the fixed vane. Simulations has verified that this approach will increase the compressor's volumetric efficiency as smaller volume of discharge gas is trapped at the end of compression stroke.

In a conventional rolling piston compressor, the piston eccentricity is dynamically balanced using two balancing masses placed on two different planes. However perfect balancing is not achieved due to manufacturing variations and the requirement to accurately position the balancing masses in different planes. The new FVC overcomes this problem by utilizing an in-plane counter weight to cancel the eccentric rotating mass. This approach is ought to produce a simpler design, a smoother compressor operation and eliminates the need to perform a dynamic balancing of the crankshaft after manufacturing process.

8.3 Simulation studies

Mathematical model have been developed to facilitate an analytical analysis of the new compressor design. Though these models are based on simplifications and assumptions, it provided a swift aid in the understanding of the compressor performance and characteristics. The compressor model consists of the geometric model, thermofluid model, dynamics model, orifice model, reed valve model, power loss model, leakage model and journal-bearing model. A brief summary of these models as follows:

Geometric model

This model describes geometry of the compressor and outputs the change in compression chamber volume as a function of crankshaft speed.

Thermofluid model

This model accounts for the variation in thermodynamic properties of the refrigerant in the working chamber. The model is based on the assumption that fluid properties are spatially independent and outputs the variation in refrigerant pressure, temperature and mass inside the chamber as a function of time.

Kinematic model

The kinematic model couples the thermodynamic and geometric model with the motor speed. Motor speed supplied by the kinematic model facilitates the power loss model to predict the mechanical losses and journal bearing model to predict the lubricant thickness and pressure distribution in the journal-bearing.

Orifice model

The orifice model accounts for the size of the suction and discharge ports. It simulates the refrigerant flow through a sharp-edged orifice and accounts for the associated pressure and flow losses. Theoretical analysis presented in chapter 6 has clarified that the discharge port dimensions has a profound effect on re-expansion losses.

Reed valve model

The reed valve model simulates the operation of the reed valve during the discharge process. The reed valve model is based on finite element method and have been validated to predict the reed deflection given the pressure difference across its face. It obtains the pressure difference across the reed valve from the discharge boundary condition and the thermofluid model.

Powerloss model

The power loss model calculates the relative velocity between key mating components and predicts the net mechanical loss given the lubricant viscosity, axial and radial clearance between mating parts and the shaft speed.

Journal-bearing model

The journal bearing model predicts the pressure distribution of a hydrodynamically lubricated crankshaft under steady-state conditions. The CFD based model facilitates a more realistic and advanced design analysis of the journal bearings. The CDF model has been validated against analytical solutions to surface the accuracy of the model.

8.4 Project contributions

This research project is expected to have a substantial impact in the design and development of EVs due to the following novel contributions:

- A new 2-in-1 electric motor drivetrain architecture that has the potential to increase the cruise range of the EVs while reducing the manufacturing cost has been introduced
- A new practical design solution that embodies the 2-in-1 motor drivetrain architecture has been presented
- A new compressing mechanism design that accommodates the requirements of the 2-in-1 motor has been designed, developed and instrumented
- The compressing mechanism has been further refined by finding a unique means to mitigate re-expansion losses
- The mathematical models developed in thesis provided an analytical means to predict the compressor performance. The maximum deviation between the predicted and measured mechanical power is found to be 10%, however a larger deviation between predicted and measured mass flow rate is observed. This can be attributed to large leakage occurring within the compressor.

Thus, this research project has expanded the boundaries of both drivetrain architecture design and the development of new a compressing mechanism design.

8.5 Future work

Development of the 2-in-1 motor

This project focused on the design and development of the compressing mechanism that is apt for the 2-in-1 motor. However, the project excluded the fabrication of the 2-in-1 motor despite generating the relevant engineering drawings (*refer to Appendix E*). Therefore, the subsequent work should focus on the manufacturing and the assembly of the 2-in-1 motor. This work can be future expanded by demonstrating the practicality of the 2-in-1 motor by installing it on a compact electric vehicle.

Experimental comparative study on the SVC and the newly designed FVC

Based on the outcomes of present investigation on fixed vane revolving compressor, followings points can be investigated further:

Oil-free and orientation free compressor

Oil sump is required to supply lubricant on rubbing surfaces and usually it is located at the bottom of compressor. Without sufficient oil flow, seizure may occur due to the lack of lubricant. An oil-free compressor, which can operate at any orientation may eliminate the necessity of the oil sump. Oil-free compressor can either be lubricated by water or using innovative design together with proper materials selection such as hard coating to reduce wear and friction.

Vibration and noise analysis

The origin of vibration in revolving vane compressor is the periodic changes in working fluid compression, angular acceleration as well as fluctuation of motor torque. Another source of noise is fluid shearing and pulsating gas flow during discharge process. Further studies on that is required regarding minimizing noise and vibration levels.

Appendix A
DRIVETRAIN ARCHITECTURE & SIMULATION

This chapter estimates the gain in energy efficiency obtained by adopting a drivetrain architecture that integrates the A/C compressor, compressor motor and drive motor in a single housing (2-in-1 motor). To facilitate this study, a mid-size EV is modelled in the ADVISOR [15] *simulation platform. The simulated test vehicle is subjected to number of standard drive cycles to predict the improvement in cruise range performance attained by the 2-in-1 motor drivetrain architecture.*

This section published substantially as :

N. S. Kumar, "Increasing the Cruise Range and Reducing the Capital Cost of Electric Vehicles by Integrating Auxiliary Unit with the Traction Drive," *Int. J. Veh. Technol.*, vol. 2016, 2016.

A1. Drivetrain architecture simulation [130]

This section simulates the 2-in-1 motor in Simulink® to estimate the efficiency gains achieved by the integrated drive-train architecture.

Mathematical model of an EV

This section models the velocity of the EV and the forces at work during a regenerative braking event. The specifications of the vehicle under consideration are tabulated in Table A.0.1.

Table A.0.1 Simulated vehicle parameters

Category	Parameter	Value
Vehicle	Vehicle type	Mid-size EV
	Vehicle Mass	1450kg
	Tyre radius	0.20m
	Coefficient of rolling friction between tyre and road	0.0015
	Coefficient of drag (Cd)	0.30
	Projected frontal area	$0.60m^2$
Traction motor and transmission	Traction motor rated power	35kW
	Motor based speed (N_{base})	2000RPM
	Transmission ratio (r)	6
	Transmission type	One speed fixed gear
	Transmission efficiency (η_{trans})	0.90
Electrical accessory load	A/C compressor motor	3kW

Figure A.0.1 depicts the Free Body Diagram (FBD) of an EV in a recuperation mode subjected to a constant deceleration, *a*:

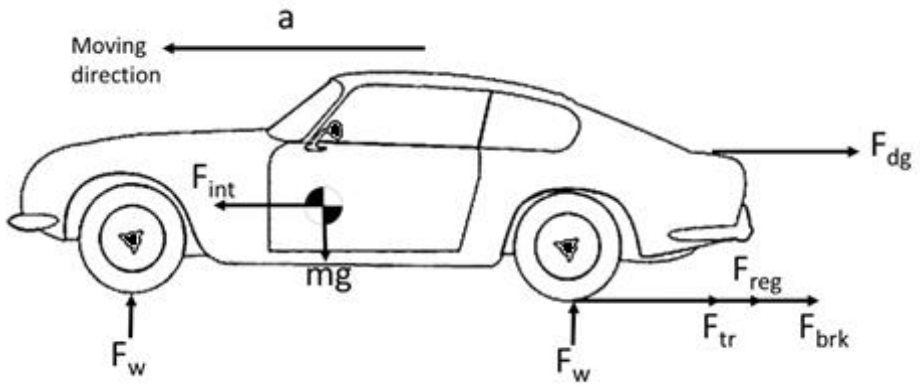

Figure A.0.1 FBD of a vehicle in a regenerative braking

The vehicle speed can be described by:

$$V(t) = V_0 + a \cdot t$$

where V_0 represents the initial velocity of the vehicle, a is the acceleration and t is time.

Adopting a non-inertial frame of reference, the forward inertial force (F_{int}) is given by:

$$F_{\text{int}} = m \cdot a$$

where m represents the mass of the body.

The four forces countering the forward inertia of the car are the traction (the road-surface-tyre friction), aerodynamic drag, frictional braking and regenerative braking force created by the motor functioning as a generator. The aerodynamic drag and the regenerative braking force are functions of vehicle's instantaneous velocity while the traction force remains constant.
Assuming the vehicle's weight is evenly distributed among the four wheels, the net traction force (F_{tr}) due the friction between the tyre and road is given by:

$$F_{tr} = \mu \cdot mg$$

where μ represents co-efficient of friction.

The drag force (F_{dg}) is described by:

$$F_{dg}(t) = \frac{1}{2}\rho[V(t)]^2 AC_d$$

The regenerative braking force produced by the motor depends on the motor's torque-speed characteristics. The torque-speed characteristics of an ideal motor can be described by the following piecewise function:

$$T_{reg} = \begin{cases} \dfrac{P_{\max} \cdot 60}{2\pi \cdot N_{base}} & if \quad N_{motor} \le N_{base} \\ \dfrac{P_{\max} \cdot 60}{2\pi \cdot N_{motor}} & if \quad N_{motor} \ge N_{base} \end{cases}$$

Given the base speed (N_{base}) and maximum power (P_{max}), equation above can be used to generate torque-speed characteristics plot for various motor configurations. For the purpose of comparison, assuming a fixed base speed of 2000RPM and varying the maximum power yields the plot shown in Figure A.0.2. Analysis of the plot conveys that a motor with a larger maximum power can produce a higher torque at lower speeds.

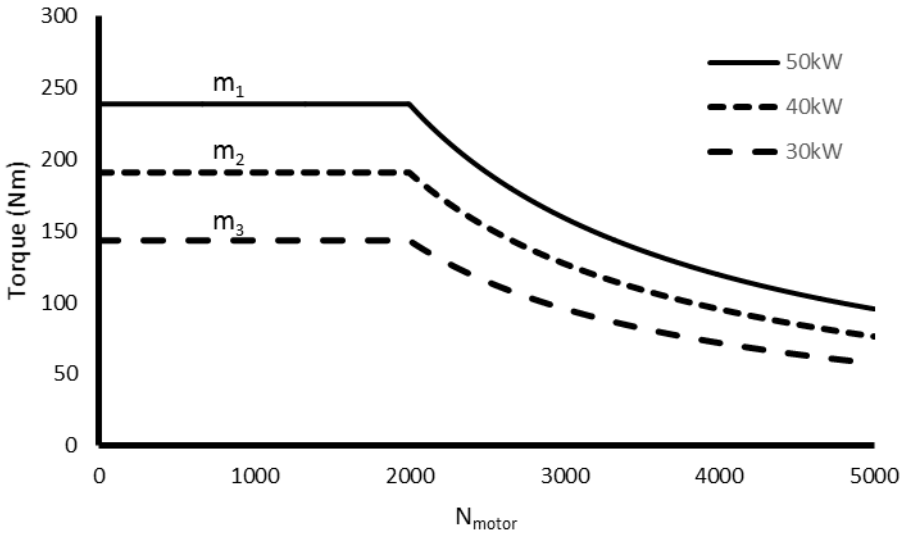

Figure A.0.2 Motor torque-speed curves

where m_1, m_2 and m_3 are the weight of 15kW, 10kW and 5kW motors respectively.

The regenerative torque acting on the vehicle's wheel is given by

$$T_{reg,wheel} = T_{reg} \cdot \eta_{trans} \cdot R$$

where the transmission ratio, R is given by $R = \frac{motor\ speed}{wheel\ speed}$

The motor speed can be calculated from the vehicle speed using

$$N_{motor}(t) = V(t) \cdot \frac{1\,rev}{2\pi r_{tyre}} \cdot 60 \cdot R$$

The braking force due to the regenerative torque can then be calculated from

$$F_{reg}(t) = \frac{T_{reg,wheel}(t)}{r_{tyre}}$$

The braking force is simply the difference between the forward inertial force and the other retarding forces

$$F_{brk}(t) = F_{\text{int}} - F_{reg}(t) - F_{dg}(t) - F_{tr}$$

The energy captured by the recuperation mechanism, E_{reg} and heat energy dissipated in the brakes, E_{brk} are given by the following equations:

$$E_{reg} = \int_0^t F_{reg}(t) \cdot V(t) dt$$

$$E_{brk} = \int_0^t F_{brk}(t) \cdot V(t) dt$$

Legislation requirements specify that vehicles from M1[7] category should be designed to decelerate to a complete stop at a minimum of 6.43m/s^2 or 0.66g from speeds up to 100km/h. Thus assuming an initial velocity of 100km/h and a deceleration of 0.66g, the variation in braking forces, the traction and the aerodynamic drag forces during a simulated braking event are shown in Figure A.0.3.

[7] M1 category belongs to passenger cars that do not exceed eight seats including the driver's seat.

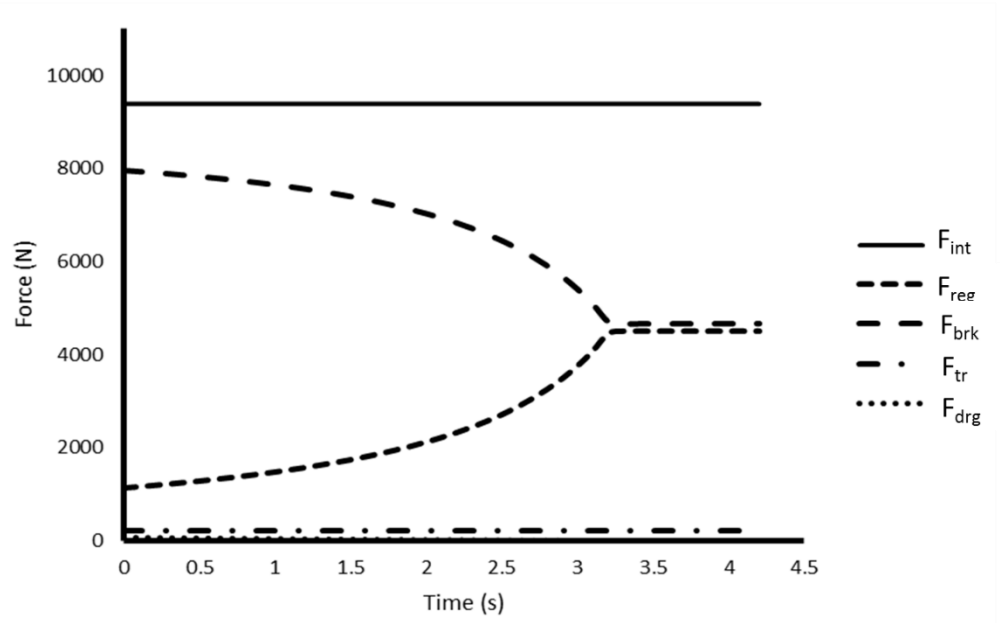

Figure A.0.3 Variation in inertial, regenerative braking, braking, tractive and drag forces as a function of time

Analysis of the plot reveals that the magnitude of the traction and aerodynamic drag forces pales in comparison to the regenerative and frictional braking forces; thus will be ignored in subsequent calculations. The result also reveals that the traction motor of the simulated vehicle was not powerful enough to produce the regenerative braking force demanded by the situation. To compensate, the frictional brakes have been applied to counter the forward inertial force. However, the application of the brakes bleeds away the recoverable energy in the inform of heat. A higher power motor can be used to reduce the magnitude of frictional torque. However, as stated in Figure A.0.2, the usage of high power motor will result in an increased weight penalty. In addition, the battery may not have the capability to absorb the large surge in regenerated power produced by a high-powered motor.

As illustrated in Figure A.0.4(a), the regenerative power generated in a convention EV is limited by the power absorbing capacity of the traction drive motor. The 2-in-1 motor circumnavigates this limitation by clutching an A/C unit with the traction drive during the braking events (see Figure A.0.4(b)). By integrating the A/C compressor with the traction motor, the added load will improve the power

absorbing capacity of the recuperation mechanism without the requirement to upgrade the traction motor's power rating.

In a conventional EV, regenerative braking torque is strictly from Traction motor.

(a)

In 2-in-1 motor, the regenerative braking torque is produced from both the A/C compressor and traction motor

(b)

Figure A.0.4 Regenerative braking torque generated in (a) a conventional EV and (b) the 2-in-1 motor

Two further simulations were performed to study the implications of clutching the A/C unit having a power rating of 3kW with the traction drive during a regenerative braking event. During the simulation, the total regenerative load was set at 38kW, a 3kW increase compared to the previous simulation. Figure A.0.5(a) and (b) shows the variation in braking forces for these two simulations. The first simulation was conducted with a deceleration rate of 0.66*g* while the second was performed at 0.30*g*. Comparing Figure A.0.5(a) with Figure A.0.3, the addition of a 3kW A/C unit load has increased the regenerative braking force thereby minimising the energy wasted in brake pads.

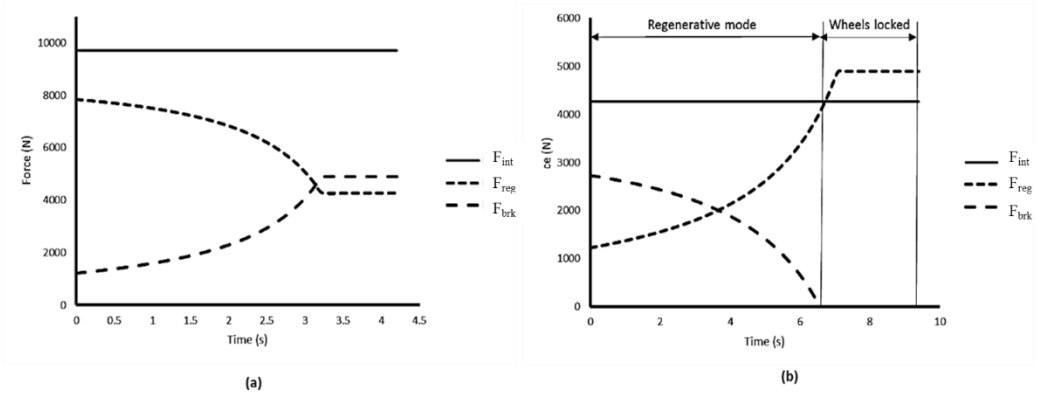

Figure A.0.5 Variation in the braking forces (F_{reg} and F_{brk}) with respect to time in comparison to the forward inertial force. (a) with a deceleration rate of 0.66*g* and (b)with a deceleration rate of 0.30*g*

Table A.0.2 provides a quantitative comparison in the energy recovered for the cases with and without 3kW A/C unit load. It can be observed that an 8% increase in the regenerative load (3kW) increases the recuperated energy by 8.5% and improves the E_{reg}/E_{brk} ratio by 10%. Therefore, the increase in recuperated energy will not only extend the range of the car but also decreases the wear on the brake pads.

Table A.0.2 Regenerative braking with and without the AUX load of 3kW

	a	**Regenerative Load**	**E_{reg}**	**E_{brk}**	**E_{reg}/E_{brk}**
Without AUX	-0.66g	35kW	118kJ	425kJ	0.278
With AUX	-0.66g	38kW	128kJ	415kJ	0.308

Figure A.0.5(b) depicts the simulation results when the vehicle decelerates at a rate of 0.30*g*. It can be observed that a combination of a lower deceleration rate and an added regenerative load causes the wheels to lock after the sixth second as the regenerative braking force exceeds the forward inertial force. Though this situation is dangerous, it can be compensated by decreasing the transmission ratio as shown in Figure A.0.6. A decrease in transmission ratio decreases the peaking value of regenerative braking force.

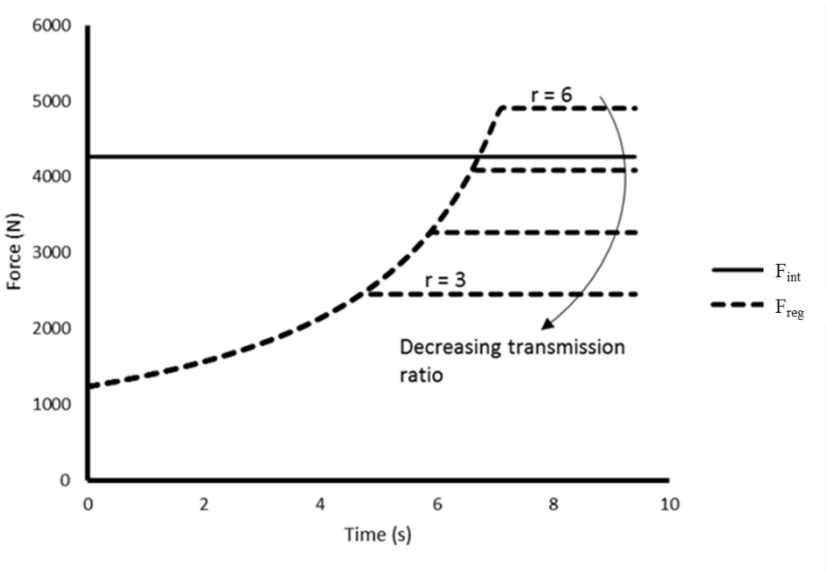

Figure A.0.6 Decreasing the regenerative braking force by varying the transmission ratio

Simulation setup

Any savings in battery energy usage for a given drive cycle corresponds to a potential increase in cruise range performance of the EV. Therefore, a study was setup in Simulink® to measure the savings in battery energy consumption achieved by the introduction of 2-in-1 motor drivetrain architecture. For the study, a MATLAB® based computer program-Advanced Vehicle SimulatOR (ADVISOR) [15], which specialises in vehicle modelling, has been extensively modified to facilitate the simulation studies. An overview of the graphical setup in Simulink® is shown in Figure A.0.7. Prior to analysis, the standard EV block diagram in ADVISOR was modified such that the all electrical loads other than A/C unit remains disabled throughout the simulation. In addition, it was assumed that components such as the wheels, final drive, gearbox and clutch operates without any inefficiency. To further simplify the modelling process, A/C compressor was assumed to operate at a peak power of 3kW thought the simulation. The principal reason for these assumptions was to isolate the A/C compressor load and to analyse the improvements in battery energy savings achieved by the introduction of 2-in-1 motor drivetrain architecture. An energy meter block was used to record the total energy discharged from the battery for a given simulation.

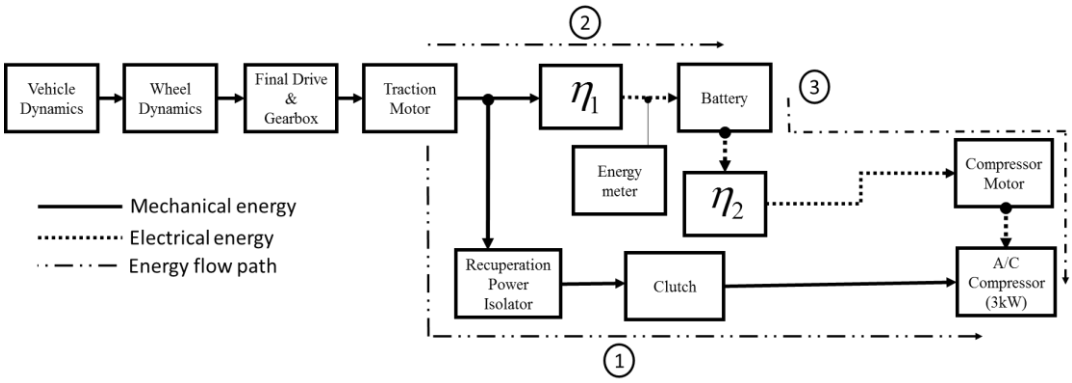

Figure A.0.7 The graphical setup in Simulink® for predicting the efficiency improvement

With reference to Figure A.0.7, A/C compressor with a power load of 3kW obtains its operating power via two distinct sources: (1) the compressor motor and (2) recuperated mechanical energy. When the vehicle recuperates, the recuperation power isolator analyses the quantity of recuperated power and activates the clutch mechanism only if the regenerative power exceeds the A/C compressor load (power flow path 1). If the regenerative power is sufficient to power the A/C compressor, a clutch physically connects A/C compressor with the traction motor and permits an immediate utilization of the recuperated mechanical energy thereby eliminating energy losses due to energy conversion. The engagement of the clutch disconnects the compressor motor from the battery, thereby conserving stored energy. Whereas, when the vehicle is not operating in regenerative mode, a dedicated motor obtains the power from the battery and drives the A/C compressor (power flow path 3).

When the energy flows through path 2 (regenerative braking), it does not undergo any form of conversion, as the mechanical energy arriving at the motor shaft can be channelled directly to drive the A/C compressor. Therefore, this energy flow path is assumed to be free from any kind of losses. Any excess power generated during the regenerative braking will be delivered to battery though energy flow path 2 for later utilization. However, in this case, the mechanical energy arriving at the motor shaft first has to be converted to electrical energy by the motor and subsequently to electrochemical energy to be stored in the battery. These energy transformations incur losses, which has been accounted for by the introduction of η_1. When the

vehicle operates in drive mode, A/C compressor motor obtains its energy from the battery. Then again, the electrochemical energy contained in the battery has to be converted and conditioned using a DC-to-DC converter to a form suitable to be used by the compressor motor. The inefficiency associated with this power flow path has been accounted for by introducing η_2.

An electric generator converts the mechanical energy to electrical energy with a typical efficiency of 95.0% [131]. Likewise, the efficiency of energy conversion in a battery from chemical to electrical (and vice versa) occurs with an efficiency of 90.0% [131]. Since the energy flow through path 1 undergoes two energy transformation (Mechanical→Electrical→Electrochemical), the net efficiency associated with path 1 can be assigned to be η_1=85.5%. Likewise, the energy flowing through path 3 undergoes a similar energy transformation but in reverse order. However, the conversion of energy from electrical to mechanical occurs at 65% efficiency in the case of small motors[131] (compressor motor). Therefore the net efficiency of η_2=61.8% can be assigned to path 3. The striking outcome of this analysis is that the regenerative energy delivered at the A/C compressor through paths 2 and 3 have a net efficiency of $\eta_1 \cdot \eta_2$=52.8%.This reveals that nearly half of the recuperated energy captured by the regenerative braking mechanism is lost before it reaches the A/C compressor.

Drive cycle analysis

A drive cycle is a schedule that governs the vehicle's speed as function of time, which is essentially a mathematical representation of a road. It is a key input for vehicle simulation as it facilitates in producing a repeatable experiment for performance comparison. In this paper we simulated the test vehicle using five EU legislative cycles listed in Table A.0.3 using ADVISOR [15]. During the investigation, the simulated vehicle was driven in the selected drive cycle and the total braking time for each cycle was recorded. Based on the results gathered from the study, it can be observed that the aggressive drive cycles such as ECE 15, ECE 15+EDUC and NEDC have a substantial period of braking events. On average, a

vehicle spends 15% of its total time in braking, signifying an immense potential in recoverable energy for all drive cycles.

Table A.0.3 EU legislative cycle analysis

Drive cycle	Distance	Total Time	Braking time	% Braking time
ECE 15	1.0km	195s	41.2s	21.1%
EUDC	7.0km	400s	48.0s	12.0%
EUDC, Low	10.6km	1224s	103.0s	8.4%
ECE 15+ EUDC	10.9km	1225s	201.8s	16.5%
NEDC	10.9km	1184s	204.3s	17.3%

For the purpose of discussion, consider simulated vehicle is operated under the ECE 15+EUDC drive cycle. The scheduled velocity vs time for the stated drive cycle is shown Figure A.0.8(a), while Figure A.0.8(b) shows the regenerative power produced by the vehicle during recuperative braking. It can be observed that the magnitude and the duration of regenerative power is proportional to the rate of change in vehicle's velocity (deceleration rate). It is also observed that regenerative periods are short events thereby confining the regenerative power to a small fraction of the drive cycle.

A constant A/C compressor load of 3kW has been superimposed over the Figure A.0.8(b) to highlight that not all regeneration events are capable of providing the necessary power to drive the A/C compressor. For example, the first regenerative power peaks at about 1kW, which is less than half of the power required to operate A/C compressor. Hence, a drive cycle can consist of large percentage of braking time, but if the changes in velocity are gradual, it might not produce the sufficient regenerative power to operate the A/C compressor.

Figure A.0.9 compares the regenerative power, the A/C compressor load and the excess power as a function of time for the ECE15+EUDC drive cycle. Excess power represents the regenerative power that is available for storage after the consumption

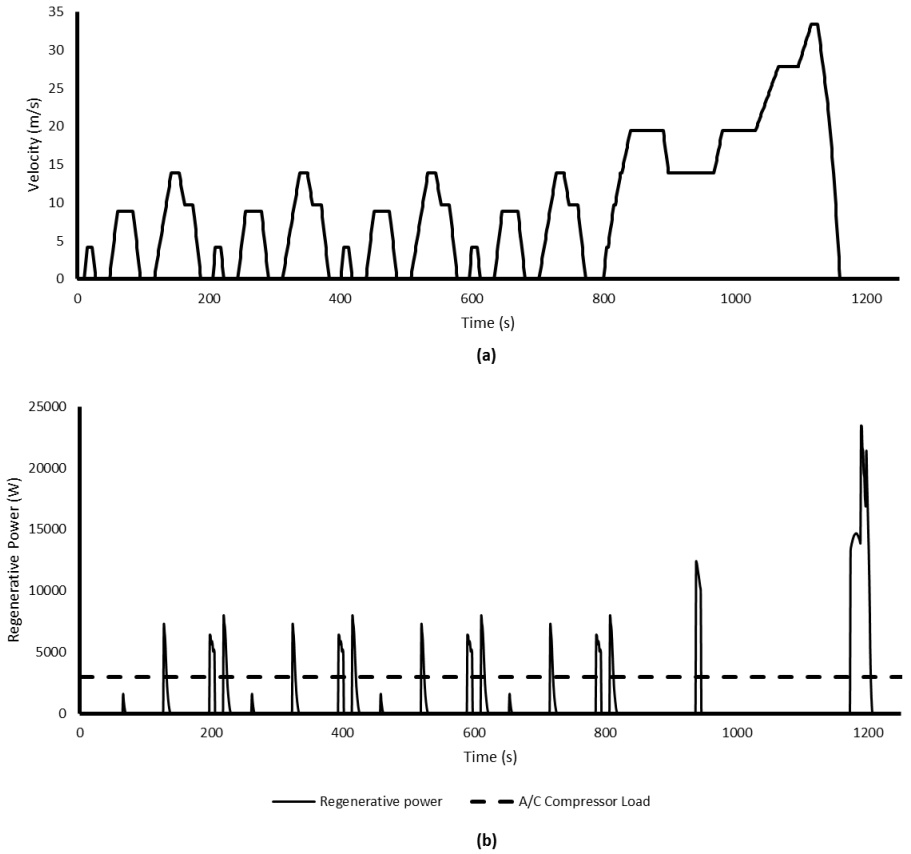

Figure A.0.8 Simulated vehicle's (a) velocity (b) regenerative power on ECE 15+EDUC drive cycle

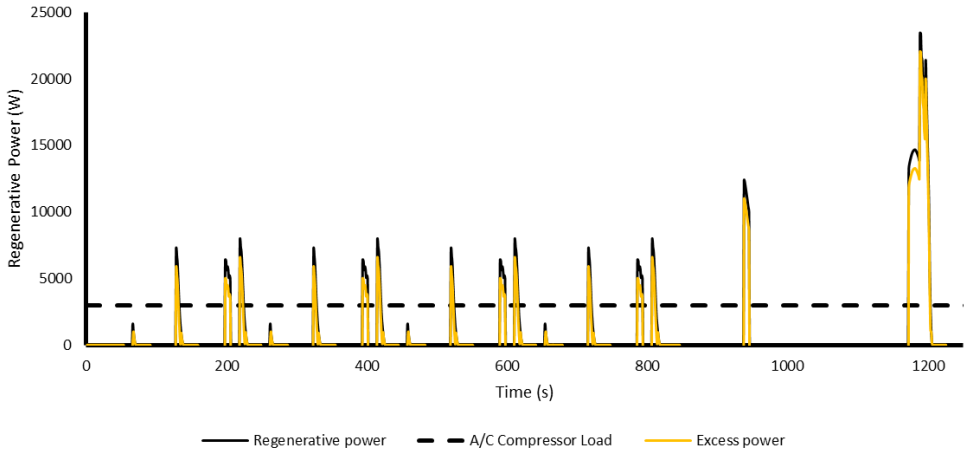

Figure A.0.9 Excess regenerative power directed to the battery

by the A/C compressor. The recuperation power isolator block has been configured such that the clutch mechanism is only activated when the regenerative power exceeds the A/C compressor load. Accordingly, the compressor motor has been

configured to cut-off when power flows through the energy flow path 1. This ensures that the energy flow path 1 is activated only when the regenerative power arriving at the motor shaft is capable of driving the A/C compressor without the need to operate the compressor motor. Notice that the excess is reduced by the magnitude of the A/C compressor load only when the regenerative power exceeds the compressor load. As with the conventional regenerative mechanism, the excess power is channelled to the battery for storage.

Reduction in battery energy consumption

During the simulation, the vehicle dynamics block was driven by the selected drive cycle and the energy consumed from the battery was measured for the two distinct cases: (1) A/C compressor motor operated from the battery (conventional drivetrain configuration) and (2) A/C compressor operated by a combination of compressor motor and clutch (2-in-1 motor drivetrain configuration). The percentage reduction in the useage of battery energy was then computed for each drive cycle and the results have been summarised in Figure A.0.10. The percentage braking time associated with each drive cycle has been superimposed over the results. Analysis of the result reveals that the improvement in the battery energy savings is proportional to the percentage braking time associated with each drive cycle. This result is expected as a higher number of braking events will provide more opportunities for the regenerative braking mechanism to operate the A/C compressor through the clutch.

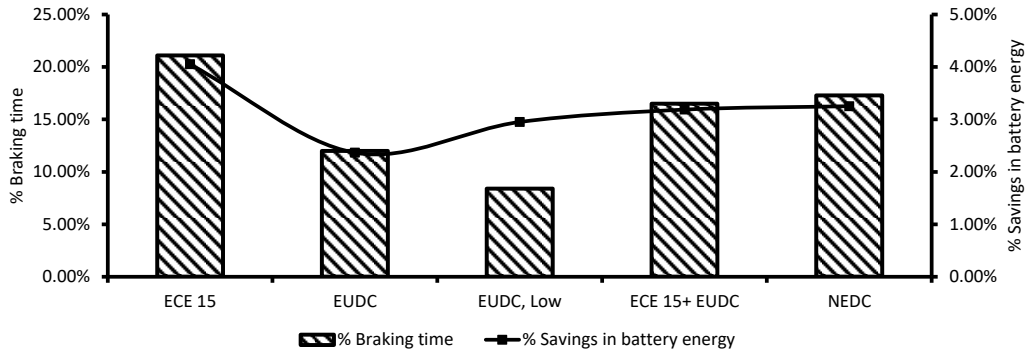

Figure A.0.10 Percentage savings in battery energy for an electric vehicle driven by 2-in-1 motor for various EU legislative drive cycles.

With reference to

Figure A.0.10, the integration of A/C compressor with the traction drive reduces the battery consumption by an average of 3.2%. This improvement in battery energy savings will directly translate in increasing the cruise range of the EV. Though this improvement seems marginal, it is expected that the percentage savings in battery energy will be higher in reality. This is because the simulation ignored a number of other losses associated with energy flow path 2 and 3. For example, the energy losses along path 2 did not account for possible devices such as DC-to-DC or AC-to-DC converter and an electrical charger. Likewise, inverters that operate the A/C compressor motor has been ignored along the path 3.

Concluding remarks

The integrated drivetrain architecture facilitates a direct mechanical coupling of the traction motor with the air conditioning compressor during braking events. The mechanical configuration of the architecture is such that the torque and speed characteristics of the drive and compressor motors can be independently controlled.

A mathematical model of an EV with the integrated drivetrain architecture was developed and simulated on number of drive train cycles. Simulations identified that a vehicle spends on average 15% of its total time in braking. Based on the analysis, a 3kW compressor load coupled with the traction drive during braking events increases the recuperable energy by 8.4%. In addition, the simulation revealed that, on average, the energy drawn from the battery is reduced by 3.2%. Based on the findings, it is evident that the integrated drivetrain architecture results in enhancing the energy capturing capacity of the regenerative braking mechanism and decreases the power consumed from the battery, both of which is expected to improve the cruise range of an EV.

Appendix B

Mitsubishi i-MiEV AC System Specifications

2. Outline of the AC system (3)

2.3 Specification of key components

(1) Electric driven compressor

Table 2.1 Electric driven compressor spec.

*L * W * H*	*291 * 162 * 157 (mm)*
Mass	*10.2kg (with Bracket)*
Compressor type	*Scroll with rare earth metal motor*
Displacement	*30 cc/rev.*
Inverter	*Integrated, suction ref. cooling*
Max. rev.	*6000 rpm*
High Voltage range	*DC 220 ~ 400 V*
Low Voltage range	*DC 8 ~ 16 V*
Max. power	*4.5 kW*
Max. input current	*20.5 A (@DC 220V)*
Refrigerant	*HFC-134a*
Ref. Lubricant	*POE oil*

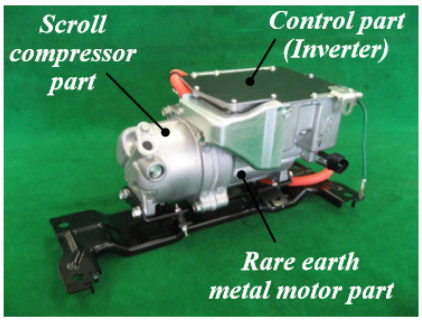

Fig. 2.3 Electric driven compressor

Oil separator is integrated due to improvement of both ref cycle capacity and efficiency.

Appendix C

Motor Specifications and Characteristics

Elektrim TECHTOP
Elektrim Techtop Motors Pte Ltd
subsidiary of Elektrim Motors & Machinery Pte Ltd

EM 112M-2
IE 1 (EFF 2) TEFC

Frequency	60
Pole	2
Output (KW)	4
Output (HP)	5.5
Speed (rpm)	3468
FLC 440V (A)	7.1
FLC 460V (A)	6.8
FLC 480V (A)	6.5
Efficiency 100%	85.5
Efficiency 75%	85.5
Efficiency 50%	83.5
Power Factor 100%	0.89
Power Factor 75%	0.85
Power Factor 50%	0.76
Tn (Nm)	12
Tmax (Tn)	2.3
Noise LwdB(A)	77
Weight (kg)	41

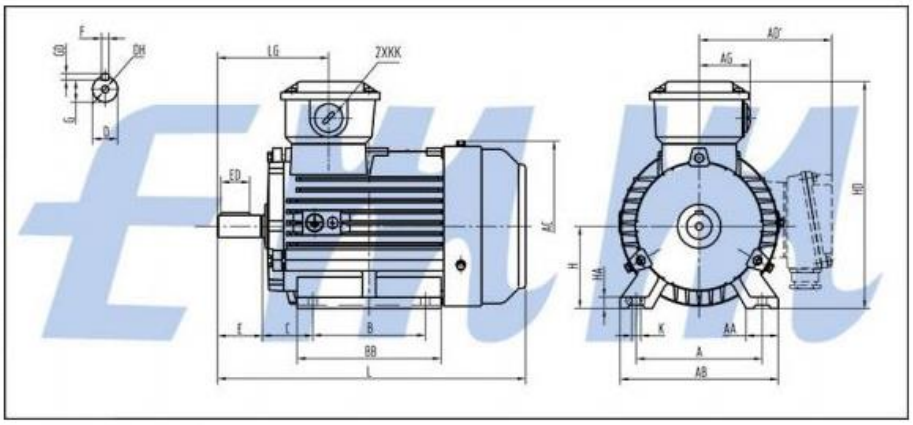

Mounting Type: B3

A	AA	AB	AC	AD	B	BB	C	CA	D	DA	DH	E	EA	F	G	H	HA	HD	K	L	LD
190	45	230	220	190	140	180	70	132	28	28	M10X22	60	60	8	24	112	15	300	12	453	82

**All dimensions in mm*

Appendix D

Mesh Independence Test

Mesh count, size and quality are important parameters when performing CFD based analysis. Hence, a mesh convergence test has to be conducted to identify the meshing threshold at which the CFD predictions are independent of the mesh quality. As shown in Figure D.0.1, COMSOL outputs element count and mesh quality prior to each simulation.

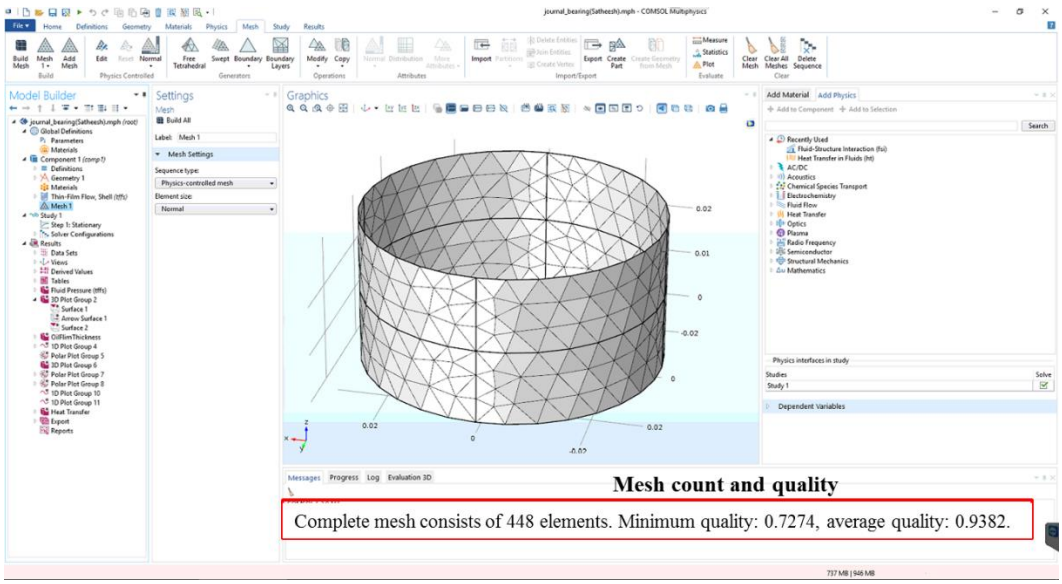

Figure D.0.1 Element count and mesh quality reported by the COMSOL software

The element count and the load bearing capacity of the journal bearing computed by COMSOL is plotted to identify the threshold at which the load bearing capacity becomes constant w.r.t element count. As shown in Figure D.0.2, increasing the element count from 400 to 2000 results in a convergence of the average load bearing capacity to 11.3kN. It is noted that increasing the element count beyond 1700 does not results in improving the average load bearing capacity prediction. Therefore, a minimum element count of 1700 was used to for the model validation and subsequent analysis involving the journal bearing.

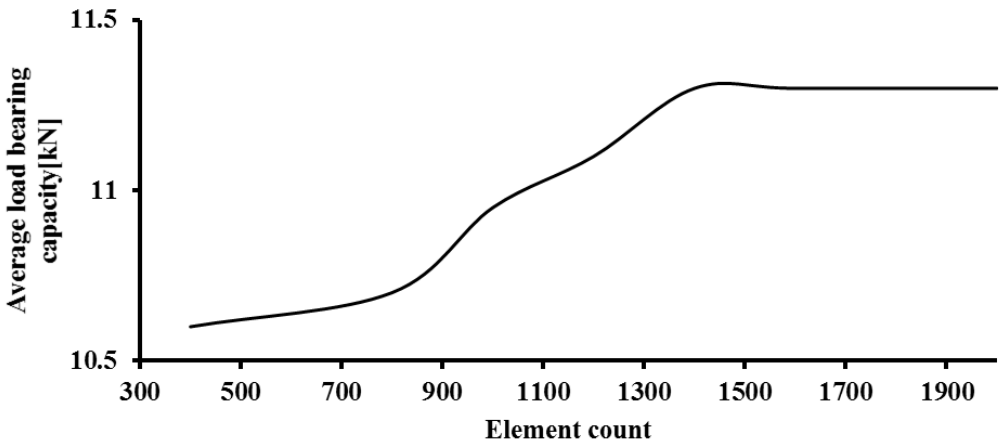

Figure D.0.2 Mesh independence test results

References

[1] "US EPA, Climate Change Division." [Online]. Available: http://www.epa.gov/climatechange/index.html. [Accessed: 28-Jul-2013].

[2] United Nations, "Adoption of the Paris Agreement," 2015. [Online]. Available: http://unfccc.int/resource/docs/2015/cop21/eng/l09r01.pdf.

[3] USDOT Center for Climate Change and Environmental Forecasting and Cambridge Systematics Inc., "Transportation's Role in Reducing U.S. Greenhouse Gas Emissions Volume 1: Synthesis Report," 2010. [Online]. Available: http://ntl.bts.gov/lib/32000/32700/32779/DOT_Climate_Change_Report_-_April_2010_-_Volume_1_and_2.pdf\npapers2://publication/uuid/9865C7B2-9DAA-42D1-A6AE-E04F572CE6DA.

[4] M. Bellis, "History of Electric Vehicles - Early Years." [Online]. Available: http://inventors.about.com/od/estartinventions/a/History-Of-Electric-Vehicles.htm. [Accessed: 28-Jul-2013].

[5] C. D. Anderson and J. Anderson, *Electric and Hybrid Cars: A History*. McFarland, 2005.

[6] "The Impact of the Electric Car." [Online]. Available: http://www.vroomvroomvroom.ca/electric-vehicles/.

[7] F. R. Kalhammer, A. Kozawa, C. B. Moyer, and B. B. Owens, "Performance and Availability of Batteries for Electric Vehicles: A Report of the Battery Technical Advisory Panel," 1995.

[8] National Electrical Manufacturers Association, "Electrical Motor Efficiency," *Engineering Toolbox*, 2005. [Online]. Available: http://www.engineeringtoolbox.com/electrical-motor-efficiency-d_655.html.

[9] Gui-Jia Su and John S Hsu, "An integrated traction and compressor drive system for EV/HEV applications," *Twent. Annu. IEEE Appl. Power Electron. Conf. Expo. 2005. APEC 2005.*, vol. 2, pp. 719–725.

[10] Delphi, "Air conditioning compressors," *US Patent 3,998,570*. Delphi, p. 12, 2006.

[11] J. R. Fischer, Steven K.; Sand, "Total equivalent warming impact (TEWI)

Calculations for Alternative Automotive Air-Conditioning Systems," *SAE*, p. 100, 1997.

[12] S. Fischer, "Comparison of Global Warming Impacts ofautomobile Air-Conditioning Concepts," in *1995 International CFC and Halons Alternative Conference*, 1995.

[13] J. T. Lee and D. Kim, "Effect of Air-Conditioning on Driving Range of Electric Vehicle for Various Driving Modes," *SAE Int.*, no. December, pp. 5–9, 2013.

[14] R. Farrington and J. Rugh, "Impact of Vehicle Air-Conditioning on Fuel Economy, Tailpipe Emissions, and Electric Vehicle Range," *Earth Technol. Forum*, no. September, p. http://www.nrel.gov/docs/fy00osti/28960.pdf, 2000.

[15] T. Markel, A. Brooker, T. Hendricks, V. Johnson, K. Kelly, B. Kramer, M. O'Keefe, S. Sprik, and K. Wipke, "ADVISOR: A systems analysis tool for advanced vehicle modeling," *J. Power Sources*, vol. 110, no. 2, pp. 255–266, Aug. 2002.

[16] K. Umezu and H. Noyama, "Air-Conditioning system For Electric Vehicles," *SAE Automotive Refrigerant & System Efficiency Symposium 2010*. SAE Automotive Refrigerant & System Efficiency Symposium 2010, pp. 1–20, 2010.

[17] M. A. Delucchi and T. E. Lipman, "An analysis of the retail and lifecycle cost of battery-powered electric vehicles," *Transp. Res. Part D Transp. Environ.*, vol. 6, no. 6, pp. 371–404, Nov. 2001.

[18] R. J. Vincent, T. W. Nehl, G. Gallegos-Lopez, and M. Naidu, "High Capacity Electric A/C Compressor with Integrated Inverter for Hybrid Automotive and Commercial Vehicles," *Downloaded from SAE Int. by Tata Steel Eur.*, no. 724, 2015.

[19] M. Naidu, T. W. Nehl, S. Gopalakrishnan, and L. Würth, "Electric compressor drive with integrated electronics for 42 v automotive HVAC systems," *2005 SAE World Congr.*, no. 724, 2005.

[20] B. A. Eleaba, "Types, principles and applications By: Eng. Bassem Abdellatif Eleaba 21/04/2012," 2012.

[21] N. Gupta, M. Jindgar, R. Dasila, and F. Semiconductor, "Fundamentals of the automotive cabin climate control system," *EDN Network*, 2012. [Online].

Available: http://www.edn.com/design/automotive/4403883/1/Fundamentals-of-the-automotive-cabin-climate-control-system.

[22] D. M. P. & A. A. Wessol, *Lubrication Fundamentals*, Second Edi., no. 1. CRC Press, 2001.

[23] M. I. Lubricants, "Mobil-Industrial-Refrigeration-Technical-Guide," 2009.

[24] P. C. Hanlon, *Compressor Handbook*. Powell's Books, 2001.

[25] A. B. Tramschek and K. T. Ooi, "Effects of port geometry. Dimensions and position on the performance of a rotary compressor," *Proc. 1992 Int. Compress. Eng. Conf. Purdue, Jul 14-17 1992*, p. 1177, 1992.

[26] X. Tojo, T. Kan, and A. Arai, "Dynamic behavior of sliding vane in small rotary compressors," *Purdue e-Pubs*, 1978.

[27] P. Shu, B. Guo, L. Li, and J. Hu, "Influence of Vane Slot Back-Pressure on the Characteristic of Vane Motion in Rotary Vane Compressor," *Purdue e-Pubs*, 1998.

[28] A. B. Tramschek, "Mathematical Modelling of Radial and Non-Radial Rotary Sliding Vane Compressors," *Purdue e-Pubs*, 1996.

[29] H. Kruse, "Experimental investigations on rotary vane compressors," in *International Compressor Engineering Conference*, 1980.

[30] H. Kaiser and H. Kruse, "An Investigation on Reciprocating and Rotary Refrigerantion Compressor," *Proceding Purdue Int. Compress. Eng. Conf.*, pp. 611–617, 1984.

[31] Y. Z. Lee and S. D. Oh, "Friction and wear of the rotary compressor vane-roller surfaces for several sliding conditions," *Wear*, vol. 255, no. 7–12, pp. 1168–1173, 2003.

[32] A. Fujiwara and N. Sakurai, "Experimental analysis of screw compressor noise and vibration," in *International Compressor Engineering Conference*, 1986.

[33] B. Sangfors, "Analytical Modeling of Helical Screw Machine for Analysis and Performance Prediction," vol. 100, no. July 1978, pp. 482–487, 1982.

[34] D. N. Shaw, "Twin screws of the future for air conditioning and refrigeration," in *International Compressor Engineering Conference*, 1990.

[35] L. Creux, "Rotary engine," US Patent No. 801182, 1905.

[36] Y. Chen, N. P. Halm, E. a. Groll, and J. E. Braun, "Mathematical modeling

of scroll compressors—part I: compression process modeling," *Int. J. Refrig.*, vol. 25, no. 6, pp. 731–750, Sep. 2002.

[37] H. Nadamoto and A. Kubota, "Power Saving with the Use of Variable Displacement Compressors," *SAE Int.*, no. 724, 1999.

[38] T. J. Skinner and R. L. Swadner, "V-5 Automotive Variable Displacement Air Conditioning Compressor." SAE International , 1985.

[39] K. Takai, S. Shimizu, and K. Terauchi, "A 7 -Cylinder IVD Compressor for Automotive Air Conditioning," 1989.

[40] C. Tian, Y. Liao, and X. Li, "A mathematical model of variable displacement swash plate compressor for automotive air conditioning system ´ matique d ' un compresseur volume ´ trique a ` plateau Mode ` me de conditionnement d ' air automobile oscillant dans un syste," *Int. J. Refrig.*, vol. 29, no. xxxx, pp. 1–11, Mar. 2005.

[41] Y. S. S. O. D. Yamamoto, "Swinging rotary compressor." Google Patents, 25-Mar-1998.

[42] M. Masuda, K. Sakitani, and Y. Yamamoto, "Development of Swing Compressor for Alternative Refrigerants," in *International Compressor Engineering Conference*, 1996.

[43] G. Lorentzen and J. Pettersen, "A new, efficient and environmentally benign system for car air-conditioning," *Int. J. Refrig.*, vol. 16, no. 1, pp. 4–12, 1993.

[44] K. Ooi, "Compressor Performance Comparison When Using R134 and R1234YF as Working Fluids," in *International Compressor Engineering Conference*, 2012.

[45] P. Reasor, V. Aute, and R. Radermacher, "Refrigerant R1234yf Performance Comparison Investigation," *Int. Refrig. Air Cond. Conf. Purdue*, pp. 1–7, 2010.

[46] W. Soedel, *Introduction to computer simulation of positive displacement type compressors*. Purdue University, School of Mechanical Engineering, 1972.

[47] D. Squarer and R. E. Kothmann, "Digital Computer Simulation of a Reciprocating Compressor-A Simplified Analysis," in *International Compressor Engineering Conference*, 1972.

[48] B. Karll, "Computer simulation of the cylinder process in a compressor based on the first law of thermodynamics," in *International Compressor*

Engineering Conference, 1972.

[49] R. Prakash and R. Singh, “Mathematical modeling and simulation of refrigerating compressors,” in *International Compressor Engineering Conference*, 1974.

[50] C. C. Hiller and L. R. Glicksman, “Detailed Modeling and Computer Simulation of Reciprocating Refrigeration Compressors,” *Int. Compress. Eng. Conf.*, pp. 12–17, 1976.

[51] E. Ng, A. Tramschek, and J. F. MacLaren, “Computer Simulation of a Reciprocating Compressor Using a Real Gas Equation of State,” *Int. Compress. Eng. Conf.*, 1980.

[52] S. Lee, R. Singh, and M. J. Moran, “First Law Analysis of a Compressar Using a Computer Simulation Model,” in *International Compressor Engineering Conference*, 1982.

[53] S. Y. Sun and T. R. Ren, “New method of thermodynamic computation for a reciprocating compressor: Computer simulation of working process,” *Int. J. Mech. Sci.*, vol. 37, no. 4, pp. 343–353, 1995.

[54] K. T. Ooi and T. N. Wong, “A computer simulation of a rotary compressor for household refrigerators,” *Appl. Therm. Eng.*, vol. 17, no. 1, pp. 65–78, Jan. 1997.

[55] Y. Chen, N. P. Halm, E. a. Groll, and J. E. Braun, “Mathematical modeling of scroll compressors—part I: compression process modeling,” *Int. J. Refrig.*, vol. 25, no. 6, pp. 731–750, 2002.

[56] M. N. Srinivas and C. Padmanabhan, “Computationally efficient model for refrigeration compressor gas dynamics ` le efficace pour e ´ tudier la Compresseur frigorifique : mode dynamique des gaz,” *Int. J. Refrig.*, vol. 25, no. 8, pp. 1083–1092, 2002.

[57] S. Brok, S. Touber, and J. Van der Meer, “Modeling of Cylinder Heat Transfer-Large Effort, Little Effect?,” *Int. Compress. Eng. Conf. Purdue Univ.*, pp. 43–50, 1980.

[58] B. G. S. S. Prasad, “Heat Transfer in Reciprocating Compressors - A Review,” *Purdue e-Pubs*, 1998.

[59] M. L. Todescat, F. Fagotti, A. T. Prata, and R. T. D. S. Ferreira, “Thermal Energy Analysis in Reciprocating Hermetic Compressors,” *Proc. Int. Compress. Eng. Conf. Purdue*, pp. 1419–1428, 1992.

[60] F. Fagotti, M. L. Todescat, R. T. S. Ferreira, and A. T. Prata, “Heat transfer modeling in a reciprocating compressor,” in *International Compressor Engineering Conference*, 1994.

[61] G. A. Longo and R. Caracciolo, “Unsteady State Analysis Of A Hermetic Reciprocating Compressor : Heat Transfer Inside the Cylinder And Valve Dynamics,” *Int. Compress. Eng. Conf.*, 2002.

[62] K. T. Ooi, “$ Heat transfer study of a hermetic refrigeration compressor.pdf,” *Appl. Therm. Eng.*, vol. 23, no. 15, pp. 1931–1945, 2003.

[63] S. Padhy, “Heat transfer model of a rotary compressor,” *Int. Compress. Eng. Conf. Purdue Univ.*, pp. 1405–1418, 1992.

[64] S. K. Padhy and S. N. Dwivedi, “Heat transfer analysis of a rolling-piston rotary compressor,” *Int. J. Refrig.*, vol. 17, no. 6, pp. 400–410, Jul. 1994.

[65] K. Jang and S. Jeong, “Experimental investigation on convective heat transfer mechanism in a scroll compressor ´ rimentale sur le me ´ canisme de transfert de chaleur par Etude expe ` spirale convection dans un compresseur a,” *Int. J. Refrig.*, vol. 29, no. 5, pp. 744–753, 2006.

[66] K. T. Ooi and J. Zhu, “Convective heat transfer in a scroll compressor chamber: A 2-D simulation,” *Int. J. Therm. Sci.*, vol. 43, no. 7, pp. 677–688, 2004.

[67] S. Sun, Y. Zhao, L. Li, and P. Shu, “Simulation research on scroll refrigeration compressor with external cooling,” *Int. J. Refrig.*, vol. 33, no. 5, pp. 897–906, 2010.

[68] A. M. Bredesen, “Influence of valve dynamics on compressor performance,” *Int. J. Refrig.*, vol. 2, no. 1, pp. 17–21, 1979.

[69] W. . Glaeser, “Failure mechanisms of reed valves in refrigeration compressors,” *Wear*, vol. 225–229, pp. 918–924, 1999.

[70] M. Costagliola, “The theory of spring-loaded valves for reciprocating compressors,” *J. Appl. Mech. Asme*, vol. 17, no. 4, pp. 415–420, 1950.

[71] J. F. T. MacLaren and S. V Kerr, “Analysis of Valve Behavior in Reciprocating Compressors,” in *Proceedings of the XII International Congress of Refrigeration*, 1967.

[72] M. W. Wambsganss and R. Cohen, “Dynamics of a reciprocating compressor with automatic reed valves,” in *Proceedings of XII International Congress of Refrigeration*, 1967, vol. 3.

[73] G. W. Gatecliff and E. R. Lady, “Forced Vibration of a Cantilever Valve of Uniform Thickness and Non-Uniform Width,” 1972.

[74] F. F. S. Matos, A. T. Prata, and C. J. Deschamps, “Numerical Simulation Of The Dynamics Of Reed Type Valves,” *Int. Compress. Eng. Conf.*, 2002.

[75] J. Friley and J. F. Hamilton, “Characterization of Reed Type Compressor Valves by the Finite Element Method,” in *International Compressor Engineering Conference*, 1976.

[76] S. Akella, N. J. Rao, E. V Venugopal, and K. Venkateswarlu, “Finite Element Analysis of Compressor Valve Dynamics,” in *International Compressor Engineering Conference*, 1988.

[77] F. Fagotti, M. de Bortoli, R. Barbieri, M. G. D. de Bortoli, and R. Barbieri, “A Finite Element Approach to Compressor Valves Motion Simulation,” 1996.

[78] P. Cyklis, “CFD simulation of the flow through reciprocating compressor self-acting valves,” *Int. Compress. Eng. Conf.*, 1994.

[79] J. Kim, S. Wang, S. Park, K. Ryu, and J. La, “Valve Dynamic Analysis of a Hermetic Reciprocating Compressor,” *Int. Compress. Eng. Conf.*, pp. 1–10, 2006.

[80] R. Ferreira and D. Lilie, “Evaluation of the Leakage Through the Clearance Between Piston and Cylinder in Hermetic Compressors,” *Int. Compress. Eng. Conf.*, 1984.

[81] Y. Huang, “Leakage calculation through clearances,” *Proc. Purdue Compress. Technol. Conf.*, pp. 35–40, 1994.

[82] P. Pandeya and W. Soedel, “Rolling piston type rotary compressors with special attention to friction and leakage,” *Int. Compress. Eng. Conf.*, pp. 209–218, 1978.

[83] T. Shiga, K. Ishijima, M. Sakainc, and I. Chu, “Analysis of The Rolling-Piston Type Rotary Compressor,” in *In: Proceedings of Purdue International Compressor Engineering Conference*, 1978, vol. 269, pp. 219–225.

[84] W. W. A. Reed, J. F. Hamilton, W. W. A. Reed, R. A. Y. W. H. Laboratories, and W. Lafayette, “Internal leakage effects in sliding vane, rotary compressors,” 1980.

[85] R. J. Rodgers, R. J. Rodgers, and J. J. Nieter, “Comprehensive Analysis of

Leakage in Rotary Compressors," *Int. Compress. Eng. Conf.*, 1996.

[86] T. Yanagisawa and T. Shimizu, "Foaming of refrigerating oil in a rolling piston type rotary compressor," *Int. J. Refrig.*, vol. 9, no. 1, pp. 17–20, 1986.

[87] T. Yanagisawa and T. Shimizu, "Leakage losses with a rolling piston type rotary compressor. II. Leakage losses through clearances on rolling piston faces," *Int. J. Refrig.*, vol. 8, no. 3, pp. 152–158, May 1985.

[88] T. Itoh, H. Kobayashi, M. Fujitani, and N. Murata, "Study on the oil supply system for rotary compressors," 1992.

[89] H. J. Kim and T. W. Lancey, "Numerical study on the lubrication oil distribution in a refrigeration rotary compressor," *Int. J. Refrig.*, vol. 26, no. 7, pp. 800–808, 2003.

[90] A. J. Lückmann, M. V. C. Alves, and J. R. B. Jr, "Analysis of Oil Pumping in a Reciprocating Compressor w F {&}," *Fluid Dyn.*, vol. 29, no. 14, pp. 1–8, 2008.

[91] A. T. Prata and J. R. Barbosa, "Role of the Thermodynamics, Heat Transfer, and Fluid Mechanics of Lubricant Oil in Hermetic Reciprocating Compressors," *Heat Transf. Eng.*, vol. 30, no. 7, pp. 533–548, 2009.

[92] E. Compressors, "Page 1 Fluid Flow in a Screw Pump Oil Supply System for Reciprocating Compressors," *Int. J. Refrig.*, vol. 34, no. 2009, pp. 1–8, 2010.

[93] N. S. D. M. Kumar, "Erfindungsmeldung Antriebsmotor für Elektrofahrzeuge mit integriertem Klimakompressor," Europe A 63 630 j, 2013.

[94] X. Hu, Z. Qu, X. Yang, and J. Sun, "Theoretical study on frictional losses of a novel automotive swing vane compressor," *Int. J. Refrig.*, vol. 36, no. 3, pp. 758–767, May 2013.

[95] I. Grace, "Comparison Of Hermetic Scroll And Reciprocating Compressors Operating Under Varying Refrigerant Charge And Load," in *International Compressor Engineering Conference*, 2002.

[96] ASHRAE, "High Efficiency Compression for," 2004.

[97] K. Okada and K. Kuyama, "Motion of Rolling Piston in Rotary Compressor," *Int. Compress. Eng. Conf.*, 1982.

[98] T. Yanagisawa, M. Mori, T. Shimizu, and Y. Ogi, "Vibration of a rolling piston type rotary compressor," *Int. J. Refrig.*, vol. 7, no. 4, pp. 237–244, Jul.

1984.

[99] S. Delmotte, “Development of a High Pressure, Oil Free, Rolling Piston Compressor,” in *International Compressor Engineering Conference*, 1994.

[100] D. Aradau and L. Costiuc, “Friction power in sliding vane type rotary compressors,” *Proc. Purdue Compress. Technol. Conf.*, pp. 907–912, 1998.

[101] K. T. OOI, X. WANG, P. K. CHEE, and C. W. Chong, “Revolving vane compressor.,” US8206140 B2, 2007.

[102] E. a. Avellone, T. Baumeister, and H. Saunders, *Marks Standard Handbook for Mechanical Engineers*, 11th ed., vol. 115, no. 1. McGraw Hill Professional,2006, 1993.

[103] Y. Serizawa, O. Matsushita, M. Shiga, M. Sutou, H. Hata, K. Sekiguchi, and Y. Nakada, “Rotary compressor with shaft balancers.” Google Patents, Jul-1993.

[104] F. Seve, A. Berlioz, R. Dufour, and M. Charreyron, “Balancing of a variable speed rotary compressor: experimental and numerical investigations,” 2000.

[105] T. Yanagisawa and T. Shimizu, “Friction losses in rolling piston type rotary compressors. III,” *Int. J. Refrig.*, vol. 8, no. 3, pp. 159–165, 1985.

[106] A. Futakawa, “Improvements in compressors with special emphasis on interesting developments in Japan,” 1984.

[107] B. J. Hamrock, B. O. Jacobson, and S. R. Schmid, *Fundamentals of machine elements*. McGraw-Hill Higher Education, 1999.

[108] R. Alizade, *Mechanism and Machine Theory*, vol. 39. New Age International (P) Limited, 2004.

[109] A. Harnoy, *Bearing design in machinery, Engineering tribology and lubrication*. Taylor & Francis, 2003.

[110] P. R. Trumpler, *Design of Film Bearings*. Macmillan New York, 1966.

[111] R. C. Juvinall and H. Saunders, *Fundamentals of Machine Component Design*, vol. 105, no. 4. Wiley Global Education, 1983.

[112] AutoDesk, “Autodesk Building Design Suite,” 2013. [Online]. Available: http://www.caddvision.nl/autodesk-building-design-suite/autodesk-building-design-suite-2013-brochure-en.pdf. [Accessed: 27-Oct-2014].

[113] R. Tiwari, “A Brief History and State of the Art of Rotor Dynamics,” *Mechanical Engineering*, 2008. [Online]. Available: http://www.iitg.ernet.in/scifac/qip/public_html/cd_cell/chapters/r_tiwari_ro

tor_bearing/chapter6/rtiwari_rd_book_06b.pdf.

[114] S. K. Padhy and S. N. Dwivedi, “Heat transfer analysis of a rolling-piston rotary compressor,” *Int. J. Refrig.*, vol. 17, no. 6, pp. 400–410, 1994.

[115] J. M. Weiksner, “Synchronizing Oil Cleanliness Standards to Machine Working Clearances,” 2000. [Online]. Available: http://www.machinerylubrication.com/Read/738/oil-cleanliness-standards. [Accessed: 27-Oct-2014].

[116] R. J. Rodgers, R. J. Rodgers, and J. J. Nieter, “Comprehensive Analysis of Leakage in Rotary Compressors,” *Int. Compress. Eng. Conf.*, 1996.

[117] W. W. A. Reed, J. F. Hamilton, W. W. A. Reed, R. A. Y. W. H. Laboratories, and W. Lafayette, “Internal leakage effects in sliding vane, rotary compressors,” 1980.

[118] P. Pandeya and W. Soedel, “Rolling piston type rotary compressors with special attention to friction and leakage,” *Int. Compress. Eng. Conf.*, pp. 209–218, 1978.

[119] SKF, “Friction losses of radial shaft seals as a function of rotational speed and shaft diameter.” [Online]. Available: http://www.skf.com/sg/products/seals/industrial-seals/power-transmission-seals/radial-shaft-seals/friction/index.html.

[120] D. Woollatt, “Reciprocating compressor valve design: optimizing valve life and reliability,” *Dresser-Rand Lit.*, 2003.

[121] H. Sheu and Y. Hu, “Nonlinear Vibration Analysis of Reed Valves,” 2000.

[122] K. T. Ooi, G. B. Chai, and E. C. Kwek, “A simple valve model to study the performance of a small compressor,” 1992.

[123] G. Prater and W. P. Hnat, “Optical measurement of discharge valve modal parameters for a rolling piston refrigeration compressor,” *Meas. J. Int. Meas. Confed.*, vol. 33, no. 1, pp. 75–84, 2003.

[124] J. R. Piechna, “Numerical Study of a Dynamic Behaviour of Simple Reed Valve,” 1984.

[125] A. K. Chopra, *Dynamics of Structures (3rd Edition)*, 4th Editio. Prentice-Hall International Series in Civil Engineering and Engineering Mechanics, 2006.

[126] Y. C. Park, “Transient analysis of a variable speed rotary compressor,” *Energy Convers. Manag.*, vol. 51, no. 2, pp. 277–287, Feb. 2010.

[127] F. Reference, D. Tools, T. Mathworks, C. Graphical, U. Interfaces, E. I. Reference, T. Language, T. Computing, M. Format, D. Analysis, P. Tips, G. Started, and E. Interfaces, "MATLAB The Language of Technical Computing," *Order A Journal On The Theory Of Ordered Sets And Its Applications*, 2006. [Online]. Available: http://www.mathworks.com/products/matlab/. [Accessed: 22-Jul-2013].

[128] NIST, "NIST Standard Reference Database," 2016. [Online]. Available: http://www.nist.gov/srd/nist1a.cfm. [Accessed: 23-Jul-2013].

[129] A. Subiantoro, "Development of a revolving vane expander.," 2012.

[130] N. S. Kumar, "Increasing the Cruise Range and Reducing the Capital Cost of Electric Vehicles by Integrating Auxiliary Unit with the Traction Drive," *Int. J. Veh. Technol.*, vol. 2016, 2016.

[131] C. M. Summers, "The Conversion of Energy," *Sci. Am.*, vol. 225, no. 3, pp. 148–160, 1971.